



The University of
Nottingham

UNITED KINGDOM • CHINA • MALAYSIA

**A holistic inverse approach on depth-sensing
indentation characterisation and its application for
predicting residual stresses in multi-phase inertia
friction welds**

Omar Adrian Iracheta Cabrera, BSc, MSc

Thesis submitted to The University of Nottingham for
the degree of Doctor of Philosophy

August 2017

Abstract

The present study is concerned with the development of an inverse analysis of the depth-sensing indentation test based on a multi-objective function (MOF) optimisation model. The input data of this model are the load-displacement ($P-h$) curve extracted from the indentation instrument and the surface topography of the residual imprint left by the indenter after the removal of the load measured via atomic force microscopy (AFM). A Swift's power law material model was considered to represent the indented material and thus, the output of the optimisation are the Young's modulus (E), yield stress (σ_y) and strain-hardening exponent (n). The optimisation problem was designed to minimise the error between both the experimental and predicted $P-h$ curves, i.e. the first objective, and pile-up profiles, i.e. the second objective, with the aim of addressing the non-uniqueness of the inverse analysis of indentation. A 3D FE model of the depth-sensing indentation test has been developed in ABAQUS in order to generate the predicted data from a set of trial material properties, i.e. E , σ_y and n . The generation of FE input files (pre-processor) and extraction of FE output files (post-processor) have been automated through MATLAB and Python subroutines. The optimisation problem was solved by the trust-region reflective algorithm available in the MATLAB Optimization Toolbox™ and thus, concisely, the model minimised the experimental and predicted data by modifying iteratively the material properties, starting from the initial guess properties specified by the user, until convergence was reached. Upon convergence, the material properties were said to describe the elastic-plastic behaviour of the indented material.

A comprehensive experimental programme was carried out in order to investigate the load dependency of the indentation response of three different materials, including a steel (CrMoV), a titanium alloy (Ti-6Al-4V) and a high-purity copper (C110). The study of the topography of the residual imprints provided a better understanding of the effects of the microstructural arrangement on the plastic displacement of material beneath the indenter. The extent of piling-up was observed to be very sensitive to the difference in material properties from grain to grain and the crystallographic plane of the indented grain. Furthermore, it was concluded that the structural arrangement of the indented material may also contribute to the asymmetry observed in the pile-up

profiles, in particular in materials with large grains relative to the projected area of the indenter, e.g. C110. This piece of work therefore, is suggested as a guideline for the use of height measurements of the residual imprint in the characterisation of the plastic behaviour of materials.

The multi-objective function optimisation model is proved to be a step forward to the characterisation of the near-surface properties as, in contrast to the $P-h$ curve, the residual imprint is strongly linked to the plastic behaviour of the indented material. Therefore, the physics governing the indentation problem were better represented. Therefore, the optimised $P-h$ curve provided a very good fit to the corresponding experimental curve, to within an error of less than 2.4% and 8.4% the maximum (h_{max}) and residual (h_r) depth, respectively, for all three materials, CrMoV steel, C110 copper and Ti-6Al-4V. Furthermore, a deviation of less than 12.4% was achieved between the area of indentation provided by the FE model and AFM instrument. Additionally, the value of maximum peak height (h_{peak}) was predicted with a maximum error of 11% in relation with the experimental pile-up profiles. Therefore, it was concluded that the optimised solution provided a very good representation of the complex mechanical response to indentation such that the volume of plastically displaced material as predicted by the optimised FE model was observed notably in accordance with experimental measurements. Furthermore, the complementary information provided by the second objective function allowed the model to distinguish between different materials showing identical indentation response – referred to in the literature as ‘mystical’ materials. In addition, a key outcome of this investigation suggested that stress-strain curves generated by mechanical tests performed at different scales, exhibit similar behaviour with only the magnitude of the stress increasing or decreasing depending upon the scale.

Part of this thesis is dedicated to the application of the proposed inverse analysis for the characterisation of three phases located across the joint of a like-to-like inertia friction weld of SCMV steel, including martensite in the tempered, quenched and over-tempered condition. This study, characterised the generation of residual stresses into two stages: the thermal strain dominated initial cooling period that accounts for the

majority of the residual stresses, and the phase transformation strain dominated final cooling period. In addition, it was concluded that at the onset of transformation from austenite to martensite, the volumetric changes experienced in the lattice relax up to 70% of the predicted tensile hoop stress found in the vicinity of the weld line near the inner surface and that the interaction of soft regions of austenite and hard regions of heat unaffected martensite accounts for up to 17% of the peak tensile stress. The indentation response of the set of optimised properties that represent each of the phases, was in very good agreement with the corresponding *P-h* curve and residual pile-up profile extracted from the indentation instrument and AFM, respectively. The capability of the inverse analysis to build the stress-strain relationship in the elastic-plastic regime using the optimised mechanical properties of the parent metal has been validated using experimental data extracted from the compressive test of an axisymmetric sample of tempered martensite [1]. The inclusion of the softer over-tempered martensite phase allowed the FE prediction to determine the proportion of the heat affected zone (HAZ) comprised by each phase in better agreement with the experimental weld-trial. Based on the interpretation of the microhardness test performed across the weld, the harder region formed due to the quenching process extends approximately 54% the length of the HAZ, whereas the rest 46% is comprised by the softer over-tempered martensitic phase. According to the FE prediction, the heat affected zone was composed by a proportion of 57% quenched martensite and 43% over-tempered martensite. Moreover, the distance from the weld line to the region where martensite fully tempered was observed to extend 79 and 71% the length of the HAZ, as determined by the FE model and experimental measurements, respectively. The presence of a softer region, OTM, between two harder regions, namely QM and TM, relaxed 7 to 11%, 1 to 6% and 12.8 to 15.3% the peak values of stress in the radial, axial and hoop directions respectively. A key observation from the results of the FE prediction was that the peak hoop residual stress is located at the boundary of the quenched and over-tempered martensite, and not at the edge of the heat affected zone. This observation was in agreement with the residual stress measurements published by Moat et al. [2].

Acknowledgements

I am truly grateful to my supervisors at the University of Nottingham, Dr Chris Bennett and Prof Wei Sun, for their guidance, encouragement and commitment to the highest standard throughout the doctoral programme. Thanks are also due to Prof Adib Becker and Dr Haofeng Chen for their insightful comments and suggestions that undoubtedly enriched this thesis.

I would also like to thank the Faculty Staff from the Wolfson Building and Nanoscale and Microscale Research Centre for providing me with the essential technical knowledge in preparation for the experimental work and guidance in operating the laboratory equipment. My gratitude also to my colleagues and friends at the Gas Turbine and Transmissions Research Centre, University of Nottingham, for their advice and guidance.

This accomplishment would not have been possible without the financial support provided by the National Council for Science and Technology (CONACyT) of Mexico, the Mexican Federal Department of Public Education (SEP) and the Roberto Rocca Education Program.

My warmest gratitude is extended to my family without whose support and encouragement, all this would never have been possible. I wish to thank my parents for their dedication and support throughout my life. Last, this work is dedicated with love to my wife Karla and our incredible son Leonardo; for your trust and patience throughout the last four years, thank you.

List of Publications

Bennett, C.J., Iracheta, O., Sun, W., *Characterisation of mechanical property variation across an inertia friction weld of a CrMoV steel*, TMS2014 Annual Meeting Supplemental Proceedings, San Diego, CA, USA., pp. 713-720.

Iracheta, O., Bennett, C.J., Sun, W., *A sensitivity study of parameters affecting residual stress predictions in finite element modelling of the inertia friction welding process*. International Journal of Solids and Structures, 2015. **71**: p. 180-193.

Iracheta, O., Bennett, C.J., Sun, W., *Characterization of material property variation across an inertia friction welded CrMoV steel component using the inverse analysis of nanoindentation data*. International Journal of Mechanical Sciences, 2016. **107**: p. 253-263.

Iracheta, O., Bennett, C.J., Sun, W., *The influence of the indentation size in relation to the size of the microstructure of three polycrystalline materials indented with a Berkovich indenter*. Materials Science and Engineering A, Accepted for publication.

Table of Contents

Abstract.....	i
Acknowledgements.....	iv
List of Publications.....	v
Table of Contents	vi
List of Figures.....	x
List of Tables	xviii
Nomenclature.....	xx
Chapter 1 - Introduction.....	1
1.1. Background	1
1.2. Research aims and objectives	1
1.3. Thesis outline	2
Chapter 2 - Literature review	4
2.1. Material characterisation using the inverse analysis of depth-sensing indentation data	4
2.1.1 The depth-sensing indentation test.....	4
2.1.2 Indentation size effects (ISE).....	7
2.1.3 Determination of material properties from P-h curves	9
2.1.3.1 Analytical-empirical models	9
2.1.3.2 The inverse analysis of the depth-sensing indentation test	11
2.1.4 Concluding remarks	21
2.2. Characterisation of material property variation in inertia friction welded components.....	21
2.2.1 Introduction	21
2.2.2 Material characterisation of the across-weld properties generated during the IFW process.....	24
2.2.3 Finite element predictions of residual stresses during IFW	29
2.2.4 Concluding remarks	31
2.3. Knowledge gaps	31
Chapter 3 - Research methodology.....	33
3.1. Experimental methods	33

3.1.1	Materials.....	33
3.1.2	Tensile testing	35
3.1.3	Inertia Friction Welding.....	36
3.1.4	Specimen preparation.....	37
3.1.5	Micro-hardness testing.....	37
3.1.6	Depth-sensing indentation test.....	38
3.1.7	Analysis of depth-sensing indentation data	41
3.1.8	Surface topography measurement.....	42
3.2.	Numerical methods.....	44
3.2.1	Finite element approach to indentation.....	44
3.2.2	Inverse analysis of the depth-sensing indentation test.....	56
3.2.3	Finite element modelling of the IFW process.....	59
Chapter 4 - Phase transformation induced residual stresses during the IFW process.....		68
4.1.	Introduction	68
4.2.	Thermo-mechanical evolution across an inertia friction weld of a SCM steel	69
4.3.	Strain components associated with heat transfer.....	71
4.4.	Evolution of residual stresses during IFW	73
4.5.	Effects of microstructural changes	76
4.5.1	Transformation strain.....	77
4.5.2	Inclusion of multiple phases.....	79
4.5.3	Effects of material properties in present phases.....	81
4.6.	Conclusions	82
Chapter 5 - Mechanical response to indentation at different loading scales		84
5.1.	Materials and tensile test	84
5.2.	Depth-sensing indentation data	89
5.3.	Measurements of residual imprints	93
5.4.	Effects of microstructure on the six-fold symmetry of Berkovich indentations	101
5.5.	Conclusions	104
Chapter 6 - Development of a multi-objective function optimisation model....		107

6.1. Introduction	107
6.2. Sensitivity of the solution to c , N and M	108
6.3. Effects of the bound constraints and initial guess vector	113
6.4. Effects of indenter tilt and surface roughness	114
6.5. Characterisation of ‘mystical’ materials.....	118
6.6. Concluding remarks	121
Chapter 7 - Recovery of elastic-plastic properties from depth-sensing	
indentation data.....	123
7.1. Introduction	123
7.2. Input data	123
7.3. Model set-up.....	128
7.4. Determination of the near surface elastic-plastic properties	129
7.4.1 Enhancement in convergence properties attained with an MOF model	
129	
7.4.2 Mechanical response to indentation as predicted by the optimisation	
model	136
7.4.3 Comparison of small volume properties and bulk properties	144
7.5. Concluding remarks	146
Chapter 8 - Characterisation of the across-weld properties in an inertia friction	
weld of SCMV steel	149
8.1. Introduction	149
8.2. Conventional and depth-sensing indentations across the HAZ.....	149
8.3. Determination of elastic-plastic properties across the weld via the multi-	
objective function optimisation technique	152
8.3.1 Robustness in predictions of the mechanical response to indentation	152
8.3.2 Constitutive relationships as determined by the MOF model.....	159
8.4. Residual stress field within the HAZ	163
8.4.1 Processing of the optimised constitutive relationships	163
8.4.2 Inclusion of the softer over-tempered martensite phase	165
8.5. Concluding remarks	170
Chapter 9 - Conclusions and suggestions for future work	172
9.1. Inverse analysis of the depth-sensing indentation test	172

9.1.1	Conclusions	172
9.1.2	Suggestions for future work	174
9.2.	FE prediction of the residual stress field in inertia friction welded components.....	176
9.2.1	Conclusions	176
9.2.2	Suggestions for future work	177
References	179
Appendix I - Multi-objective function optimisation model MATLAB code.....		194

List of Figures

Figure 2.1. Typical $P-h$ curve recorded during the depth-sensing indentation test.	5
Figure 2.2. Schematic diagram of the surface profile after full loading and unloading.	6
Figure 2.3. Classical and CMSG plasticity theories compared [32] to experimental results of Berkovich indentation on electro-polished nickel as reported by Pethica et al. [10]......	8
Figure 2.4. Dimensionless function (Equation 2.9), evaluated at a representative stress (σ_r) corresponding to plastic strain $\varepsilon_r=0.033$, generated with the expanded material space considered by Ogasawara et al. [60].	14
Figure 2.5. Schematic diagram of a typical inertia friction welding machine [80]. ..	22
Figure 2.6. Stages of the IFW process [81]......	22
Figure 2.7. a) Schematic diagram of the typical thermo-mechanical behaviour and b) generated metallurgical zones in IFW welds.	24
Figure 3.1. Dimension in mm of tensile specimens for a) CrMoV steel, C110 copper and b) Ti-6Al-4V.....	35
Figure 3.2. Geometry of the workpieces welded by the IFW process.	36
Figure 3.3. SEM images of the Berkovich indenter tip using secondary electrons at an acceleration voltage of 10.0 kV.....	38
Figure 3.4. Schematic diagram of indentation sites across the IFW joint. Units are in mm unless otherwise specified. The diagram is for illustration purposes only and thus not in scale.	41
Figure 3.5. Schematic top view and cut view of a residual indentation left by a three-side Berkovich indenter. The diagram assumes piling-up dominated deformation.	43
Figure 3.6. Schematic of the geometry of the Berkovich indenter showing a six-fold symmetry.....	44
Figure 3.7. Geometry and boundary conditions defined in the 3D indentation model. One-sixth of the domain.....	46

Figure 3.8. FE solution to indentation problem using tetrahedral elements with reduced integration and hexahedral elements with both reduced and full integration.....	46
Figure 3.9. Geometry and boundary conditions defined in the 3D indentation model. Full domain.	47
Figure 3.10. Sensitivity of h_{max} to the mesh size at the contact zone. CM refer to the coarsest mesh.....	49
Figure 3.11. Local stiffness of the deformable body at a point beneath the tip of the indenter.....	50
Figure 3.12. Effects of the mesh size on the shape of the loading curvature of indentation.....	50
Figure 3.13. Sensitivity of h_{max} to loading steps.	51
Figure 3.14. $P-h$ curves predicted using second order elements.....	52
Figure 3.15. Effects of the a) yield strength and b) elastic modulus on the predicted empirical parameters of loading and unloading.	54
Figure 3.16. Effects of the variation of σ_y , E , ν , and n on the maximum indentation depth (h_{max}).....	55
Figure 3.17. Sensitivity of surface topography to the strain-hardening exponent n . Plot in the direction U1 normalised as a ratio of radial distance (r) to total length (L) in the radial direction.....	56
Figure 3.18. Flow chart of the multi-objective function optimisation procedure.	59
Figure 3.19. Welding model set-up and boundary conditions.	61
Figure 3.20. Sensitivity of the interfacial mesh size on the final upset value.....	63
Figure 3.21. Levels of yield stress taken from the hot compression testing in SCMV steel carried out by Bennett et al. [81] at different temperatures. The yield stress of austenite on cooling has been obtained from linear extrapolation.	65
Figure 4.1. Transformation paths for each FE simulation of IFW.....	69
Figure 4.2. Sequence of micrographs showing the characteristic regions comprising the HAZ generated by IFW in the SCMV steel.	70
Figure 4.3. Microhardness profile across the HAZ at mid-wall of a SCMV steel weld trial.	70

Figure 4.4. Temperature profile at the start of the initial cooling period along an axial line at the MD..... 72

Figure 4.5. a) Temperature profile and b) associated response in the evolution of the von Mises stress at a point in the mid-wall of the weld line during cooling. 72

Figure 4.6. Contour plots of Simulation A showing the residual stress field at the end of the a) welding stage, b) initial cooling period and c) final cooling period. 74

Figure 4.7. Evolution of the predicted von Mises stress field by the FE model (simulation A) at three radial distances: a) 1 mm depth from the ID, b) mean diameter, c) 1 mm depth from the OD..... 75

Figure 4.8. Radial displacement in the outer surface at the end of the initial cooling period..... 76

Figure 4.9. Residual stress field in the as-welded condition predicted by the FE model neglecting phase transformations (simulation A) at a) 1 mm depth from the ID, b) MD and c) 1 mm depth from the OD compared with the simulation accounting for the effect of the phase transformation strains (simulation B) at d) 1 mm depth from the ID, e) MD and f) 1 mm depth from the OD. 79

Figure 4.10. Effects of the variation in mechanical properties arising from phase transformations occurring across the HAZ on the residual stress field predicted in the as-welded component at a, d) 1 mm from the ID, b, e) MD and c, f) 1 mm from the OD. 81

Figure 4.11. Sensitivity on the peak von Mises stress to small variations in material properties (shown in x-axis) of the present phases (identified by markers). 82

Figure 5.1. Engineering stress – engineering strain curves extracted from tensile testing of specimens of CrMoV steel, C110 copper and Ti-6Al-4V. 85

Figure 5.2. Microstructure as observed a) in C110 by optical microscopy and by SEM in b) CrMoV and c) Ti-6Al-4V. 86

Figure 5.3. Sensitivity of hardness value to the indentation load for a) C110, b) CrMoV and c) Ti-6Al-4V. Error bars represent 1 standard deviation..... 88

Figure 5.4. Optical micrographs showing residual imprints of indentations at various loads on C110 copper. 89

Figure 5.5. Indentation $P-h$ curves (left) and calculated Martens hardness (right) for a, b) C110 copper, c, d) CrMoV steel and e, f) Ti-6Al-4V. Error bars are one standard deviation. 91

Figure 5.6. AFM topography of CrMoV steel surface after mechanical polishing using a) 1 μm diamond suspension and b) 0.06 μm colloidal silica. 92

Figure 5.7. Effects of surface preparation on hardness at different load values. 93

Figure 5.8. a) Height sensor measurement and b) pile-up patterns along the three edges of the residual imprint after the indentation at 240 mN of a polished surface of CrMoV steel with 1 μm diamond suspension. 94

Figure 5.9. a) Height sensor measurement and b) pile-up patterns along the three edges of the residual imprint after the indentation at 240 mN of a polished surface of CrMoV steel with 0.06 μm colloidal silica. 94

Figure 5.10. a) Height sensor measurement and b) cross-section profile of the imprint in C110 formed by a Berkovich indenter loaded to 120 mN. 96

Figure 5.11. a) Height sensor measurement and b) cross-section profile of the imprint in C110 formed by a Berkovich indenter loaded to 36 mN. 97

Figure 5.12. Residual imprints left by an indenter tilted with respect to the normal of the surface by 2° around a, b) U1, c, d) U3, and e, f) U1 and U3. 98

Figure 5.13. a) Top view and b) cut view AA showing the equivalent plastic strain beneath a perfectly sharp indenter and perfectly aligned with the normal of the surface. The plastic equivalent strain (PEEQ) profile corresponds to a load $P = P_{max}$ 100

Figure 5.14. a) Pile-up patterns and b) plastic equivalent strain (PEEQ) along section OA. 100

Figure 5.15. a) Optical micrograph and b) surface topography after a macrohardness Vickers indenter test at 20 kgf performed on the C110 specimen. The c) surface profile has been extracted from scans along segments AA' and BB'. 103

Figure 5.16. Residual imprints left by the Berkovich indenter pressed with a maximum load of a) 240 mN and b) 30 mN in Ti-6Al-4V as observed under BSE/SEM (left) and AFM (right).....	104
Figure 6.1. Effects of scaling coefficients on the optimised parameters.	108
Figure 6.2. Global contribution of each objective function along the optimisation procedure set up with a scaling coefficient of a) $c_1 = c_2 = 1$, b) $c = 0.75$ and c) $c = 0.25$	111
Figure 6.3. Iteration history showing the negligible sensitivity of the optimisation parameter a) E , b) σ_y and c) n to the number of data points M and N along the P - h curve and pile-up profile, respectively.	113
Figure 6.4. Convergence of simulations starting +40 (dashed line) and -40% (solid line) apart from the target values.....	114
Figure 6.5. Pile-up profile in its original geometry and disturbed by $\pm R_a = 5$ nm to represent the surface roughness after a 1 μm diamond suspension polishing procedure.....	115
Figure 6.6. Iteration history showing the negligible sensitivity of the MOF model to the surface roughness represented as noise generated by disturbing the pile-up profile data points with random values within $\pm R_a$	115
Figure 6.7. a) Height measurements and b) pile-up profiles of a residual imprint left by a Berkovich indenter tilted 2° around both the +U1 and +U3 axes.	116
Figure 6.8. Uniaxial constitutive relationship built by evaluating the optimised parameters into Swift's model. Subsets a) and b) are respectively concerned with the properties extracted from the indentation performed with an indenter tilted 2° around both the +U1 and +U3 axes, and 1° around the +U3 axis.	117
Figure 6.9. Different elastic-plastic materials that yield indistinguishable P - h curves, i.e. mystical materials [73].	119
Figure 6.10. Iteration history through a) SOF and b) MOF optimisation model using material B as the initial guess parameters.	120
Figure 7.1. P - h curves and pile-up patterns selected for recovering the mechanical properties of a), b) CrMoV steel, c), d) C110 copper and e), f) Ti-6Al-4V.	125

Figure 7.2. Iteration history through the minimisation problem of a), c), e) single objective and b), d), f) multiple objectives for the determination of elastic-plastic properties of CrMoV steel. 131

Figure 7.3. Iteration history through the minimisation problem of a), c), e) single objective and b), d), f) multiple objectives for the determination of elastic-plastic properties of C110 copper..... 133

Figure 7.4. Iteration history through the minimisation problem of a), c), e) single objective and b), d), f) multiple objectives for the determination of elastic-plastic properties of Ti-6Al-4V..... 135

Figure 7.5. Fitting of optimised curve to experimental curve via the single- and multiple- objective function optimisation model for the corresponding material: a) CrMoV steel, b) C110 copper and c) Ti-6Al-4V..... 137

Figure 7.6. Top views of the residual imprints on specimens of a) CrMoV steel, b) C110 copper and c) Ti-6Al-4V. The left column presents the height measurements provided by the AFM and the right column the FE predictions using the optimised properties..... 140

Figure 7.7. Experimental pile-up profile in indentations of a), b) CrMoV steel, c), d), C110 copper and e), f) Ti-6Al-4V fitted by the single- (left) and multiple- (right) objective function optimisation model..... 143

Figure 7.8. Constitutive relationship as determined by the multiple-objective function optimisation model (dashed lines). The engineering stress-engineering strain extracted from the tensile test has been superimposed (solid lines). 145

Figure 7.9. Pile-up profile extracted from the residual imprint left by the Berkovich indenter in CrMoV steel loaded to 0.24 and 0.12 *N*. Data have been normalised with h_0 for comparison. 146

Figure 8.1. Microhardness profile across the HAZ of an SCMV steel weld trial. Error bars in the mean HM measurements represent 1 standard deviation. ... 150

Figure 8.2. Experimental *P-h* curves corresponding to tempered martensite (TM), quenched martensite (QM) and over-tempered martensite (OTM) phase. 151

Figure 8.3. Height measurements in the characteristic regions a) QM, b) OTM and c) TM. Measurements below the reference (0 nm) have been suppressed to show the topography around the indentation in more detail. In addition, the projected area of the indenter (A_p) has been superimposed (dashed line) to illustrate the apparent extent of plastic recovery.....	152
Figure 8.4. Evolution of the optimisation parameters from the initial guess values starting at LG and UG.	155
Figure 8.5. Relative difference [%] between each pair of optimisations at the initial (guess) and final (converged) iteration.....	156
Figure 8.6. Comparison of P - h curves obtained from experimental data and FE model using the optimised parameters for martensite in the a) tempered, b) quenched and c) over-tempered condition.	157
Figure 8.7. Contour plot (one-sixth of the domain) showing the plastic strains on the indented surface as predicted by the FE model at P_{max} (dotted) and P_0 (solid). The constitutive behaviour corresponds to optimised properties for QM as reported in Table 8.2.....	158
Figure 8.8. Comparison of pile-up profiles obtained from experimental data and FE model using the optimised parameters for martensite in the a) tempered, b) quenched and c) over-tempered condition.	159
Figure 8.9. Comparison of the stress-strain curve generated experimentally from a compression test on a SCMV steel sample [1] and the curve built using the optimised material properties predicted by the inverse analysis.....	161
Figure 8.10. Schematic illustration of the impression left by a Vickers indenter loaded at 0.5 kg and the projected area of the Berkovich indenter penetrating the tempered martensite lattice.....	161
Figure 8.11. Processing of material properties to account for the temperature-dependency of the a) yield stress and b) Young's modulus and the continuity between phases at the transformation temperatures.....	165
Figure 8.12. Volume fractions across the joint as predicted by the a) four-phase and b) three-phase FE model.....	166
Figure 8.13. Contour plots showing the von Mises stress generated in the as-welded condition as predicted by the a) three-phase (TM, AUST, QM) and b) four-	

phase (TM, AUST, OTM, QM) FE model. The material database includes the constitutive behaviour of the corresponding phases as characterised by the MOF model.	168
Figure 8.14. Residual stress profiles predicted in the as-welded component at a, b, c) 1 mm from the OD, d, e, f) MD and g, h, i) 1 mm from the OD by the three-phases (TM, AUST, QM) and four-phases (TM, AUST, OTM, QM) FE model. The stress direction is indicated by the title of the ordinate.....	169
Figure 8.15. a) Retained austenite volume fraction as an indicative of martensitic transformation and b) hoop residual stress map. Colour map from white to black represents a higher volume fraction and more positive stress in a) and b) respectively.	170

List of Tables

Table 3.1. Chemical composition of studied materials (weight %) as per a) Columbia metals, b) Aircraft materials, c) US Patent 20150083284 and d) VSMPO-Trius.	34
Table 3.2. Initial process parameters for welding	36
Table 3.3. Parameters used in the different depth-sensing indentation tests.	40
Table 4.1. Simulations to examine the effects of the inclusion of multiple phases in the FE model	68
Table 5.1. Uniaxial properties of CrMoV, C110 and Ti-6Al-4V extracted from the engineering stress-engineering strain curve.	85
Table 5.2. Vickers hardness values of CrMoV steel, C110 copper and Ti-6Al-4V. .	89
Table 5.3. Imprint area of indentation measured via AFM (A) compared with the area projected by an ideal indenter at h_{max}	95
Table 5.4. Ratio of maximum pile-up to maximum indentation depth as measured via atomic force microscopy.	102
Table 6.1. Relative error [%] between optimised and target parameters and number of iteration.....	109
Table 6.2. Results of the optimisation procedure assuming an indenter tilted 2° around both the +U1 and +U3 axes, and 1° around the +U3 axis.....	117
Table 6.3. Sets of dissimilar mechanical properties that exhibit identical indentation response, i.e. mystical materials.....	119
Table 6.4. Set up and results for optimisation of mystical materials	120
Table 7.1. Deviation between experimental P - h curves and those predicted by the FE model using the mechanical properties determined from the tensile test.	126
Table 7.2. Residual indentation depth as measured by the indentation instrument (h_r) and AFM (h_o).	127
Table 7.3. Bound constraints imposed to the optimisation procedures of CrMoV steel, C110 copper and Ti-6Al-4V.	128
Table 7.4. Initial guess parameters selected to initialise the optimisations of CrMoV, Ti-6Al-4V and C110 using single- and multiple-objective functions...	129

Table 7.5. Characterised properties of CrMoV after single- and multi-objective function optimisation.....	132
Table 7.6. Characterised properties of C110 copper after single- and multi-objective function optimisation.....	134
Table 7.7. Characterised properties of Ti-6Al-4V after single- and multi-objective function optimisation.....	136
Table 7.8. Imprint area of indentation measured via AFM (A) compared with predicted area by the FE model after convergence (A_{FE}).....	138
Table 7.9. Mean values of the peak pile-up height (h_{peak}) and residual depth (h_0) as predicted by the SOF and MOF.	143
Table 7.10. Constitutive parameters as determined by the uniaxial tensile test and inverse analysis of depth-sensing indentation data via the MOF model.	146
Table 8.1. Values of hardness and area of the residual imprints measured in indentations used in the optimisation procedures.	152
Table 8.2. Set up and results for the optimisation of the across-weld properties in an inertia friction weld of SCMV steel.	154
Table 8.3. Lengths covered by the martensite in the quenched and over tempered condition, in proportion to the length of the HAZ, as predicted by the FE model and those inferred from the microhardness test (Figure 8.1).	167

Nomenclature

Roman symbols

A	Imprint area of indentation measured via atomic force microscopy
A_c	Contact area at the interface of the workpieces
A_e	Projected area of the elastic contact
A_p	Projected area of the indenter
A_{c1}, A_{c3}	Temperatures in the equilibrium phase diagram at which austenite begins to form during heating (lower critical temperature) and at completion of austenite transformation (upper critical temperature)
A_{gauge}	Gauge area
A_{r3}	Temperature in the equilibrium phase diagram at which austenite begins to transform to ferrite during cooling
c	Scaling coefficient in MOF model
C	Loading curvature of indentation
C_c, C_f	Contact compliance and frame compliance
d	Size of the elements at the contact zone beneath the indenter
E	Young's modulus
E^*	Reduced modulus
E_k	Kinetic energy
$f_1(x_j), f_2(x_j)$	First and second objective function in the optimisation model
f_s	Surface traction
F	Axial load during welding
h	Indentation depth
h_0, h_{peak}	Residual depth and maximum pile-up height measured by the AFM
h_c	Plastic contact depth measured from the tip of the indenter
h_{max}, h_r	Maximum and residual depth recorded in the $P-h$ curve
HM, HV	Martens and Vickers hardness
i	Iteration number during optimisation procedure

I	Moment of inertia
k_e, k_p	Representative underlying element stiffness and penalty stiffness
K	Strength coefficient
n	Strain-hardening exponent
N, M	Number of interpolated sample points included to define the P - h curve and geometry of the residual imprint, respectively.
M_A, M_B	Martensitic transformation constants
p	Normal pressure during welding
P	Indentation load
P_i, P_{max}	Initial and maximum indentation load
P_L, P_U	Loading and unloading portion of the P - h curve
PSI_g	Gauge pressure
r_i, r_o	Inner and outer radii at the contact of the weld interface
R_a	Average roughness
s	Simulation time step in FE of IFW
S	Slope of the unloading curve as h tends to h_{max}
t	Time
T	Average element temperature
T_{Ae}, T_{As}	Austenite transformation end and start temperatures
T_e, T_s	Environment and surface temperatures
\bar{T}	Torque
u	Nodal velocity
$U1, U2, U3$	Global coordinates of the indentation space. The direction of the application of the indentation load is aligned with U1.
ν	Poisson's ratio
\mathbf{x}	Vector of material properties
y	Axial coordinate of the residual imprint

Greek symbols

β_{IJ}	Fractional length change due to transformation from phase I to phase J
δ_{ij}	Kronecker delta
$\varepsilon_e, \varepsilon_p, \varepsilon_T$	Elastic, plastic and thermal strain components
ε^{Tr}_{IJ}	Transformation strain from phase I to phase J
$\dot{\varepsilon}$	Effective strain rate
$\dot{\varepsilon}_0$	Limiting strain rate
$\dot{\varepsilon}_{ij}$	Deviatoric strain rate tensor
$\dot{\varepsilon}^{Tr}_{IJ}$	Transformation strain rate
θ	Indenter half-angle
μ	Coulomb friction coefficient
ζ_J	Austenite volume fraction
$\dot{\zeta}_J$	Transformation volume fraction rate
ζ_M	Martensite volume fraction
σ_y	Yield stress
$\bar{\sigma}$	Flow stress
σ'_{ij}	Deviatoric stress tensor
$\bar{\sigma}_0$	Flow stress as a function of effective strain and limiting strain rate
σ_r, ε_r	Representative stress at the representative plastic strain ε_r of uniaxial deformation
$\sigma_r', \varepsilon_r'$	Representative stress at the representative plastic strain ε_r' of equi-biaxial deformation
ψ_1, ψ_4	Austenitic transformation constants
ω	Angular velocity

Abbreviations

AUST	Austenite
AFM	Atomic force microscopy
FPZ, PDZ, UZ	Fully-plasticised, partially deformed and undeformed zones

HAZ	Heat affected zone
ID, MD, OD	Inner, mean and outer diameters
IFW	Inertia friction welding
ISE	Indentation size effect
LG, UG	Lower and upper guess vectors in an optimisation procedure
LS, HS	Lowest and highest stiffness $P-h$ curve from a set of indentations.
MOF	Multi-objective function
$P-h$	Load displacement curve
QM, TM, OTM	Martensite in the quenched, tempered and over-tempered condition
SCMV	Super Chromium-Molybdenum-Vanadium
SEM	Scanning electron microscopy
SOF	Single-objective function
WL	Weld line

Chapter 1 - Introduction

1.1. Background

In the pursuit of mechanical components with a superior performance, different material processing technologies have been designed to manufacture components that exhibit a combination of various, and sometimes conflicting properties, e.g. hardness and toughness. For instance, the inertia friction welding (IFW) process was designed to conceive welds of dissimilar materials with the aim of tailoring varying material properties across a component [3].

Traditional mechanical testing techniques however, e.g. the tensile and compressive test, are not able to measure the local mechanical response of a material at a very small scale. Therefore, recent years have seen an increased interest in the mechanical characterisation of materials via the depth-sensing indentation test as it provides an easy, cost-effective and in some cases non-destructive method of evaluating properties from very small volumes of materials. The depth-sensing indentation test has found numerous applications such as the characterisation of thin films and surface coatings [4-6], investigation of single crystals [7, 8] and in the determination of residual stresses [9]. This study proposes the application of the depth-sensing indentation technique to characterise the property variation in a material subjected to mechanical and thermal loads during the IFW process.

1.2. Research aims and objectives

The present study concerns the development of an inverse analysis of the depth-sensing indentation test based on a multi-objective function (MOF) optimisation model to recover the mechanical properties of small volumes of material. Therefore, the indentation response recorded by the load-displacement ($P-h$) curve was complemented with the information provided by the geometry of the residual imprint of indentation measured via atomic force microscopy (AFM) so as to address the non-uniqueness issue of the inverse analysis of indentation.

The proposed inverse analysis was applied to improve the material database of a Super Chromium Molybdenum Vanadium (SCMV) steel in the fully heat-treated condition which has been used to develop an FE methodology to simulate the IFW process [1]. Therefore, three phases that exist across the joint of an inertia friction welded SCMV steel, namely martensite in the tempered, quenched and over-tempered conditions, have been characterised by means of the inverse analysis.

An experimental programme, based on three single materials including a steel (CrMoV) a high purity copper (C110) and a titanium alloy (Ti-6Al-4V) has been carried out in order to provide a better understanding into the effects of the indentation scale on the mechanical response of the material and to prove the generality of the model to recover the elastic-plastic mechanical properties of a variety of materials.

1.3. Thesis outline

Chapter 2, the literature review, discusses the state-of-the-art in material characterisation techniques based on the depth-sensing indentation test. In addition, it provides an introduction to the existent methodologies concerned with the investigation of the microstructural evolution during the IFW process.

Chapter 3 introduces the experimental programme carried out to extract and interpret the input data for the optimisation model, i.e. the $P-h$ curve and the geometry of the residual imprint. Details of the FE models employed for the development of this study, including a 3D model of the indentation test and a 2.5D model of the IFW process, are also presented.

Chapter 4 presents the outcomes of a sensitivity study of the factors affecting residual stress predictions in FE modelling of the IFW process, in which the importance of accounting for the material property variation across the joint is highlighted.

Chapter 5 analyses the data extracted from the depth-sensing indentation test performed on the three materials, CrMoV steel, C110 high purity copper and Ti-6Al-

4V. The analysis investigates the effects of the microstructure on the response of the material to indentation, the gap between the small scale properties measured by the depth-sensing indentation instrument and large scale (or bulk) properties and the effects of the metallographic preparation of specimens.

In **Chapter 6**, the power of the multi-objective function optimisation model to converge to a unique solution is presented with theoretical-experimental (FE simulated) data. Furthermore, pairs of ‘mystical’ materials, i.e. materials with different sets of mechanical properties that exhibit an identical indentation response, were optimised. In addition, the experimental error investigated in Chapter 5 is accounted for in this assessment.

Chapter 7 proves the generality of the multi-objective function optimisation model to recover the elastic-plastic mechanical properties of three different materials, CrMoV, C110 and Ti-6Al-4V. This chapter discusses in detail the gap between the scale-dependent mechanical response to indentation of a crystalline material and the solution of the conventional FE model of indentation based on the continuum mechanics approach.

Chapter 8 presents the application of the multi-objective function optimisation model to provide a solution to a current engineering problem. Therefore, the three phases located across the joint of a like-to-like IFW of an SCM steel have been characterised. This chapter also investigates via FE modelling the residual stress field in the as-welded component due to the interaction of four phases (austenite and martensite in the quenched, tempered and over-tempered condition) formed during IFW of SCM steel.

The main conclusion and contributions of this research are detailed in **Chapter 9** and suggestions for future work are presented.

Chapter 2 - Literature review

2.1. Material characterisation using the inverse analysis of depth-sensing indentation data

2.1.1 *The depth-sensing indentation test*

The depth-sensing indentation test emerged as a new technique during the early 1980's [10-12] to deal with the mechanical characterisation of elastic properties (Young's modulus and hardness) of small volumes of material. The capability of this technique to provide elastic information of the material is achieved by including an unloading stage preceded by the loading stage. The indentation test can be set up either as load or depth controlled; during the load control test, the indentation depth, h , is recorded as a function of the applied load, P , and vice versa during the depth control test, such that a load-depth ($P-h$) curve is generated. Depth-sensing indentation test is categorised by ISO 14577 [13] as follows:

- Macroindentation: $2 \text{ N} \leq P_{max} \leq 30 \text{ kN}$
- Microindentation: $P_{max} < 2 \text{ N}$ and $h_{max} > 0.2 \text{ }\mu\text{m}$
- Nanoindentation: $h_{max} \leq 0.2 \text{ }\mu\text{m}$

where P_{max} and h_{max} are the maximum indentation load and depth respectively. Since the residual impression left by the indenter at full load is in the nano- or micro-scale, the area of contact is not measured directly as in conventional indentation (e.g. via optical microscopy) but is rather determined from the indentation depth at full load, provided the geometry of the indenter is known.

The significant improvements achieved, make the depth-sensing indentation test suitable for measuring not only the hardness of materials, but also the elastic modulus. Furthermore, more advanced methods allow the study of residual stresses, properties of materials at high temperatures, scratch resistance and film adhesion [14].

In a load controlled test, the depth-sensing indentation instrument records the depth of penetration beneath the surface of the specimen as a function of the controlled load applied through an indenter [14], as schematically illustrated by the typical load-displacement ($P-h$) curve shown in Figure 2.1.

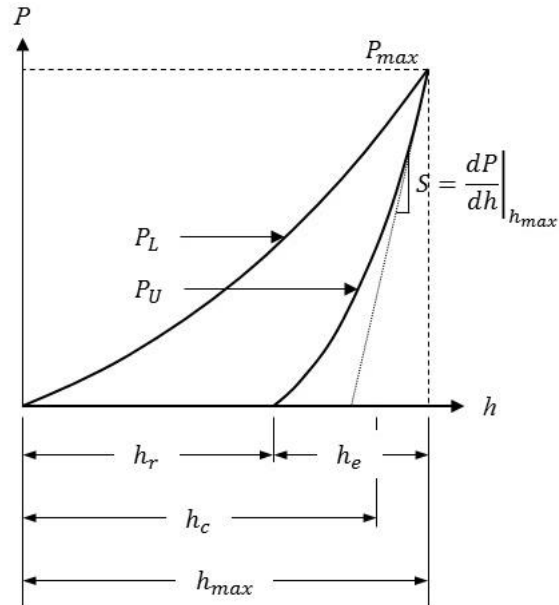


Figure 2.1. Typical $P-h$ curve recorded during the depth-sensing indentation test.

The loading portion of the $P-h$ curve (P_L) involves a combination of both elastic and plastic deformation and is well approximated by Kick's Law for elastic, elastic-perfect plastic and elastic-plastic materials using conical or pyramidal perfectly-sharp indenters [15-19]:

$$P_L = Ch^2 \quad 2.1$$

where P_L is the loading force, h is the indentation depth and C is the loading curvature, which is related to the geometry of the indenter tip and the material properties of the specimen. As the indenter moves into the material, a peripheral contact is established between the indenter and the deformed surface of the specimen at a distance h_c measured from the tip of the indenter, known as the plastic contact depth, as illustrated in Figure 2.2.

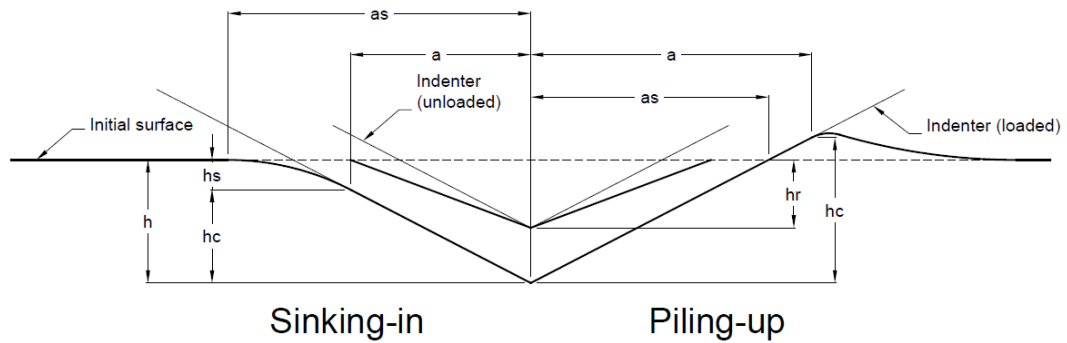


Figure 2.2. Schematic diagram of the surface profile after full loading and unloading.

Furthermore, when the contact involves plastic deformation the surface near the indenter tends to either sink-in or pile-up. During the fully plastic regime, it is observed that this behaviour is dependent on the strain hardening exponent n and the ratio E/σ_y [14] as follows: low- or non-strain-hardening materials (e.g. a highly work-hardened metal) with a high value of E/σ_y deform more locally causing plastically displaced material to pile-up around the indenter due to the incompressibility of plastic deformation. Sinking-in on the other hand is more pronounced for strain-hardening (e.g. a heavily annealed metal) or non-strain hardening materials with a low value of E/σ_y as the plastically displaced material is accommodated mainly by far-field elastic displacements such that hardened material due to plastic deformation pushes deeper the softer material located at the outermost of the plastic zone. As expected, the accurate determination of the contact area, and consequently the hardness value, is affected by these phenomena. Piling-up and sinking-in of material results in a residual impression the sides of which are deformed into concave and convex shapes, respectively. Consequently, piling-up and sinking-in cause the actual contact area to be respectively greater than and less than the cross-sectional area of the indenter at the indentation depth. Upon unloading, it is assumed that only elastic displacements are recovered (h_e in Figure 2.1) and therefore after the load is completely removed, the indenter leaves an impression in the specimen of residual depth h_r [20]. The slope dP/dh at $h = h_{max}$ is known as the contact stiffness S . The loading curvature C , the contact stiffness S and the ratio of residual depth to maximum indentation depth h_r/h_{max} , are three characteristic parameters typically used to interpret a single $P-h$ curve. It is to be noted that the measured displacements are the sum of the

displacements in the specimen, the contact compliance (C_c), and the elastic displacements of the load frame of the instrument, i.e. the frame compliance (C_f). Therefore, the total compliance of the testing system is:

$$C_T = C_f + C_c \quad 2.2$$

where C_c is given by the inverse of the contact stiffness, i.e. $C_c=1/S$ [20]. Different sources of error during the indentation test may induce an offset to the depth measurements and therefore before any analysis is performed, experimental $P-h$ curves must be corrected for initial penetration, instrument compliance and in some cases, thermal drift [14]. Furthermore, at low indentation depths, the self-similarity of the indenter is lost due to tip imperfections and therefore the indenter tip shape must be calibrated by an area function to account for the dependency of the true contact area to indentation depth as proposed by, e.g. Oliver and Pharr [20] or McElhaney et al. [21] to account for pile-up/sink-in effects in addition. Alongside piling-up and sinking-in, one of the major issues that affect the validity of depth-sensing indentation data is the material related indentation size effects [14].

2.1.2 Indentation size effects (ISE)

According to the dislocation theory, the plastic flow strength, or hardening, in solids is due to the combined effects of strain gradients and plastic strains. Large strain gradients inherent in small indentations generate dislocations that are necessary to accommodate the lattice curvature resulting from non-uniform plastic deformation, i.e. to account for the permanent shape change at the surface, and thus are known as geometrically necessary dislocations (GNDs). These dislocations, in addition to the statistically stored dislocations (SSDs), accumulate a total density of dislocations and contribute to the increase in plastic flow strength. Therefore, GNDs are explained as an extra storage of deformation defects in the presence of a plastic strain gradient [22, 23]. SSDs on the other hand, are created by uniform plastic deformation through random interactions among dislocations and therefore size-dependent plasticity, also commonly referred to as indentation size-effect (ISE), at small indentation depths, has

been attributed to GNDs resulting from strain gradients [8, 24, 25]. Therefore, it is observed that the measured hardness increases significantly with decreasing indentation depth in indentation tests at the submicron scale [26]. Since strain gradient effects are not accounted for by the conventional plasticity theory, due to the absence of an intrinsic material length scale in the constitutive model, typical FE simulations assume that the indentation depth is sufficiently deep so that continuum mechanics still applies, and are therefore limited to simulating indentations at depths larger than any microstructural size parameter, i.e. macroindentation. Based on the concept of GNDs, a few analytical relationships between both microindentation [24, 27] and nanoindentation [28] hardness and indentation depth have been proposed, and a handful of FE models have been developed to account for strain gradient plasticity, either by invoking a higher-order C^I continuum, e.g. the mechanism-based strain gradient (MSG) plasticity theory [29, 30], or a more conventional C^0 continuum theory, e.g. the conventional mechanism-based strain gradient (CMSG) plasticity theory [31]. The latter avoids the necessity of satisfying additional boundary conditions as the higher-order strain is implemented in the constitutive model and thus the equilibrium equations are identical to those in conventional continuum theories. As confirmed by Swaddiwudhipong et al. [32] (Figure 2.3) the finite element solution based on CMSG plasticity theory agrees better with the experimental indentations at sub-micron level on electro-polished nickel reported by Pethica et al. [10] when compared to the classic plasticity FE formulation. A deviation of $\sim 25\%$ between classical and CMSG plasticity theory is observed.

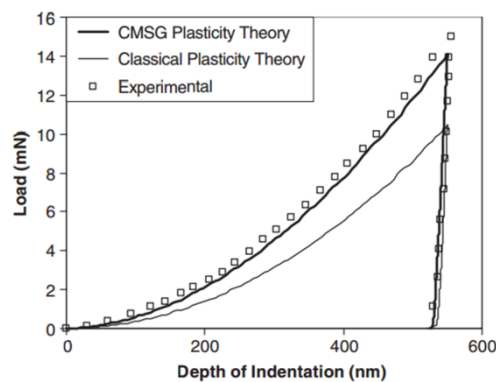


Figure 2.3. Classical and CMSG plasticity theories compared [32] to experimental results of Berkovich indentation on electro-polished nickel as reported by Pethica et al. [10].

Both MSG and CMSG adopt Taylor's hardening model [33] to account for strain gradients, however other rate-dependent hardening models have been used to study ISE, e.g. Bassani and Wu's model in the work presented by Liu et al. [34, 35]. Notwithstanding, hardness depth dependence can also be influenced by experimental artefacts such as the effects of surface hardening (e.g. due to mechanical polishing [36]), tip imperfections [21, 28], surface oxidation or contamination [37], surface roughness, etc. and it is therefore very difficult to quantify the effects of GNDs on the ISE.

2.1.3 Determination of material properties from P-h curves

2.1.3.1 Analytical-empirical models

Based on Sneddon's work [38], Ternovskii et al. [39] presented one of the initial attempts for measuring the elastic modulus from instrumented indentation data as follows:

$$S = \frac{dP}{dh} = E^* \sqrt{A_e} \quad 2.3$$

where S is the contact stiffness, A_e is the projected area of the elastic contact and E^* , the reduced modulus is introduced to account for the elastic behaviour between the non-rigid indenter and the specimen as follows [40]:

$$\frac{1}{E^*} = \frac{(1 - \nu^2)}{E} + \frac{(1 - \nu_i^2)}{E_i} \quad 2.4$$

Here, E and ν are the Young's modulus and Poisson's ratio for the specimen and E_i and ν_i are the respective parameters for the indenter. Equation 2.3 however, is limited to conical indenters and is valid only under the assumption of small deformation, and therefore, it must be corrected to account for large strains and the non-axisymmetric geometry of pyramidal indenters as suggested by King [41] and Hay [42]. Experimental studies carried out by Tabor [40, 43] concluded that for most types of

indenters in common use, the Vickers hardness (HV) at full plastic deformation is equivalent to

$$HV = c\sigma_r \quad 2.5$$

where $c = 3$ and σ_r is the stress level at 8% plastic strain [43]. In 1992 Oliver and Pharr [20] presented one of the most widely adopted methods for determining hardness and elastic modulus using nanoindentation experiments. For brevity, the method is not replicated in the present study and therefore the reader is referred to the main source [20, 44] for details. The formulation however, is based on Sneddon's [45] elastic model of load and penetration for a conical indenter and therefore, the Oliver-Pharr method is limited to materials that sink-in. Consequently, a deviation of up to 25% [46, 47] in the prediction of the hardness and the Young's modulus could be expected in materials that pile-up. A study conducted by N'jock et al. [48] concluded that a better approximation to the actual contact area when piling-up predominates is achieved following the method proposed by Loubet et al. [49]; the maximum error in the value of the reduced Young's modulus of five different materials that exhibited pile-up deformation mode was found to be at least 50% smaller compared to the value predicted by the Oliver-Pharr method.

More recent approaches rely upon the finite element method in order to account for the complex phenomena involved in the problem of plastic deformation, i.e. time-dependent contact boundary conditions and geometric and material nonlinearities. Details on the displacement-based finite element formulation and the solid mechanical foundations of the indentation problem have been provided by various authors, e.g. [17, 19, 50, 51]. Based on the results of FE simulations of the indentation problem with Vickers and Berkovich indenters, Giannakopoulos et al. [17] and Larsson et al. [19] respectively, derived semi-analytical equations to relate the indentation load and hardness to the indentation depth. Their approach builds upon Johnson's 'expanding cavity model' [52] by including the influence of the plastic hardening and consequently, taking into account the piling-up/sinking-in effect. A close agreement (< 5.5%) between the predicted and experimental Vickers hardness of Al 6061-T6 was

achieved. The predicted hardness and indentation loads with a Berkovich indenter approached closely, to within 5%, the experimental values for Al 7075-T6. The proposed equations however, were derived from the numerical results of indentation of Al 6061-T6 and Al 7075-T6 and their validity with other constitutive behaviours is not guaranteed.

2.1.3.2 The inverse analysis of the depth-sensing indentation test

The inverse analysis of indentation is a characterisation technique that attempts to recover the mechanical properties of the indented material using a $P-h$ curve extracted from the depth-sensing indentation test. In the absence of an analytical solution to the problem of elastic-plastic indentation, different approaches have been proposed to relate the $P-h$ curve to the material properties as discussed below.

Giannakopoulos and Suresh [53] and Venkatesh et al. [18] presented a methodology for the determination of elastic-plastic properties of materials (E^* , σ_y and n) from experimentally determined $P-h$ curves with Vickers and Berkovich indenters. Empirical formulations were derived from the result of a parametric analysis taking into account the effects of sink-in and pile-up on the true contact area. The proposed methodology predicted the reduced modulus of a 1070 steel with a maximum error of 9.1%, but the capability to predict the plastic behaviour was not evaluated.

Cheng and Cheng [15, 16, 54, 55] derived the widely known dimensionless functions, for isotropic elastic-plastic solids following the work-hardening rule, in an attempt to define the loading and unloading curves as a function of the mechanical properties of the indented material (E , σ_y , ν and n) and the shape of the indenter defined by the half-angle θ . By applying the Π theorem [56] in dimensional analysis, the following dimensionless functions were established:

$$\frac{P}{Eh^2} = \Pi_\alpha \left(\frac{\sigma_y}{E}, \nu, n, \theta \right) \quad 2.6$$

$$\frac{1}{Eh^2} \frac{dP}{dh} \Big|_{h=h_{max}} = \Pi_{\delta} \left(\frac{\sigma_y}{E}, v, n, \theta \right) \quad 2.7$$

$$\frac{h_r}{h_{max}} = \Pi_{\phi} \left(\frac{\sigma_y}{E}, v, n, \theta \right) \quad 2.8$$

where Π_{α} , Π_{δ} and Π_{ϕ} , the dimensionless functions, were evaluated and validated by means of finite element calculations defined with several sets of values of E , σ_y and n . Although derived for conical indentation, the scaling functions apply to indentation using pyramidal indenters. Ma et al. [57] introduced an additional dimensionless function based on the results of FE simulations of indentation in power-law materials with E , σ_y and n ranging from 30 to 300 GPa, 30 to 3000 MPa, and 0 to 0.5, respectively. The proposed approach defines the ratio of the additional residual area after unloading to the area of a profile indenter at full loading ($\Delta A/A$), as a function of n and σ_y/E . This approach however, requires experimental techniques to measure the indentation residual profiles, such as atomic force microscopy or scanning probe microscopy. The inverse analysis carried out in this study predicted the Young's modulus and yield stress of a single crystal aluminium with a deviation of 9.86 and 2.61% respectively, in comparison with the results provided by a uniaxial tension test. The uniqueness of the solution of the inverse analysis was not addressed in this study.

Tho et al. [58] suggested that errors are reduced if the ratio of plastic work to total work (W_P/W_T) is used as the third characteristic parameter, instead of h_r/h_{max} , as the former is determined from the entire $P-h$ curve unlike h_r/h_{max} which is determined from two points. W_T is represented by the area under the loading curve and W_P is the area bounded by the loading and unloading curves. Therefore, a new set of dimensionless functions were constructed by fitting the numerical results of 510 FE analyses of indentation of materials encompassing a domain of $10 \leq E^*/\sigma_y \leq 1000$ and $0.0 \leq n \leq 0.6$. Values of E^* , σ_y and n were predicted with this model. This study however, concluded that the relationship between elastic-plastic material properties and the $P-h$ curve is not one-to-one. Therefore, they proposed an extension of this approach by including a second indenter in an attempt to reduce the number of possible solutions [59]. The elastic-plastic material properties of five different materials (Al6061,

Al7075, steel, iron and zinc) were recovered by the inverse analysis of dual indentations, resulting in accurate predictions of Young's modulus, yield stress and strain hardening exponent with a deviation of less than 4, 2.5, and 0.05% respectively for all five materials, compared with literature values.

Dao et al. [47] employed the concept of representative stress (σ_r) in an attempt to reduce the number of apparent unknown variables in the dimensionless function for a given indenter half-angle θ , and a fixed value of $\nu = 0.3$. The derivation assumed (E^* , σ_r , n) as the independent material constitutive parameters, instead of (E , σ_y , n) as proposed by Cheng and Cheng [16], where E^* accounts for the effects of an elastic indenter through Equation 2.4. The dimensionless functions were constructed with the results of a parametric study, carried out using the large-strain formulation in FE modelling of sharp indentation, of 76 different materials with Young's modulus to yield stress ratios (E/σ_y) and strain hardening exponents ranging from 25 to 700 and from 0 to 0.5 respectively. A representative stress, corresponding to a representative strain of 3.3%, was identified as a stress level where the dimensionless function of the indentation-loading curve proposed by Cheng and Cheng becomes independent of the strain hardening exponent n , such that Equation 2.6 can be expressed as follows,

$$\Pi_1 \left(\frac{E^*}{\sigma_r} \right) = \frac{C}{\sigma_r} \quad 2.9$$

However, the independence of $C/\sigma_{0.033}$ to n in Equation 2.9 is satisfied only in a limited range of materials exhibiting a Swift's power-law hardening behaviour as illustrated in Figure 2.4.

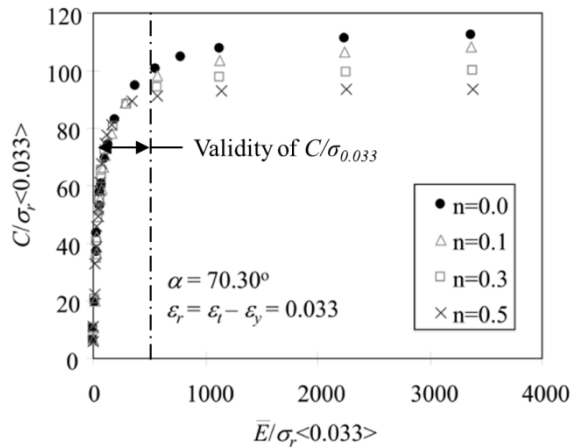


Figure 2.4. Dimensionless function (Equation 2.9), evaluated at a representative stress (σ_r) corresponding to plastic strain $\varepsilon_r=0.033$, generated with the expanded material space considered by Ogasawara et al. [60].

Dao's inverse analysis [47] was verified with six P - h curves of each of two aluminium alloys (6061-T6511 and 7075-T651). An improvement in the determination of the reduced modulus in excess of 10% was achieved by this method compared with Oliver and Pharr's [20] approach. Good estimates of the reduced modulus E^* and the value of the representative stress $\sigma_{0.033}$ were obtained, with errors of less than 11 and 9% respectively, compared with experimental data, although less precision for determining the strain hardening coefficient was found, with mean errors of up to 30%. Significant scatter was observed in the predicted values of yield stress obtained individually for each of the six P - h curves of Al 6061-T6511 and Al 7075-T651 compared with experimental results, which included errors of up to 55%. However, the averaged value of the predicted yield stress approximated well that measured experimentally. Bucaille et al. [61] suggested the use of dual indenters to improve the predictions of the strain hardening exponent, one with a half-angle of $\theta = 70.3^\circ$ and a second indenter with $\theta < 70.3^\circ$, e.g. $\theta = 60, 50$ or 40.3° . Extending Dao's work, a parametric analysis based on FE modelling of the indentation test of 24 combinations of elastic-plastic properties was carried out in order to construct dimensionless functions analogous to Equation 2.9, corresponding to each of the indenter geometries, i.e. Π_{1-60° , Π_{1-50° , and $\Pi_{1-42.3^\circ}$. Values of representative strain were identified for each conical indenter angle and an expression of the representative strain, ε_r , as a function of the half-angle θ was established:

$$\varepsilon_r = 0.105 \cot \theta \quad 2.10$$

A significant improvement in the prediction of the strain hardening exponent of an aluminium alloy Al 7075-T651 was achieved by this method (error = 64%) compared with their predictions following Dao's method (error = 175%). They concluded that reducing the half-angle of the second indenter improves the accuracy of the inverse analysis, although as the indenter becomes sharper, the effects of friction become more significant. A consistent computational study using dual indenters and the concept of representative strain was carried out by Chollacoop et al. [62]. The inverse analysis included three characteristic parameters from the Berkovich (70.3° conical) indentation, i.e. C , S and W_T/W_P , and one from the 60° conical indentation, i.e. the loading curvature C . The study considered the same aluminium alloys (Al 6061-T6511 and Al 7075-T651) as those investigated by Dao et al. [47]. The proposed inverse analysis reduced the average of the relative errors in the prediction of σ_y of Al 6061-T6511 and Al 7075-T651 from 25.7 to 14.6% and 38.3 to 13.2% respectively, compared to Dao's inverse analysis using a single indenter.

However, the definition of representative stress adopted by Dao et al. [47], Chollacoop et al. [62] and Bucaille et al. [61] is related to the total strain during uniaxial loading and therefore has a weak physical basis when considering conical or spherical indentation, as the stress field beneath the indenter is essentially equi-biaxial superimposed with a hydrostatic pressure [60]. On this basis, Ogasawara et al. [60] defined a new representative strain related to the plastic strain of equi-biaxial deformation, which plotted on the uniaxial stress-strain curve corresponds to:

$$\sigma_r'(\varepsilon_r') = K \left(2 \frac{\sigma_r}{E} + 2\varepsilon_r \right)^n \quad 2.11$$

where the apostrophe differentiates the stress and strain under equi-biaxial loading. Based on the new definition of a representative strain and extensive numerical simulations on an expanded material property space, compared to the range suggested by Dao et al. [47], Ogasawara et al. [60] identified an optimised value of representative

strain $\varepsilon_r = 0.0115$ for a Berkovich indenter (represented by an equivalent conical indenter with $\theta = 70.3^\circ$) that ensures the critical normalised relationship between load and material parameters is essentially independent of the work-hardening exponent. This value allowed all FE simulated curves included in this study to fit the dimensionless function of the indentation-loading curve (Equation 2.9) within a total error of at least one order of magnitude smaller than that of the function defined at a representative strain of $\varepsilon_r = 0.033$ as suggested by Dao et al. [47]. Additionally, the representative strain was found to be essentially a linear function of $\cot\theta$ (from 60° to 80°):

$$\varepsilon_r = 0.0319 \cot \theta \quad 2.12$$

The difference between the coefficients of this equation and the relationship derived by Bucaille et al. [61] (Equation 2.10) is due to the definition of representative strain adopted in this work. An excellent agreement of less than 3% error was achieved between the target and recovered material properties, namely the strength coefficient K and strain-hardening exponent n , from the inverse analysis based on the new formulation of representative strain. A variation of this method, also proposed by Ogasawara [63], employs the total work of indentation, W_T , and the contact stiffness, S , to find the representative strain, ε_r , and the strain hardening exponent, n , respectively. The plastic properties of three power-law materials (brass, gold and aluminium) were recovered from target (FE simulated) $P-h$ curves with the proposed inverse analysis achieving maximum errors in the predicted values of strength coefficient K , strain-hardening exponent n and representative stress σ_r of 16.5, 16.6 and 1.9%, respectively. Furthermore, this method proved its capability to differentiate the material properties of five materials that have identical $P-h$ curves.

Nonetheless, both the semi-empirical and dimensionless functions rely on extensive data fitting and therefore their physical meaning is weak and additionally, their validity is limited by the conditions defined in the parametric analysis used to construct them, e.g. the material space and the assumptions made to represent the physics of the process. Furthermore, the concept of representative strain lacks a strong physical

meaning as the full triaxial strain state under the indenter is simplified assuming uniaxial conditions [60]. The representative stress is not easily determined as it is not a physical property of the material and consequently, it has been shown to be dependent on the material properties and the shape of the indenter [64].

The optimisation approach involves finding the combination of material properties that define the predicted $P-h$ curve that best fits the experimental $P-h$ curve. Numerically, the method minimises the optimisation function, which is typically defined as the residual between the experimental and the material dependent predicted $P-h$ curve. The predicted curve can be generated via FE or using semi-empirical functions and the material properties are modified through an iterative procedure until convergence is reached. The former avoids the necessity of fitting parameters, although the computation time is significantly increased. Extending the work of Zeng and Chiu [65], Luo et al. [66] noted that the loading curve for an elastic-plastic material is always between the curves for elastic and elastic-perfect plastic materials. A set of semi-analytical equations were established based on a parametric analysis of 44 FE simulations of the indentation test of elastic, elastic-perfectly plastic and elastic-plastic materials with Young's modulus, yield stress and strain hardening exponent ranging from 10 to 210 GPa, 30 to 2000 MPa and 0 to 0.5, respectively. An optimisation procedure was proposed to recover the mechanical properties of the material by minimising the residual between the semi-analytical equations and the $P-h$ curve. This model however, shows a very high sensitivity to the initial guess values, resulting in errors in the optimised values of E , σ_y and n , respectively, ranging from 0-25%, 2-136% and 1-400% compared to the target properties. Luo and Lin [67] extended this work by including a second conical indenter with a half-angle $\theta = 60^\circ$, in addition to the conical indenter of $\theta = 70.3^\circ$, as an attempt to remove the non-uniqueness problem of the single indenter optimisation approach. The reliability of this inverse method was tested with five representative materials (numerically generated $P-h$ curves). Significant improvements were achieved with this approach and it was capable of predicting Young's modulus, yield stress and the strain hardening exponent with an error of less than 2, 10.4 and 11.3% respectively in all of the materials considered. Compared with the best match of the single curve optimisation approach described by

Luo et al. [66], the errors in the prediction of E , σ_y and n of steel were reduced from 6 to 2%, 50 to 0% and 53 to 1%, respectively. Constantinescu and Tardieu [68] proposed a gradient-based numerical optimisation to identify the constitutive parameters of a Maxwell viscoelastic and a Norton-Hoff elastic-viscoplastic material. The optimisation function $f(\mathbf{x})$

$$f(\mathbf{x}) = \frac{1}{2} \sum_{i=0}^I [F_i^{comp}(\mathbf{x}) - F_i^{exp}]^2 \quad 2.13$$

depends implicitly on the constitutive parameters \mathbf{x} through the solution of the direct (FE) indentation problem. Therefore at a depth i , $F_i^{comp}(\mathbf{x})$ and F_i^{exp} are respectively, the loads from the predicted and experimental $P-h$ curve. The predicted parameters of a Maxwell material (Young's modulus and viscosity) approached the target values to within 0.02%. For the case of the Norton-Hoff material, Young's modulus and viscosity parameters were well identified to within 5 and 10%, respectively, of the target values. However, the objective function presented a lack of sensitivity to the power coefficient and the yield stress and therefore these values were far away (up to 40 and 52%) from the target constitutive parameters. Kang et al. [69] performed the optimisation of elastic-plastic properties (E , σ_y and n) using predicted curves generated via finite element modelling [69] and dimensionless functions [70] with a value of representative strain as determined by Ogasawara et al. [60]. The optimisation model was defined in accordance to Equation 2.13. The model coupled with 3D FE simulations of conical, Vickers and Berkovich indentation [69] achieved convergence to within 1% error of the target (FE model) solutions. However, less accurate results were achieved for the case of a target curve generated from an experimental indentation test of Al 2024-T351 using a Berkovich tip, particularly in the prediction of the strain hardening exponent where the maximum error was up to 69.12%, depending on the set-up of the initial guess parameters. On the other hand, the optimisation of the dimensionless functions of indentation [70] converged at maximum errors of 1.42, 25.1 and 53.44% when compared with the target parameters E , σ_y and n respectively. The target curve in this study was generated from a 2D axisymmetric FE model with conical indenter of half-angle $\theta=70.3^\circ$. These errors are

significantly higher compared to the respective errors obtained with the equivalent optimisation approach combined with FE modelling [69]. However, the implementation of a second indenter of $\theta=60^\circ$ reduced the maximum errors of σ_y and n to 5.14 and 4.45% respectively.

Although different methods to solve the inverse analysis of indentation have been proposed, the fundamental issue of the problem still remains: the solution of the inverse analysis of indentation, purely based on experimentally obtained load-depth curves is not unique. This concern emerged from the observation that under some circumstances, two or more different materials, for which constitutive models are defined by a different set of material properties, exhibit indistinguishable $P-h$ curves [58, 66, 71-75]. This means that the number of possible solutions of the inverse analysis of indentation is not finite. Tho et al. [74] attributed the non-uniqueness of the reverse analysis based on a single conical or pyramidal indenter to the existence of an intrinsic relationship among the three characteristic parameters (C , S , h_r/h_{max}). This implies that only two out of the three characteristic parameters can be obtained independently from the indentation $P-h$ curve of a single indenter, and hence an infinite number of solutions to the inverse analysis of indentation are expected when solving for the three unknown material properties (E , σ_y and n). The existence of only two independent characteristic parameters has been supported consistently by Alkorta et al. [46] and Le et al. [76]. The suggestion of using dual indenters with different half-angles emerged from the idea that two or more $P-h$ curves could provide additional information of the behaviour of the same material under different conditions of loading. However, it has been reported that even the dual (or multiple) indentation analysis fails to provide a unique solution [75, 76] as different sets of material properties can lead to indistinguishable $P-h$ curves even when different indenters are used. This material pairs are known as ‘mystical’ materials [71]. However, given that in the present study only an indenter of a Berkovich type has been used, ‘sibling’ materials seems a more appropriate term. Furthermore, this technique requires indenters of different geometries and indentations in the specimen taken at different locations separate to one another in order to avoid measuring the mechanical properties of the material strain hardened by the indentation process. Therefore, the material

properties recovered from these multiple sets of data define a variety of elastic-plastic material properties.

A few authors have explored the gains attained by measuring the residual imprint in addition to the $P-h$ curve. The work presented by Bolzon et al. [77] using pseudo-experimental data (FE simulated) concluded that information from residual imprints improves the optimisation of material properties. The objective function was defined as follows:

$$w(\mathbf{z}) = \alpha \sum_{i=1}^{N_h} \left(\frac{h_i^{exp} - h_i^{com}(\mathbf{z})}{h_{max}^{exp}} \right)^2 + \beta \sum_{j=1}^{N_u} \left(\frac{u_j^{exp} - u_j^{com}(\mathbf{z})}{u_{max}^{exp}} \right)^2 \quad 2.14$$

where the subscripts *exp* and *com* refer to experimental and computed quantities, respectively, h_i is the indentation depth at a force i and u_j the displacement at a point j from the axis of symmetry. The factors α and β take a value of 1 ($\alpha = \beta = 1$) to include both the data from the $P-h$ curve and residual imprint. In a further study [78], experimental residual imprints of a Rockwell hardness test at macro-scale ($h_{max} = 260 \mu\text{m}$) in pipeline steel were measured using a contact profilometer. A genetic algorithm was invoked to minimise Equation 2.14; the mean values of the identified properties by means of the suggested approach, deviated between 17.8 – 20.9% and 5.6 – 16.7% from the experimental values of E and σ_y . Moy et al. [79] adapted Bolzon's [77] function by using only the value of maximum pile-up ($h_{pile-up}$) and therefore the second term in Equation 2.14 was modified accordingly. The minimisation was performed using a trust region algorithm. The elastic-plastic properties (E , σ_y and n) of an Al 2024 alloy in the as-received and two age-hardened conditions were investigated. The inclusion of the maximum pile-up height significantly improved the prediction of the material properties, particularly the discrepancies between the predicted and experimental value of n and σ_y , decreased from a maximum of 64.29% to 7.61% and from 38.75 to 11.75%, respectively. For the case of E the improvement was less marked with errors reduced from a maximum of 11.70 to 10.79%.

2.1.4 Concluding remarks

Including data extracted from residual imprint measurements is encouraging in the sense that the plastic flow of material around the indenter is strongly linked to the plastic properties and thus this is valuable information to compliment the lack of sensitivity of the $P-h$ curve to the plastic behaviour of the indented material. However, the volume of the plastically displaced material in micro- and nanoindentation can be of the same order of magnitude as the microstructural features of the tested material and thus, both the reaction forces measured by the instrument and the contact evolution at the indenter-material interface are severely affected. The latter, may lead to non-smooth surface profiles and loss of indentation symmetry (e.g. axisymmetry in a conical indentation) which makes the data difficult to interpret.

Notwithstanding the knowledge of ISE, the inverse analyses proposed to date have failed to perform preliminary studies to determine the effects of size parameters on the depth-sensing indentation data before moving onto characterising material properties. Furthermore, the influence of the non-homogeneity of real engineering materials on the measurements of the residual imprints has not been investigated.

2.2. Characterisation of material property variation in inertia friction welded components

2.2.1 Introduction

Inertia Friction Welding (IFW) is a joining technique in which the energy for welding is first stored in a flywheel as kinetic energy and then dissipated through frictional heating. It is considered a solid-state joining technique as no bulk melting takes place at the interfaces to be welded, instead coalescence is obtained through the combined effects of pressure and relative motion of the mating workpieces to cause heating through friction and consequently plastic deformation with the purpose of forming enough primary atomic-level bonds [3].

The IFW machine (Figure 2.5) is designed to convert kinetic energy into thermal energy at the interfaces to be welded through friction when one stationary workpiece

and one rotary workpiece are brought into contact. The flywheel, which is coupled to the rotary workpiece, is accelerated to a predetermined initial speed (N rpm) by a drive motor, as illustrated in stage a) of Figure 2.6, thus storing a specific amount of kinetic energy into it [80]. The welding process starts at stage b) when the two sections to be joined are brought into contact by an axial force (F), which is applied through the stationary workpiece while the rotating power is simultaneously cut off. The frictional heating between the faying surfaces causes the flywheel to decelerate (transition from stage b to c) by dissipating its kinetic energy as thermal energy and thus resulting in an increase in the temperature of the workpieces around the interface. Once the forging temperature is reached, the softened material plastically deforms until it is expelled around the joint generating the characteristic “flash” and “upset” of the IFW process. The axial load is maintained for the initial part of the cooling period after the flywheel comes to rest at stage c) to consolidate the weld [81].

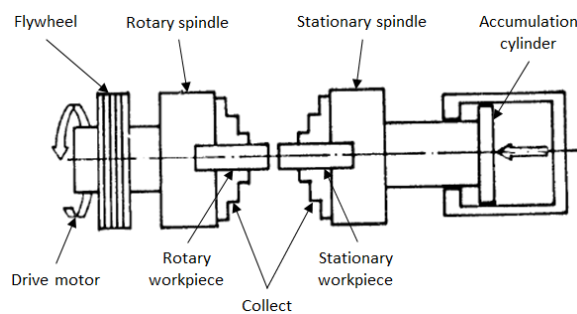


Figure 2.5. Schematic diagram of a typical inertia friction welding machine [80].

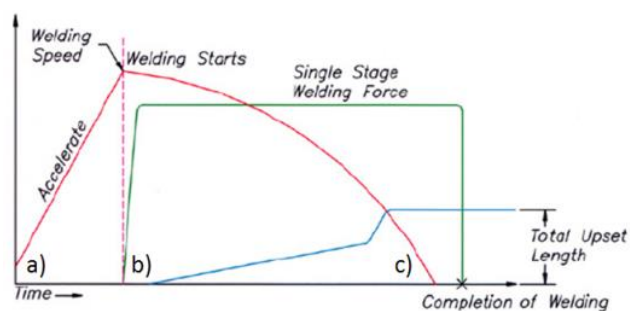


Figure 2.6. Stages of the IFW process [81].

In terms of thermo-mechanical cycles, the process can be separated into two general stages: a welding stage or heating stage and a cooling stage. The welding stage is

characterised by an instantaneous discharge of kinetic energy as a heat flux at the faying surfaces and high strain rates. During the early period of welding, contact between workpieces is made over the asperities of the surfaces and hence the real contact area is smaller than the apparent contact area. In this period a sliding condition is fulfilled in which asperities are deformed by frictional shear stresses following a Coulombic friction law ($\tau_{fric} = \mu p$) and therefore heat is generated through friction. However during the last period of welding, initiated once the real contact area equals the apparent contact area as a result of plastic flow of material, frictional shear stresses become independent of normal pressure (p) and the sliding condition is now replaced by a sticking condition. Here, the frictional shear stress takes the value of the shear yield stress of the workpiece material ($\tau_{fric} = \tau_y$) and heat is generated by plastic deformation rather than friction [82, 83]. Plastic strain is confined to a narrow region in the vicinity of the weld line (WL), reaching the highest values at the WL as shown schematically in Figure 2.7a. Next to the WL is the fully plasticized zone (FPZ), where a combination of high peak temperature, plastic strain and strain rates causes grain refinement due to dynamic recrystallization. Larger grains compared to the parent metal grain size are found in the partly deformed zone (PDZ) due to grain growth caused by high temperature and lower strain and strain rates compared to the FPZ. Away from the weld line, but inside the heat-affected zone (HAZ), an undeformed zone (UZ) is located where material is subjected to thermal effects but plastic deformation does not occur. In this zone material may experience grain growth and also precipitate growth or dissolution, depending on the alloy and initial microstructure. The IFW process is controlled by three process parameters: the moment of inertia and initial speed of the flywheel and the applied axial force. Tumuluru [84] concluded that the speed of rotation and moment of inertia of the flywheel are the controlling factors affecting weld microstructures of low alloy steels.

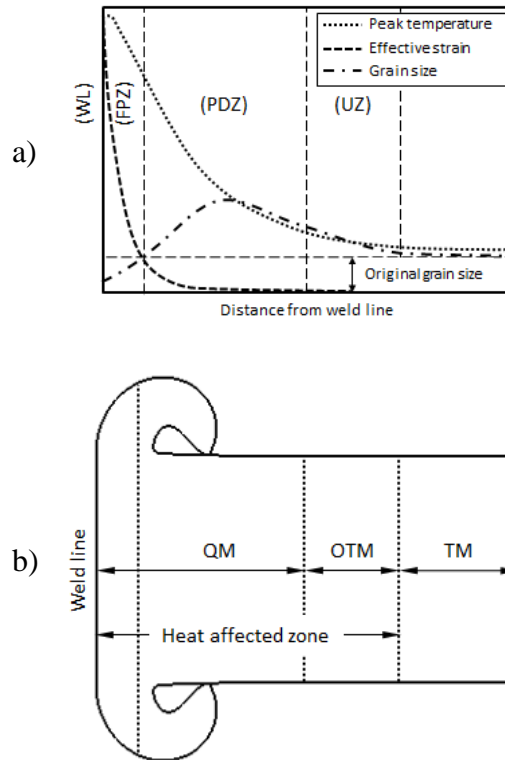


Figure 2.7. a) Schematic diagram of the typical thermo-mechanical behaviour and b) generated metallurgical zones in IFW welds.

2.2.2 Material characterisation of the across-weld properties generated during the IFW process

The abrupt thermal variations ranging from room temperature to temperatures approaching the melting point of the materials being welded, as well as the severe plastic deformation at high rates induced by the IFW process, can cause a wide range of microstructures to be developed in the weld region. Therefore, some investigations have been carried out to characterise the microstructures formed from the parent material during IFW. Electron microscopy alongside synchrotron X-ray diffraction in weld trials of SCMV to Aermet 100 steel were performed by Moat et al. [85, 86] in an attempt to understand the hardness variation across the weld. Within SCMV, the hardness increase in the vicinity of the weld line was attributed to the formation of quenched martensite, as suggested by the presence of retained austenite and the asymmetry of the ferrite (200) reflection. The hardness drop further away within the HAZ corresponds to a region showing the coarsest lath structure and the lowest degree

of stored deformation, as revealed by a low degree of (110) ferrite refection. Therefore, softening of SCMV in this region was attributed to the over-tempering of martensite. In the absence of martensite, the hardness peaks in Aermet 100 was explained as a result of the ordering effect of cobalt (FeCo ordering) generated due to a combination of temperature, in addition to plasticity or residual stresses. Preuss et al. [87] investigated the microstructure across the weld region in nickel-based superalloy RR1000 tube structures joined by IFW. High intensity synchrotron X-rays measurements alongside FEGSEM imaging were carried out to study the γ' distribution; electron backscattered diffraction (EBSD) maps provided information of the stored energy of the material. By comparing the stored energy, to assess the level of plastic deformation, with the full-width at half-maximum measurements from X-rays diffraction, it was concluded that the hardness drop at the weld line is due to the presence of a fully recrystallized microstructure. On the other hand, the hardness peak near the weld line is due to work hardening and the small grains arising from the beginning of recrystallization. Further away from the weld line, the dissolution of tertiary γ' leads to a hardness trough. This region is bounded by a hardness peak located in the edge of the HAZ resulting from an increase in misfit between the coherent γ and γ' . Similar experimental approaches provide a detailed description of the hardness variation resulting from the different microstructures in the as-welded condition of a variety of similar and dissimilar materials joined by IFW, e.g. RR1000 to RR1000 [88], RR1000 to IN718 [89], Mar-M247 to LSHR (Low Solvus High Refractory alloy) [90], Ni76Cr19AlTi to 4Cr10SiMo [91]. However, none of these investigations characterised the actual elastic-plastic properties of the different microstructural regions.

Some authors have investigated the bulk properties of the as-welded condition. Mortensen et al. [92] investigated the tensile and impact properties in inertia friction welded 416 steel. Tensile tests performed in post-weld tempered specimens suggested that brittle fracture was not a result of the brittle martensite in the weld. This test also suggested that the welded 416 steel is stronger for the small diameter, as a result of the tangential reorientation of sulphur inclusions to a greater extent as the distance from the centre increases. The value of impact strength after IFW, measured using the

Charpy impact test, was equal to the parent material. Taban et al. [93] carried out tensile tests experiments to evaluate the tensile strength in inertia friction welds of 6061-T6 to AISI 1018. The specimens fractured through the dynamically recrystallized region in the aluminium at an average tensile stress between 170 and 250 MPa. These values are dependent on the forge pressure, being higher at higher pressures. The values of tensile strength are at some extent similar to those reported for tensile specimens of 6061-T6, i.e. 275 MPa [94]. A qualitatively similar result was reported by Zhu et al. [95] for welds of Nimonic 80A to 4Cr10Si2Mo as the tensile strength of the weld was determined to be slightly higher (~3.5%) than that of the as-received 4Cr10Si2Mo. EDS analysis confirmed that the weld fractured on the 4Cr10Si2Mo side. A diffusion zone of 100 μm in width at the weld interface was measured by EDS which, in conjunction with the heat affected microstructure, may explain the difference in tensile strength between the as-received and as-welded 4Cr10Si2Mo. In contrast, inertia friction welds of Inconel 751 to Austenite Steel 21-4N, tested at room temperature, fractured at the side of the former even when its tensile strength is slightly higher than that of the 21-4N [96]. At higher temperatures however, e.g. 1000 $^{\circ}\text{C}$, the strength of 21-4N decreases much faster than Inconel 751 and thus the deformation would mainly occur in the 21-4N side.

Only a very few investigators have attempted to characterise the local properties across the joint in the as-welded condition. Zhu and co-workers [91, 95, 96] proposed a method to calculate the strength in different positions across the joint by using the microstrain (ε') and lattice parameter (a) measured from X-Ray Diffraction (XRD) patterns as follows:

$$\sigma = M'Gb^{1/2}[3(2\pi)^{1/2}\varepsilon'] \quad 2.15$$

where σ is the strength, M' a constant dependent on the strength of the parent metal, G the shear modulus of the parent metal, b the Burgers vector calculated from the cell size ($b=a/\sqrt{2}$, for the fcc structure, where a is the lattice parameter), and ε' the microstrain derived from Equation 2.16 [97]:

$$\varepsilon' = \frac{\beta \cot g\theta}{2} \quad 2.16$$

where β is the peak width from X-Ray Diffraction (XRD) patterns and θ the angle at the reflection peak analysed. A good match ($\sim 2.8\%$) was achieved between the lowest predicted strength and the weld strength of an inertia friction weld of Inconel 751 to 21-4N [96]. Tiley et al. [98] applied the strength model developed by Parhasarathy et al. [99] in order to predict the levels of yield stress across the joint of inertia friction welds of LSHR nickel-base superalloy. The model used the chemical compositions measured with the atom probe topography technique and average grain diameters of the matrix γ and γ' precipitates at different locations across the weld. Hardness values were predicted using Tabor's relationship assuming a constraint factor of 2.6, i.e. $\sigma_y = 2.6\text{HV}$, and compared with measured hardness values (HV) across the weld. The constraint factor of 2.6 was selected to limit hardness predictions to within the range of experimental values (error $< 7.5\%$) as the investigation was focused on a parametric analysis to assess the contribution of strengthening mechanisms to the hardness. It was concluded that γ' particles are the most significant strengthening mechanism. Attallah et al. [100] characterised the variation in elastic modulus in the as-welded and post-weld heat-treated conditions of an inertia friction weld of Ti-6Al-2Sn-4Zr-6Mo. The load-depth curves obtained via depth-sensing indentation test at microscale (maximum load of 2N) were used to calculate the elastic modulus. Due to the multiphase microstructure of this alloy, both α -Ti and β -Ti phases contribute to the measured value of elastic modulus and therefore assuming the rule of mixture applies, the measured elastic modulus in Ti-6246 can be represented as:

$$E_{Ti-6246} = E_{\alpha}V_{f/\alpha} + E_{\beta}(1 - V_{f/\alpha}) \quad 2.17$$

Therefore, using the values of elastic modulus (E_{β}) [101] and volume fraction ($1-V_{f/\alpha}$) [102] of β -Ti reported previously, the elastic modulus of α -Ti (E_{α}) was predicted with a difference of $\sim 5.5\%$ compared with the elastic modulus of α -Ti in Ti-6Al-4V [103]. Quinta da Fonseca [104] proposed the use of in-situ surface strain recording via either image correlation (IC) or electronic speckle pattern interferometry (ESPI) in order to

capture the cross-weld strain variation during tensile loading. Both techniques measure surface displacements at local positions or sections, depending on the magnification and spatial resolution, from which the strain profile is generated through differentiation of displacements. This method was tested in an inertia friction welded component of ferritic steel; the proof stress measured via both IC and ESPI was compared with the yield stress measured from the microhardness profile across the weld. The increase in proof stress as the weld line is approached was correctly predicted by the strain mapping techniques, yet the hardness trough near the edge of the HAZ could not be resolved. Preuss et al. [105] employed this approach in three nickel base superalloys, 720Li, RR1000 and Inconel 718. A good agreement was observed between the Vickers microhardness profile and the predicted proof stress, although the approach was not quantitatively validated.

Furthermore, phase transformations not only result in variations in physical properties but are also accompanied by volumetric changes arising from atomic rearrangements in the crystal structure. Consequently, the associated volumetric strains can be expected to alter the state of stress in the welded component. By combining energy-dispersive synchrotron X-ray diffraction and neutron diffraction, Moat et al. [106] conducted experimental studies to measure lattice strains produced due to phase transformations in SCMV during IFW. Peak residual tensile stresses were observed in the hoop direction within the HAZ at regions approaching the inner and outer diameters. Hoop tensile stresses were found to increase towards the weld line, but then drop into compression in the vicinity of the weld line as a result of the positive volumetric strain in the lattice due to austenite to martensite transformation [85]. The residual stress measurements carried out by Preuss et al. [105] using a neutron diffractometer also revealed substantially higher magnitudes of stress in the hoop direction in the as-welded condition of three nickel-based superalloys, namely Inconel 718, Alloy 720Li and RR1000. In contrast, radial stresses showed the least stress values. Another characteristic feature in the residual stress field was observed in these three materials, which involves the formation of axial compressive stresses towards the OD and tensile towards the ID. The magnitude of the axial stresses were somewhere between that of the radial and hoop direction. A consistent trend of residual

stresses was observed by Iqbal et al. [107] on IFW specimens generated from RR1000 heat-treated to obtain grains. It was therefore concluded that the generation of residual stresses in RR1000 during IFW is independent of the starting microstructure of the parent material.

2.2.3 Finite element predictions of residual stresses during IFW

The first attempt to develop a fully coupled thermo-mechanical model for the IFW process was presented by Moal and Massoni [108] in 1995 with the FE code INWELD. The code included an adaptive remeshing procedure and used axisymmetric elements to mesh the components; each node was defined with a three-component velocity vector to account for the torsional effects. The predicted rotational velocity was in very good agreement with experimental measurements. However, the evolution of the axial shortening was overestimated by the model at the end of the welding process, which was attributed to an inaccurate determination of the rheological, friction and thermal coefficients when the temperature reaches a value near the melting point of the material. Using a similar approach to model the torsional effects, Lee et al. [109] extended the DEFORM-2D code to a 2.5D model with the development of a special axisymmetric element. The capability of the FE model to predict the slowdown of the flywheel was satisfactorily validated against analytical solutions of energy decay and shear stress used to represent the torsional behaviour. Additionally, a good agreement was found between the predicted and measured upset.

Different thermo-mechanical FE models of the IFW process of similar [110-112] and dissimilar [113, 114] materials have been published in the literature. A variety of investigations have been carried out using the FE method to address the effects of the welding parameters, including the work of Jeong et al. [114], Balasubramanian et al. [115] and Wang et al. [116] among others. However, the numerical analysis to predict the evolution of residual stresses during IFW has received little attention in the past and only a very limited number of studies exist in the literature. Wang et al. [117] developed a representative coupled thermo-mechanical FE model based on the energy input method described by Balasubramanian et al. [118] to simulate the inertia welding of RR1000 nickel-based superalloy tubes. The heat input and upset data were obtained

experimentally and defined as boundary conditions in the FE model, thus neglecting friction at the interfaces of the weld and the torsional deformation. The peak temperatures experienced along the mid-wall line in an inertia welding trial were inferred by comparing the distribution of γ' particles with curves of γ' volume fractions as a function of temperature, generated by heating “matchstick-like” samples using an electro-thermal mechanical testing (ETMT) machine. The thermal fields predicted by the FE model satisfactorily matched the values inferred from thermal simulations with discrepancies ranging from 70–100 °C. In the same way, the FE model was capable of predicting the final residual stress with a good level of agreement, although slightly overestimated, with the experimental results obtained by neutron diffraction measurements. This study demonstrated the dependency of the size of the HAZ on the initial rpm of the flywheel, being smaller for higher rpm as most of the heat is generated early during the welding process expelling much of the hot material into the flash. This model was improved by Grant et al. [83] by including a better material database, a more representative heating model, and by assuming an elastic-plastic material model to predict residual stresses. In this study, the thermal histories predicted by the FE model were mimicked in “matchstick-like” samples of RR1000 using an ETMT machine. The peak temperatures experienced in the welding trials and in the matchstick samples were inferred from the resultant volume fractions following the same procedure described by [117]. The FE model prediction slightly underestimated by about 20°C the inferred peak temperatures in the inertia welding trial. The predicted residual stress field in the as-machined condition was in very good agreement with neutron diffraction measurements [119] in the hoop and radial directions. However, significantly smaller predicted values were found in the axial direction, partly attributed to an inappropriate tooling arrangement defined in the model. This study demonstrated the dependency of the thermal behaviour on the weld pressure but concluded that residual stresses near the weld line in the hoop direction are independent of the welding pressure as these are limited by the low yield strength values of the alloy at high temperatures.

Bennett et al. [81] developed a modelling tool based on DEFORM-2D to simulate both a mono-material weld of Inconel 718 and a dual-material weld of Inconel 718 to

AerMet 100. In this study the importance of volumetric changes associated with phase transformations on the prediction of post-weld residual stresses was highlighted by a reduction in the von Mises stress predicted in the HAZ. This work was advanced further [120] using experimental data to compare the predictions of the FE model to the residual stresses and the width of the region in which martensite transformed to austenite during the welding stage; both predictions were in good agreement with experimental data. However, a further development of the material model was suggested to improve the residual stress predictions.

2.2.4 Concluding remarks

The FE approach can provide valuable information regarding the effects of the thermo-mechanical field on the materials being welded. However, in the absence of a methodology capable of providing information of both the parent and child phases involved during the IFW process, the effects of phase transformation strains and the interaction of material phases having different mechanical properties on the evolution of residual stresses during IFW remain unaddressed. The importance of an accurate prediction of the residual stress field is highlighted as the structural integrity of the IFWed component in service is defined by the as-welded mechanical properties, the residual stresses generated during welding and the degree of stress relief during the subsequent heat-treatment.

2.3. Knowledge gaps

The critical review of the literature regarding the methodologies aiming to recover elastic-plastic properties from depth-sensing indentation data has identified the following knowledge gaps:

1. Although multiple methodologies concerned with the inverse analysis of the depth-sensing indentation test have been proposed, the non-uniqueness issue remains unaddressed.

2. Very little attention has been paid to the understanding of the complex plastic behaviour of multiple crystals as they are being displaced by the indenter. In addition, research into the effects of the surface condition prior to indentation, e.g. surface roughness and tilting, has been little explored.
3. The dependency of the elastic and plastic mechanical response of the material to the scale of the load at which the measurements are taken is still unclear.
4. It is felt that the continuum mechanics approach in FE modelling has been used without consideration of nano-scale effects to investigate the complex problem of indentation.
5. The majority of the investigations concerning the inverse analysis of indentation have overlooked the divergence between the small scale properties measured via indentation and the large scale properties extracted from other techniques, e.g. tensile testing.

In addition, it was found that only a few investigations [81, 120] on the generation of residual stresses during IFW based on FE modelling have accounted for stresses associated with volumetric changes occurring during phase transformations in the material within the HAZ. This is, in part, due to the absence of a methodology capable of characterising the mechanical properties formed across the weld is still absent. Consequently, the sensitivity of the residual stress field in the as-welded condition to the strains generated due to the contribution of mechanical and thermal loadings remains unclear.

Chapter 3 - Research methodology

3.1. Experimental methods

This section provides details of the experimental programme carried out throughout the development of a characterisation technique based on the inverse analysis of the depth-sensing indentation test. Before moving onto the characterisation of the material property variation across the inertia friction weld of SCMV steel, three different materials were used to test the capabilities of the inverse analysis and to assess some of the factors affecting the recovery of elastic-plastic properties from the depth-sensing indentation test.

3.1.1 Materials

Three materials with different elastic-plastic behaviours have been selected for investigating the sensitivity of the indentation response to the loading conditions, microstructure and specimen preparation procedure. These materials include a steel (CrMoV), a titanium alloy (Ti-6Al-4V) and an oxygen-free high purity copper (C110). CrMoV steel was used in the tempered condition and therefore the as-received sample was austenitised at 940 °C, oil quenched and tempered at 570 °C for 45, 20 and 120 minutes, respectively. The material composition is included in Table 3.1.

Table 3.1. Chemical composition of studied materials (weight %) as per a) Columbia metals, b) Aircraft materials, c) US Patent 20150083284 and d) VSMPO-Trius.

Element	Material			
	C110 ^a	CrMoV ^b	SCMV ^c	Ti-6Al-4V ^d
Cu	99.99	-	-	-
Pb	0.001	-	-	-
P	0.0003	0.020	≤ 0.007	-
S	0.002	0.020	≤ 0.002	-
C	-	0.35-0.43	0.35-0.43	-
Si	-	0.10-0.35	0.10-0.35	-
Cr	-	3.0-3.5	3.0-3.35	-
Mo	-	0.80-1.10	0.80-1.10	-
Mg	-	-	0.4-0.7	-
Ni	-	≤ 0.30	≤ 0.30	-
As	-	-	≤ 0.002	-
Sb	-	-	≤ 0.008	-
Sn	-	0.03	-	-
Mn	-	0.40-0.70	-	0.01
V	-	0.15 - 0.25	0.15 - 0.25	4.04
Ti	-	-	-	88.83
Fe	-	Balance	Balance	0.14
Al	-	-	-	6.85
Nb	-	-	-	0.03

In order to prove the applicability of the inverse analysis technique proposed in this study to solve a real engineering challenge, the three characteristic phases in the as-welded condition of a like-to-like inertia friction weld of Super-Chromium-Molybdenum-Vanadium (SCMV) steel have been characterised. SCMV is a low alloy ferritic steel of the CrMoV family, which provides an enhanced ultimate strength to weight ratio and plain section fatigue strength, an improved hardenability and an equivalent or better notch fatigue strength, ductility and fracture toughness. This is achieved by the employment of a triple vacuum melt route (VIM/EFR/VAR) to

increase the cleanness of the material and a two-stage heat-treatment, comprised by austenitisation at 935°C for 30 minutes and oil quenching and lastly, tempering at 570°C for 300 minutes. Therefore, SCMV in the fully heat-treated condition exhibits tempered martensite as white nodular precipitates sitting on the lath packets [121]. SCMV has a similar composition to CrMoV, having the same range percentage by weight of carbon, silicon, chromium, molybdenum and vanadium. However, SCMV is manufactured such that some further trace elements or contaminants are controlled to contain less than a specified concentration, as shown in Table 3.1.

3.1.2 Tensile testing

In order to determine the bulk properties of each of these three materials, at least two tensile test specimens were prepared and tested as per ASTM E8/E8M-15a [122]. Flat specimens were cut via electrical discharge machining (EDM) from a 3 mm sheet of Ti-6Al-4V and round specimens were machined from 25.4 mm bars of both CrMoV and C110. The dimensions of the tensile specimens are provided in Figure 3.1.

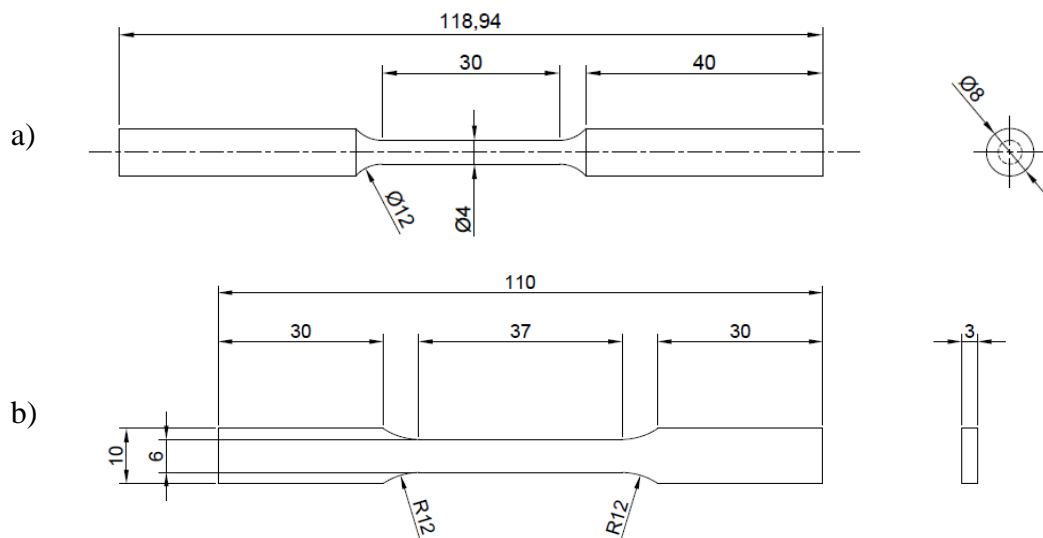


Figure 3.1. Dimension in mm of tensile specimens for a) CrMoV steel, C110 copper and b) Ti-6Al-4V.

All specimens were tested in an Instron Servohydraulic Test Machine at room temperature and crosshead velocity of 0.25 mm/min (strain rate $\sim 10^{-4} s^{-1}$) in order to ensure quasi-static conditions. A video gauge and an extensometer with gauge length

of 25 mm were used for measuring strain in the flat and round specimens, respectively. The yield stress was determined by using the 0.2% offset method.

3.1.3 Inertia Friction Welding

The aim of this study was the development of a characterisation technique based on the inverse analysis of the depth-sensing indentation technique in order to measure the mechanical response of small volumes of material, where the conventional testing techniques are not applicable. The proposed method was applied for characterising the different material phases formed across the joint of an inertia friction welded component of SCMV steel. Therefore, as a representative sample of the joint, a thin cross-weld slice section was taken from an inertia friction weld trial produced from two shaft sections of SCMV in the heat-treated condition. Details of the geometry of the workpieces and the predefined parameters for welding are provided in Figure 3.2 and Table 3.2, respectively.

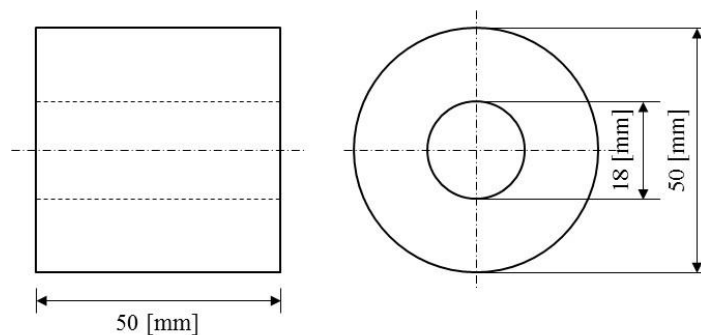


Figure 3.2. Geometry of the workpieces welded by the IFW process.

Table 3.2. Initial process parameters for welding

Input	Value
Flywheel moment of inertia, (I)	30.973 [N-m-s ²]
Kinetic energy, (E_k)	232780 [J]
Axial force, (F)	117834 [N]

3.1.4 Specimen preparation

Indentation specimens of CrMoV, Ti-6Al-4V, C110 and the cross-weld section of SCMV-SCMV were mounted in a conductive resin and then ground with abrasive paper down to 1200 grit (15.3 μ m), followed by polishing with 5 and 1 μ m diamond suspension. Ultimately, specimens were polished with colloidal silica down to 0.06 μ m for a minimum of 20 minutes in order to reduce the size of the hardened layer formed due to mechanical polishing.

In order to better understand the influence of the microstructure on indentation, an additional set of specimens were etched after polishing as follows: CrMoV steel and the IFWed section using 5% Nital for 50 s, Ti-6Al-5V with Kroll's reagent (1.5 mL HF, 4mL HNO₃ and 94 mL H₂O) for 10 s, and C110 with a solution consisting of 5 g Fe(NO₃)₃, 25 mL HCl and 70 mL distilled water for 20 s. The microstructures were observed using a Nikon Eclipse LV100ND optical microscope and a Phillips XL30 ESEM-FEG scanning electron microscope (SEM) using both secondary (SE) and backscattered (BSE) electrons diffraction.

3.1.5 Micro-hardness testing

The majority of the studies in the literature regarding the inverse analysis of indentation fail to perform a preliminary analysis to assess some of the factors affecting the interpretation of depth-sensing indentation data for the determination of material properties. Therefore, in order to bridge the gap between macro- and micro-scale properties, microhardness measurements at decreasing loads have been performed using a Buehler hardness tester with the aim of determining the load independent hardness, i.e. macroscopic hardness. Therefore, a Vickers hardness test has been carried out in specimens of titanium, steel and copper at indentation loads within the range of 25 to 2500, 100 to 1000 and 25 to 300 gram force, respectively. Five indentations per load were performed at an offset of at least three times the diagonal of the residual imprint. In the same spirit and in order to locate the hardened and softened zones formed due to IFW, a microhardness scan along the mid-wall line was performed from base material to base material, at an offset of 250 μ m between

indentations, using a Vickers indenter with a load of 500 gram force. Indentations at this load are considerably larger than the grain size yet small enough to avoid averaging the hardness over areas affected by the thermo-mechanical field to a significantly different degree. The extracted microhardness profile was analysed to approximate the location of the weld line and the regions comprised of martensite in the quenched, over-tempered and tempered conditions.

3.1.6 Depth-sensing indentation test

Depth-sensing indentation tests were conducted using a Micro Materials Ltd. NanoTest™ NTX equipped with a Berkovich indenter. The NanoTest™ head has a load range of 0-500 mN and maximum load and depth resolutions better than 100 nN and 0.1 nm, respectively. A new Berkovich diamond indenter with a tip radius of less than 20 nm, shown in Figure 3.3, has been used to perform the indentations. The properties of the indenter were taken as $E = 1000$ GPa and $\nu = 0.07$ for calibration and analysis [14].

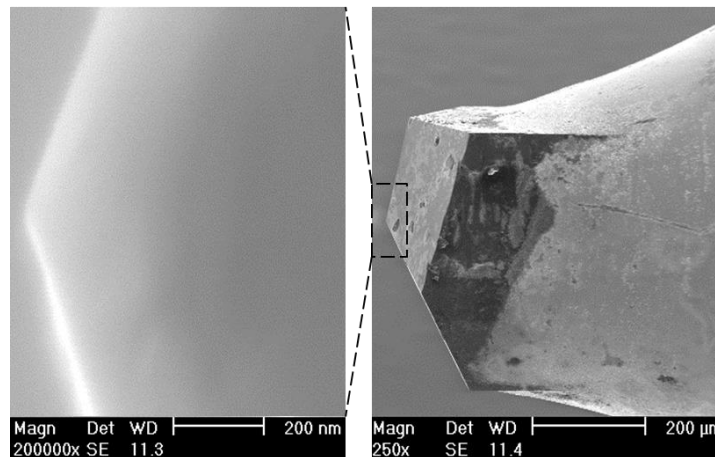


Figure 3.3. SEM images of the Berkovich indenter tip using secondary electrons at an acceleration voltage of 10.0 kV.

Sample fixtures may add to the compliance of the instrument and thus, cyanoacrylate adhesive has been used to glue the mounted sample to the instrument holder. Before testing, both the indenter area function and the load frame compliance were calibrated using a standard sample of fused silica ($E = 72$ GPa, $\nu = 0.17$ and $H = 9$ GPa [123]) in compliance with ISO 14577 [13]. In order to remove the effects of surface roughness

on the results, indentation loads were selected to reach maximum indentation depths of at least 20 times the average roughness (R_a) of the specimen in accordance to ISO14577 [13]. R_a is defined by ISO 4287/1-1997 [124] as the arithmetic average surface height deviations measured from the mean plane:

$$R_a = \frac{1}{L} \sum_{j=1}^L Z_j \quad 3.1$$

where Z_j is the profile height function analysed in terms of height (Z) and position (j) over the evaluation length L . Given that the polishing procedure affects the surface of the specimen to a depth of about the same size as the nominal grit due to strain-hardening or cold-working [14], indentations were performed at sufficient load to ensure indentation depths of at least three times the thickness of the strain-hardened layer as suggested by Liu et al. [36]. Therefore, the indenter has been loaded from an initial contact force (P_i) of 0.1 mN to a maximum force (P_{max}) within the range of 30-480 mN at a loading and unloading rate of 10 mN/s for CrMoV and Ti-6Al-4V. C110 on the other hand was loaded and unloaded at a rate of 4 mN/s in order to obtain a similar number of data points, considering that this material is indented with less than half the load of all other materials. In specimens of CrMoV, a dwell period of 30 s at P_{max} was applied so as to ensure the unloading data used for analysis purpose were mostly elastic. In addition, the load was held constant for a period of 30 s at $0.1P_{max}$ to establish the rate of displacement produced by thermal expansion in the system, that is, thermal drift. Therefore, thermal drift corrections were performed in addition to these curves. However, due to the complications in the inverse analysis caused by a non-continuous $P-h$ curve, this load-time sequence was avoided in C110 and Ti-6Al-4V and instead, a single loading and unloading ramp was defined. In order to assess the sensitivity of the $P-h$ curves to the loading-unloading rate, an extra set of indentations in titanium at a rate of 1.5 mN/s have been performed. Sets of five indentations were performed per indentation test, at an offset of at least 20 times the maximum depth as suggested by ASM International [123], in order to avoid overlapping of plastic strain-hardened zones. The possible sensitivity of the depth-sensing indentation data to the thickness of the mechanically-hardened layer due to

polishing has been assessed by polishing an additional sample of CrMoV to 1 μm using a diamond suspension. This material was selected for assessment as the fine microstructure, compared to those of the Ti-6Al-4V and C110, is expected to affect to a lower extent the experimental data. Table 3.3 provides details of the parameters used in each set of indentations.

With the intention of having an equivalent level of uncertainty in the extracted data, the P - h curves reaching similar indentation depths have been selected to recover the properties of the material via the inverse analysis of indentation. Therefore, as indicated in Table 3.3, $P_{max} = 240$ mN for Ti-6Al-4V and CrMoV, and $P_{max} = 120$ mN for C110. Those identified with an asterisk have been used in the inverse analysis procedure as detailed in the following section.

Table 3.3. Parameters used in the different depth-sensing indentation tests.

Specimen	Ti-6Al-4V		CrMoV		C110
L-U rate [mN/s]	10	1.5	10		4
Polishing [μm]	0.06	0.06	0.06	1	0.06
P_{max}	480	✓			
	360	✓			
	240	✓*		✓*	✓
	180			✓	✓
	120	✓		✓	✓*
	60				✓
	36				✓
	30	✓	✓	✓	

* Indentation parameters of the P - h curves used in the inverse analysis.

Building upon the experience gained from the analysis of the depth-sensing indentation data extracted from the three single materials, the indentation experiment for the SCMV-SCMV IFW was set as follows: indentations were performed using a single loading and unloading ramp at 10 mN/s, i.e. no dwell period at P_{max} , from a $P_i = 0.02$ mN to a $P_{max} = 240$ mN. The system was left over night to thermally stabilise

to reduce thermal drift effects during measurements. A dwell period of 20 s at 90% unload was defined for drift correction in the indentation schedule to confirm the negligible effects of heat transfer; this time is approximately the same as the time for application or removal of the test force. The indentation unit has been setup to conduct five rows of indentations, with an offset of 50 μm , along the joint at distances of 0, 0.5, 1.5, 3, 4.25, 4.5, 4.625, 4.75, 5.25, and 8 mm from the weld line as illustrated in Figure 3.4. Therefore, depth-sensing indentations are aligned with microhardness impressions, to at least 250 μm above the microindentations scan line so as to test strain free volumes of material.

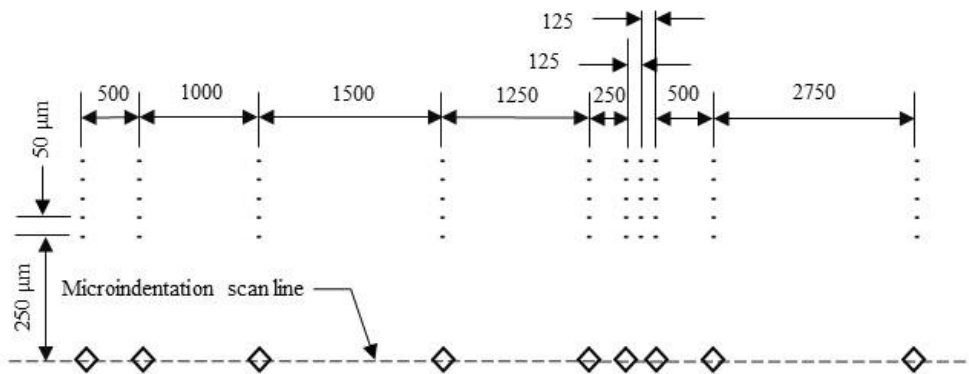


Figure 3.4. Schematic diagram of indentation sites across the IFW joint. Units are in mm unless otherwise specified. The diagram is for illustration purposes only and thus not in scale.

3.1.7 Analysis of depth-sensing indentation data

With the purpose of bridging the gap between the properties at macro (tensile test) and micro (depth-sensing indentation) scale, the Martens hardness from each $P-h$ curve has been calculated, as this can be reasonably compared with the Vickers microhardness value. The Martens hardness employs the actual surface contact area of the indentation such that for a Berkovich tip:

$$HM = \frac{P}{26.44h^2} \quad 3.2$$

where h is the depth measured from the initial indentation depth, preferably after reaching and holding the specified maximum test force if a load-time sequence has

been defined. This comparison allowed validating the suitability of a depth-sensing indentation experiment to represent the mechanical behaviour of the bulk material, or otherwise. The variability of a set of indentations has been assessed by computing the standard deviation about the mean HM. Since the $P-h$ curve showing the HM closest to the mean HM does not necessarily represent the bulk (uniaxial test) properties of the material, both the curves with the highest and lowest HM from a set of indentations have been selected to carry out this study. Furthermore, comparisons between $P-h$ curves set up with different indentation parameters were performed in order to provide a detailed assessment of some of the factors affecting the interpretation of $P-h$ curves.

3.1.8 Surface topography measurement

The residual imprints of the indents of interest were measured by means of atomic force microscopy (AFM), using a Bruker FastScan Bio Icon AFM in the peak force mode. As it was impractical to analyse every indentation for a given set of indentation parameters, surface topography measurements were taken only from the indents which exhibited the highest (HS) and lowest (LS) stiffness for each set of indentations. Owing to the equivalency of the projected areas, the same parameters were defined to measure the surface topography regardless of the material, i.e. 512 lines of 512 sample data points per scan line, scanned in a squared frame between 20 to 25 μm at a scan rate of half a line per second (0.5 Hz). The Z step height of the FastScan head is limited to $\pm 3 \mu\text{m}$. Bruker RTESPA-300 etched silicon probes of tip radii in the range 8 to 12 nm, as per manufacturers' specifications, were used. The cantilever is coated with Al reflective, as this is recommended for highly reflective samples, and has a spring constant of 40 N/m.

AFM images in the three single materials were taken between 30 and 45 days after the indentations were made; after 90 days, the surface of C110 in particular started to deteriorate due to surface contamination. Based upon this premise, residual imprints across the IFW joint were measured within a time period of less than 24 hrs after the indentation experiments were conducted.

Before analysing the height measurements, a first-order plane fit has been applied to the heights of each pixel in the image in order to correct for tilting. Line profiles in each direction of the bisector of the side of the triangular impression were extracted (segments OA, OB and OC in Figure 3.5) in order to assess the non-symmetry of the indentation imprint. In order to measure the actual area of indentation, a bearing analysis was conducted to indentations in the single material specimens. By using bearing analysis, it is possible to quantify the percentage of the surface (the “bearing ratio”) that lies above or below a reference plane [125], i.e. the bearing depth. The bearing depth was determined by the discontinuous change of slope in the pile-up profile method as suggested by Lim et al. [126] to determine the edge of the contact between indenter and indented material. Roughness statistics were reported from areas neighbouring the residual imprint and following ISO 4287/1-1997 [124] standard, as previously detailed in Equation 3.1.

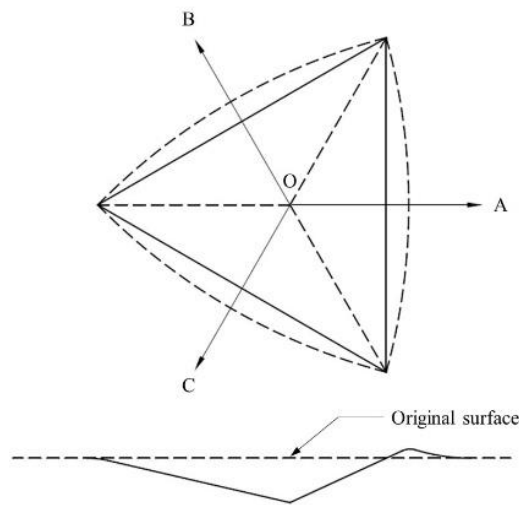


Figure 3.5. Schematic top view and cut view of a residual indentation left by a three-side Berkovich indenter. The diagram assumes piling-up dominated deformation.

3.2. Numerical methods

3.2.1 Finite element approach to indentation

3.2.1.1 Geometrical representation and boundary conditions

The indentation test of a bulk metal, using a Berkovich indenter, has been numerically simulated using the ABAQUS Standard 6.12-3 FE code. Given that the Berkovich indenter is a triangular-base pyramid having a six-fold symmetry, only a sixth of the problem has been modelled as schematically illustrated by the shaded part of Figure 3.6.

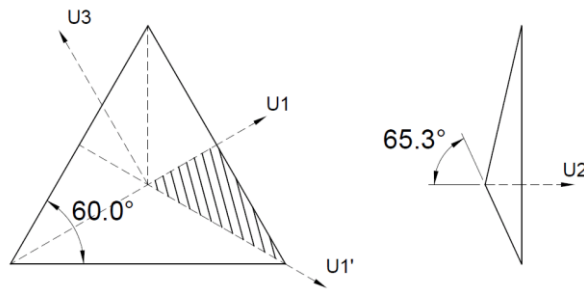


Figure 3.6. Schematic of the geometry of the Berkovich indenter showing a six-fold symmetry.

As presented in Figure 3.7, the Berkovich indenter has been modelled as a 3D discrete rigid body using 3-node 3D rigid triangular facet elements (R3D3 in ABAQUS). The specimen was defined as a 3D deformable body and has been discretised using tetrahedral elements (C3D4 in ABAQUS) owing to their capability to approximate complex boundaries, such as the plasticised material around the indenter. Hexahedral shaped elements with reduced integration were also tested, however due to the imposed large rotations beneath the indenter hourglass modes were observed. Full integration elements eliminated the mesh instabilities, yet the solution was penalised in computation time. Computations using tetrahedral and hexahedral elements, both with reduced and full integration, provided consistent results as shown in Figure 3.8. Boundary conditions in the deformable body (specimen) are defined as follows: the nodes of plane *I* represent the surface of the specimen and therefore are allowed to displace in the three directions (U_1 , U_2 , U_3), yet are not allowed to cross the planes of symmetry (*II* and *III*) in fulfilment with the compatibility equations. However, the

displacement of nodes in the contact areas is governed by a master-slave surface-to-surface boundary condition. The master-slave contact interaction between the indenter (master) and the specimen surface (slave) was defined with zero contact friction since the effect of friction on the indentation process can be assumed negligible [19]. The contact pair has been defined using a surface-to-surface formulation that considers the shape of both the slave and master surfaces in the region of contact. The contact constraints are imposed according to a penalty method in which the contact pressure (p_c) at a point in the deformable body is proportional to the penetration distance (h):

$$\begin{aligned} p_c &= 0; (h < 0) \\ p_c &= k_p h; (h \geq 0) \end{aligned} \tag{3.3}$$

where k_p is a large penalty stiffness coefficient used to minimise the penetration of the slave surface into the master surface at the constraint locations. By default, ABAQUS sets the penalty stiffness (k_p) to 10 times a representative underlying element stiffness (k_e). Therefore the surfaces separate if the contact pressure reduces to zero and two separated surfaces come into contact when the contact pressure is greater than zero. The nodes in the planes of symmetry (*II* and *III*) and bottom surface (*IV*) can only deform in their own planes. The motion of the rigid body is determined by a reference point (RP) located at a node in the tip of the Berkovich indenter and therefore the loading and boundary conditions associated with the indenter have been assigned to this point. The RP, and therefore the indenter, is only allowed to translate in the vertical direction ($U1 = U3 = UR1 = UR2 = UR3 = 0$). A force of one-sixth the indentation load in the vertical direction is defined at the RP. The analysis has been split into two static load control steps; during the loading step a load of $P/6$ N is applied to the reference point in the rigid indenter, and during the unloading step the load is reduced to 0.0 N.

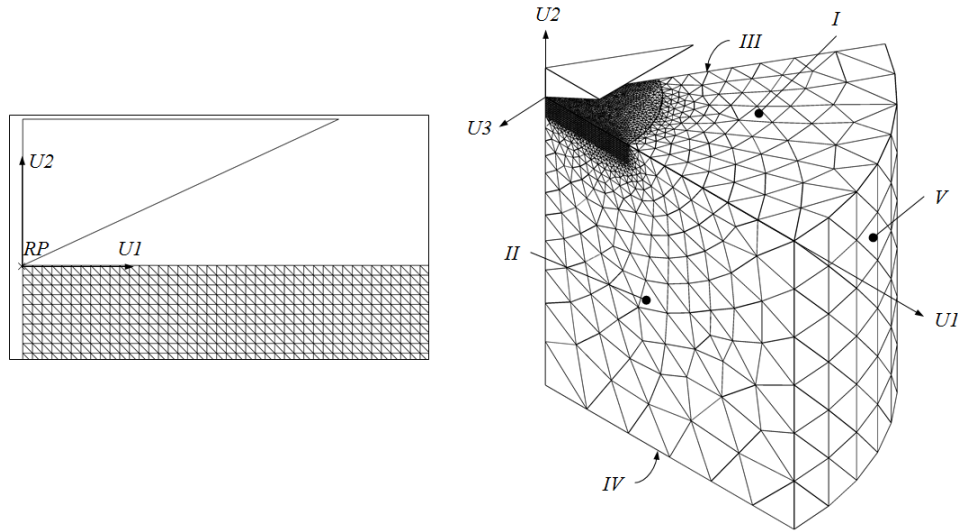


Figure 3.7. Geometry and boundary conditions defined in the 3D indentation model. One-sixth of the domain.

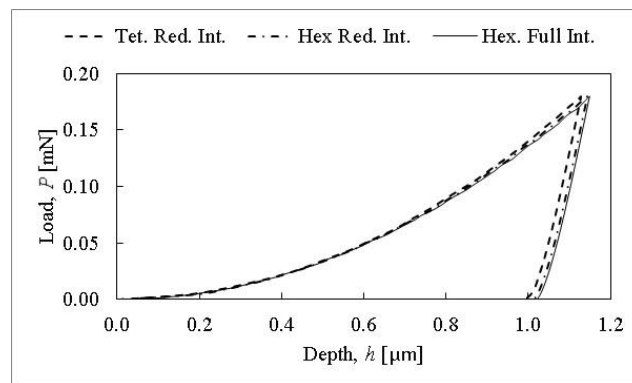


Figure 3.8. FE solution to indentation problem using tetrahedral elements with reduced integration and hexahedral elements with both reduced and full integration.

In addition, the full domain was simulated in order to investigate the sensitivity of the pile-up to the degree of misalignment between the normal to the surface and the centreline of the indenter. Boundary conditions were defined as illustrated in Figure 3.9: the nodes in the bottom of the domain (plane *I*) are constrained in the three directions ($U1 = U2 = U3 = 0$), the cylindrical surface *II* is traction free and the displacement of the nodes of plane *III*, that come in contact with the indenter, is governed by a master-slave surface-to-surface boundary condition. The RP of the rigid body was constrained such that the indenter is only allowed to translate in the vertical direction ($U1 = U3 = UR1 = UR2 = UR3 = 0$). An elastic-perfectly plastic material

model and a ratio of Young's modulus to yield stress (E/σ_y) of approximately 150 was assumed so as to promote a piling-up deformation mode.

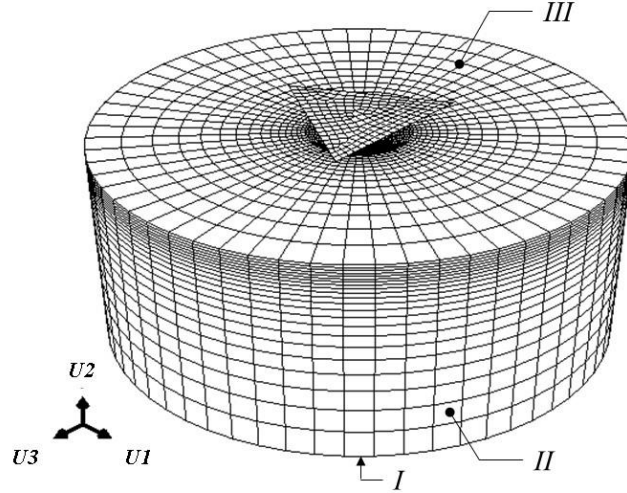


Figure 3.9. Geometry and boundary conditions defined in the 3D indentation model. Full domain.

3.2.1.2 Material constitutive model

The model assumes a rigid indenter pressed into an isotropic, elastic-plastic, rate independent, semi-infinite body under quasi-static and isothermal conditions. The classic plasticity theory has been adopted and therefore the model is valid only for indentation tests carried out at sufficiently deep indentation depths so that the effects of the characteristic microstructural size parameters and strain gradients are negligible. The material constitutive model has been defined using a Swift's power law hardening rule as, unlike Ludwik's model, K and n are interrelated and thus a reduced number of independent parameters are required and consequently less optimisation parameters. Thus, the elastic-plastic true stress-true strain behaviour is assumed to be

$$\sigma = \begin{cases} E\varepsilon_T & \text{for } \sigma \leq \sigma_y \\ K\varepsilon_T^n & \text{for } \sigma \geq \sigma_y \end{cases} \quad 3.4$$

where σ is the stress at the corresponding total strain $\varepsilon_T = (\varepsilon_e + \varepsilon_p)$, ε_e and ε_p are the elastic and plastic strain components, E represents the Young's modulus, K the

strength coefficient and n the strain hardening exponent. In order to ensure continuity at $\varepsilon_p = 0$,

$$\sigma_y = E\varepsilon_y = K\varepsilon_y^n$$

$$K = \sigma_y \left(\frac{E}{\sigma_y} \right)^n \quad 3.5$$

Therefore the complete material constitutive relationship when $\sigma > \sigma_y$ is modelled by

$$\sigma = \sigma_y \left(1 + \frac{E}{\sigma_y} \varepsilon_p \right)^n \quad 3.6$$

Consequently, Young's modulus (E) the initial yield stress (σ_y) and the strain hardening exponent (n) are sufficient to describe the stress–strain relationship.

3.2.1.3 Mesh studies

This section describes the use of the FE model detailed previously to investigate the sensitivity of the predicted maximum indentation depth (h_{max}) to variations in model parameters, such as the mesh size and load step increments. Given the FE model has been defined as a load controlled analysis, h_{max} is an appropriate value to study the model parameters as it is related to the elastic and inelastic strain energy absorbed by the specimen during loading. The full loading curve however, has been assessed to investigate the quality of the mesh. The mesh sensitivity study carried out to establish the optimum mesh refinement at the contact zone beneath the indenter started with a coarse mesh of size ratio (d/h_{max}) equal to unity, where d is the length of the mesh and h_{max} is the maximum indentation depth obtained from experimental data; therefore the mesh sizes span from ~ 1.2 to $0.2 \mu m$. As shown in Figure 3.10, h_{max} reaches convergence at a contact mesh size of $0.6 \mu m$, since the relative difference in h_{max} can be considered negligible ($\Delta h_{max} < 0.71\%$) compared with the value predicted by the finest mesh.

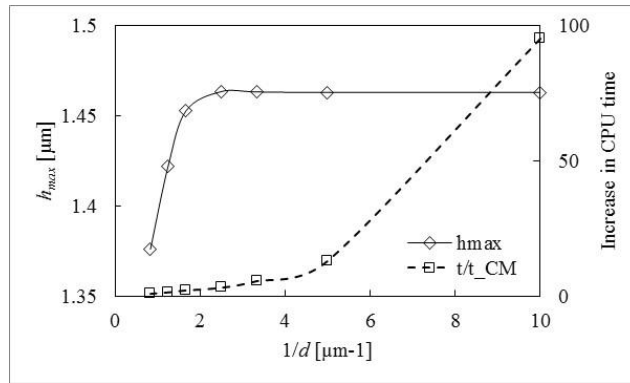


Figure 3.10. Sensitivity of h_{max} to the mesh size at the contact zone. CM refer to the coarsest mesh.

Finer mesh sizes ($< 0.6 \mu\text{m}$) are expected to provide more accurate results given the contact conditions between the indenter and the specimen are better represented during the simulation but also at an expected higher computation cost as illustrated in Figure 3.10. During loading, the nodes at the edges of the perfectly-sharp indenter come first into contact with the surface of the specimen and consequently the elements of the specimen are deformed until the surfaces of the indenter and the specimen generate an interface of contact governed by the shape of the indenter, in fulfilment with the surface-to-surface contact pair defined in the FE model. However, a contact condition may arise in which one node of the indenter exerts a load between two nodes of the deformable body, particularly in nodes along the edges of the indenter and more significantly at nodes at the edges approaching the perfectly sharp tip of the indenter. Therefore as the element density in the deformable body increases, the distance between nodes decreases and the accuracy of the model to follow the downward displacement of the indenter increases. The improved accuracy in representing the shape of the indenter gained by a finer mesh results in a better enforcement of contact constraints as the loading procedure continues and consequently a better prediction of the underlying element stiffness, which is of vital importance when using the penalty method. As can be seen, the difficulties in representing the contact conditions by coarser meshes are highlighted by fluctuations in the predictions of local stiffness (P/dh), as illustrated in Figure 3.11, which consequently results in distorted loading curvatures as observed in Figure 3.12.

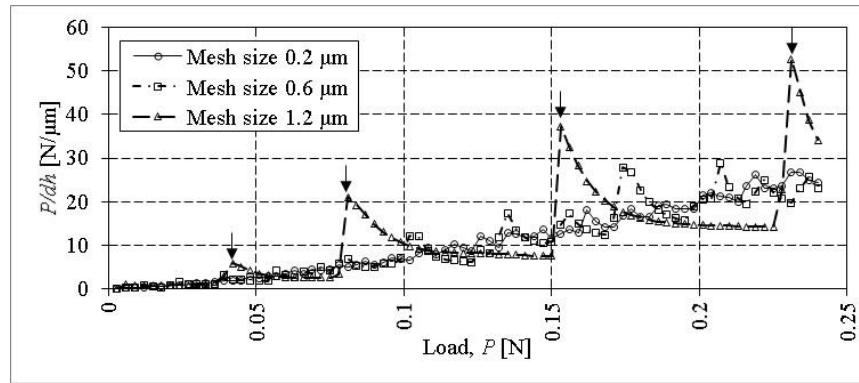


Figure 3.11. Local stiffness of the deformable body at a point beneath the tip of the indenter.

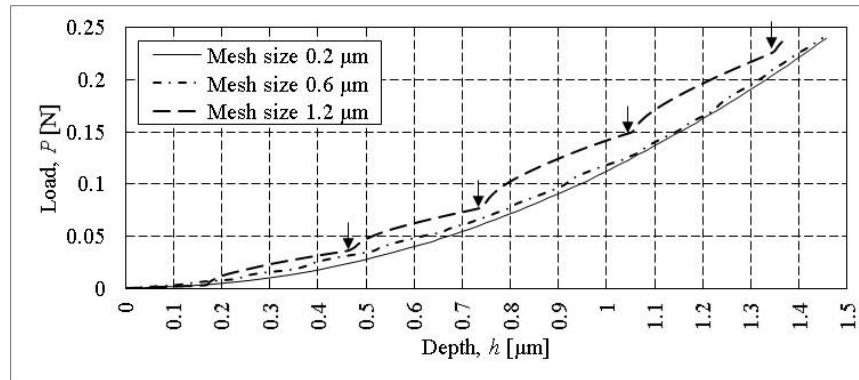


Figure 3.12. Effects of the mesh size on the shape of the loading curvature of indentation.

The general trend is an increase in stiffness as the load is increased, which is associated with the higher resistance to deformation as more nodes in the deformable body come into contact with the edge of the indenter. Figure 3.11 and Figure 3.12 include a coarse mesh of $1.2 \mu\text{m}$ for a better appreciation of the effects of the mesh size on the shape of the loading curvature; the peaks in stiffness indicated with arrows in Figure 3.11 generate the distortions in the shape of the corresponding loading curvature indicated in Figure 3.12. These fluctuations are therefore attributable to the discrete nature of the numerical contact conditions. Therefore, although a higher computation time is expected, the reduced error induced to the optimisation procedure by a smoother loading curve generated by a finer mesh of approximate size of $0.2 \mu\text{m}$ makes it a more favourable option for this study. Furthermore, a negligible deviation in h_{max} ($< 0.004\%$) is predicted by this mesh size, compared to the solution provided by a model

discretised with a mesh of $d = 0.1 \mu\text{m}$ as seen in Figure 3.10. It is to be noted that in order to ensure equilibrium is satisfied in the solution of the FE model, an increase in mesh density may require an increase in the number of load increments. Figure 3.13 provides evidence of the almost negligible sensitivity of h_{max} to the number of steps used in the solution process ($\Delta h_{max} < 0.08\%$), where Δh_{max} is the relative increment in h_{max} predicted by a model defined with 80 loading steps compared to a model of 200 steps. However, as expected the run times are significantly increased by increasing the number of load steps in more than 90% for a 200 loading steps model, relative to the computation time of an 80 loading steps model ($\Delta t/t_{N=80}$). Therefore, it was concluded that 80 load increments provide a robust solution that ensures equilibrium is satisfied at every load increment when using a mesh at the contact zone of approximate size of $0.2 \mu\text{m}$.

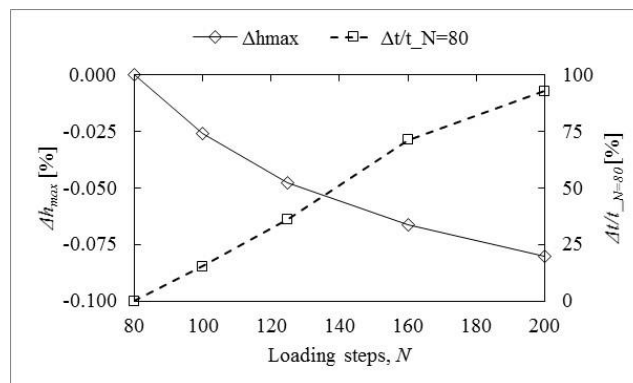


Figure 3.13. Sensitivity of h_{max} to loading steps.

However, since the optimisation procedure involves the iterative solution of a highly non-linear problem with an added complexity of a constantly changing non-linear material property database, and considering the effects of the loading increments on the prediction of indentation depth is negligible, an automatic increment FE model with defined initial, minimum and maximum increment sizes will be used in this study with the intention of ensuring the robustness of the optimised solution. Having discussed the advantages of a proper fit between the surface of the indenter and the elements of the deformable body on the accuracy to capture the indentation depth h , it is reasonable to investigate the necessity of using quadratic elements (C3D10) to mesh the deformable body. Two simulations modelled with quadratic elements of 0.6 and

0.2 μm of length were run and compared with the curve predicted by the model meshed with 0.2 μm linear elements as illustrated in Figure 3.14. As expected, the sensitivity of h_{max} to the element mesh size is negligible when using quadratic elements as the distance between any 2 nodes, and the added capability of a quadratic variation of displacement is more able to represent the contact conditions. The change in h_{max} between the 0.2 μm quadratic element model, relative to the 0.2 μm linear element model, is less than +0.8%. However, the computation time of the quadratic solution is drastically increased by a factor of 56, which makes it computationally unaffordable for the optimisation algorithm. Quadratic elements however, can be used to assess some of the factors affecting depth-sensing indentation data such as tip imperfections arising from the complexity of manufacturing indenters with ideal geometry and wear occurring in practice, and the pile-up/sink-in phenomena. A difference of -0.9% in the FE prediction of h_{max} was observed with an indenter modelled as non-ideal, relative to the model assuming a perfectly sharp indenter. In order to account for the non-ideal geometry, the tip of the indenter was assumed flat with a triangular area of approximately $0.0032 \mu\text{m}^2$, which corresponds to the imperfection usually observed in experimental Berkovich indenters [127].

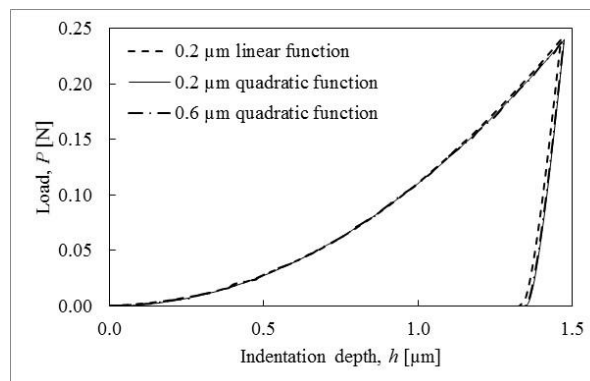


Figure 3.14. P - h curves predicted using second order elements.

3.2.1.4 Sensitivity of the depth-sensing indentation test to the material constitutive parameters

The sensitivity of the predicted $P-h$ curves, with respect to an FE simulation using a set of reference material properties, to the individual variation of up to $\pm 20\%$ in the values of these properties is presented in Figure 3.15. The reference model is based on the mechanical properties corresponding to a high strength steel, i.e. $E/\sigma_y = 150$ and $n = 0.1$. The yield strength largely influences the indentation depths of the $P-h$ curve as can be appreciated in Figure 3.15a due to the larger load (P) required to produce yielding and consequently plastic flow, yet the shape of the unloading curve appears to remain unaltered. This is not the case for the variation of the Young's modulus, which slightly modifies the loading requirements and consequently the indentation depth, but also changes the unloading shape defined by the contact stiffness (S) due to the known dependency of S to the elastic modulus E (see Equation 2.3), as shown in Figure 3.15b. Therefore, it is possible to conclude the loading portion of the curve is largely influenced by the yield strength whereas the unloading portion is more sensitive to the Young's modulus of the bulk metal.

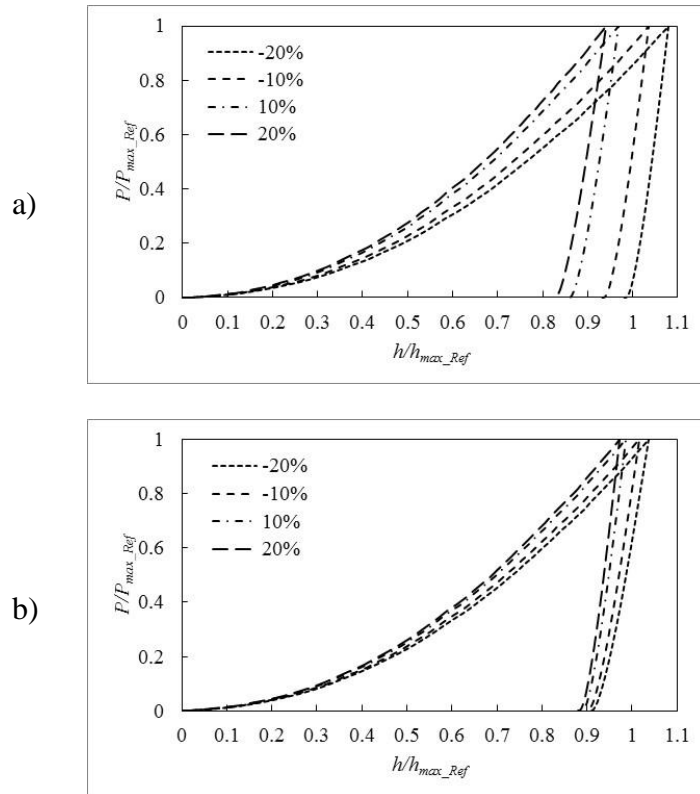


Figure 3.15. Effects of the a) yield strength and b) elastic modulus on the predicted empirical parameters of loading and unloading.

The sensitivity of the predicted indentation depth, h , at P_{max} is shown in Figure 3.16 to be almost negligible to the variation of the Poisson's ratio and the strain hardening exponent compared to E and σ_y . Furthermore, unlike the strain hardening exponent, Poisson's ratio of metals has been studied extensively in the past and it is typically accepted to be around 0.3 in the elastic regime, increasing to 0.5 in the plastic regime [128]; therefore it is not included as an optimization parameter in this study but it is rather considered as a constant mechanical property of magnitude of 0.3. Figure 3.16 also highlights the predicted value of h_{max} is affected by both the magnitude of E and σ_y in a ratio of 0.17:1% and 0.34:1% respectively.

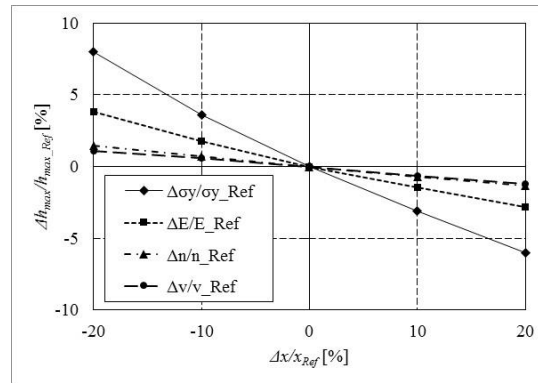


Figure 3.16. Effects of the variation of σ_y , E , ν , and n on the maximum indentation depth (h_{max}).

Having evaluated the sensitivity of h_{max} to the material properties that govern the indentation response, it is possible to approximate the sensitivity of σ_y , which is found to be strongly related to h_{max} (Figure 3.16), to the simulation parameters selected in this study. As reported previously, the deviation in h_{max} between the solutions established using mesh sizes of length $d = 1$ and $2 \mu m$ is less than -0.004% . Assuming a linear relationship between σ_y and h_{max} , this discrepancy reflects in a deviation of $+0.01\%$ σ_y . Moreover, the first order of the displacement function established by the linear elements results in a stiffer solution relative to that of the second order of the quadratic elements, which in turn represents an approximate relative change of less than $+2.8\%$ in the prediction of yield stress. Similarly, setting up an automatic step increment induces a difference of approximately -1.75% to the yield stress prediction, relative to that of a model defined with 200 fixed loading steps. On the other hand, the assumption of a perfectly sharp indenter results in an overestimation of h_{max} that accounts for up to a difference of approximately -2.7% in the magnitude of σ_y .

The degree of pile-up/sink-in is one of the most serious factors that complicate the interpretation of indentation data as this cannot be directly related to the $P-h$ curve [14]. The study of the topography of indentation provides additional information to the optimisation model as it directly relates with the plastic behaviour of the material, as shown in Figure 3.17. In the case of Berkovich indentation, maximum piling-up occurs at the centre of the edges, along the direction U1, in materials with limited capacity to strain-harden. Near the corners on the other hand, the flow of material appears

unrelated to the plastic constitutive behaviour and therefore data along the direction U1' is discarded in the optimisation algorithm. Other materials with different ratios of E/σ_y , e.g. 100 and 450, were evaluated and a consistent outcome was observed.

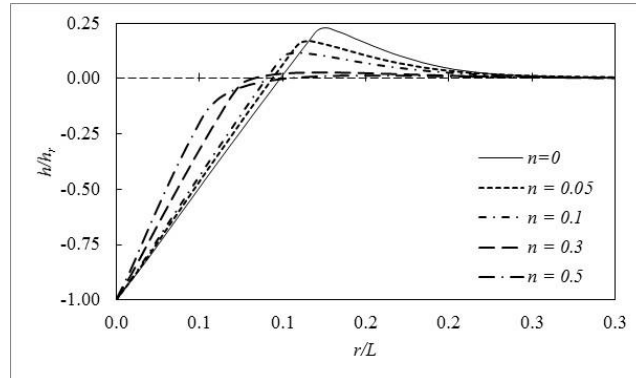


Figure 3.17. Sensitivity of surface topography to the strain-hardening exponent n . Plot in the direction U1 normalised as a ratio of radial distance (r) to total length (L) in the radial direction.

3.2.2 Inverse analysis of the depth-sensing indentation test

The inverse analysis presented in this study is based on an iterative optimisation procedure to find the set of material properties that generates the predicted $P-h$ curve that best fits the corresponding experimental curve. The optimisation model has been defined as follows:

$$f(\mathbf{x}) = \left[\begin{array}{c} \sum_{k=1}^N f_1(\mathbf{x}) \\ \sum_{l=1}^M f_2(\mathbf{x}) \end{array} \right]^2$$

where

$$f_1(\mathbf{x})_k = c \cdot [h_k^{exp} - h(\mathbf{x})_k^{pre}] \quad 3.7$$

$$f_2(\mathbf{x})_l = (1 - c) \cdot [y_l^{exp} - y(\mathbf{x})_l^{pre}]$$

subject to

$$\mathbf{x} = [E, \sigma_y, n]^T$$

$$x_j^L \leq x_j \leq x_j^U, \quad j = 1, 2, 3$$

The vector \mathbf{x} contains the optimisation parameters, i.e. the values of the material properties, and $f(\mathbf{x})$ is the objective function to be minimised. The space of possible solutions has been limited by a set of bound constraints, where x_j^L and x_j^U represent the lower and upper boundaries of x_j . The model can be considered a multi-objective function optimisation since $f(\mathbf{x})$ is the weighted sum of squares between two sets of experimental (*exp*) and predicted data (*pre*), i.e. those related to the *P-h* curve and residual imprint stored respectively in vectors $f_1(\mathbf{x})$ and $f_2(\mathbf{x})$. Therefore, h_k is the indentation depth at a load step k , y_l the axial coordinate of the residual imprint at the corresponding radial coordinate stored in data point l . Both physical data extracted from experimental indentation and FE simulated data have been linearly interpolated in order to evaluate the objective function at the specific sample points, i.e. k and l . Therefore, both constants N and M , the respective number of interpolated sample points included to define the *P-h* curve and residual imprint, are limited by the raw data. This is in order to avoid the linear interpolation of more than one point within two experimental data points, which consequently induce additional error to the model. Bearing in mind that the capabilities of the indentation sensing instrument allows generating significantly more data points to define the *P-h* curve compared with those to define the pile-up profile, scaling coefficients (c and $1-c$) have been introduced with the purpose of equilibrating the contribution of each objective function on the squared

2-norm of the residual. With the aim of keeping the number of calibration parameters to a minimum, and given that both measurements, i.e. the displacement of both the indenter and material along an edge of the indenter in the U2 direction, are of the same order of magnitude, it is reasonable to define the sum of the scaling coefficients equal to unity. Therefore, the contribution of an objective function diminishes as the respective scaling coefficient reduces.

In view of the complex state of stress and the mechanics of contact developed due to the loads imposed by a hard indenter to an elastic-plastic solid, and that the objective function depends implicitly on the constitutive behaviour of the material through the FE solution to the forward problem of indentation, the objective function is expected to be non-convex. Therefore, the reliable and robust trust-region algorithm has been invoked to solve the optimisation problem. The basic idea of the trust-region reflective algorithm is (step 1) building an approximate model which reasonably ‘reflects’ the behaviour of the objective function in a neighbourhood, the trust region, around a current point x_i of the solution of the optimisation problem $f(x_i)$ at the i -th iteration. Then, (step 2) a trial step s_i is computed by minimising the approximate model, known as the trust-region sub-problem, and (step 3) the solution is taken as the next iterate point if the valued objective function is reduced, i.e. x_i is updated to x_i+s_i if $f(x_i+s_i) < f(x_i)$; otherwise, the current point remains unchanged, i.e. $x_i+s_i = x_i$. Lastly (step 4), the trust region is enlarged if the approximate model fits the original problem well or reduced if otherwise [129]. Steps 1 to 4 are repeated until convergence. Equation 3.7 has been coded in a MATLAB script (Appendix I) using the *lsqnonlin* function available in the Optimization Toolbox™, which is based on Coleman and Li’s [130] interior-reflective Newton method. The trust-region sub-problem is formulated as described in the MATLAB product documentation [131]. In summary, the vector x_i is iteratively modified using a trust-region-reflective algorithm, starting from the initial guess vector (x_0) defined by the user until convergence is reached as detailed in Figure 3.18. The model is said to converge when the absolute change in either the solution vector ($\|x_i - x_{i+1}\|$) or the residual ($|f(x_i)-f(x_{i+1})|$) is less than a specified threshold value. Of course, the stopping criterion does not guarantee a minimiser.

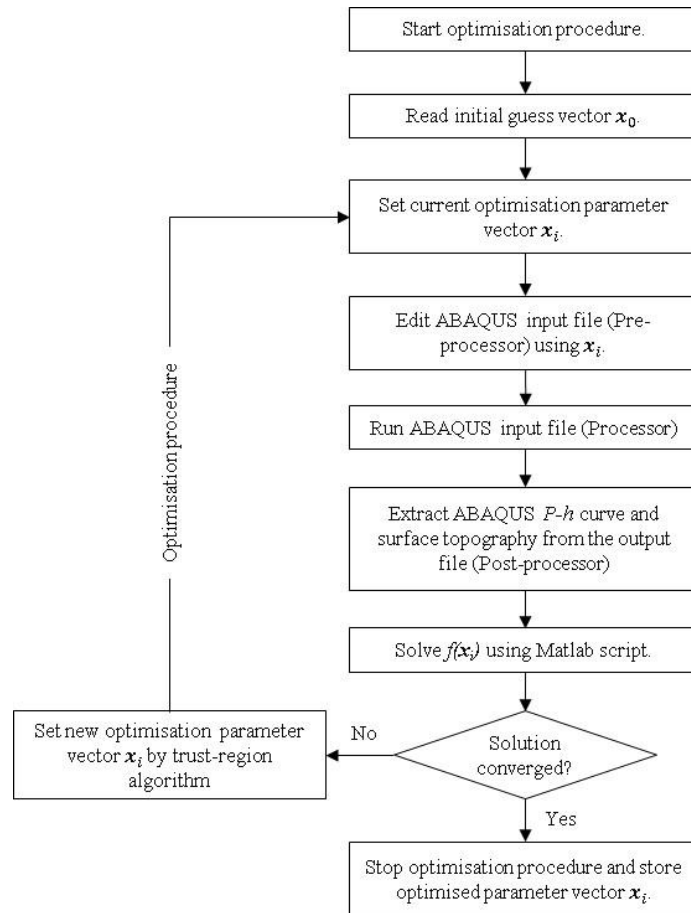


Figure 3.18. Flow chart of the multi-objective function optimisation procedure.

3.2.3 Finite element modelling of the IFW process

This section presents the development of a finite element (FE) model based on the commercial software DEFORM to predict the final residual stress field in an inertia friction welded component of a SCM steel. The FE model considers the elastic and inelastic components of strain resulting from mechanical deformation, temperature changes in the material and volumetric changes associated with phase transformations. Several simulations were run using this FE model in order to address the sensitivity of the final residual stress field to the individual effects of the microstructural changes and the interrelationship of multiple phases. The outcomes of this study motivated the development of the characterisation technique based on the inverse analysis of the depth-sensing indentation test in order to provide a more accurate representation of the

constitutive behaviour across the weld so as to improve the accuracy of the residual stress predictions in FE modelling of the IFW process.

The FE analysis has been split into two models to represent different parts of the welding process, a welding model and a cooling model. The welding model extends in time from the beginning of the process to the complete deceleration of the flywheel, whereas the cooling model consists of an initial period of 45 s with the axial force (F) applied and a second period of 3600 s with no axial force to simulate the final cooling period after the welded component has been removed from the welding machine. Therefore, the final nodal displacements, nodal temperatures and volume fractions calculated in the welding model were exported to the cooling model as the initial conditions.

3.2.3.1 Geometrical representation and boundary conditions

Due to symmetry in the geometry and material of the workpieces, only a quarter of the model was included in the analysis; the stationary workpiece and the stationary die were replaced by a rigid plane as shown in Figure 3.19. In the cooling model the rigid plane is removed and instead a boundary condition to restrict the movement in the z -axis yet allowing elastic recoveries in the r -axis was defined in the interface of the rotary workpiece to simulate the bonding of material at the interface. Thermal exchange with the surroundings is prescribed on the external surfaces of the workpieces with an air temperature of 20°C.

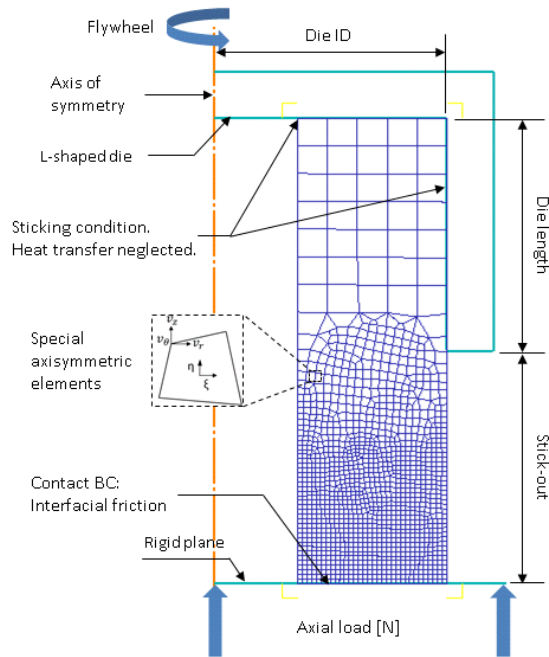


Figure 3.19. Welding model set-up and boundary conditions.

In order to ensure the rotational speed is transmitted to the rotary workpiece, a sticking condition was defined between the “L-shaped” die and the rotary workpiece as a velocity boundary condition. However, heat transfer was neglected at die-workpiece interface since thermal interactions during welding are mainly dominated by conduction within the workpieces [132]. An inter-object contact condition in the outer nodes of the rotary workpiece was defined for the case of any self-contact during the simulation. The frictional traction (f_s) was defined by a contact boundary condition at the interface of the rotary workpiece and the rigid plane using the representative technique described as follows. The surface traction in the model is defined by a classic Coulomb friction model throughout the process,

$$f_s = \mu p \quad 3.8$$

where μ is the friction coefficient and p is the normal pressure. Since the friction coefficient cannot be determined experimentally, an *apparent coefficient of friction* has been defined as derived by Bennett et al. [81]:

$$\mu^s = \frac{(E_{exp}^{s+1} - E_{exp}^s)}{-\omega \cdot \Delta t \cdot p \cdot [2\pi/3 \cdot (r_o^3 - r_i^3)]} \quad 3.9$$

Here, the numerator represents the experimental energy loss ($-ΔE_{exp}$) as a function of the angular velocity (ω) obtained from the rpm measured during the inertia welding trial, Δt is the time period, p is the normal pressure, r_o the outer radius and r_i the inner radius of the contact at the weld interface. The apparent coefficient of friction defines the average contact condition over the entire interface area for a given time period assuming contact is maintained across the interface with constant values of contact pressure (p) and interface area (r_o, r_i). Using the calculated apparent coefficient value and Equation 3.8, the torque is computed during the analysis by integrating the cross product of surface traction (f_s) and the radial distance (r) over the contact area (A_c) as expressed in Equation 3.10.

$$\bar{T} = \int_{A_c} f_s \times r dA_c \quad 3.10$$

For a given time-step (s) DEFORM updates the available kinetic energy after the losses due to friction as follows:

$$E_{num}^{s+1} - E_{num}^s = -\Delta t \cdot \omega \cdot \bar{T} \quad 3.11$$

Where E_{num}^{s+1} and E_{num}^s are the rotational kinetic energies predicted by the model at the next and current time steps, ω the angular velocity, Δt the time period and \bar{T} the generated torque. Using the pre-set parameters for welding described in Table 3.2, the torsional motion of the rotary die was defined in the FE model using a movement control based on kinetic energy (E_k), moment of inertia (I), and an efficiency parameter to take into consideration other factors of the system that inherently contribute to the energy losses. An efficiency of 0.75 has been determined based on a parametric analysis. The total amount of kinetic energy available to generate heat was calculated using [133]:

$$E_k = \frac{1}{2} \cdot I \cdot \omega^2 \quad 3.12$$

where the value of moment of inertia (I) and the nominal angular velocity (ω) were taken from the specifications of the inertia friction welding machine. In addition, the axial load during welding was introduced in DEFORM as a constant force (F) derived from the welding parameters:

$$F = PSIg \cdot A_{gauge} \quad 3.13$$

where $PSIg$ is the pressure in the hydraulic cylinder acting on the gauge area A_{gauge} .

Special axisymmetric elements defined with a three-component velocity vector [109] were used to mesh the workpiece in order to include torsional effects. A mesh convergence study was carried out in order to establish the optimum mesh refinement at the contact zone where the gradients of strain and temperature are expected to be large. As observed in Figure 3.20, a sufficiently dense mesh capable of capturing the thermo-mechanical events while not overly-demanding the computing resources was established by an interface mesh size of 0.5 mm. The final upset value was used as the convergence criterion as it defines the final overall length in order to satisfy the geometric design and represents the integration of the thermo-mechanical phenomena described in the FE methodology. Considering that the mesh is not severely distorted at the onset of welding by the low pressure IFW process studied in this work, an adaptive remeshing procedure was not included in order to avoid an excessive computation time and interpolation errors.

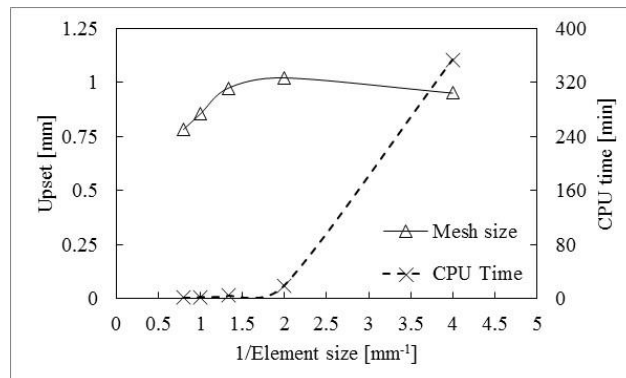


Figure 3.20. Sensitivity of the interfacial mesh size on the final upset value.

3.2.3.2 Material constitutive model

The deformable bodies were represented by a two viscosity viscoplastic model during the welding stage, whereas upon cooling the material model was switched to elastic-viscoplastic in order to capture the evolution of the residual stress field. In order to calculate a consistent stress in rigid, or nearly rigid regions of the workpiece showing near zero deformation rates (the first viscosity) during the welding stage, the strain rate takes a limiting value in the stress-strain relationship defined in the pre-processor of the FE model. Therefore at values of effective strain rate ($\dot{\bar{\epsilon}}$) below the limiting strain rate ($\dot{\bar{\epsilon}}_0$), the material was considered rigid and the stress-strain rate relationship is defined by the viscoplastic constitutive equation:

$$\dot{\epsilon}_{ij} = \frac{2}{3} \frac{\dot{\bar{\epsilon}}_0}{\bar{\sigma}_0} \sigma'_{ij} \quad , \quad \text{with } \bar{\sigma}_0 = f(\bar{\epsilon}, \dot{\bar{\epsilon}}_0) \quad , \quad \text{for } \dot{\bar{\epsilon}} \leq \dot{\bar{\epsilon}}_0 \quad 3.14$$

in which $\dot{\epsilon}_{ij}$ represents the deviatoric strain rate tensor, $\dot{\bar{\epsilon}}$ the effective strain rate, $\bar{\sigma}_0$ the effective stress and σ'_{ij} the deviatoric stress tensor. For the plastic regions however, the Levy-von Mises flow rule can be used to relate the stress tensor to the strain rate tensor [133]. During the welding stage, flow stress has been defined as a function of strain, strain rate and temperature in order to cover the wide range of thermo-mechanical events experienced by the material during the IFW process as follows:

$$\bar{\sigma} = f(\epsilon, \dot{\epsilon}, T) \quad 3.15$$

and therefore the original material database for SCM V steel in the tempered condition [81] was introduced unaltered during this stage. Ludwik's hardening model has been used to idealise the plastic behaviour of the material phases at a given strain rate and temperature such that

$$\sigma = \sigma_y + K \epsilon_p^n \quad 3.16$$

where σ is the flow stress at the corresponding plastic strain ϵ_p and σ_y the yield stress. The strength coefficient (K) and the strain-hardening exponent (n) were fitted with the

experimental data of tempered martensite. As shown in Figure 3.21, tempered martensite destabilises at above 600°C and starts to transform to austenite at approximately 834°C (A_{c1}) [120]. Upon cooling however, austenite exists at lower temperatures than the A_{c1} temperature [120] and therefore the high temperature values (beyond A_{c1}) of yield stress were linearly extrapolated as illustrated in Figure 3.21. Ludwik's relationship was used for the austenitic phase in a similar manner as for tempered martensite using the stress value extrapolated to room temperature as the austenite yield stress. The yield stress (σ_y) of quenched martensite was correlated to the average hardness (HV) recorded by the microhardness test using Tabor's relationship [134] (Equation 2.5). The accuracy of Tabor's relationship was tested by comparing the correlated value of flow stress to the Vickers hardness level in the base metal (tempered martensite), with the flow stress obtained experimentally by the hot compression test. This relationship provided an excellent approximation (< 0.08% error) to the yield stress in the tempered martensite. Ludwik's relationship was employed to represent the strain hardening in the plastic region, and a reduction in yield stress due to temperature similar to the tempered martensite phase was assumed to cover the range of temperatures in which the quenched martensite phase exists.

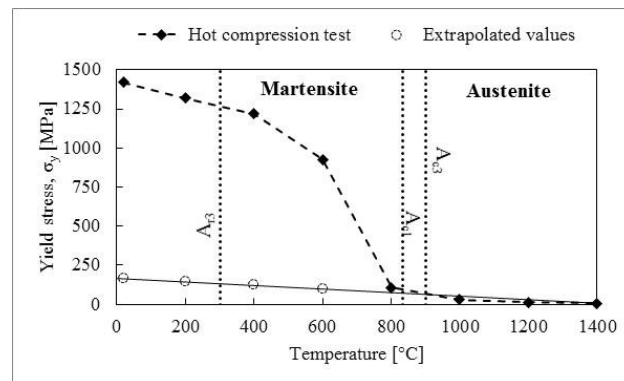


Figure 3.21. Levels of yield stress taken from the hot compression testing in SCMV steel carried out by Bennett et al. [81] at different temperatures. The yield stress of austenite on cooling has been obtained from linear extrapolation.

3.2.3.3 Thermo-mechanical analysis

During the welding stage, material within the fully plasticised zone (FPZ) and partially deformed zone (PDZ) is progressively deformed by the rigid sections as these are

moved towards the interface of the weld by the axial load (F). Since the displacement is strongly dependent on the local temperature as the flow stress of the material is a function of strain, strain rate and temperature (Equation 3.15), the mechanical solution and the thermal solution are fully coupled by the FE model carried out in this study. Therefore, the FE model updates for each time step the nodal velocity vector (u , v , and w components in the radial (r), axial (z) and hoop (θ) directions respectively) satisfying the minimum work-rate principle, from which the key mechanical variables are calculated. The minimum work-rate principle states that the best approximation of the actual velocity distribution is at the lowest work rate; the work rate involves a balance of body forces and surface tractions. Therefore, the work rate function has to be solved for the case when the variation is stationary [135]. The thermal formulation is based on an energy balance of heat generated by friction and plastic deformation, with the heat absorbed and transferred by the material, as detailed elsewhere [135]. Subsequently, in the same time step the nodal temperatures satisfying the energy balance, considering the previous temperature state, are calculated and the thermal strain, ε_T due to changes in temperature is obtained by DEFORM using Equation 3.17 [133],

$$\varepsilon_T = \alpha^* \Delta T + \sum \Delta \varepsilon_T^{prev} \quad 3.17$$

where α^* is the tangential coefficient of thermal expansion. At the end of each time step, the total strains are accumulated in the welded parts according to:

$$\varepsilon_{total} = \varepsilon_e + \varepsilon_p + \varepsilon_T + \varepsilon^{Tr}_{IJ} \quad 3.18$$

where ε_e and ε_p are respectively the elastic and plastic strain components associated with mechanical deformation, ε_T is the thermal strain and ε^{Tr}_{IJ} are inelastic strains due to phase transformation. The nodal temperatures were analysed by the DEFORM-HT add-on according to the energy balance to simulate additional effects in the material including phase volume fraction, distortion and residual stresses. DEFORM-HT is coded with different kinetics models to define the conditions and manner in which one phase is transformed into another [133]. The kinetics of transformation upon heating

was included using a diffusion-type function as shown in Equation 3.19 [133] to calculate the volume fraction of tempered martensite transformed to austenite:

$$\xi_J = 1 - \exp \left\{ M_A \left(\frac{T - T_{AS}}{T_{Ae} - T_{AS}} \right)^{M_B} \right\} \quad 3.19$$

where ξ_J is the volume fraction of the austenite phase, T is the average element temperature, T_{AS} is the transformation start temperature, T_{Ae} is the transformation end temperature, and M_A and M_B are constants. M_A , M_B , T_{AS} , and T_{Ae} were obtained experimentally for SCMVs steels in a previous study [120]. A simplified form of the Magee's equation [133] was employed for representing the kinetics of transformation from austenite to martensite as follows:

$$\xi_M = 1 - e^{(\psi_1 T + \psi_4)} \quad 3.20$$

where, ξ_M is the volume fraction of martensite, T is the average element temperature, and ψ_1 and ψ_4 are constants determined in a previous study [81]. Volumetric strains generated due to phase transformations are calculated in the FE model using [133]:

$$\dot{\varepsilon}^{Tr}_{ij} = \sum \beta_{IJ} \dot{\xi}_J \delta_{ij} \quad 3.21$$

where $\dot{\varepsilon}^{Tr}_{ij}$ is the transformation strain rate from phase I to phase J , β_{IJ} is the fractional length change, $\dot{\xi}_J$ is the transformation volume fraction rate, and δ_{ij} is the Kronecker delta. The fractional length parameter has been defined in the FE model according to a previous experimental analysis in SCMVs steels [1].

Chapter 4 - Phase transformation induced residual stresses during the IFW process

4.1. Introduction

Polymorphic transformations during IFW of SCMV not only result in variations in physical properties but are also accompanied by volumetric changes arising from atomic rearrangements in the crystal structure.

Transformation induced strains are crucial in the analysis of metal working processes such as IFW as the associated volumetric changes modify the residual stress field and will certainly affect the final dimensions after processing. Therefore, the accuracy of the FE model depends on an appropriate representation, at an affordable computational cost, of the metallurgical evolution across the joint.

The aim of this chapter is therefore to investigate, via FE modelling, the sensitivity of the final residual stress state to the phase transformation strain component and the strains arising due to the interrelationship of multiple phases. Therefore, four FE models were set up in this study with increasing complexity of material model as summarised in Table 4.1.

Table 4.1. Simulations to examine the effects of the inclusion of multiple phases in the FE model

Simulation	Tempered martensite	Austenite	Quenched martensite
A	✓	-	-
B	✓	✓*	-
C	✓	✓	-
D	✓	✓	✓

*Austenite phase defined with identical material properties as tempered martensite.

Simulation A is a single phase model which included just the material properties of the original tempered martensite parent metal; this model neglected transformation strains. Simulation B included tempered martensite at low temperatures and austenite at high temperatures using the original parent metal properties for both phases over the entire range of temperatures; this simulation included transformation strains but no details of different properties between phases. Simulation C is a two-phase model similar to B with additional properties of the austenite phase at lower temperatures on cooling. Simulation D was defined as a three-phase model similar to C but allowing the transformation of austenite to an additional phase on cooling, quenched martensite. The last three simulations highlighted the interrelationships and effects of transformation strains generated throughout the transformation paths schematically illustrated in Figure 4.1.

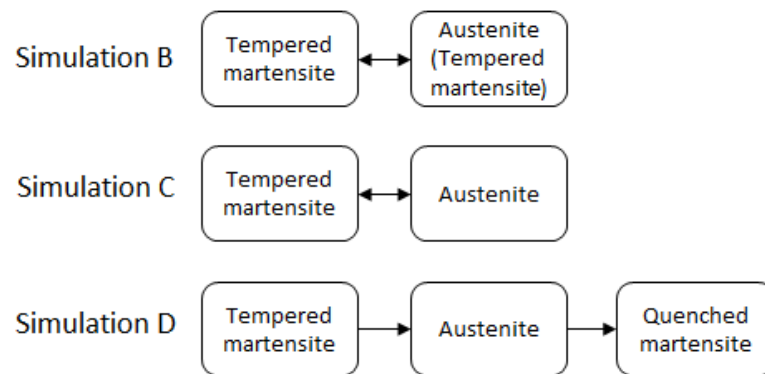


Figure 4.1. Transformation paths for each FE simulation of IFW.

4.2. Thermo-mechanical evolution across an inertia friction weld of a SCM V steel

During the welding stage of a SCM V steel, part of the body-centred-cubic (bcc) tempered martensite in the base metal reaches temperatures above A_{c1} ($\sim 834^{\circ}\text{C}$) [120] within the HAZ and thus transforms to face-centred-cubic (fcc) austenite. The bcc structure is not as tightly packed as the fcc structure and thus upon heating the microstructure experiences a negative (decrease) volumetric change. During the cooling stage however, fcc austenite exposed to rapid cooling rates transforms back to quenched martensite (QM) and small volume fractions of retained austenite as observed by Moat et al. [85] at temperatures below A_{r3} ($\sim 300^{\circ}\text{C}$) [120], resulting in a

highly distorted bcc lattice due to the presence of carbon atoms that remain in solution. This structure is known as a body-centred-tetragonal (bct) lattice, which in turn results in a positive (increase) volumetric change [81].

A steep temperature gradient can be inferred from the abrupt change in flow direction [136]; as revealed in Figure 4.2, material flows radially outward along the weld interface in the vicinity of the weld line and tends to align with the centre line of the shaft away from the weld line. Therefore, as a result of the rapid cooling rates, the FPZ and PDZ are comprised of QM [85, 86], which is responsible for the hard region located between 0 to 3 mm from the weld line in the microhardness profile shown in Figure 4.3. However, the FPZ (0 to ~ 0.5 mm) is identified as QM further hardened as a result of the grain size reduction due to dynamic recrystallization [85, 86]. Temperatures in the UZ, which is located in the region adjacent to the base metal (between ~ 3 to 5 mm), remain below the A_{c1} yet reach sufficiently high levels such as to promote coarsening in the precipitates [137], leading to the formation of over-tempered martensite (OTM) which consequently leads to the hardness trough shown in the microhardness profile at ~ 4.75 mm.



Figure 4.2. Sequence of micrographs showing the characteristic regions comprising the HAZ generated by IFW in the SCMV steel.

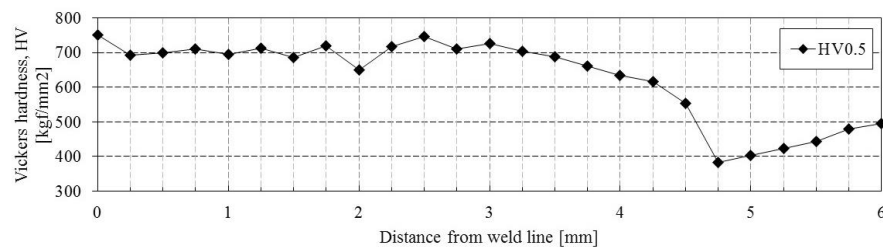


Figure 4.3. Microhardness profile across the HAZ at mid-wall of a SCMV steel weld trial.

4.3. Strain components associated with heat transfer

During the IFW process, the large temperature gradients developed within the component promote the build-up of residual stresses due to volumetric changes, associated with thermal expansion/contraction and phase transformations, being constrained by the rigid or nearly rigid regions of material. This section describes the mechanisms by which heat transfer affects the total strain in the material.

Figure 4.4 shows the temperature profile reached at the start of the initial cooling period and the linear cooling rate (dT/dt) between the start and the end of this period along an axial line at the MD. The initial cooling period starts after 10 s, when the flywheel has completely decelerated, and ends 45 s after. High temperatures are reached in the vicinity of the weld line (~ 0 to 3 mm) at the end of the welding stage and the early period of time of initial cooling, given that the heat flux generated by friction is rapidly transferred inwards by conduction without heat losses through convection and radiation as the contacting surfaces are not exposed to the surroundings. As a consequence, higher peak temperatures are reached at the mean diameter (MD) despite the rate of heat input being a function of the radial distance and angular velocity. In contrast, free surfaces at the inner (ID) and outer (OD) diameters experiences convective and radiative heat losses. Therefore, during the initial cooling period, material away from the weld line (~3 to 24 mm) and the surrounding environment act as a heat sink leading to fast cooling rates (dT/dt) as illustrated by the dashed line in Figure 4.4. Thermodynamically, the system tends to reach isothermal conditions and thus a thermal boundary is generated at ~ 12 mm from the weld line where the linear rate of change in temperature between the start and the end of the initial cooling period (or the start of the final cooling period) goes from negative to positive. This means that at the end of the initial cooling period, using the start of the initial cooling period as the reference state, the material between the weld line and the thermal boundary is releasing heat and therefore contracting, whereas the opposite occurs outside this region, between the thermal boundary and the die-workpiece interface. Therefore, the build-up of residual stresses during the initial cooling period is dominated by thermal strains.

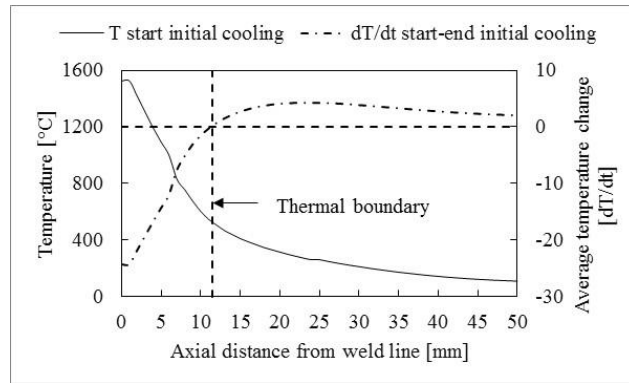


Figure 4.4. Temperature profile at the start of the initial cooling period along an axial line at the MD.

As observed in Figure 4.5a, the frictional heat flux at a point in the weld interface at the MD is rapidly transferred through the material resulting in large temperature differentials. Therefore, as seen in Figure 4.5b, the von Mises stress reaches a maximum at the end of the initial cooling period (45 s) given that thermal strains are proportional to temperature changes in the material. Hence, above 90% of the final residual stress is generated during the first 25 s of cooling. The stress reduction at the end of the initial cooling period (45 s) is attributed to the recovery of elastic strain energy in the form of work due to the material stiffness after the axial loading has been removed. During the final cooling period (45 - 3600 s), when heat transfer is also influenced by convection and radiation, the temperature change throughout the welded component approximates constant values (Figure 4.5a) as the cooling time approaches the end of the final cooling period and thus the build-up of residual stresses due to thermal strains in the material is almost negligible (< 2%).

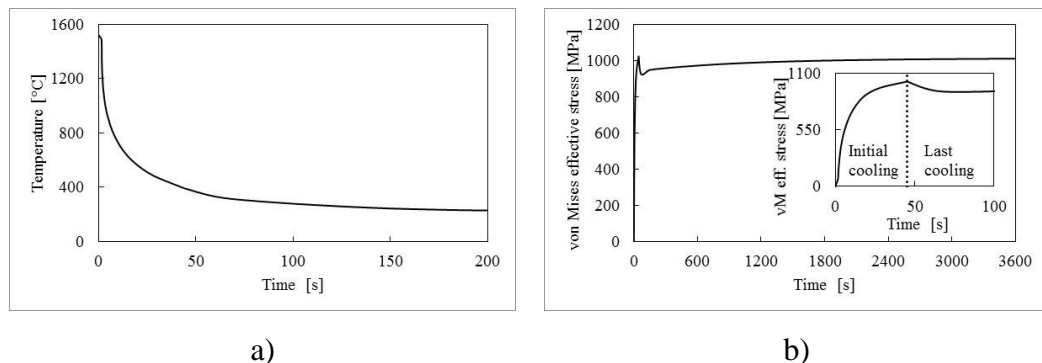


Figure 4.5. a) Temperature profile and b) associated response in the evolution of the von Mises stress at a point in the mid-wall of the weld line during cooling.

4.4. Evolution of residual stresses during IFW

This section introduces the state of stress induced by the IFW process in the component throughout the two general thermo-mechanical stages: the welding stage and the cooling stage, which is comprised of an initial and final cooling period. Dissimilar stress fields are expected at different radial distances from the centre line given the strong dependency on the distribution of pressure and friction over the weld interface to the radial distance [138] as seen in Figure 4.6. Low residual stresses are generated due to plastic deformation during the welding stage as the high temperatures reached in this stage reduce the yield stress of the material being welded, as seen in Figure 4.6a. The build-up of residual stresses during the initial cooling period is dominated by thermal strains due to high cooling rates experienced by the material located in regions near the weld line, as previously explained, and the constraint imposed by the axial load. During the final cooling period, the rate of temperature change has decreased significantly leading to moderate changes in the final residual stress field in the HAZ and a stress reduction beyond the HAZ due to near constant cooling rate (dT/dt) for a prolonged time without the presence of mechanical constraints. In order to analyse quantitatively the characteristics of the residual stress field, line scans in the axial direction were extracted from the FE solution at a distance of 1 mm depth from the ID, the MD and 1 mm depth from the OD as presented in Figure 4.7a, b and c, respectively. The peak value generated near the OD (Figure 4.7c) during the initial cooling is attributed to the radial constraint imposed by the die; this was determined by modifying the “stick-out” distance. Stick-out refers to the axial distance from the weld line to the edge of the L-shaped die in the prior-welding condition as illustrated in Figure 3.19. The location of the peak value above mentioned was observed to change accordingly with the stick-out distance. However, this peak vanishes during the final cooling period once the welded component has been removed from the dies due to stress redistribution as illustrated by the solid line in Figure 4.7c.

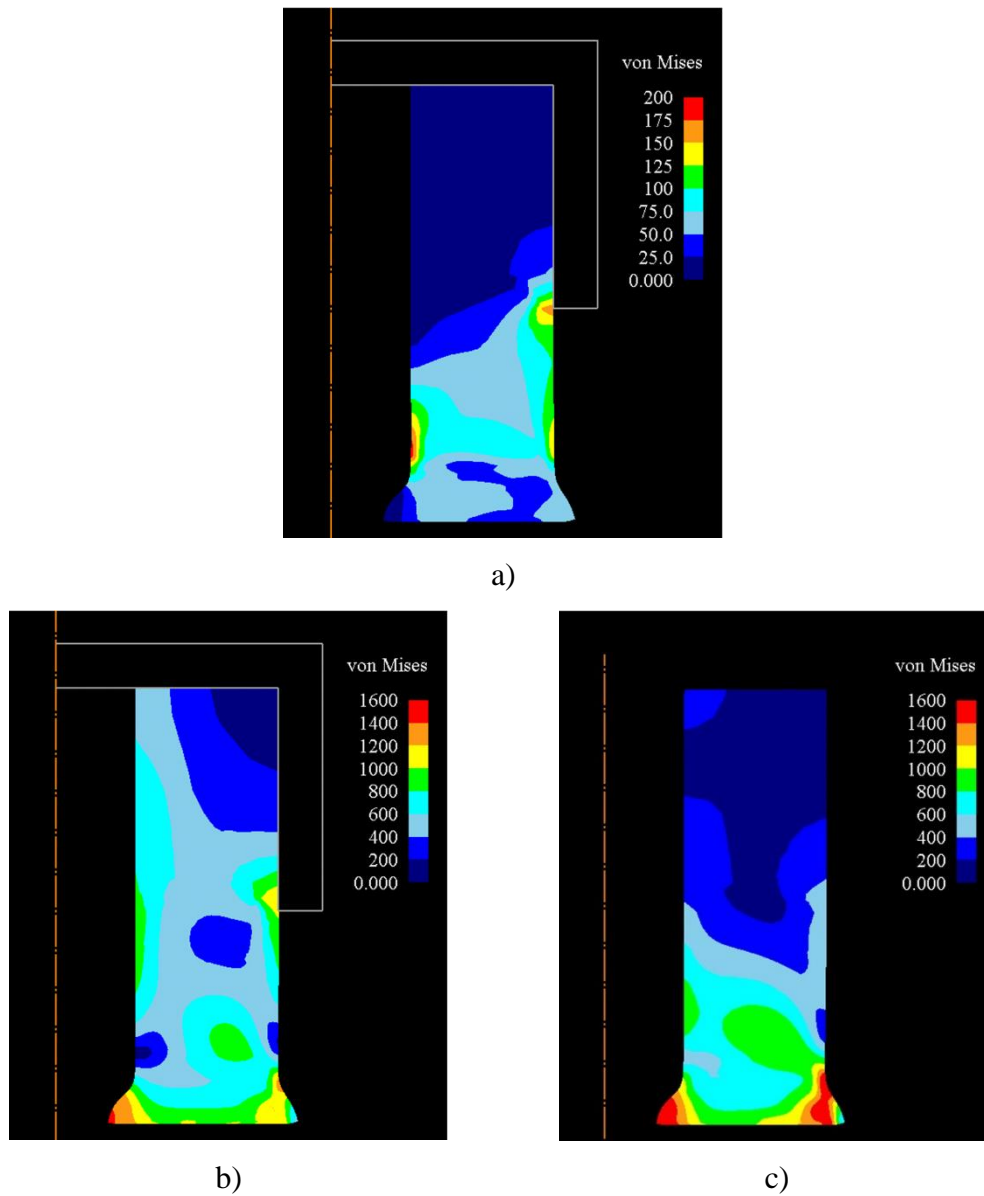


Figure 4.6. Contour plots of Simulation A showing the residual stress field at the end of the a) welding stage, b) initial cooling period and c) final cooling period.

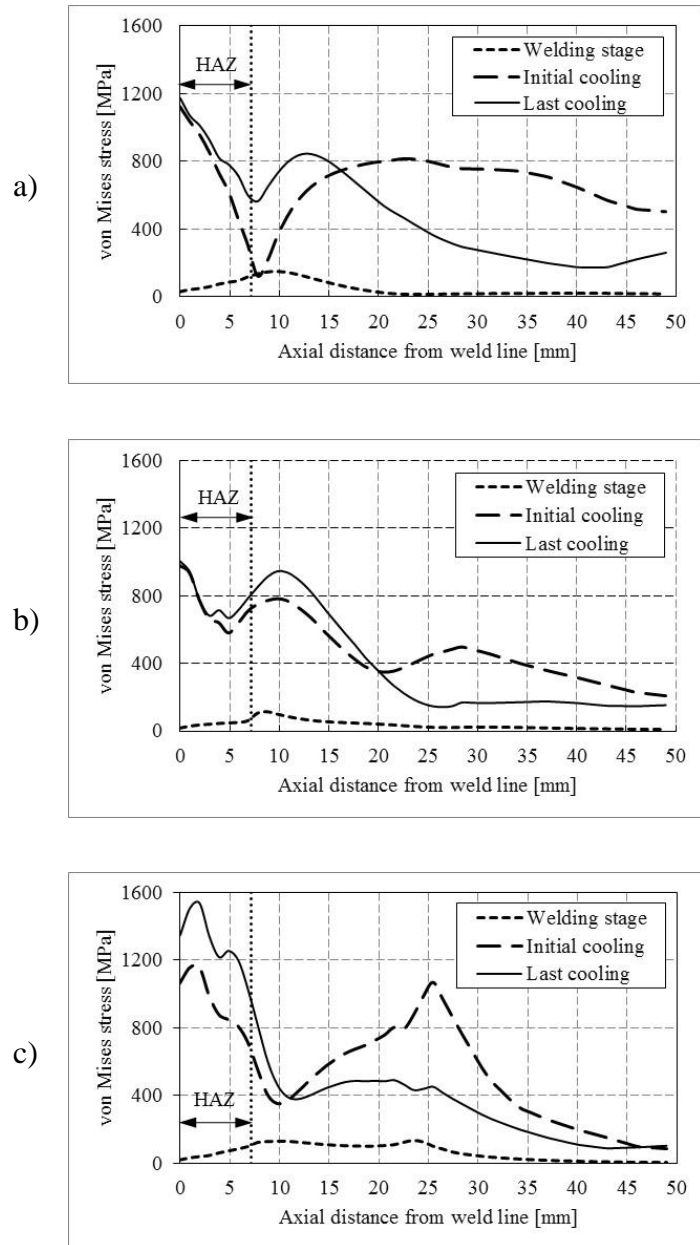


Figure 4.7. Evolution of the predicted von Mises stress field by the FE model (simulation A) at three radial distances: a) 1 mm depth from the ID, b) mean diameter, c) 1 mm depth from the OD.

It is important to note that during the welding stage and initial cooling period, a key on the inner face of the die seats on a keyway machined at the rear face of the rotary workpiece in order to transmit torque and to hold both workpieces concentric to each other and aligned with the line of action of the axial force. In order to ensure the transmission of the rotational speed of the flywheel, a sticking condition can be defined in the FE model at this boundary as described in Chapter 3, assuming the workpiece-

die arrangement remains concentric throughout the process and a zero offset between surfaces. However, the latter assumption may not be fulfilled if material undergoes excessive thermal contraction. Therefore, in order to identify whether the peak generated at a distance related to the die stick-out is an artificial feature resulting from an over constrained model due to an inappropriate representation the clamping condition, the sticking boundary condition at the die-workpiece interface was replaced by a frictional contact condition. As can be seen in Figure 4.8, material beyond approximately 15 mm from the weld line is experiencing a positive radial displacement due to thermal expansion. Between 25 to 50 mm radial displacement is ceased by the mechanical constraint in the opposite direction imposed by the inner surface of the die which means material contraction does not occur in this section. Therefore a sticking condition can be used as an appropriate representation of the clamping conditions.

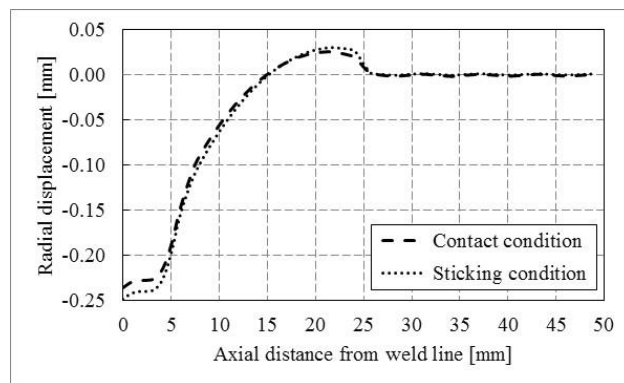


Figure 4.8. Radial displacement in the outer surface at the end of the initial cooling period.

4.5. Effects of microstructural changes

The transformation strain component modifies the total strain only after the temperature within the HAZ is below A_{r3} , which is not reached during the initial cooling period of the IFW of SCMV steel in this case. During the final cooling period, most of the heat has been dissipated, the rate of change in temperature (dT/dt) reaches near constant values throughout the welded components and the transformation strain within the HAZ becomes the dominant strain component in the generation of residual stresses. This section presents a study on the sensitivity of the final residual stress field

predicted by the FE model to the transformation strain and the interrelationship of two or more phases.

4.5.1 Transformation strain

Figure 4.9 shows the residual stress field in the as-welded component as predicted by the FE model neglecting phase transformations (simulation A) compared with the FE model accounting for the effects of the phase transformation strain component (simulation B) at three different locations of the wall-thickness, that is, at 1 mm depth from the ID, at the MD and at 1mm depth from the OD. In order to provide a more detailed quantitative information, values of residual stress were plotted instead of showing the full residual stress field.

When phase transformations are neglected (simulation A), the radial stress predicted at regions approaching the inner and outer surface of the welded components are expected to be negligible given the constraint-free condition of the material located near these surfaces. However, in the vicinity of the weld line, radial stress is expected as an effect of the thermal strains generated due to heat transferred by conduction from the MD, where peak temperatures are reached as explained previously, towards the OD and ID. As can be seen in Figure 4.9a, b and c, in the vicinity of the weld line, the FE model predicts an increase in magnitude of the radial stress towards the MD, which agrees with the experimental results presented by Grant et al. [83] for a single-phase material. Axial stresses behave in a very particular manner as illustrated in the same set of figures; in the region between 0 and ~15 mm from the weld line positive axial stresses are observed close to the ID, becoming negative as the OD is approached. However, beyond ~15 mm the sign of the axial stresses is reversed, becoming negative at the ID and positive at the OD. This is attributed to material expanding and contracting oppositely at specific regions along the workpieces as discussed in section 4.3. This trend is also observed in the experimental maps of residual stress presented by Grant et al. [83]. The maximum residual stress predicted by the FE model is a tensile hoop stress observed at the weld line near the inner surface in Figure 4.9a, which is also in agreement with the experimental investigation carried out by Grant et al. [83]. As inferred from Figure 4.9a and b, hoop residual stresses are responsible for the high

von Mises stress at the weld line in the ID and MD shown in Figure 4.7. However, the peak von Mises stress is predicted at the OD at approximately 2.5 mm from the weld line (illustrated in Figure 4.7c), which is dominated by the axial component stress. As the initiation and/or growth of cracks is influenced by tensile stresses, this would suggest that attention should be paid to the residual stress generated at the ID. The stress trough visible at approximately 7, 5 and 10 mm from the weld line in Figure 4.7a, b, and c, respectively, is attributed to the reduction in magnitude and relative difference of the three components of stress as illustrated in Figure 4.9a, b, and c at the same axial distances. Austenite starts to transform back to martensite from the edge of the HAZ towards the weld line as lower temperatures are reached at early stages of cooling in the far field, and thus when phase transformations are considered by the FE model (simulation B), the peak values of residual stress displace towards the edge of the HAZ (~ 7 mm from the weld line) due to the mismatch between the levels of flow stress of the tempered martensite at high temperatures and low temperatures defined in the FE model. According to the FE model, the peak residual stress is a tensile hoop stress located at the ID near the edge of the HAZ as shown in Figure 4.9d. However, there is a reduction in the magnitude of the peak stress and in general in all three components of stress located within the HAZ when phase transformations are considered in the FE simulation, which is attributed to the positive volumetric change experienced in the lattice during the transformation of austenite back to martensite on cooling, as explained in section 4.2. Consequently, there is a relaxation of up to 70% of the tensile hoop stress found in the vicinity of the weld line at the ID. As can be seen in Figure 4.9d, e and f, a region of compressive hoop stress exists near the edge of the HAZ, which changes to a tensile value at the HAZ boundary. These trends are in close agreement with the residual stress maps provided by Moat et al. [2], which in turn provides strong evidence of the validity of the FE models carried out in this study.

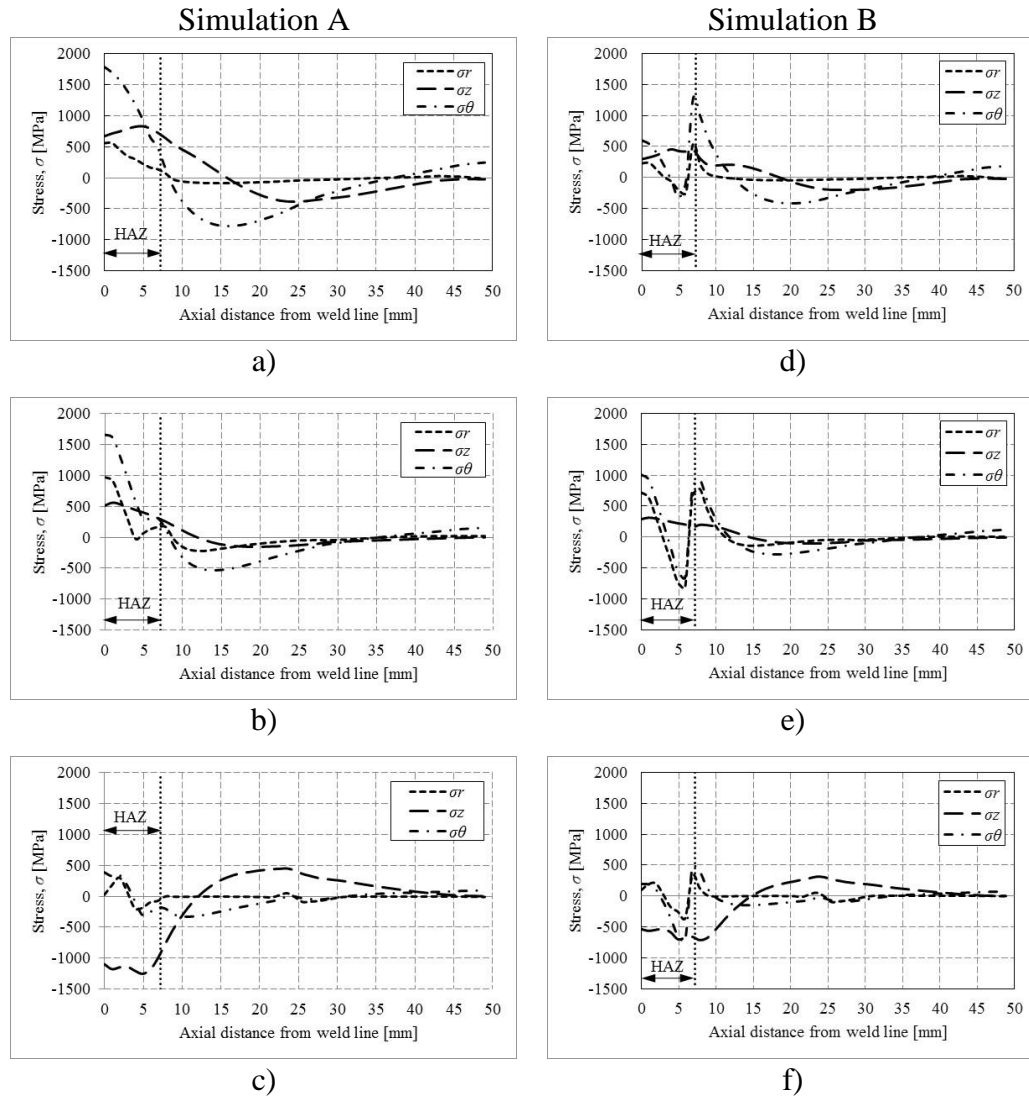


Figure 4.9. Residual stress field in the as-welded condition predicted by the FE model neglecting phase transformations (simulation A) at a) 1 mm depth from the ID, b) MD and c) 1 mm depth from the OD compared with the simulation accounting for the effect of the phase transformation strains (simulation B) at d) 1 mm depth from the ID, e) MD and f) 1 mm depth from the OD.

4.5.2 Inclusion of multiple phases

In a similar manner as for simulation B, simulation C presents a stress reduction in the vicinity of the weld line compared to A as shown in Figure 4.10d, e and f. However, as austenite formed during the welding stage and the early stage of the initial cooling period remains unaltered until the end of this period given that temperatures within the HAZ remain above A_{r3} ($\sim 300^\circ\text{C}$) [120], harder regions (martensite) interact with softer regions (austenite) in simulation C at the onset of cooling until the HAZ is fully

transformed to martensite and small fractions of austenite ($< 2.7\%$), or retained austenite, at the end of the final cooling period. Therefore the interaction of strain components associated to different mechanical properties further modifies the residual stress field predicted by simulation C, leading to an increase of up to 17 % in the peak tensile stress found at the ID in the hoop direction at regions approaching the edge of the HAZ. In the vicinity of the weld line the evolution of residual stresses is correspondingly affected to accommodate strain components generated at the edge of the HAZ. The inclusion of the slightly harder quenched martensite phase formed in simulation D compared to the tempered martensite obtained in simulation C induced almost negligible residual stresses as the total strain (Equation 3.18) generated after the martensitic phases are formed, tempered in simulation C and quenched in simulation D, is similar given that the transformation strain and thermal strains are identical and that the elastic and plastic strains generated during the welding stage play a minor role in the generation of residual stresses during the cooling stage. Based on this information, it is possible to conclude that the two-phase material model is representative of the material model including three-phases, thus providing a useful simplification in terms of the total material data required.

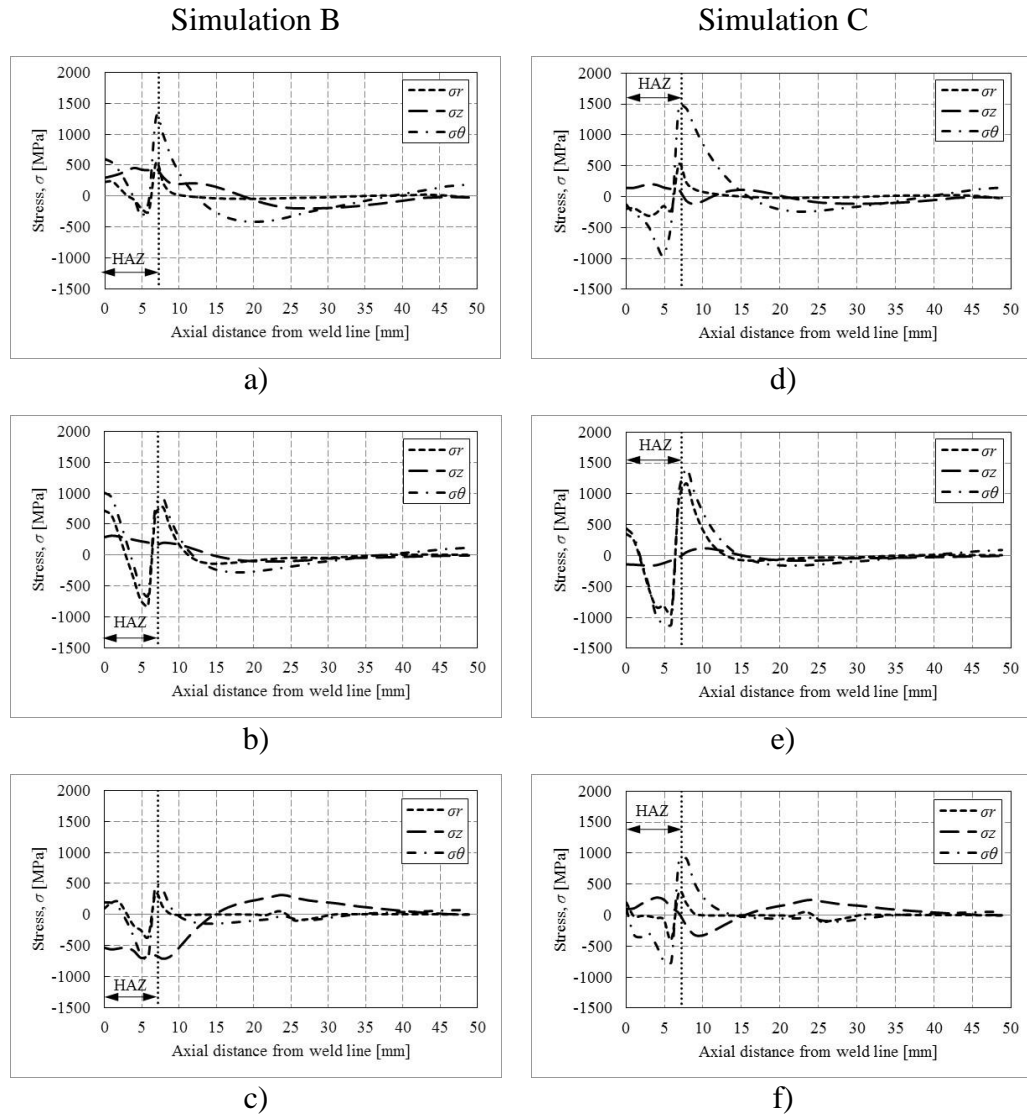


Figure 4.10. Effects of the variation in mechanical properties arising from phase transformations occurring across the HAZ on the residual stress field predicted in the as-welded component at a, d) 1 mm from the ID, b, e) MD and c, f) 1 mm from the OD.

4.5.3 Effects of material properties in present phases

This section assesses the sensitivity of the prediction of residual stresses from the FE model to the approaches taken to define the material database from the parent material. As can be seen in Figure 4.11, the strength coefficient (K) and the strain-hardening exponent (n) introduced in the power law used to define the plastic behaviour of each phase are less significant on the von Mises peak stress compared to the effects induced by the elastic properties due to the almost negligible variation in the flow stress induced by K and n . An approximate variation of 1:1 is observed when increasing the

Young's modulus (E) in the quenched martensite phase as the higher the value the lower the total elastic strain component, according to the constitutive equations for isotropic linear elastic materials with thermal strain. Recalling from section 4.5.1 austenite interacts with martensite during the final cooling period, and a higher yield strength (σ_y) results in higher elastic strains recovered after the mechanical constraints are removed. Strain recovery modifies the stress tensor and therefore the increase in von Mises stress can be attributed to an increased difference between any two sets of principal stresses induced by elastic stresses.

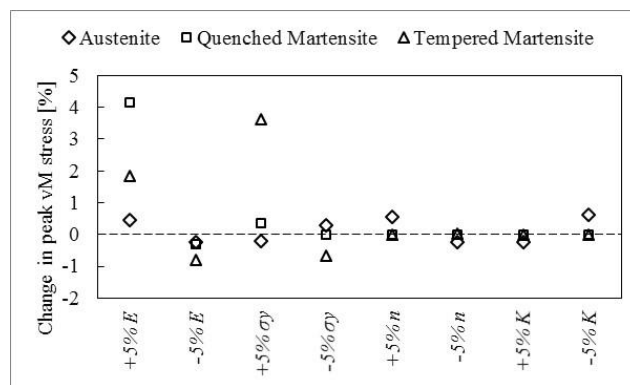


Figure 4.11. Sensitivity on the peak von Mises stress to small variations in material properties (shown in x-axis) of the present phases (identified by markers).

4.6. Conclusions

The investigation discussed in this chapter provided an insight into the individual effects of the volumetric changes resulting from the thermal and transformation strain components as well as the interrelationship of these components on the build-up of residual stresses. The following outcomes highlight the importance of taking into account the transformation strains and the variation of mechanical properties across the weld so as to provide accurate residual stress predictions in FE modelling of the IFW process:

- Residual stresses are largely generated during the initial cooling period, when the total strain is dominated by thermal strains resulting from the large temperature differentials developed during this period. Therefore, the build-up of residual stresses was shown to be highly sensitive to the elastic properties

and therefore the need for a more accurate representation of elastic-plastic properties was suggested.

- The phase transformation strain component becomes dominant during the final cooling period, when most of the heat has been dissipated and the rate of change in temperature (dT/dt) reaches near constant values throughout the welded components. Volumetric changes experienced in the lattice at the onset of transformation from austenite to martensite relax up to 70% of the tensile hoop stress found in the vicinity of the weld line at the ID. Additionally, the final residual stress state in the component is very sensitive to the interrelationship between the thermo-mechanical properties defining each of these phases. Hence, the interaction of soft regions of austenite and hard regions of heat unaffected martensite accounts for up to 17% of the peak tensile stress in regions approaching the edge of the HAZ at the ID.

Therefore, a characterisation technique based on an inverse analysis of the depth-sensing indentation test has been developed for measuring the mechanical properties across the joint. The depth-sensing indentation test has been adopted owing to its capability of measuring very small volumes of material, where the conventional tests are not applicable.

Chapter 5 - Mechanical response to indentation at different loading scales

A very diverse set of methodologies has been developed for determining mechanical properties from depth-sensing indentation experiments. However, most studies are based on theoretical-experimental data, e.g. FE simulated, and the few approaches which are related to the tests on real engineering materials have failed to address the effects of the evolution of the microstructure under the indenter on the inverse approach. Therefore, this chapter is devoted to the presentation of a preliminary study conducted for assessing some of the factors that may pose a detrimental effect on the determination of material properties from depth-sensing indentation data, such as Indentation Size Effects (ISE) and the metallographic preparation of indentation specimens.

5.1. Materials and tensile test

As shown in Figure 5.1, the three materials selected for this study, CrMoV steel, Ti-6Al-4V and C110 copper cover a wide range of elastic-plastic behaviours, including an elastic-perfectly plastic, a linear hardening and a power law hardening material. Table 5.1 reports on the extracted uniaxial properties; the yield stress was determined by using the 0.2% offset method and the plastic behaviour has been idealised using Swift's power law rule (Equation 3.6) by fitting the engineering stress-engineering strain curve to up to an engineering total strain of 4%.

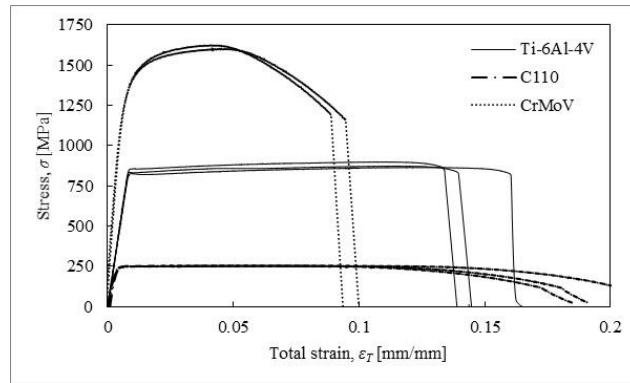


Figure 5.1. Engineering stress – engineering strain curves extracted from tensile testing of specimens of CrMoV steel, C110 copper and Ti-6Al-4V.

Table 5.1. Uniaxial properties of CrMoV, C110 and Ti-6Al-4V extracted from the engineering stress-engineering strain curve.

Material	E [MPa]	σ_y [MPa]	n
C110	99543	249	0.0090
CrMoV	204233	1325	0.1055
Ti-6Al-4V	103116	839	0.0315

C110, as observed in Figure 5.2a, is a polycrystalline high purity copper with a microstructure consisting of equiaxed grains with sizes ranging from 30 to 100 μm . As observed in Figure 5.2b, CrMoV in the fully heat-treated condition exhibits tempered martensite as white spheroidized precipitates of cementite (Fe_3C) sitting on the lath packets [139]. The metallography in Figure 5.2c shows the two-phase microstructure of Ti-6Al-4V, which is comprised by an equiaxed α phase and an intergranular β phase. As determined in the SEM by backscattered electron diffraction, the size of the (darker) α -grains is between 20-30 μm . Under the action of an external load, the average properties of the measured individual grains define the constitutive behaviour of the material tested and thus, a typical microindentation Vickers hardness can provide information on the dependency of the material to microstructural length parameters.

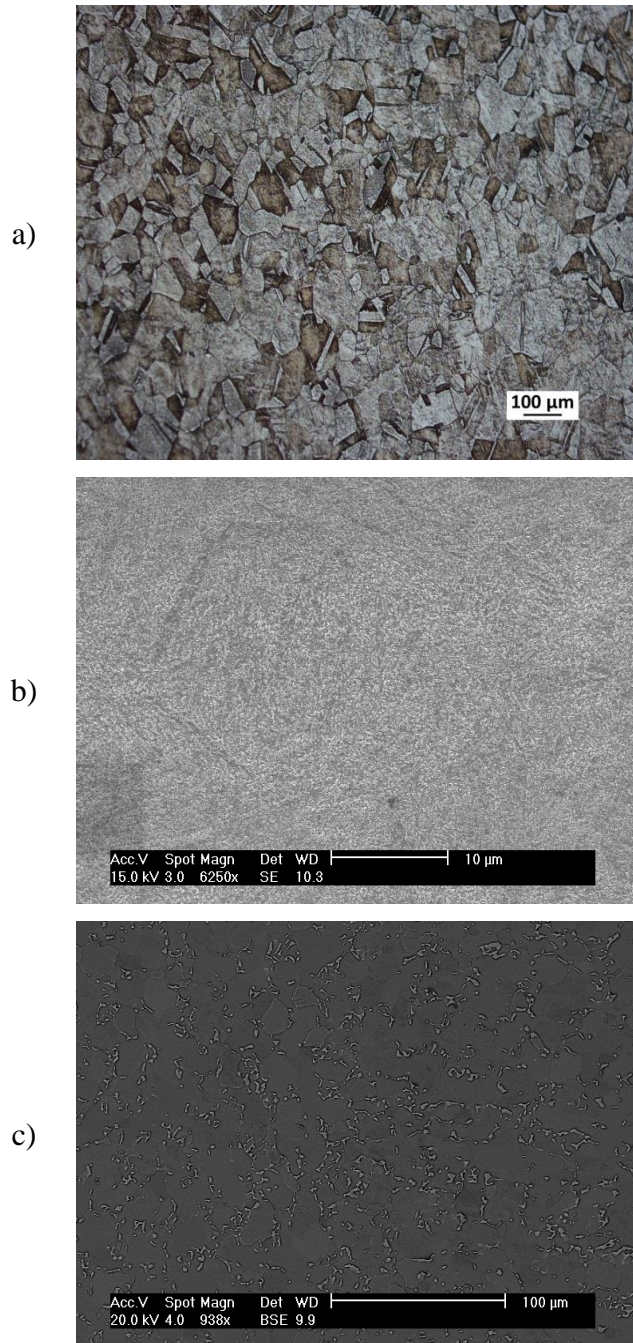


Figure 5.2. Microstructure as observed a) in C110 by optical microscopy and by SEM in b) CrMoV and c) Ti-6Al-4V.

The Vickers microhardness test measured near constant hardness values of 95 ± 4.3 kgf/mm² at loads ranging from 25 to 1000 gram-force in C110, and 484 ± 12.7 kgf/mm² within a load range of 100 to 1000 gram-force in CrMoV as shown in Figure 5.3a and b, respectively. Each data point represents the mean value of five measurements and the error bars represent ± 1 standard deviation. Furthermore, due to

the very low levels of impurities in C110 (< 0.01 wt. %), which are randomly and uniformly distributed in the grains, within these indentation loads the hardness value resulted also insensitive to the location of the indentation, e.g. within a grain, on a grain boundary or over an area shared by a number of grains as illustrated in Figure 5.4. In contrast, the hardness of Ti-6Al-4V shows a clear dependence on the magnitude of load as observed in Figure 5.3c. Less scattered data is observed as the load increases, as the number of grains measured increases and possibly due to hardness being less sensitive to other factors that contribute to ISE, such as surface roughness and tip roundness. It is also noticeable that within the range of loads covered by the microhardness tester ($P < 1000$ gf), the hardness magnitude never converges to a constant value. Therefore, using a macrohardness tester loaded to 2.5 and 30 kgf it was concluded that a hardness of 312.2HV_{2.5} can be taken as load-independent as indicated by the dashed line in Figure 5.3c. In addition, considering only the hardness values at their respective highest test load, a mean Vickers hardness of 481.8HV_{1.0} for CrMoV, 97.1HV_{1.0} for C110 is observed to be load-independent. These values are used throughout this thesis and therefore are summarised in Table 5.2 for the ease of referencing.

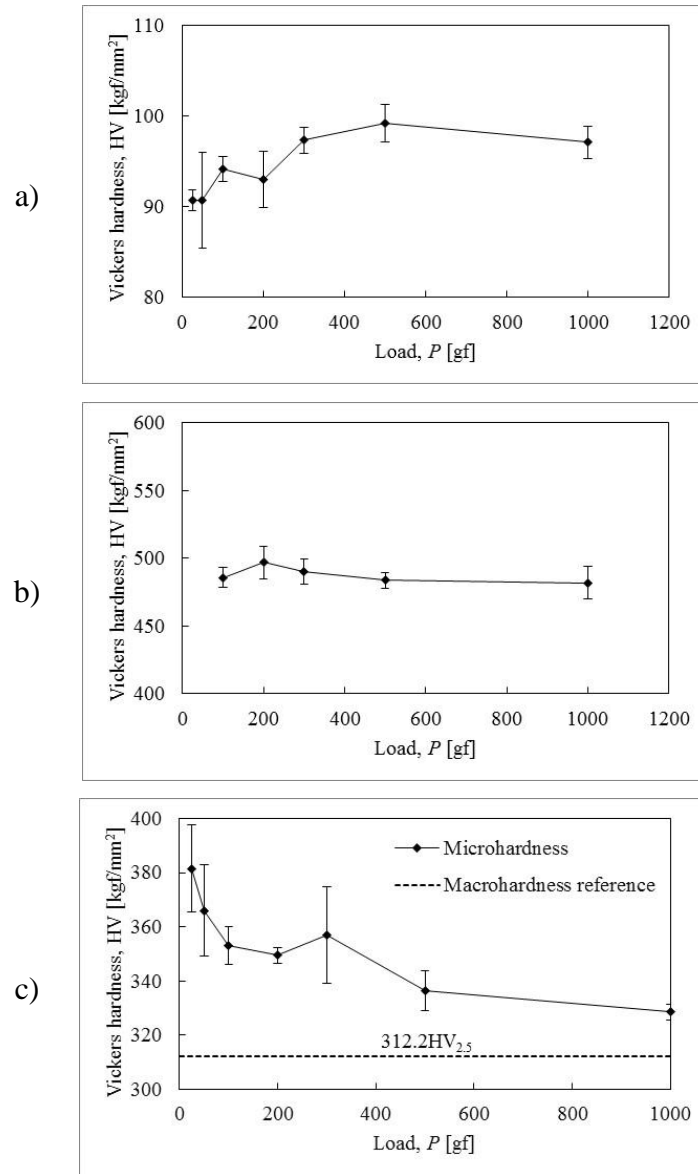


Figure 5.3. Sensitivity of hardness value to the indentation load for a) C110, b) CrMoV and c) Ti-6Al-4V. Error bars represent 1 standard deviation.

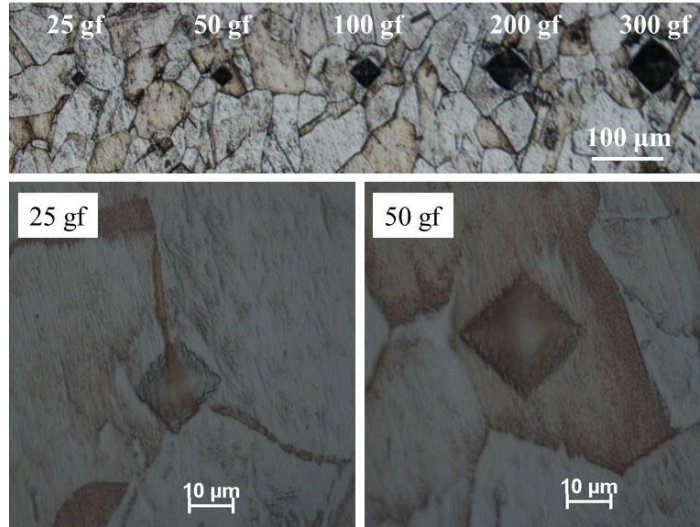


Figure 5.4. Optical micrographs showing residual imprints of indentations at various loads on C110 copper.

Table 5.2. Vickers hardness values of CrMoV steel, C110 copper and Ti-6Al-4V.

Material	Load [kgf]	HV [kgf/mm ²]
C110 copper	0.3	91.1
CrMoV steel	1.0	481.8
Ti-6Al-4V	2.5	312.2

5.2. Depth-sensing indentation data

The recovery of the uniaxial stress-strain relationship of the material via the inverse analysis of a $P-h$ curve is challenging in the first instance as the yield process during indentation involves a triaxial strain at a wide range of intensities. Furthermore, each set of indentations comes associated with uncertainties due to inhomogeneity in the specimen material as well as measurement errors such as calibration and operator bias, which consequently results in scatter or variability in the collected data as observed in the left column of Figure 5.5. The projected area, calculated from the respective $P-h$ curve and assuming an ideal geometry ($A_p = 24.56h^2$), of the Berkovich indenter at full load of $P = 0.48$ N for Ti-6Al-4V, $P = 0.24$ for CrMoV and $P = 0.12$ N for C110 copper is that of an equilateral triangle of side a of approximately 18.16, 9.97 and 13.84 μm respectively. Therefore, the area covered by the indenter is of the same order of magnitude as that of the microstructural features of the tested materials and thus the

forces measured by the instrument become strongly dependent on the microstructure of the material. Hence, the inhomogeneity of the materials is expected to induce variability in the extracted data, as can be assessed from the variability among values of Martens hardness (HM), calculated from each set of $P-h$ curves as a function of load. As observed in the right column of Figure 5.5, the variability of HM tends to decrease as the indentation load increases in the same way as observed in the microhardness measurements. Besides, in all three materials the effects of size parameters (ISE) are still significant even at the maximum load tested for the specimens of Ti-6Al-4V, CrMoV steel and particularly in C110 copper as inferred by the deviation of the measured HM from the load-independent hardness value, i.e. 1.5, 13.5 and 40% respectively. It is to be recognised that the surface area employed in the calculation of Martens hardness neglects the piling-up of material around the indenter and thus overestimates the magnitude of hardness, which means that the ISE in the $P-h$ curves are even greater in reality. This represents a further challenge to the inverse analysis of the depth-sensing indentation test as the local properties of the volume of material measured by the indenter are not always representative of the bulk properties of the material. The extra set of indentations performed in Ti-6Al-4V at a significantly lower loading and unloading rate (1.5 mN/s) shows a lack of sensitivity to strain rate as illustrated in Figure 5.5f; reducing the strain rate, as derived by $\dot{\epsilon} = \frac{dh_p}{dt} \frac{1}{h_p}$ [14], by as much as 84% results in a hardness difference of less than 1.6%. The variability of the data also appears insensitive to the indentation strain rate at this indentation load, yet error bars are not included for clarity.

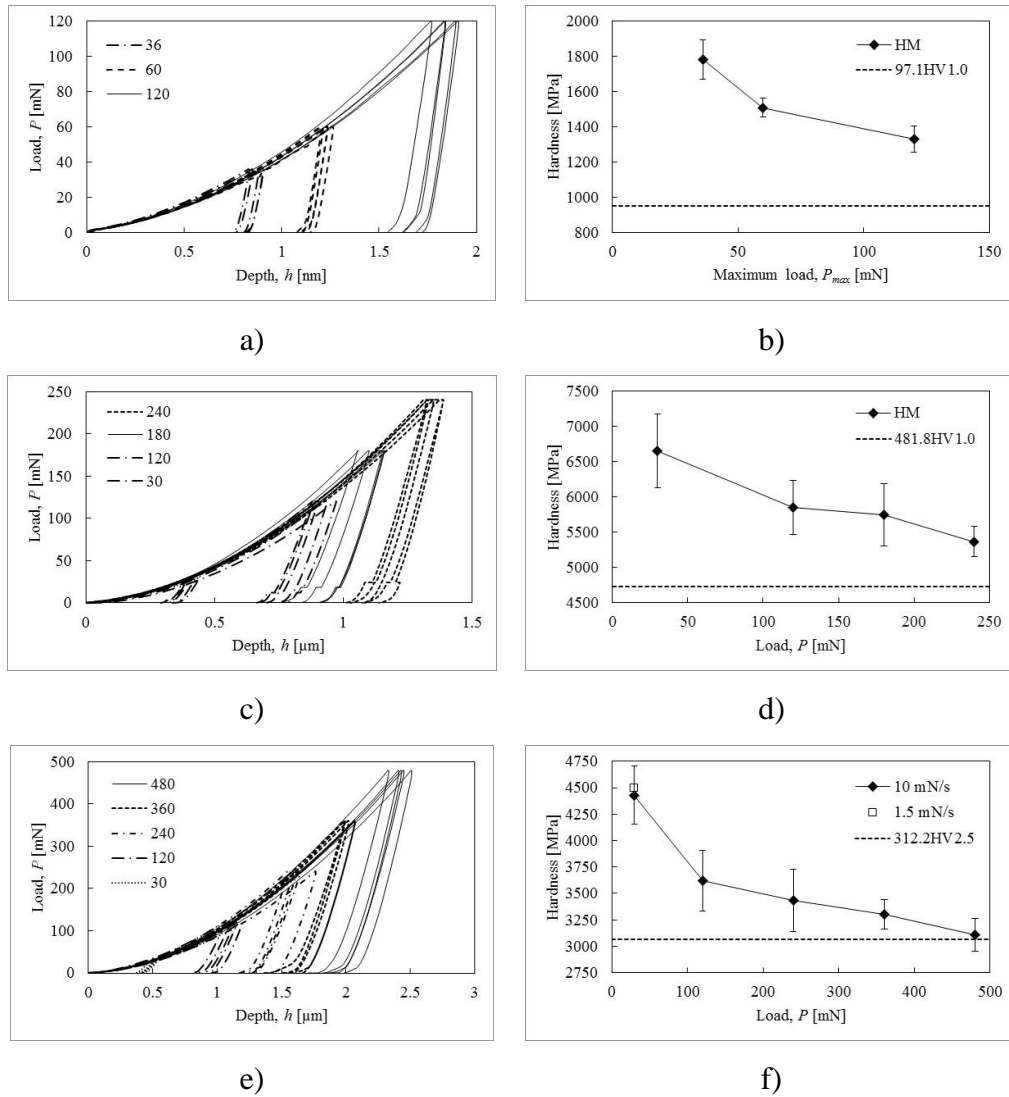


Figure 5.5. Indentation P - h curves (left) and calculated Martens hardness (right) for a, b) C110 copper, c, d) CrMoV steel and e, f) Ti-6Al-4V. Error bars are one standard deviation.

On top of ISE, length parameters affecting the measured hardness value may be introduced by the conditions of the surface of the specimen. Figure 5.6 shows the AFM scan of the surface topography resulting from two different mechanical polishing procedures. Although the surface after polishing using 1 μm diamond suspension appears to be very rough, the average roughness ($R_a = 4.98 \text{ nm}$) is negligible compared with the indentations performed in CrMoV steel, i.e. $h_{max} > 400 \text{ nm}$. As per ISO14577 [13], at indentations depths beyond $20R_a$ the effects of surface roughness are negligible.

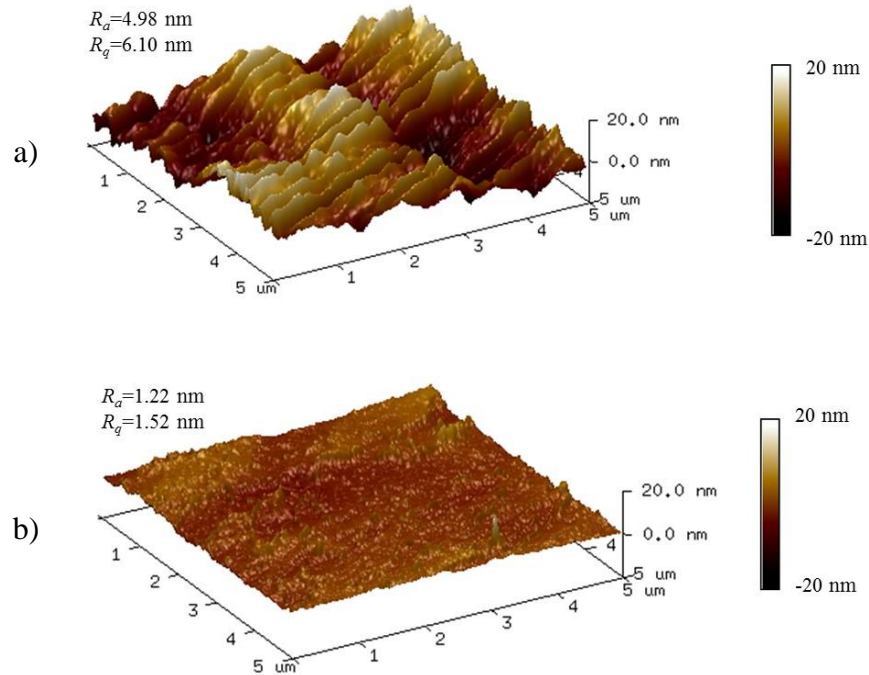


Figure 5.6. AFM topography of CrMoV steel surface after mechanical polishing using a) 1 μm diamond suspension and b) 0.06 μm colloidal silica.

Furthermore, Figure 5.7 suggests that the effects of the metallographic procedure, i.e. surface roughness and the thickness of the strain-hardened layer can be discarded as length parameters affecting hardness measurements. This is somewhat expected as the maximum indentation depths reached in these experiments are between 0.9 to 1.4 μm . The deviation in HM between polishing procedures is within experimental error and hence error bars are excluded for clarity. Notwithstanding, this outcome is based on the strain-hardened surface of CrMoV, a material with low capacity to strain-harden ($n \sim 0.1$). In contrast, the near surface hardness value of materials with high reservoirs for strain-hardening, such as annealed high purity copper ($n \sim 0.45$), are more sensitive to the surface polishing procedure [36]. As a final remark, it is strongly advisable to perform a final polishing on the specimen immediately before the indentation test and the surface measurements immediately after indentation. The foregoing with the aim of preserving a good condition of the surface through the pre- and post-indentation stages, as it was observed that past 90 days after indentation, the surface of C110 in particular started to deteriorate due to surface contamination.

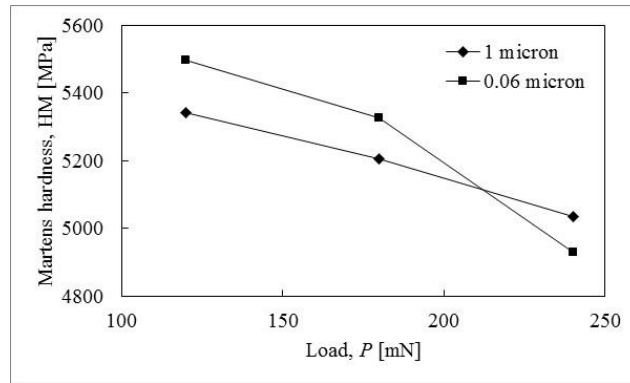


Figure 5.7. Effects of surface preparation on hardness at different load values.

5.3. Measurements of residual imprints

The AFM provided measurements of the value of maximum residual depth left on the material surface at unloading (h_0) in good correspondence with those returned by the sensing device of the indentation instrument (h_r) after instrument compliance and thermal drift correction. The relative difference ($\Delta h/h_r$) spans within a range of 3-15%, which is a result of the uncertainty introduced by the indentation instrument and the calibration of both the X, Y and Z planes of the AFM scanning device and the AFM probe.

Notwithstanding, the extracted P - h curves in this study are insensitive to the polishing procedure, the smoother surface produced after polishing with colloidal silica (Figure 5.9) induces less noise compared with the surface polished using a diamond suspension (Figure 5.8). Data below the original surface has been obscured so as to show the topography around the residual imprint in more detail. Figure 5.8b and Figure 5.9b show the Y coordinate relative to the maximum depth measured by AFM (h_0) in the abscissa and the X coordinate from the indenter centreline normalized by the same value h_0 in the ordinate. Generally, materials with limited capacity to strain-harden are more likely to pile-up, yet comparing these figures suggests that this is not the case for a material exposed to a near surface strain-hardening resulting from the metallographic procedure, provided that the ratio of h_{max} to the thickness of the strain-hardened layer is above unity, since an equivalent degree of pile-up is observed in both specimens, i.e. $Y/h_0 \sim 0.2$.

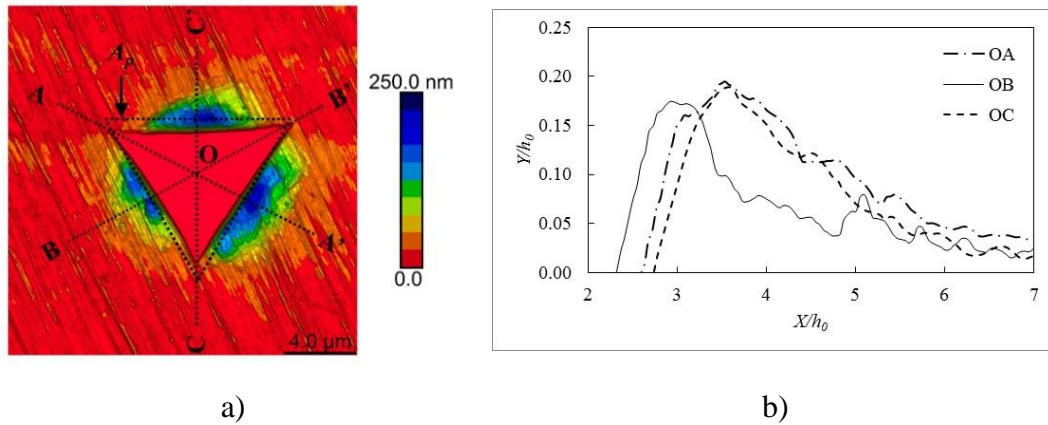


Figure 5.8. a) Height sensor measurement and b) pile-up patterns along the three edges of the residual imprint after the indentation at 240 mN of a polished surface of CrMoV steel with 1 μm diamond suspension.

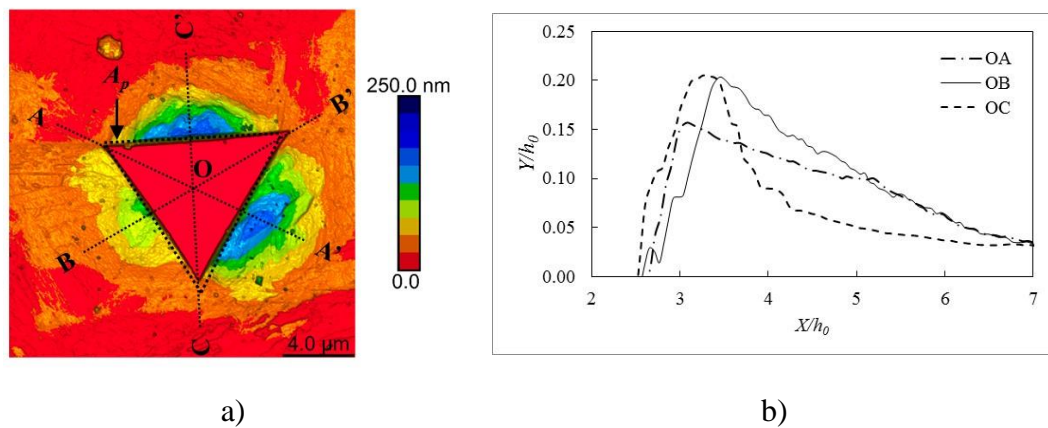


Figure 5.9. a) Height sensor measurement and b) pile-up patterns along the three edges of the residual imprint after the indentation at 240 mN of a polished surface of CrMoV steel with 0.06 μm colloidal silica.

Focusing on the height measurements within the indentation included in Figure 5.8a and Figure 5.9b, some recovery during unloading is evident since the side of the residual imprint deforms into a convex shape as a result of material shrinkage, which is more noticeable in the near surface strain-hardened specimen. The superimposed dashed lines represent the projected area (A_p) by the indenter at h_{max} assuming a perfectly sharp indenter, i.e. $A_p = 24.56h_{max}^2$, which in both cases is larger than the actual area (A) of the residual imprint left by the Berkovich indenter measured using AFM. As summarised in Table 5.3, in specimens of CrMoV steel indented at $P_{max} = 240$ mN, A recovered at some extent as the average ratio $A/A_p = 0.835$. Surface

topographic measurements of both the LS and HS indentation for each specimen are included in Table 5.3; the variation in A is due to experimental error. Furthermore, it is clearly visible in Figure 5.8a that the near surface strain-hardened layer due to mechanical polishing, indented at the same load of 240 mN, is more prone to recover. This is also confirmed by the average ratio $A/A_p = 0.755$. In addition, from the results in Table 5.3, it is possible to conclude that the recovery of the area of indentation during unloading in CrMoV steel is not affected by ISE, as the result of halving the indentation load is a reduction of the average A/A_p ratio of barely 0.025.

Table 5.3. Imprint area of indentation measured via AFM (A) compared with the area projected by an ideal indenter at h_{max} .

Specimen	Indentation	A [μm^2]	A_p [μm^2]	A/A_p
CrMoV 240 mN*	HS	29.83	39.39	0.76
	LS	34.84	46.58	0.75
CrMoV 240 mN	HS	37.10	43.41	0.85
	LS	39.00	47.41	0.82
CrMoV 120 mN	HS	15.42	18.66	0.83
	LS	17.56	22.29	0.79
C110 120 mN	HS	79.90	76.24	1.05
	LS	88.86	89.12	0.99
C110 36 mN	HS	21.32	17.09	1.25
	LS	22.24	20.06	1.1

* Specimen polished with 1 μm diamond suspension

Measurements of A in Ti-6Al-4V were not possible to obtain due to its irregular topography. In contrast to the behaviour of CrMoV upon unloading, in specimens of C110 copper indented at 120 mN, the measured area A although visibly deformed, closely matches A_p (superimposed in Figure 5.10a), i.e. the average A_p/A ratio is close to unity. This is in accordance with Tabor's [40, 43] observation that for some metals, the contact radius left in the surface by a conical indenter does not recover during unloading, that is, only the depth recovers. The case in which the ratio A_p/A exceeded unity (shown in Figure 5.10a) results from the misalignment of the indenter relative to the normal of the surface. From geometry, a maximum tilt angle of 1.8° is measured

between the experimental points along the edge OA' , and the edge of an ideal perfectly sharp indenter after the removal of the load ($P = 0$) as illustrated in Figure 5.10b. Similarly to CrMoV steel, in C110 copper, any recovery during unloading appears to be independent from ISE as at lower loads, e.g. 36 mN, A is not less than A_p . The increased ratio A_p/A results from a more pronounced misalignment in excess of 3.7° that consequently leaves a largely deformed imprint as can be seen in Figure 5.11a. The misalignment of the indenter centreline from the normal of the surface is caused by a combination of the non-flat surface produced during the metallographic preparation and the misalignment between the centrelines of the sample mounting and instrument holder.

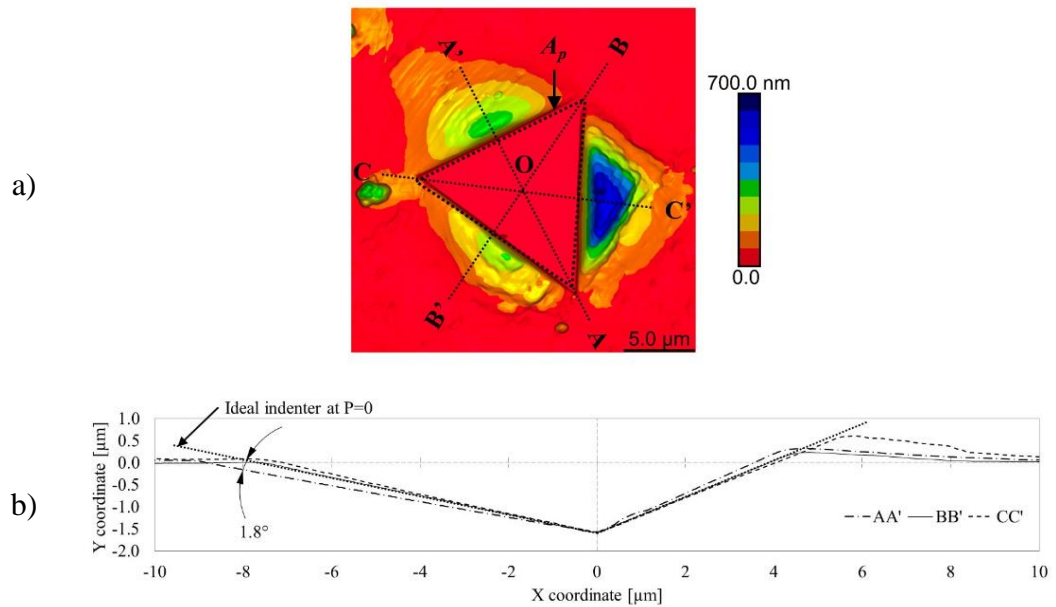


Figure 5.10. a) Height sensor measurement and b) cross-section profile of the imprint in C110 formed by a Berkovich indenter loaded to 120 mN.

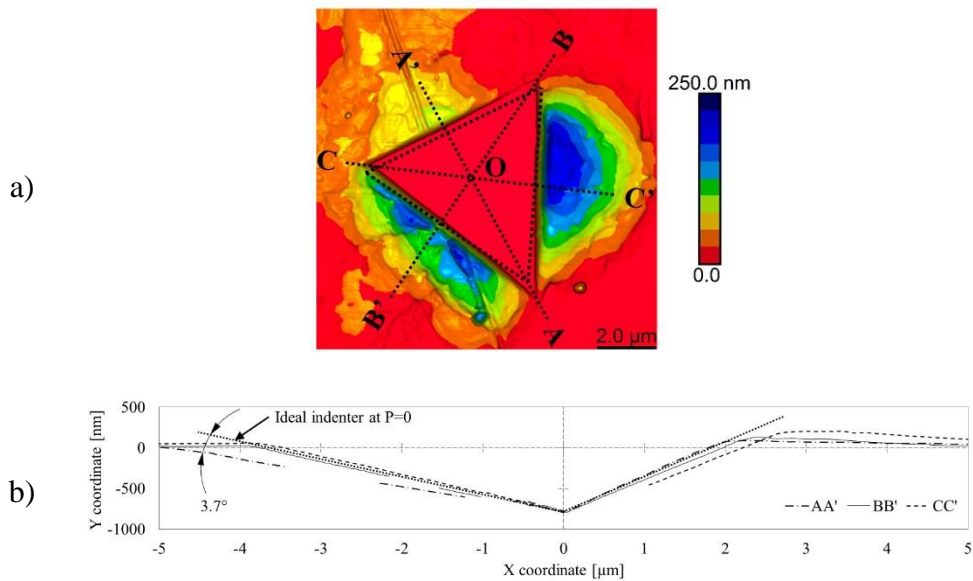


Figure 5.11. a) Height sensor measurement and b) cross-section profile of the imprint in C110 formed by a Berkovich indenter loaded to 36 mN.

Therefore, in order to discard the arbitrary tilt between the normal of the sample surface and the centreline of the indenter as the main cause of the uneven pile-up patterns along the three edges, FE simulations were performed assuming an indenter tilted by 2° around the axes +U1 (Figure 5.12a), +U3 (Figure 5.12c) and both around +U1 and +U3 (Figure 5.12e). The FE model simulates the full domain of a load-controlled test as detailed in section 3.2.1.1. The other two cases in which the indenter is tilted around U3 in the negative direction, i.e. 2° around -U3, and 2° around both +U1 and -U3, were also analysed yet the effects of the indenter tilt was observed to a lesser extent compared with their counterparts and hence, are not included in Figure 5.12. It is evident from this figure that a misaligned indenter not only distorts the shape of the residual imprint but the effect is also reflected in maximum pile-up height (h_{peak}) as observed in the corresponding figures (Figure 5.12b, d and f). For instance, the effects of indenter tilt were maximum along the edge OB' of the residual imprint formed after an indentation performed with an indenter tilted 2° around both the +U1 and +U3 axes, as the maximum pile-up was observed to be 7.4% lower in relation to that of an indentation performed with a perfectly aligned indenter.

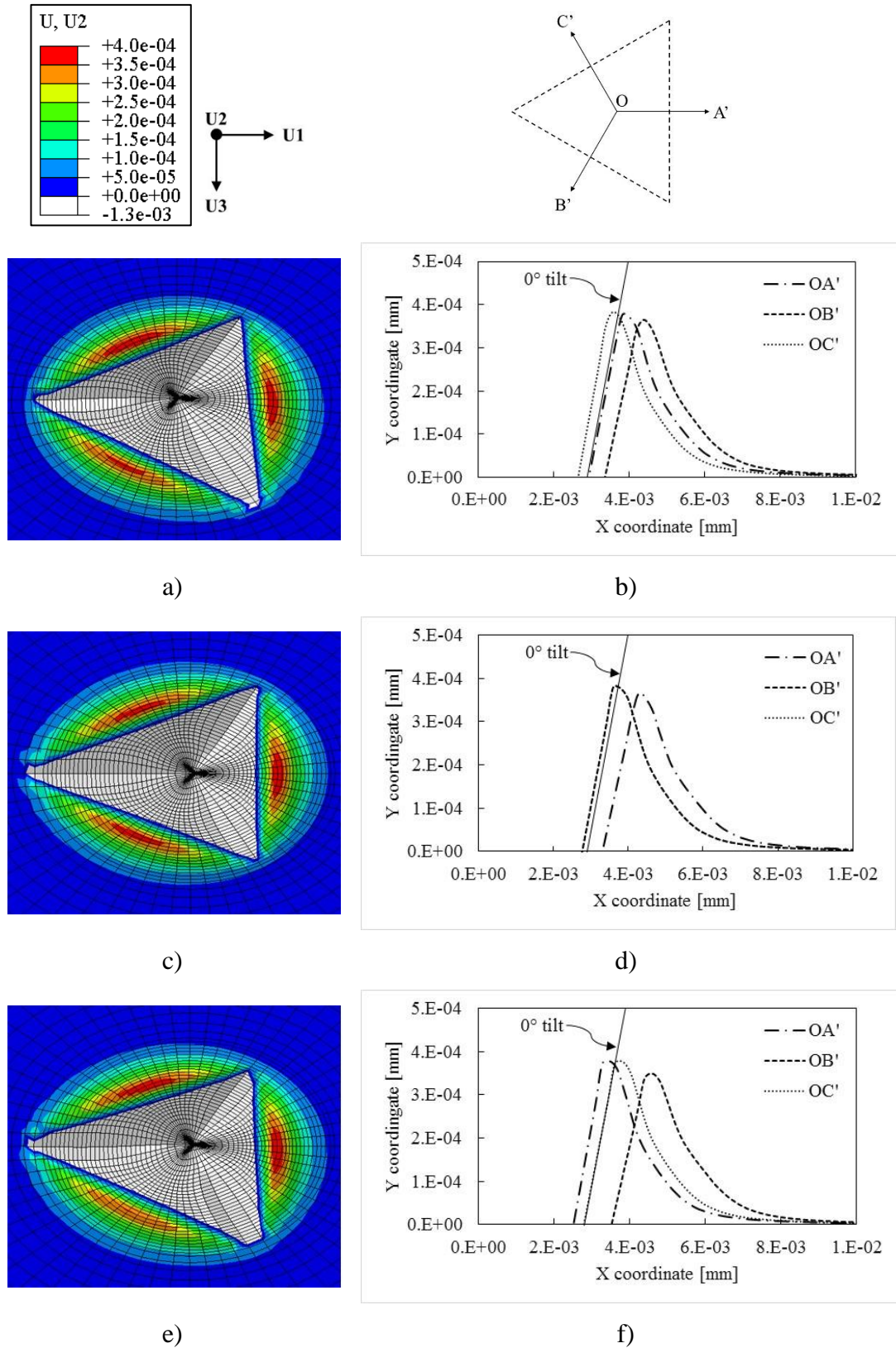


Figure 5.12. Residual imprints left by an indenter tilted with respect to the normal of the surface by 2° around a, b) U1, c, d) U3, and e, f) U1 and U3.

This is related to the shape of the plastic strain field generated beneath the indenter and could be better explained for the case of tilting around an individual axis, e.g. the U3 axis as follows: The mechanism by which the pile-up phenomenon occurs involves local plasticity at different strain levels, being higher along the edges of the indenter and increasing towards the tip, as can be seen in Figure 5.13a for the case of no tilting. Therefore, a high strain concentration is located beneath the indenter, decreasing in magnitude beyond the points of contact at the specimen-indenter interface as shown in Figure 5.13b. The result is that the severely strain-hardened material causes the surrounding material to displace plastically and pile-up around the indenter due to the incompressibility of plastic deformation. Comparing the plastic equivalent strain along section OA' in Figure 5.14a, the region within the contact zone (indicated by vertical dashed lines in Figure 5.14a and arrows in Figure 5.14b) is strain hardened to a higher and lesser degree when the indenter is tilted 2° around the positive and negative U3 axis respectively, compared with that of the case of a perfectly aligned indenter. Therefore, an indenter tilted 2° around the positive and negative axis resulted in a shift of the point of maximum pile-up by 3% below and 0.4% above, respectively, the maximum pile-up reached when the indenter is perfectly aligned as can be seen in Figure 5.14a. However, the accuracy of the quantitative information here presented is limited by the capacity of the linear elements to represent the contact conditions. The tilt case of 2° around +U3 is qualitatively in contrast with Figure 5.10 and Figure 5.11, as the material piles-up higher at the edge opposite to the corner at which the indenter is tilting, which suggests that the structural arrangement of the indented material may also contribute to the asymmetry in the pile-up patterns as discussed in the following section.

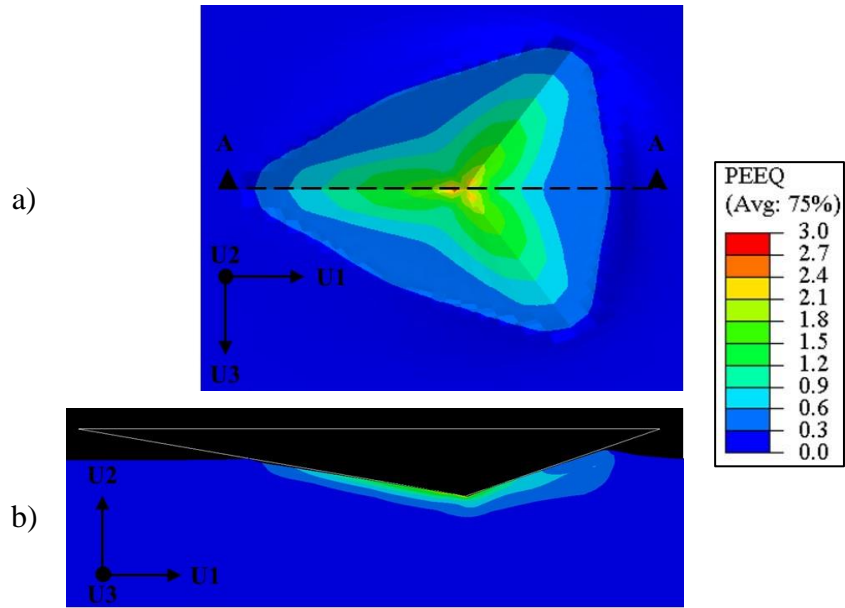


Figure 5.13. a) Top view and b) cut view AA showing the equivalent plastic strain beneath a perfectly sharp indenter and perfectly aligned with the normal of the surface. The plastic equivalent strain (PEEQ) profile corresponds to a load $P = P_{max}$.

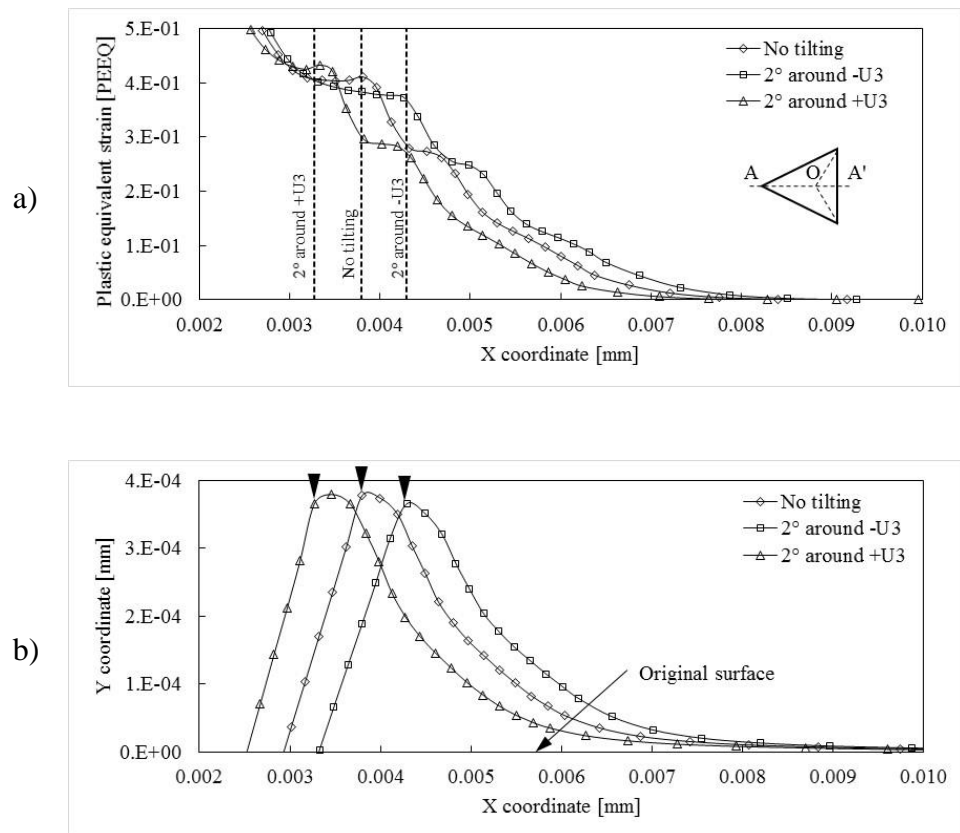


Figure 5.14. a) Pile-up patterns and b) plastic equivalent strain (PEEQ) along section OA.

5.4. Effects of microstructure on the six-fold symmetry of Berkovich indentations

Besides the disturbance of the pile-up pattern resulting from experimental uncertainty, the contact evolution at the indenter-material interface may be strongly dependent on the crystallographic orientation of individual grains, the mismatch of material properties from grain to grain and the directionality of these properties, i.e. anisotropy.

Recalling from section 5.1, the grain sizes in C110 copper range from 30 to 100 μm and thus some indentations may be situated entirely within a single grain. The predominant piling-up of material at one of the edges of the triangular impression of indentation may be explained by the strong dependency of single grains of high purity copper on the crystallographic orientation of the indented surface [140]. Furthermore, copper is known for its highly anisotropic behaviour with Young's modulus values of 66.7, 130.3 and 191.1 GPa along the [100], [110] and [111] crystallographic orientations, respectively [141].

Altogether, the misalignment of the indenter and the dependency of plastic flow on the crystallographic orientation, results in a loss of indentation symmetry, e.g. the one-sixth fold in a Berkovich indenter, which makes the data difficult to interpret. As observed in Figure 5.10, the maximum pile-up value, along the edge OA' after indentation at 120 mN, is in excess of 70% above the maximum height at the other two edges (OB' and OC'). A consistent trend is observed after indentation with a maximum load of 36 mN, where the discrepancy between highest and lowest value is approximately 62% as shown in Figure 5.11. Nonetheless, the degree of piling-up appears independent of ISE as it was found that the ratio h_{peak}/h_0 for the two indentations at each indentation load, i.e. 120 and 36 mN were very similar as reported in Table 5.4. This observation was also shown by the residual imprints left in CrMoV steel at indentation loads of 240 and 120 mN. Both values, h_{peak} and h_0 , included in Table 5.4 represent respectively the average of the maximum pile-up height and

maximum depth measured from the pile-up profiles extracted from the three directions of the triangular residual imprint.

Table 5.4. Ratio of maximum pile-up to maximum indentation depth as measured via atomic force microscopy.

Indentation	h_0 [μm]	h_{peak} [μm]	h_{peak}/h_0
C110 120 mN	1.68	0.39	0.23
	1.57	0.39	0.25
C110 36 mN	0.79	0.14	0.18
	0.83	0.18	0.22
CrMoV 240 mN	1.07	0.15	0.14
	1.00	0.16	0.16
CrMoV 120 mN	0.65	0.08	0.12
	0.69	0.12	0.17

The dependency of plastic flow on the microstructure is expected to reduce as the number of grains in contact with the indenter increases as the specimen behaves more isotropically, given that the crystallographic orientations of the individual grains in a polycrystalline material are totally random [141]. Therefore, a macrohardness test using a Vickers indenter loaded at 20 kgf was performed on the C110 copper material. The micrograph presented in Figure 5.15a reveals apparent slip lines randomly oriented as a larger number of grains were indented and thus the contact response resembles more that of a continuum, isotropic material. This consequently results in a more homogeneous plastic deformation as observed in the topographic image (Figure 5.15b) where the expected eight-fold symmetry of deformation is better approached for this indentation case. The height profile in Figure 5.15c, extracted from scans along the diagonals of the residual imprint, shows that plastic flow during indentation was constrained at equivalent distances from the centreline of the indenter. Still, the point of maximum pile-up is asymmetric (P in Figure 5.15b) as the average of the diagonals of indentation ($d_{av} = 592 \mu\text{m}$) is not significantly larger than the grain size (30-100 μm) and consequently, the dependency of plastic flow to the microstructure has not completely vanished in this case. The indented surface was measured using an Alicona

G5 focus variation instrument as the macroindentation could not be conveniently imaged in the AFM.

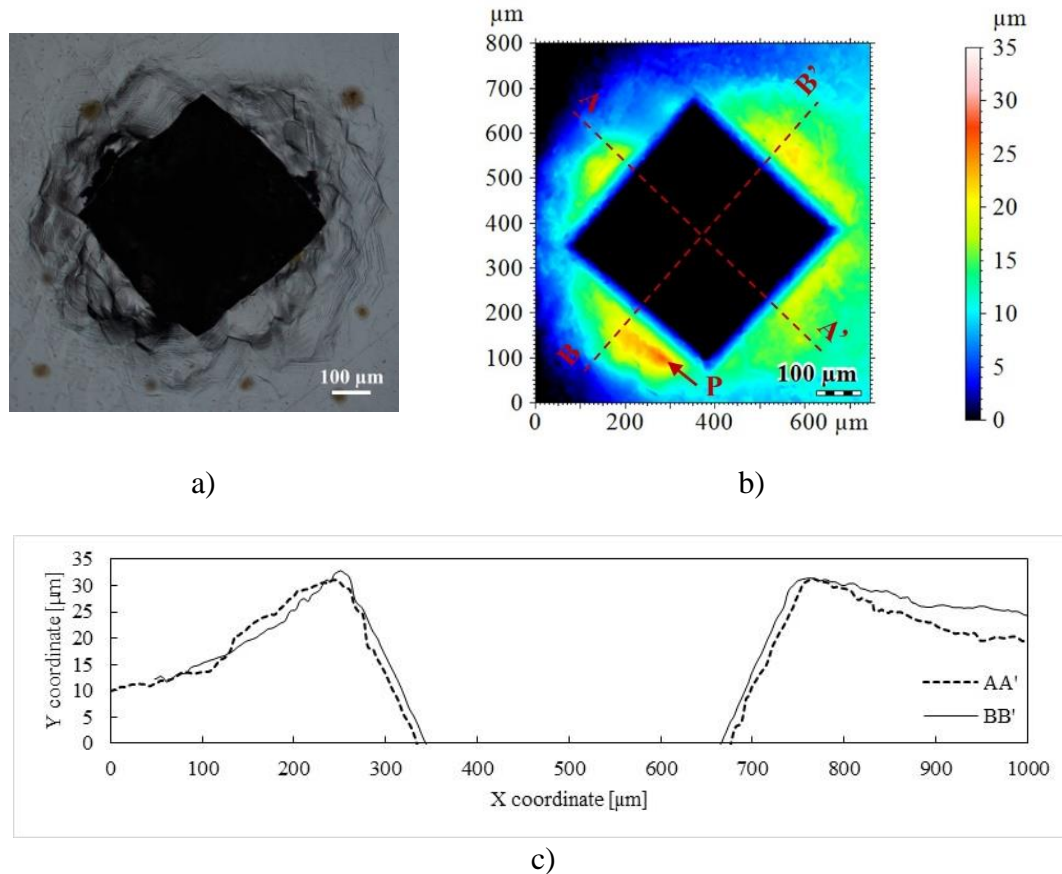


Figure 5.15. a) Optical micrograph and b) surface topography after a macrohardness Vickers indenter test at 20 kgf performed on the C110 specimen. The c) surface profile has been extracted from scans along segments AA' and BB'.

The data extracted from Ti-6Al-4V is more drastically affected as the measured volume is a mixture of α -Ti and β -Ti phases both of significantly different material properties. For instance, the elastic modulus of α -Ti and β -Ti are 132.2 ± 12.2 and 81.1 ± 13.1 GPa, respectively [103], in contrast with the value of 103.1 ± 2.1 GPa as determined from the tensile test. As can be seen in Figure 5.16, free surfaces of intergranular β -Ti pile-up higher than the α matrix after indentation at a load of 240 mN. This irregular pile-up pattern around the indenter is also observed in indentations at lower load, e.g. 120 mN, restricted to a single grain which provides evidence of the anisotropic plastic deformation mechanism of Ti-6Al-4V alloys and its dependency on the crystallographic orientation of the indented grain as suggested by the crystal

plasticity FE simulations performed by Han et al. [142]. Such an uneven piling-up, caused either by a misaligned indenter with the surface or the plastic flow of individual grains, is a detriment to the determination of material properties from the inverse analysis of depth-sensing indentation, as any single indentation may define a variety of constitutive behaviours.

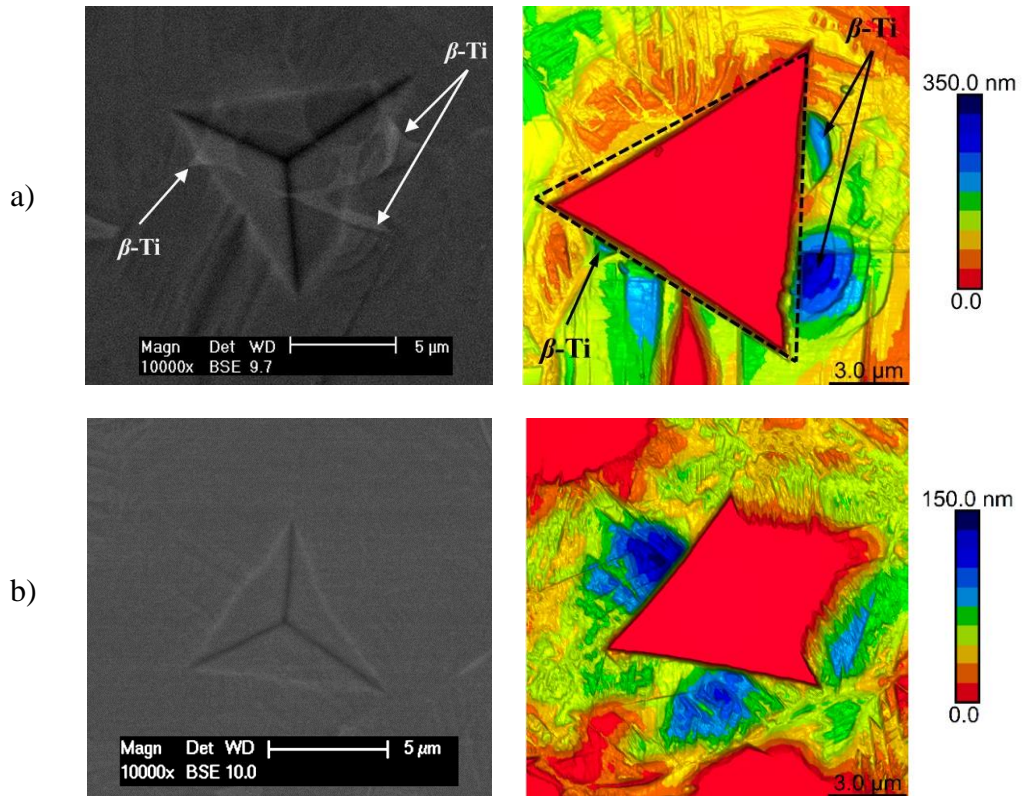


Figure 5.16. Residual imprints left by the Berkovich indenter pressed with a maximum load of a) 240 mN and b) 30 mN in Ti-6Al-4V as observed under BSE/SEM (left) and AFM (right).

5.5. Conclusions

The first conclusion that can be drawn seems logical, but it is sometimes overlooked: the focus of the characterisation via indentation tests is not strictly an alternative to large scale mechanical testing, but rather allows the investigation of the near surface properties of a material of interest. Given that the mechanical response of a small volume of material to indentation does not necessarily represent, nor behaves as, that of the bulk material, the investigator must be aware of the gap between the behaviour of the material at different scales so as to justify whether the indentation test fulfils the objectives of the research, or otherwise.

Other key results on the measurement and use of the topography of the indentation imprint can be summarized as follows:

- The mechanical response of materials with limited capacity to strain-harden ($n < 0.1$) is little sensitive to the polishing procedure provided that the ratio of grit size to indentation depth is below unity. Shallow indentations, or indentations in materials with high strain-hardening may require other procedures, e.g. electropolishing.
- The effects of the indenter tilt on the pile-up pattern were investigated based on a continuum mechanics approach FE model. It was observed that an indenter tilted by 2° towards one of the corners contributed up to 3% to the asymmetry of the pile-up patterns. However, the indenter misalignment alone does not explain the significant asymmetry piling-up in C110 copper and thus it was suggested that it was rather dominated by the crystallographic orientation of the grain tested [140, 141].
- Experiments have shown that although reasonably smooth and continuous data can be extracted with the AFM, height profiles of the surface topography are severely distorted by the contact response of individual grains, the extent and magnitude of the anisotropic effects, the crystallographic orientation of the indented grains and the atomic mismatch at the grain boundaries. Therefore, the use of the pile-up/sink-in pattern for the characterisation of the plastic behaviour is recommended only for polycrystalline materials of very small grain sizes relative to the size of indentation, or single crystals with negligible anisotropy so as to ensure symmetry of indentation.
- If anisotropic behaviour is expected, the investigator must be aware that both the yield stress and the work-hardening as well as the Young's modulus are dependent on the crystallographic orientation of the material [128, 141] and

consequently, the properties measured at small scale indentation are valid only within the grain tested.

- As the physical properties of single crystals depend on the crystallographic direction relative to that in which measurements are taken, it is advisable to determine the plane of indentation and the orientation of the indenter edges relative to the crystallographic orientations.
- It is strongly advisable to perform the surface measurements immediately after indentation so as to avoid measuring any artefacts modifying the indented surface, e.g. surface contamination. On the same basis, it is recommended to perform the final polishing on the specimen immediately before the indentation test in order to avoid erroneous measurements due to surface contamination.

Chapter 6 - Development of a multi-objective function optimisation model

6.1. Introduction

This chapter encompasses a study of the capability of the proposed technique to execute an inverse analysis of depth-sensing indentation data so as to characterise the elastic-plastic mechanical properties of power-law strain-hardening materials and to distinguish between ‘mystical’ [71] materials.

The inverse analysis here described has been executed using the nonlinear least-squares solver (*lsqnonlin*) included in the MATLAB Optimization Toolbox™. Although some authors have implemented the different solvers included in this toolbox, e.g. [69, 70, 77, 78], the scrutiny of the behaviour of the model inside the ‘black box’ and the effects of the input parameters have been overlooked. Therefore, a section of this chapter was devoted to the understanding of the path traced by the model throughout iterations. The justification of the parameters used to calibrate the model was discussed in great detail and the sensitivity of the solution with respect to uncertainties arising from the experimental indentation test has been assessed.

This study has been performed using theoretical-experimental (FE simulated) data, hereafter referred to as the target curves and properties. Therefore, the target raw data were extracted from the result of the forward analysis of indentation using as input the target properties of a material equivalent to a SCMV steel, that is $\mathbf{x} = [212850, 1420, 0.15]$. The extracted data has been interpolated at $N = 82$ and $M = 31$ data points to define the target $P-h$ curve and pile-up profile, respectively. The selected number of data points N and M ensure that only one point was linearly interpolated within two (raw) data points. A wide range of possible solutions were allowed within a continuous space delimited by the bound constraints so as to include the range of mechanical properties of steels [143, 144]: $180\,000 \leq E \leq 260\,000$, $1000 \leq \sigma_y \leq 2500$ and $0 \leq n \leq 0.25$. On that basis, the model was set to start near the lower bounds and thus the initial guess vector $\mathbf{x}_0 = [180\,000, 1000, 0.05]$, unless otherwise specified.

6.2. Sensitivity of the solution to c , N and M

After a parametric study using both pile-up ($E/\sigma_y = 148$, $n = 0.15$) and sink-in ($E/\sigma_y = 1555$, $n = 0.4$) materials, it was observed that both the error and the number of iterations to converge to the target solution are influenced by the contribution of the second objective function, as illustrated in Figure 6.1. The value of c that produced the best fit and fastest convergence was found to be 0.25 for a $P-h$ curve and pile-up profile defined by N and $M \sim 2.7N$ data points. The fastest convergence occurred at the limiting values $c = 0$ and $c = 1$ as a result of the less restrictive single-optimisation model in these cases. Given that the information provided by the residual imprint is strongly linked to the plastic behaviour of the material, the solution was significantly improved as a compromise between the contributions of each objective function was reached. As seen in Figure 6.1, a scaling coefficient $c = 0.25$ resulted in a reduction of the error in the predicted values of σ_y and n by more than 9 and 24% respectively, compared to the model neglecting the contribution of the second objective function, i.e. $c = 1$. Conversely, the Young's modulus is related to the contact stiffness of the unloading curve (Equation 2.3) and hence the solution was relatively insensitive to the participation of the multiple objective functions. The information used to construct the graph in Figure 6.1 is detailed in Table 6.1; an extra column has been included with the result of the minimisation of the multi-objective function disregarding the scale coefficients, i.e. the components of each objective function are multiplied by a coefficient $c_1 = c_2 = 1$.

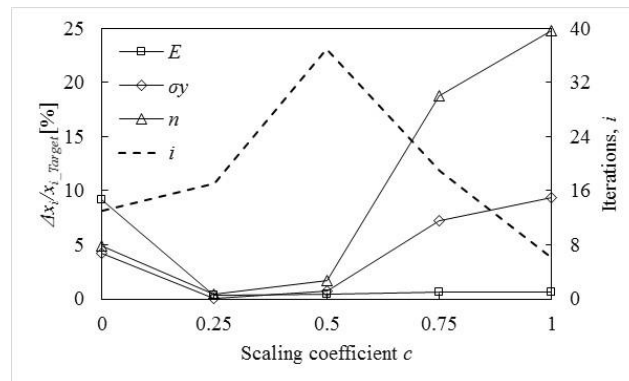


Figure 6.1. Effects of scaling coefficients on the optimised parameters.

Table 6.1. Relative error [%] between optimised and target parameters and number of iteration.

Parameter	$c = 0$	$c = 0.25$	$c = 0.5$	$c = 0.75$	$c = 1$	$c_1 = c_2 = 1$
$\Delta E/E_{Target}$	9.14	0.35	0.42	0.66	0.62	0.40
$\Delta \sigma_y/\sigma_y_{Target}$	4.22	0.01	0.76	7.26	9.37	0.75
$\Delta n/n_{Target}$	4.89	0.47	1.72	18.78	24.80	1.67
i	13	17	37	19	6	27

Due to the architecture of the *lsqnonlin* code, at every iteration, a vector-valued function containing the scaled components of each objective function was returned to the optimisation algorithm (the *lsqnonlin* solver), which implicitly computed the sum of squares of the components (referred to as the squared 2-norm of the residual) of $f_1(\mathbf{x})$ and $f_2(\mathbf{x})$ (See Equation 3.7). Therefore, the components of both $f_1(\mathbf{x})$ and $f_2(\mathbf{x})$ were ‘artificially’ reduced by c and $1 - c$, respectively, with the purpose of equilibrating the global contribution of each objective function. Consequently, the global contribution of each of these functions was not uniquely influenced by the magnitude of the scaling coefficients but also by the magnitude of the residual computed at each sample point and the number of sample points. This could be explained by studying the minimisation problem without scaling the respective components. During the early iterations ($i \leq 3$ in the current analysis), the normalised sum of squares of the unscaled components of the objective functions, i.e.

$$A_i = \frac{1}{N} \sum_{k=1}^N [h_k^{exp} - h(\mathbf{x})_k^{pre}]^2$$

$$B_i = \frac{1}{M} \sum_{l=1}^M [y_l^{exp} - y(\mathbf{x})_l^{pre}]^2 \quad 6.1$$

were of the same order of magnitude as can be inferred from the dashed line in Figure 6.2a. Note A_i and B_i , the normalised error computed between the experimental and predicted $P-h$ curve and pile-up profile at iteration i , respectively, were not scaled so as to assess how well the optimised parameters in \mathbf{x} fit the experimental data. However,

the global contribution of $f_2(\mathbf{x})$ to $f(\mathbf{x})$ was weaker as B_i was a few times smaller than A_i , or in other words, the predicted pile-up profile at the current point \mathbf{x}_i provided a better fit to the respective experimental data than A_i . Otherwise, the global contribution of $f_1(\mathbf{x})$ diminishes. It can be seen in Figure 6.2a, that the information provided by the P - h curve drove most of the optimisation procedure in a ratio of approximately 3:1 and hence, the purpose of the scaling coefficients is to equilibrate the unbalanced global contribution of each objective function. The same trend was observed starting at a different initial guess, e.g. $\mathbf{x} = [200000, 1300, 0.1]$. Figure 6.2b and c, illustrate the outcome of the same assessment carried out in the optimisation procedures using $c = 0.25$ and $c = 0.75$. Accordingly, the global contribution of $f_1(\mathbf{x})$ and $f_2(\mathbf{x})$ to $f(\mathbf{x})$ was more sensitive to c during the early iterations and thus, a scaling coefficient of $c = 0.25$ increased the global contribution of $f_2(\mathbf{x})$ in excess of 65% unlike $c = 0.75$, that diminished it to below 3%. However, as the iterative procedure progressed beyond $i > 3$, A_i and B_i remained in the same order of magnitude when $c = 0.25$ as illustrated in Figure 6.2b. Given that the magnitude of c in this case reduced the computed error between the experimental and predicted P - h curves ‘artificially’ to a greater extent, the optimisation algorithm tried to improve the minimisation of $f(\mathbf{x})$ by finding a vector \mathbf{x} that improves the fitting between the experimental and predicted geometry of the pile-up. For this reason, A_i was between 4 and 5.25 times higher than B_i . In contrast, when $c = 0.75$, A_i became nearly an order of magnitude smaller than B_i at $i > 3$, as it was now the error between the experimental and predicted pile-up pattern which was being reduced artificially to a greater extent. As the solution approached convergence, the minimisation problem scaled using $c = 0.25$ reached a better compromise between the global contribution of each objective function and ratio A_i/B_i and hence, the information provided by both the P - h curve and the geometry of the pile-up was better exploited.

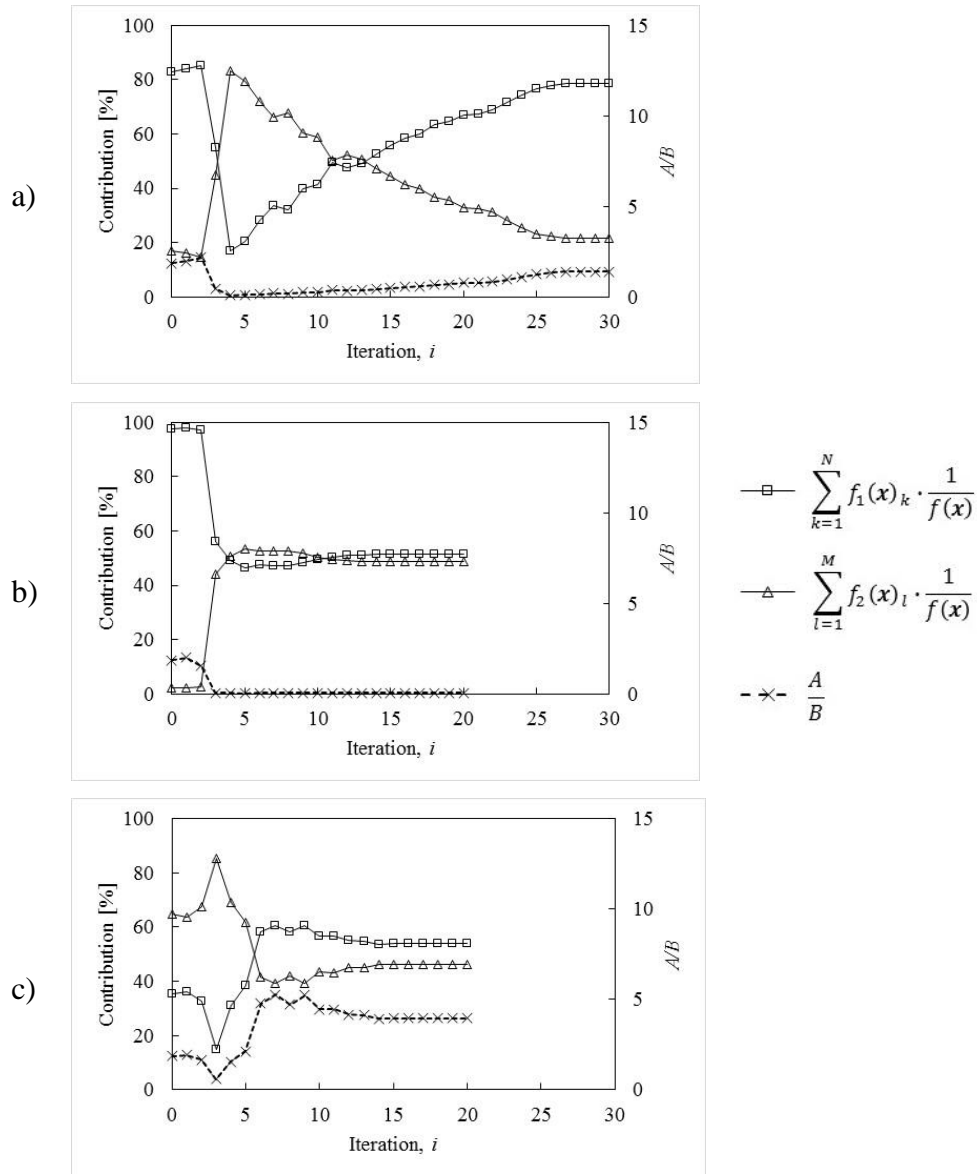


Figure 6.2. Global contribution of each objective function along the optimisation procedure set up with a scaling coefficient of a) $c_1 = c_2 = 1$, b) $c = 0.75$ and c) $c = 0.25$.

In order to better understand the influence of the number of data points N and M on the solution, two additional optimisation analyses were run as follows: For the first analysis, N was kept constant at 82 while for the second analysis, M was kept constant at 31; the respective counterpart, M and N , was computed accordingly to set a ratio $N/M \sim 5$. Similarly, the global contribution of each objective function was greatly driven by c only during the early iterations, when the normalised squared 2-norm of the residual of both $f_1(x)$ and $f_2(x)$ were of the same order of magnitude. Interestingly, during the early iterations, the global contribution of $f_1(x)$ and $f_2(x)$ as well as the ratio

A_i/B_i were equivalent provided that the ratio N/M was maintained constant. Additional pairs of optimisation analyses with ratios $N/M \sim 2, 3, 4$ and 7.5 were run in order to support the latter observation. Throughout the rest of the iterations, the global contribution of $f_1(\mathbf{x})$ and $f_2(\mathbf{x})$ varies so as to improve the minimisation of $f(\mathbf{x})$ as detailed previously. Notwithstanding, as illustrated in Figure 6.3, this study concluded that the influence of the number of data points is negligible on the solution as both simulations using target curves defined by $N/M \sim 5$ data points reached convergence to within a difference of less than 0.5% in relation with the solution provided by the reference model, i.e. $N = 81$ and $M = 31$ ($N/M \sim 2.7$).

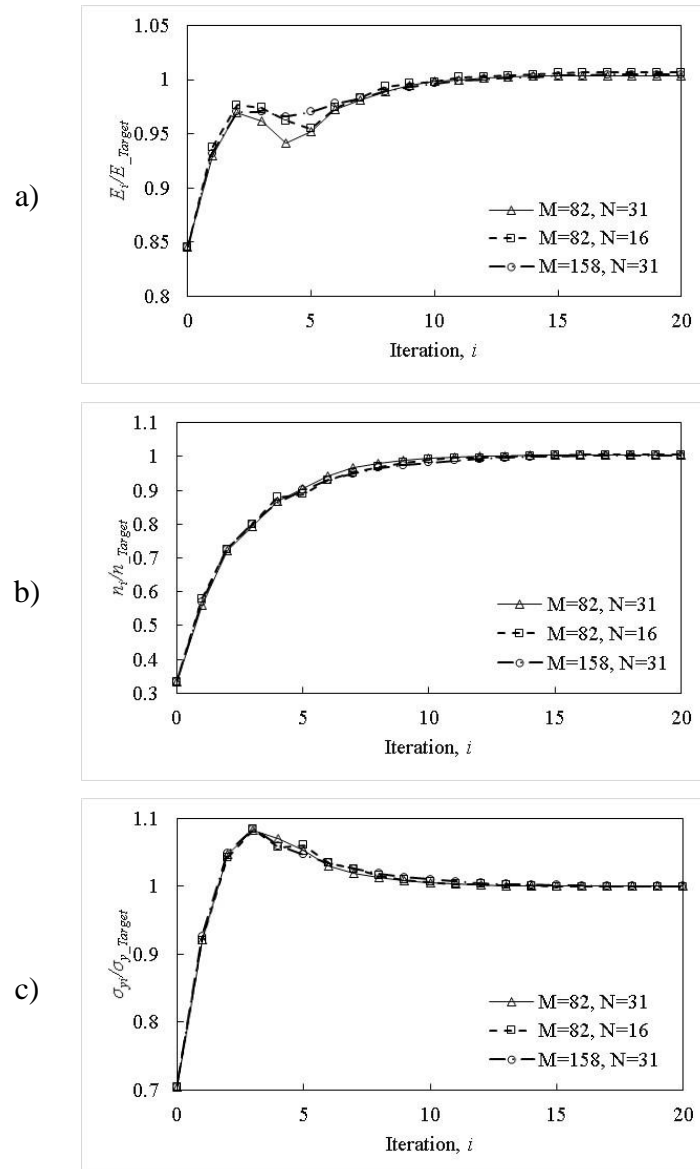


Figure 6.3. Iteration history showing the negligible sensitivity of the optimisation parameter a) E , b) σ_y and c) n to the number of data points M and N along the P - h curve and pile-up profile, respectively.

6.3. Effects of the bound constraints and initial guess vector

The *lsqnonlin* MATLAB code limits the components of \mathbf{x}_0 between the lower and upper bounds and reset the components that violate these bounds to the interior of the range defined by the bounds. Therefore, the bound constraints were extended so as to allow possible solutions for ideally, any metal and thus: $0 \leq E \leq \infty$, $0 \leq \sigma_y \leq \infty$ and $0 \leq n \leq 1$. Numerical results suggests that the approach is insensitive to the size of the

space delimited by the bound constraints provided that the constitutive parameters in x_0 are feasible for defining an elastic-plastic power law material. On that basis, the sensitivity of the optimisation model to the initial guess vector has been assessed by initialising the model at $\pm 40\%$ the target properties. Recalling from Chapter 3, the optimisation algorithm is based on Coleman and Li's [130] interior-reflective Newton method which is not particularly sensitive to the starting point [145]. As illustrated in Figure 6.4, after convergence has been reached, the difference in the solution vector relative to the target properties was less than 0.5% regardless to the position of the initial guess vector.

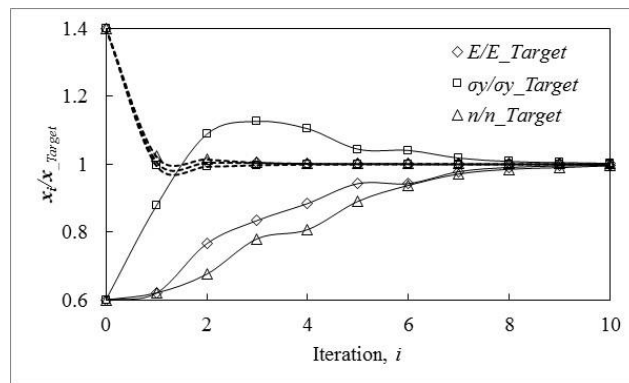


Figure 6.4. Convergence of simulations starting +40 (dashed line) and -40% (solid line) apart from the target values.

6.4. Effects of indenter tilt and surface roughness

As previously reported in Chapter 5, the metallographic preparation of the specimen using a typical 1 μm diamond suspension produces surfaces with an average roughness (R_a) of up to 5 nm. Therefore data points along the pile-up profile have been disturbed by random values of $\pm R_a$ (Figure 6.5) and used as the target curve in the optimisation procedure. The trust-region-reflective algorithm proved to be a robust method to achieve convergence even when noise and outliers were accounted for. As shown in Figure 6.6, the solution of all three optimisation parameters reached convergence within less than 2% away from the target values, regardless of the initial guess.

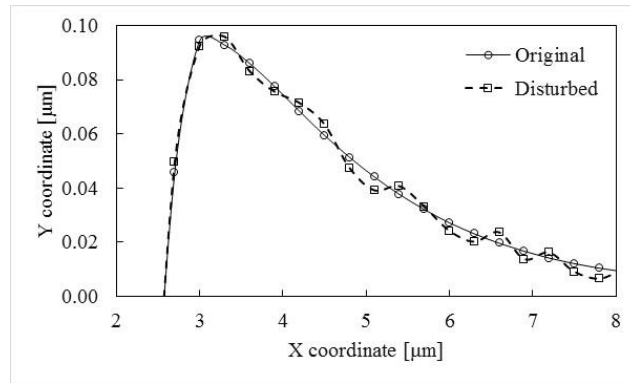


Figure 6.5. Pile-up profile in its original geometry and disturbed by $\pm R_a = 5$ nm to represent the surface roughness after a 1 μm diamond suspension polishing procedure.

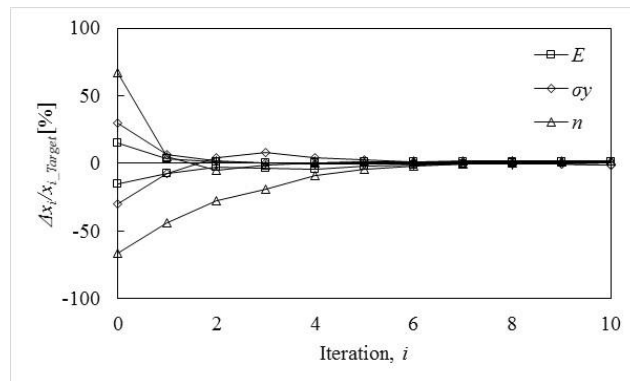


Figure 6.6. Iteration history showing the negligible sensitivity of the MOF model to the surface roughness represented as noise generated by disturbing the pile-up profile data points with random values within $\pm R_a$.

Furthermore, in order to understand the influence of the uneven piling-up around the residual imprint as a consequence of any arbitrary tilt between the normal of the sample surface and the centreline of the indenter, an additional 3D simulation was run such that the model represents the indentation test of an elastic-plastic body by a Berkovich indenter tilted 2° around both the +U1 and +U3 axes. As observed in Figure 6.7, this tilting case largely degenerated the angle α and shifts the magnitude of the maximum pile-up along all three directions, i.e. the six-fold symmetry was disrupted. Therefore, the extracted P - h curve together with the pile-up pattern along edges OA', OB' and OC' of the residual imprint are taken as the target curves. Table 6.2 clearly reveals the detrimental effect to the solution caused by this tilting case as errors are found in excess of 22, 33 and 47% in the optimised E , σ_y and n respectively. The large variability

reported in Table 6.2 was a consequence of the model trying to find a minimiser to the $P-h$ curve and a ‘shifted’ pile-up profile, which defines a variety of elastic-plastic behaviours as illustrated in Figure 6.8. In all three cases, the optimised E converged to either one of the bound constraints, which was a consequence of the algorithm attempting to fit the ‘shifted’ pile-up pattern while trying to adjust the $P-h$ curve to the target indentation response. It is interesting that the mean of the optimised parameters were in fairly good agreement with the target properties, as the error in the predicted E , σ_y and n respectively, drastically reduced to below 3, 13 and 28%.

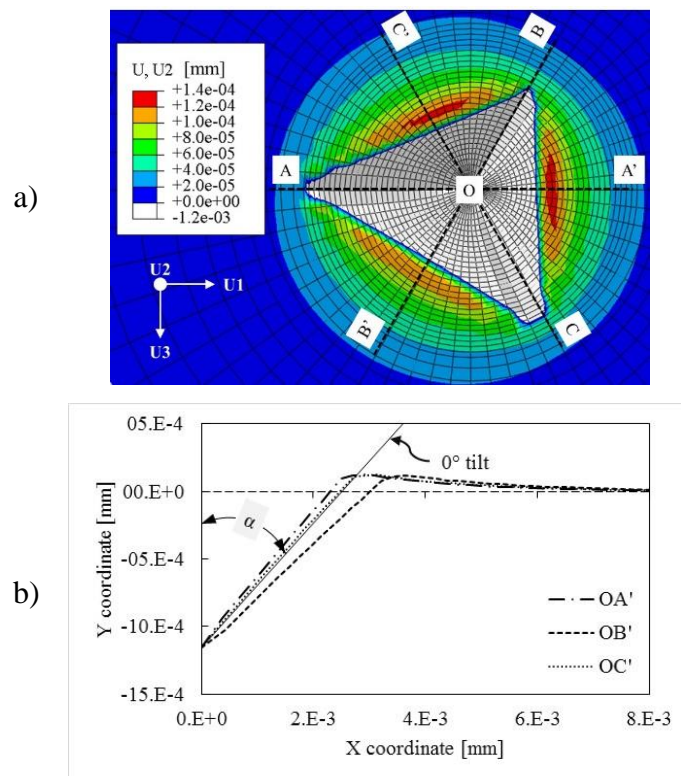


Figure 6.7. a) Height measurements and b) pile-up profiles of a residual imprint left by a Berkovich indenter tilted 2° around both the +U1 and +U3 axes.

Table 6.2. Results of the optimisation procedure assuming an indenter tilted 2° around both the +U1 and +U3 axes, and 1° around the +U3 axis.

Parameter	OA'	OB'	OC'	Mean ± 1 Std. Dev.
Indenter tilted 2° around both +U1 and +U3				
E [MPa]	180000	258616	181625	206747 ± 36683
σ_y [MPa]	1865	1165	1737	1589 ± 304
n	0.0875	0.1522	0.0928	0.1108 ± 0.0293
Indenter tilted 1° around +U3				
E [MPa]	180000	224005	221532	208512 ± 20187
σ_y [MPa]	1700	1391	1405	1499 ± 142
n	0.0962	0.1273	0.1244	0.1160 ± 0.0015

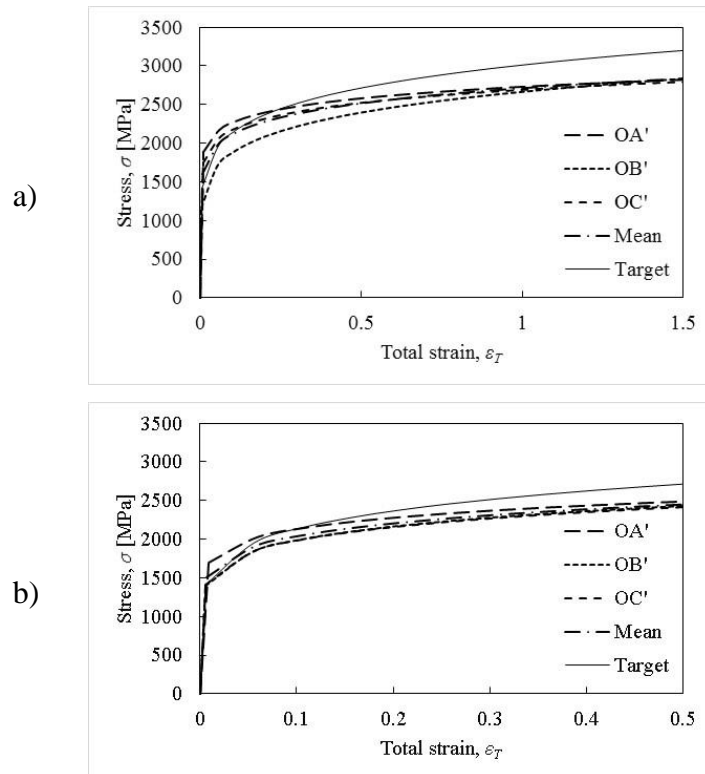


Figure 6.8. Uniaxial constitutive relationship built by evaluating the optimised parameters into Swift's model. Subsets a) and b) are respectively concerned with the properties extracted from the indentation performed with an indenter tilted 2° around both the +U1 and +U3 axes, and 1° around the +U3 axis.

Given that ISO 14577 [13] recommends that the surface tilt should be within 1°, an analogous assessment as the above mentioned was performed assuming a 1° tilt

towards one of the corners of indentation, i.e. rotated around the +U3 axis. The foregoing concluded that the solution to E , σ_y and n deviated respectively in up to 5.2, 2 and 17% from the target properties, provided that the pile-up profile in the direction of tilting, e.g. along the edge OA' using the directions of Figure 6.7a, is not selected for optimisation as this direction exhibited the higher deviation compared with an ideal (0° tilting) pile-up profile. Notwithstanding, the mean values deviated within less than 2, 5.5 and 16% from the target parameters and therefore a good match can be observed in Figure 6.8b between the target and optimised stress-strain curve.

6.5. Characterisation of ‘mystical’ materials

Several authors have reported the existence of materials that yield indistinguishable $P-h$ curves regardless of the difference in the constitutive parameters and indenter geometry [58, 66, 73, 75], which implies that the number of possible solutions to the inverse analysis of indentation purely based on experimentally obtained $P-h$ curves is infinite. The mystical materials illustrated in Figure 6.9 exhibit very different elastic and plastic behaviours, yet the coefficient of variation between $P-h$ curves is expected to be less than 0.5% [73]. Details of the constitutive parameters that define the stress-strain curves is included in Table 6.3. Bearing this in mind, the capability of the proposed optimisation model to distinguish between mystical materials has been tested by forcing a condition of best fit between the target and predicted curve such that the initial point is a local minimum. Therefore the inverse analysis is run using a (FE simulated) target $P-h$ curve that corresponds to the mechanical properties of material A, i.e. here the target properties, whereas the initial guess vector corresponds to the properties of material B, as detailed in Table 6.3.

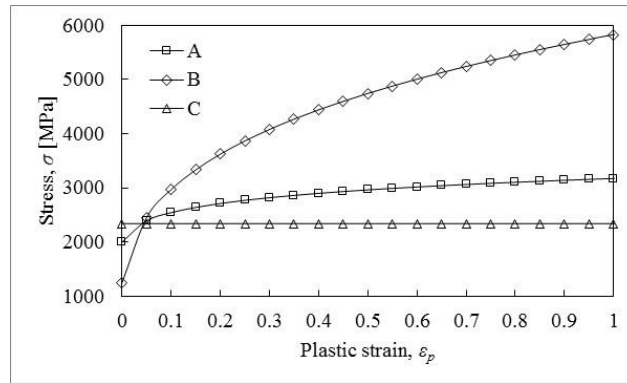


Figure 6.9. Different elastic-plastic materials that yield indistinguishable $P-h$ curves, i.e. mystical materials [73].

Table 6.3. Sets of dissimilar mechanical properties that exhibit identical indentation response, i.e. mystical materials.

Material	Parameter		
	E	σ_y	n
A	200000	2000	0.1
B	212900	1245	0.3
C	192570	2340	0

As shown in Figure 6.10a, a single-objective function (SOF) model was incapable of converging to the target properties since the information provided solely by the $P-h$ curve is limited. On the other hand, the non-uniqueness issue of the inverse analysis of indentation was positively addressed by a multi-objective function (MOF) model as the additional information is linked with the plastic behaviour of the material. The enrichment of the model allowed the optimisation algorithm to circumvent the condition of local minimum and converge to the target properties as seen in Figure 6.10b. The same positive outcome was observed using the properties of material C (Table 6.3) as the initial guess vector. The results of the optimisations concerning the SOF and MOF, presented in Table 6.4, highlights the superior performance of the proposed approach over the more conventional SOF. The indentation response measured by the $P-h$ curve is insensitive to the plastic properties, in particular to the strain-hardening exponent, and hence the SOF model lacks of information to search for a better point, which in turn resulted in optimised parameters carrying forward the error throughout the optimisation, i.e. 5.2, 38.9 and 200%. In contrast, the second

objective allowed the minimisation of the error to 0.14% in E , 0.15% in σ_y and 0% in n as summarised in Table 6.4.

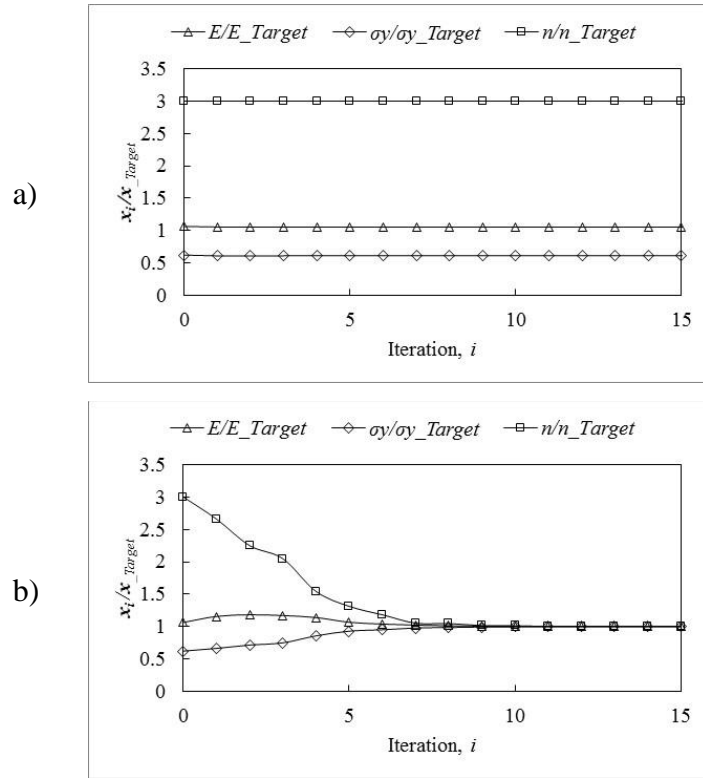


Figure 6.10. Iteration history through a) SOF and b) MOF optimisation model using material B as the initial guess parameters.

Table 6.4. Set up and results for optimisation of mystical materials

Model	Parameter	Target properties	Initial guess	Bound constraints	Optimised properties	Error [%]
SOF	E [MPa]	200000	212900	≥ 0	210468	5.2
	σ_y [MPa]	2000	1245	≥ 0	1223	38.9
	n	0.1	0.3	0 - 1	0.3	200
MOF	E [MPa]	200000	212900	≥ 0	200287	0.14
	σ_y [MPa]	2000	1245	≥ 0	1997	0.15
	n	0.1	0.3	0 - 1	0.1	0
MOF	E [MPa]	200000	192570	≥ 0	199968	0.02
	σ_y [MPa]	2000	2340	≥ 0	2001	0.05
	n	0.1	0	0 - 1	0.1	0

6.6. Concluding remarks

The objective pursued in this chapter was an in-depth study of the performance of the proposed characterisation technique to recover elastic-plastic properties of power-law materials from the inverse analysis of the depth-sensing indentation test. The strong dependency of the residual imprint left by the indenter to the plastic behaviour of the indented material was exploited to complement the information provided by the $P-h$ curve and so address the non-uniqueness issue of the inverse analysis of indentation. Therefore, the inverse analysis is based on a multi-objective function optimisation model that finds a solution to minimise the error in both the $P-h$ curve and the pile-up profile. The model was implemented in the MATLAB environment in order to invoke the *lsqnonlin* solver available in the Optimization Toolbox™ and to execute the pre-processing of FE models. Furthermore, MATLAB was linked to ABAQUS through a Python script in order to automate the post-processing of FE data.

The outcome was a robust model that has been proven to be capable of converging the three target parameters, E , σ_y and n , to within less than 0.5% error, despite the values selected as the initial guess. Furthermore, the methodological assessment of the proposed approach drew the following conclusions:

- The use of scaling coefficients, which sum to unity, can be adopted to equilibrate the global contribution of each objective function. The best compromise was found by reducing the components of the residual of the objective function concerning the data from the $P-h$ curve; it was observed that the solution was approached faster and more accurately when c takes a value of 0.25.
- Reducing the overall error by ‘artificially’ reducing the contribution of the $P-h$ curve, which otherwise was observed to drive most of the optimisation procedure in a ratio of approximately 3:1 when the scaling factors are excluded ($c_1 = c_2 = 1$), established a better equilibrium between the contributions of each

objective function. Consequently, the information from both objective functions were better exploited, resulting in a faster convergence and an improved approximation to the target properties.

- The very strong convergence properties, the robustness and reliability of the trust-region algorithm [129] was reflected in a solution insensitive to the definition of bound constraints and the values of the initial guess. Furthermore, allowed the model to account for experimental errors arising from the metallographic preparation of the specimen such as surface roughness and the possibility of an arbitrary tilt.
- Even accounting for noise and outliers along the pile-up profile, the MOF model approaches the target parameters E , σ_y and n to within less than 2% error.
- The uneven piling-up arising from the misalignment between the indentation axis and the normal of the surface impinges on the solution as a single indentation may define a variety of constitutive behaviours. It has been shown that although a misalignment of 2° around both the +U1 and +U3 axes may significantly affect the solution due to the variability in the pile-up profiles along the three edges of the indenter, the mean of the optimised parameters E , σ_y and n approached the target parameters with a maximum error of 3, 13 and 28%, respectively. Limiting the surface tilt to within 1° , as recommended by ISO 14577 [13], reduced the corresponding mean errors to 2, 5.6 and 16%.
- The superior performance of the proposed MOF optimisation model, compared with a single-objective function model, was highlighted by its capability to distinguish between materials showing similar indentation responses, referred to in the literature as ‘mystical’ materials. While the single-objective function model was trapped on a local solution, in excess of 5.2, 38.9 and 66.7% away from the (global) target E , σ_y and n respectively, the multi-objective function optimisation converged to the target properties within an error of less than 0.15% in all three parameters.

Chapter 7 - Recovery of elastic-plastic properties from depth-sensing indentation data

7.1. Introduction

This chapter discusses the outcomes of a critical appraisal of the capabilities of the proposed inverse method to cope with the task of recovering the elastic-plastic properties of a CrMoV steel equivalent to SCM440. In order to prove the generality of the model, two additional materials with significantly different elastic-plastic behaviour and microstructure, i.e. a Ti-6Al-4V titanium alloy and a C110 high purity copper, have been included in the assessment. Only the indentation with the best agreement between the residual depth indicated from the indentation instrument and measured from the AFM has been selected as input data for the optimisation procedure.

7.2. Input data

Figure 7.1 includes the $P-h$ curves and the respective pile-up profiles for indentations in CrMoV steel, C110 copper and Ti-6Al-4V. Bearing in mind the considerable effects of size parameters in the extracted data, it was deemed reasonable to compare the experimental $P-h$ curves with those obtained by means of the forward analysis of indentation (FE modelling) using the uniaxial material properties extracted from the tensile tests.

As previously mentioned, the displacement measured by the depth-sensing indentation instrument has been corrected for frame compliance in order to ensure that the contact stiffness is that of the specimen only. Furthermore, $P-h$ curves from the tests on CrMoV have been corrected for thermal drift. A load-time sequence in experimental depth-sensing indentation test is typically designed to assess the repeatability of the test in a specific material and to avoid capturing anything other than elastic displacements during the (final) unloading stage [20], therefore it is common practice to include hold periods, e.g. at maximum load (P_{max}) to ensure stable material response before unloading. As can be seen in Figure 7.1a, time-dependent deformation was

recorded by the indentation instrument over the dwell period defined at P_{max} . However, in the absence of a time-dependent parameter in the material model, the FE simulation was incapable of resolving the displacements taking place during the load holding periods for the indentation experiment in CrMoV. In contrast, not including a dwell period in the indentation experiment, or a very short hold period succeeded by a slow unloading rate, may result in an initial increase of indentation depth upon unloading due to creep [146] as illustrated in Figure 7.1c. Notwithstanding, as evidenced in Figure 7.1a and c, these materials exhibited little time-dependent deformation under the specified loading conditions and thus, the inconsistency with the FE approximation assuming a Swift's material model was not a detriment to the optimisation procedure.

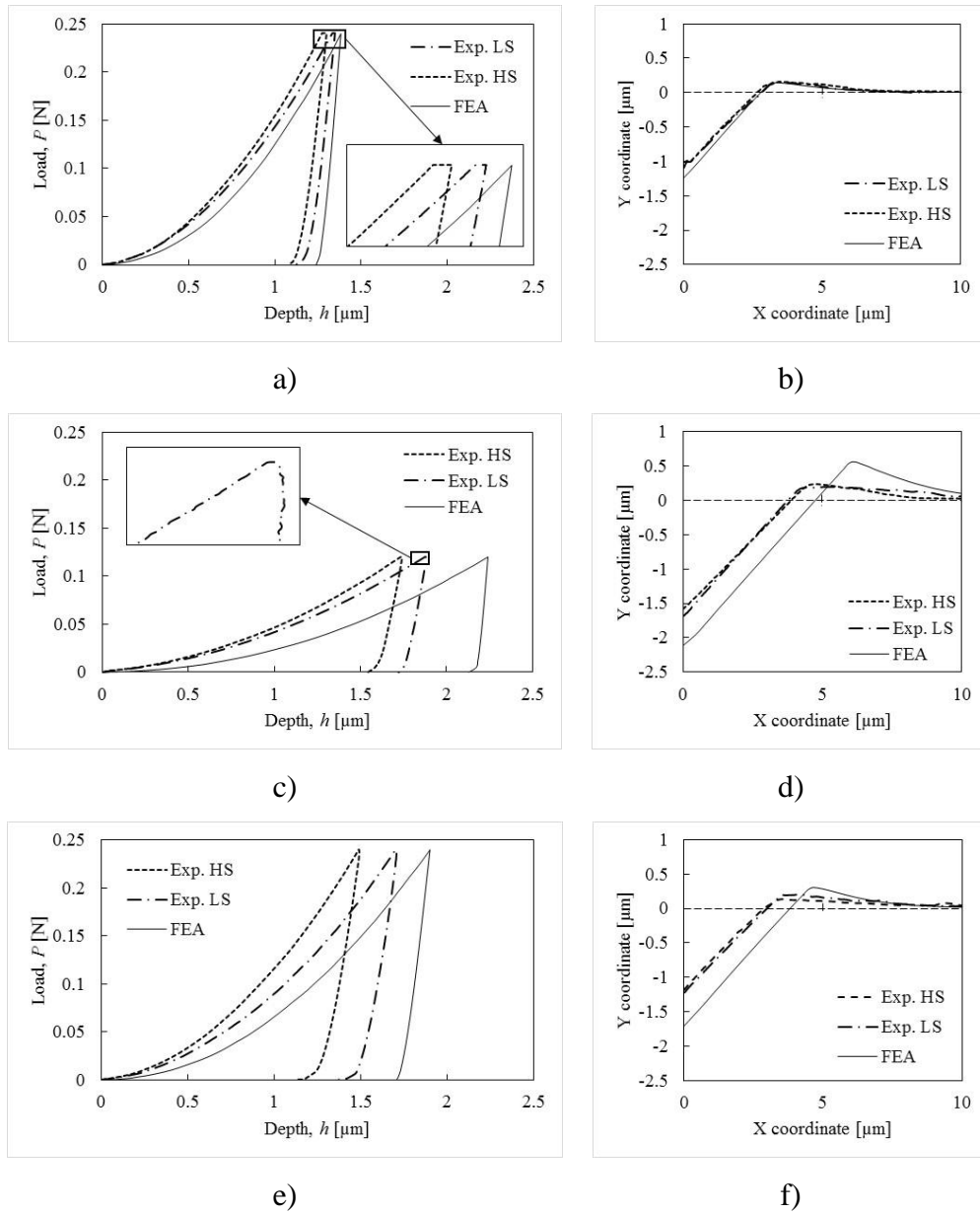


Figure 7.1. P - h curves and pile-up patterns selected for recovering the mechanical properties of a), b) CrMoV steel, c), d) C110 copper and e), f) Ti-6Al-4V.

The FE prediction overestimated the respective experimental h_{max} by 2-6% in CrMoV, 16-22% in C110 and 10-22% in Ti-6Al-4V, as summarised in Table 7.1, which is a consequence of the absence of a length parameter in the continuum mechanics approach formulated in the FE model. Consequently, the different local properties within grains contributed to the relative difference between experimental and predicted h_{max} . In addition, Table 7.1 provides details of the stiffer behaviour of all three materials at low indentation loads as the HM value calculated from the P - h curves was

higher by 6-16% in CrMoV, 43-68% in C110 and 2-34% in Ti-6Al-4V compared with the respective load-independent HV reported in Chapter 5. The Martens hardness values computed from the FE simulated loading curves (HM_{FE}) are in reasonable agreement with the load-independent Vickers hardness reported in Chapter 5, which confirms that HM and HV are effectively comparable. For instance, HM_{FE} diverged from the measured HV in specimens of CrMoV steel and C110 copper by less than 0.4 and 1.2%, respectively, as included in Table 7.1. The largest difference of 18% between HM_{FE} and HV in Ti-6Al-4V might be indicative of different mechanisms producing ISE or the dependency of hardness to the effects of a two-phase microstructure.

Table 7.1. Deviation between experimental $P-h$ curves and those predicted by the FE model using the mechanical properties determined from the tensile test.

Specimen	Indent	h_{max_Exp} [μm]	$\frac{h_{max_FE}}{h_{max_Exp}}$	HM [MPa]	$\frac{HM_{FE}}{HV}$	$\frac{HM}{HV}$
CrMoV	LS*	1.30	1.02	5495	1.004	1.16
	HS	1.35	1.06	5000		1.06
C110	LS	1.88	1.16	1282	1.012	1.43
	HS*	1.74	1.22	1502		1.68
Ti-6Al-4V	LS*	1.71	1.10	3113	0.82	1.02
	HS	1.49	1.22	4091		1.34

* Indentation data used for optimisation

The dependency of the response to indentation on the microstructural arrangement was also reflected on the residual depth left on the surface (h_0) after the removal of the load, with FE predictions overestimating the measurements provided by the AFM by up to 31%, as detailed in Table 7.2. Given that the ideal six-fold symmetry in the residual imprint left by a Berkovich indenter is not satisfied in polycrystalline materials with grain sizes of the same order of magnitude of the area of indentation, as discussed in Chapter 5, only the most characteristic pile-up pattern has been selected for the optimisation analysis. Furthermore, only data points in the direction (e) of the bisector of the side of the triangular impression are included as indicated in Figure 7.6. It is important to note that the ratio of maximum residual depth left on the material surface

after the removal of the load (h_0) measured by the AFM to the residual depth reported by the depth sensing instrument (h_r) was not equal to unity, but differed by up to 7, 2 and 11% in the specimens of CrMoV steel, C110 copper and Ti-6Al-4V, respectively. This can be associated with the contribution of calibration errors in both the depth sensing indentation and AFM instruments. Consequently, only the indentation with the best agreement between the depth measured via the indentation instrument and AFM has been selected as input data for the optimisation procedure as identified with an asterisk in Table 7.1, i.e. LS to recover the properties of CrMoV steel and HS for C110 copper. Given the irregular topology of Ti-6Al-4V, the LS indentation was used regardless of the largest h_{0_Exp}/h_{r_Exp} ratio. In order to avoid convergence issues due to the significantly deviated residual depth h_0 in relation with h_r , only the data above the free surface was used in the inverse analysis of Ti-6Al-4V.

Table 7.2. Residual indentation depth as measured by the indentation instrument (h_r) and AFM (h_0).

Specimen	Indent	h_{0_Exp} [μm]	h_{0_Exp}/h_{r_Exp}	h_{0_FE} [μm]	h_{0_Exp}/h_{0_FE}
CrMoV	LS	1.08	0.97	1.71	0.88
	HS	1.00	0.93		0.81
C110	LS	1.69	0.98	2.11	0.80
	HS	1.57	1.02		0.74
Ti-6Al-4V	LS	1.22	0.89	1.24	0.71
	HS	1.18	1.04		0.69

By means of the previous assessment it was possible to conclude that the data extracted from the depth-sensing indentation test was not representative of the bulk uniaxial properties as determined by the tensile test. Notwithstanding, the intention of this study was not to recover the uniaxial tensile properties but to determine the near surface constitutive behaviour of the material, bearing in mind that the depth-sensing indentation test was designed to measure small volumes of materials, where the conventional mechanical testing techniques are not applicable, e.g. the tensile test.

7.3. Model set-up

For each material, the space of possible solutions for the Young's modulus and strain hardening exponent has been limited by bound constraints taking as a guide the work of Waterman and Ashby [143] and Altan et al. [144], respectively. In the spirit of Tabor [134], the stress at 8% plastic strain of C110, CrMoV and Ti-6Al-4V computed from the HM of the HS curves, the stiffer response, was calculated as 486, 1832 and 1268 MPa, respectively. Therefore, in order to allow a wider range of material properties so as to account for ISE, the optimisation model is subject to the bound constraints specified in Table 7.3.

Table 7.3. Bound constraints imposed to the optimisation procedures of CrMoV steel, C110 copper and Ti-6Al-4V.

Material	E (GPa)	σ_y (MPa)	n
CrMoV	180 – 260	1000 - 2000	0 – 0.25
C110	50 – 150	300 - 600	0 – 0.25
Ti-6Al-4V	50 - 200	1000 - 1800	0 – 0.25

As introduced in Table 7.4, four sets of constitutive parameters, arbitrarily selected to cover the range of material properties delimited by the bound constraints, have been defined as the initial guess in order to assess the convergence power of the model. Although it was concluded in Chapter 6 that the solution of the optimisation model is insensitive to the number of data points N and M that define the P - h curve and pile-up profile, respectively, care has been taken to determine the distance that defines the far-field of the pile-up profile, i.e. the furthest X coordinate point measured from the indenter centreline. This with the intention of capturing the height measurements along the pile-up profile with a reasonable number of data points (M), spread out at intervals to within 350 nm and 500 nm in all three materials. This was observed to be fundamental to improve convergence given the strong dependency of the plastic deformation of material beneath the indenter on the microstructural arrangement. As mentioned previously, in Chapter 5, the two-phase microstructure of Ti-6Al-4V resulted in a highly irregular topography (Figure 7.6e) whereas the dependency of the elastic-plastic behaviour of single crystals of C110 copper to the crystallographic

direction relative to that in which measurements were taken resulted in a significant degree of asymmetry in the pile-up profiles (Figure 7.6c). In view of the significant error induced by these surfaces to the model, a preliminary assessment was carried out to confirm that a scaling coefficient c between 0.5 and 0.25 was suitable to equilibrate the contribution of each function to be minimised as proposed in Chapter 6.

Table 7.4. Initial guess parameters selected to initialise the optimisations of CrMoV, Ti-6Al-4V and C110 using single- and multiple-objective functions.

Material	Parameter	R1	R2	R3	R4
CrMoV	E_0 [MPa]	150000	220000	250000	190000
	σ_{y0} [MPa]	1400	2000	2500	1000
	n_0	0.05	0.15	0.25	0
C110	E_0 [MPa]	95000	70000	80000	150000
	σ_{y0} [MPa]	600	300	350	500
	n_0	0.25	0	0.05	0.15
Ti-6Al-4V	E_0 [MPa]	90000	200000	100000	150000
	σ_{y0} [MPa]	1000	1800	1100	1500
	n_0	0	0.25	0.05	0.15

7.4. Determination of the near surface elastic-plastic properties

7.4.1 *Enhancement in convergence properties attained with an MOF model*

Figure 7.2, Figure 7.3 and Figure 7.4 present the iteration history through the optimisations of the CrMoV steel, C110 copper and Ti6Al4V materials respectively. Overall, the trust-region-reflective algorithm provides a robust solver to the minimisation problem with the Single (SOF) and Multiple Objective Functions (MOF). It can be seen that in general, the MOF model converged faster than the SOF model.

In Figure 7.2, it can be seen that the MOF model converged to consistent solutions regardless of the initial guess parameters, while the SOF model showed a weaker

convergence capability. In fact, for the optimisation with initial guess parameters of $\mathbf{x}_0 = [250000, 2500, 0.25]$ the SOF model was incapable of recovering from a local solution. Interestingly, during the first 2 iterations both the MOF and SOF passed through similar values, but during the proceeding iterations, the SOF remained trapped in the local solution for σ_y and n . As can be noticed in Table 7.5, the MOF tends to converge at lower E and higher σ_y compared to the SOF model. The reason for this trend can be attributed to the known dependency of the pile-up/sink-in phenomenon to both the ratio of E/σ_y and n [14] and thus the pile-up profile is effectively adding more constraint to the model. This could also explain the capability of the MOF model to jump out of the local solution previously mentioned (compare iteration $i = 4$ in both Figure 7.2a and b). Overall, a less scattered set of solutions was achieved using the MOF model, compared with that of the SOF model, with a variability, measured as the relative difference between the mean value and one standard deviation, of 1.00% for E , 1.67% for σ_y and 7.80% for n as reported in Table 7.5. In contrast, the SOF achieved solutions to E , σ_y and n with one standard deviation of up to 1.27, 5.63 and 27.94% for the corresponding parameters. Therefore, the convergence of the optimisation model was enhanced by the addition of a second objective.

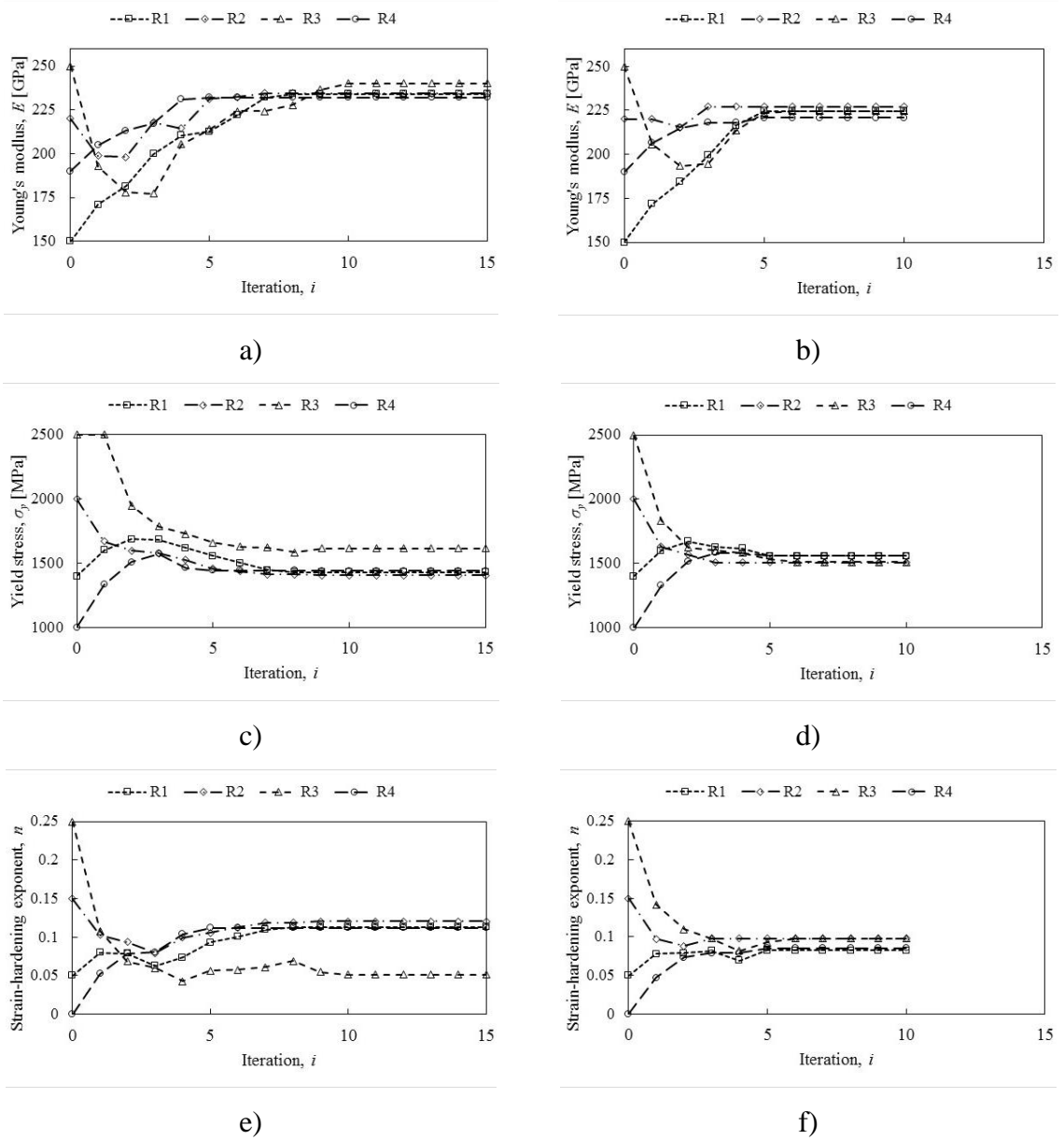


Figure 7.2. Iteration history through the minimisation problem of a), c), e) single objective and b), d), f) multiple objectives for the determination of elastic-plastic properties of CrMoV steel.

Table 7.5. Characterised properties of CrMoV after single- and multi-objective function optimisation.

Initial guess	Single-objective function			Multi-objective function		
	E [MPa]	σ_y [MPa]	n	E [MPa]	σ_y [MPa]	n
R1	233950	1431	0.1131	224551	1560	0.0823
R2	234248	1407	0.1203	227019	1507	0.0977
R3	240095	1616	0.0515	224546	1510	0.0977
R4	232138	1441	0.1121	220753	1560	0.0851
Mean	235108	1474	0.0993	224217	1534	0.0907
Std. Dev. [%]	1.27	5.63	27.94	1.00	1.67	7.80

Likewise, the MOF model reached more consistent solutions to the constitutive parameters of C110 copper as observed in Figure 7.3a-f. Therefore, a superior convergence performance of the MOF over the SOF was highlighted by the reduced variability in the solution as reported in Table 7.6. In contrast, as presented in Table 7.6, the SOF model converged to dissimilar sets of material properties. Surprisingly, the iteration history throughout the MOF model (Figure 7.3b, d and f) reveals that convergence was reached after the second iteration in the majority of the optimisation trials, despite the significant variation of at least 100% between the upper and lower parameter (E , σ_y and n) selected to initialise the optimisation. A trend similar to the optimisation history of CrMoV steel can be observed in Figure 7.3 and Table 7.6 with the solutions provided by the MOF model reaching a lower E and higher σ_y value, respectively, compared with those of the SOF.

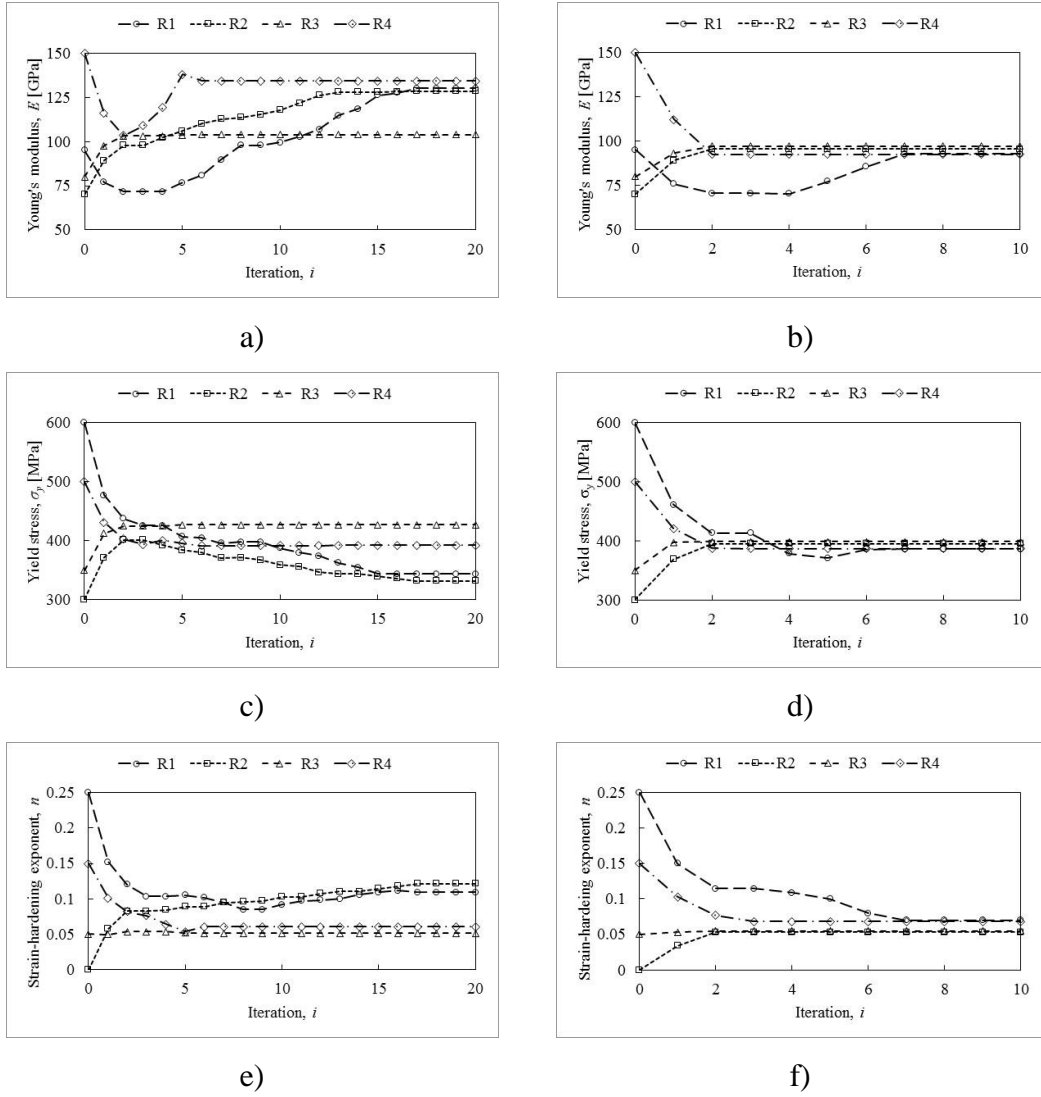


Figure 7.3. Iteration history through the minimisation problem of a), c), e) single objective and b), d), f) multiple objectives for the determination of elastic-plastic properties of C110 copper.

Table 7.6. Characterised properties of C110 copper after single- and multi-objective function optimisation.

Iteration	Single-objective function			Multi-objective function		
	E [MPa]	σ_y [MPa]	n	E [MPa]	σ_y [MPa]	n
R1	130109	343	0.1095	92610	386	0.0699
R2	128474	332	0.1213	95511	395	0.0530
R3	103843	427	0.0513	97147	398	0.0549
R4	134154	392	0.0607	92413	387	0.0684
Mean	124145	374	0.0857	94420	392	0.0616
Std. Dev. [%]	9.6	10.2	35.2	2.1	1.4	12.5

For the case of Ti-6Al-4V, the plastic displacement of material beneath the indenter is a result of the constitutive response of both the α and β grains to indentation and their interaction with neighbouring grains, which is beyond the capabilities of the conventional continuum plasticity approach used in the FE formulation. Error is therefore inherent in the MOF algorithm and hence, the consistency in the optimised n is slightly affected as reported in Figure 7.4 and Table 7.7. Notwithstanding, the MOF model achieved a reduced variability in the converged solution for all three parameters compared with that of the SOF model as reported in Table 7.7. Furthermore, the SOF model was susceptible to converge on a local solution as was the case for the optimisation R1; as observed in Figure 7.4a, c and d, the model reached an apparent local solution for σ_y and n at the sixth iteration as a result of the lack of information in the $P-h$ curve to describe the plastic behaviour of the indented material. It is to be noted through the iteration history followed by the SOF optimisation, that the lower bound constraint imposed on the model ($\sigma_y > 1000$ MPa) prevented a further reduction in the value of σ_y as shown in Figure 7.4c, which otherwise would result in an enlarged error.

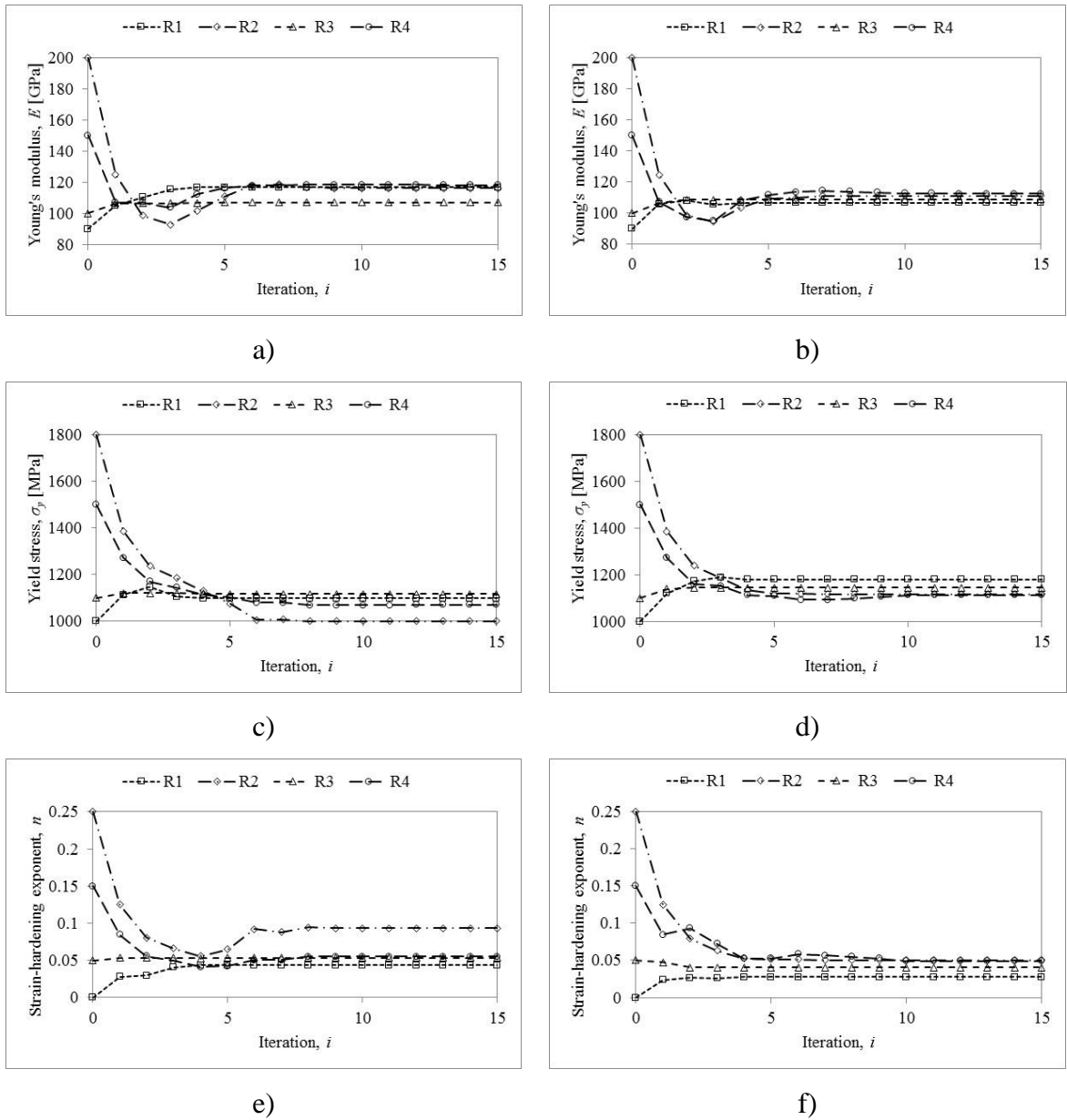


Figure 7.4. Iteration history through the minimisation problem of a), c), e) single objective and b), d), f) multiple objectives for the determination of elastic-plastic properties of Ti-6Al-4V.

Table 7.7. Characterised properties of Ti-6Al-4V after single- and multi-objective function optimisation.

Initial guess	Single-objective function			Multi-objective function		
	E [MPa]	σ_y [MPa]	n	E [GPa]	σ_y [MPa]	n
R1	116568	1099	0.0432	106468	1179	0.0276
R2	116083	1000	0.0935	110912	1117	0.0504
R3	107029	1117	0.0534	108822	1144	0.0407
R4	118139	1070	0.0552	112476	1113	0.0490
Mean	114455	1071	0.0613	109669	1138	0.0419
Std. Dev. [%]	3.80	4.14	31.14	2.06	2.31	21.70

7.4.2 Mechanical response to indentation as predicted by the optimisation model

The trust-region-reflective algorithm is a highly regarded method for its strong fitting capabilities [129] and thus, as evidenced in Figure 7.5, the recovered properties using both the SOF and MOF model led to remarkably consistent P - h curves, in very good agreement with the corresponding experimental curves. Therefore, for clarity, Figure 7.5 compares the experimental P - h curve with that of the indentation response of only one of the optimised sets of material properties provided by the SOF and MOF model. The maximum indentation depth (h_{max}) measured by the indentation instrument in specimens of CrMoV steel, C110 copper and Ti-6Al-4V was predicted by the SOF model with a 2.5, 2.7 and 1.4% error, respectively; the MOF model slightly reduced the corresponding errors to 2.4, 1.5 and 1.4%. Similarly, the depth after the load has completely removed (h_r) in specimens of CrMoV steel, C110 copper and Ti-6Al-4V, respectively, was predicted with errors of 5.6, 6.6 and 8.4% by the SOF and 5.0, 11.0 and 7.4% by the MOF. The largest error in the MOF solution to h_r of C110 can be attributed to the mismatch between the micro-scale plastic deformation measured experimentally around the indenter (pile-up) and macro-scale deformation predicted by the FE model. The main concern with the SOF model is that the nearly indistinguishable P - h curves represent the indentation response of a variety of material properties as reported in Table 7.5 to Table 7.7, i.e. the solution was not unique.

A slight variation along the indentation loop can be attributed to the complexity of representing the true contact mechanics involved in a depth-sensing indentation operation in an FE model, including the deformation of the indenter, the effects of tip imperfections and misalignment of the indenter and the individual crystal behaviour of the indented grains.

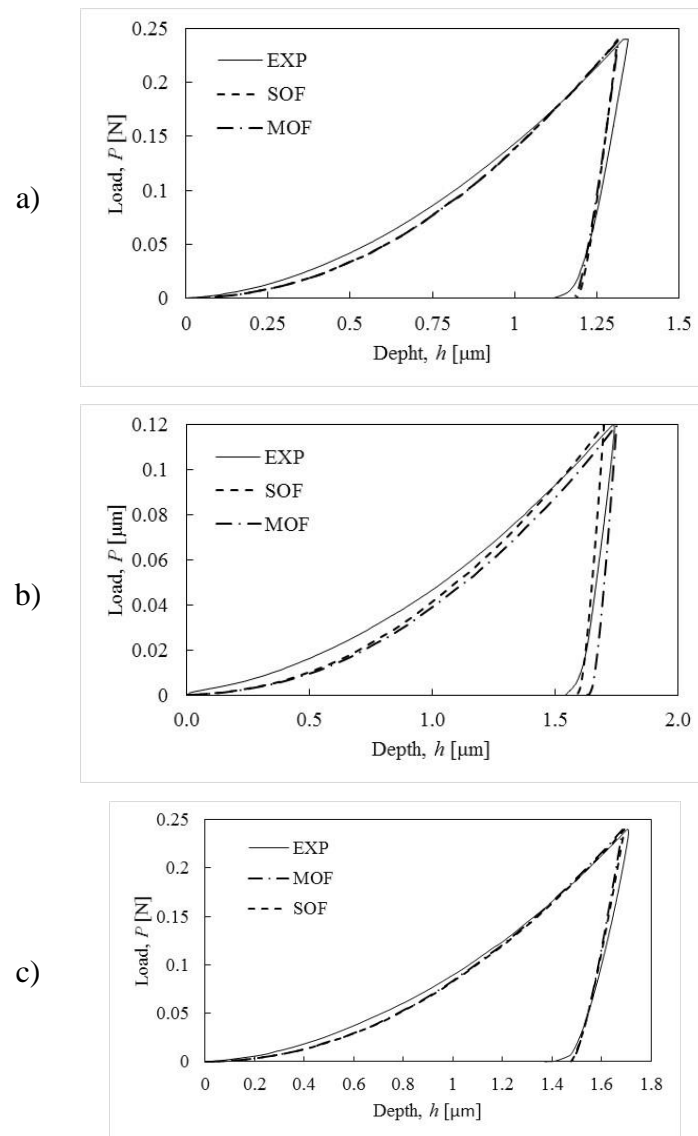


Figure 7.5. Fitting of optimised curve to experimental curve via the single- and multiple- objective function optimisation model for the corresponding material: a) CrMoV steel, b) C110 copper and c) Ti-6Al-4V.

The MOF optimisation model proved to be a step forward to the characterisation of the near-surface properties as, in contrast to the $P-h$ curve, the residual imprint is strongly linked to the plastic behaviour of the indented material. Therefore, the physics of the indentation problem was better represented as can be demonstrated by studying the volume of displaced material, as predicted by the MOF model, compared with experimental measurements taken via AFM. After convergence, the FE model approximated the area of the residual imprint extracted from the AFM scans performed in CrMoV steel, C110 copper and Ti-6Al-4V with an error of 5.1, 10.8 and 12.4%, respectively, as reported in Table 5.3. The residual area was quantified as the area beneath the free (reference) surface, yet due to the highly irregular topography of Ti-6Al-4V (Figure 7.6e), the reference depth was offset to -100 μm from the free surface in this case. The image processing software ImageJ was used to approximate the area of indentation predicted by the FE model as the ABAQUS post-processor does not allow easy extraction of the surface area from a set of nodal coordinates. Moreover, the convex shape of the sides of the triangular area of indentation in CrMoV and Ti-6Al-4V, resulting from the recovery of displacements upon unloading, as discussed in a previous chapter, was very well predicted by the FE model as can be seen by comparing Figure 7.6a with b and Figure 7.6e with f. In addition, the straight sides of the residual imprint predicted from the recovered properties of C110 copper (Figure 7.6d) were consistent with the experimental measurements (Figure 7.6e).

Table 7.8. Imprint area of indentation measured via AFM (A) compared with predicted area by the FE model after convergence (A_{FE}).

Material	A [μm^2]	A_{FE} [μm^2]	$\Delta A/A$ [%]
CrMoV	39.0	37.0	5.1
C110	79.9	71.3	10.8
Ti-6Al-4V	46.1	51.8	12.4

The size of regions A, B and C as predicted by the optimised FE model (Figure 7.6b and d), discussed below, has been superimposed on the corresponding top view provided by the AFM (Figure 7.6a and c) to prove the strong capabilities of the MOF model to represent the elastic-plastic deformation history experienced by the indented

material. Referring to Figure 7.6a and b, both the AFM measurement and FE prediction showed that the volume of plastically displaced material was confined to a region adjacent to the indenter-material interface, identified as region C, and reached a maximum pile-up height within region A. Accordingly, the pile-up height decreased away from the indenter centreline and towards the intersections of the indenter edges, i.e. the corners of the triangle. Also in agreement with experimental measurements, the FE model provided evidence that in the neighbourhood of the corners of the triangle the material does not show a dominant plastic flow behaviour, i.e. piling-up or sinking-in. This behaviour was consistently delimited by region B in both the real and predicted residual imprint. Examining the predicted plastic flow of material in Figure 7.6d, it was observed that C110 copper piled-up predominantly towards the bisector of the side of the triangular impression within region A. Moving away from the centreline of the indenter, the height decreased until the free surface was reached beyond region C. It was also noticeable a steeper decrease in height, compared with the imprint in CrMoV, as the corners of the triangle are approached. These trends and the regions where they occurred were highly consistent with the experimentally measured residual imprint as can be demonstrated by tracing the drawings of regions A, B and C of Figure 7.6d on Figure 7.6c. In contrast, it resulted evident that the complex plastic deformation behaviour of the double-phase microstructure of Ti-6Al-4V was beyond the capabilities of an FE model based on the continuum mechanics approach. However, the height measurements in the direction in which the pile-up profile was extracted (direction e in Figure 7.6), was represented accordingly by the FE model as discussed below.

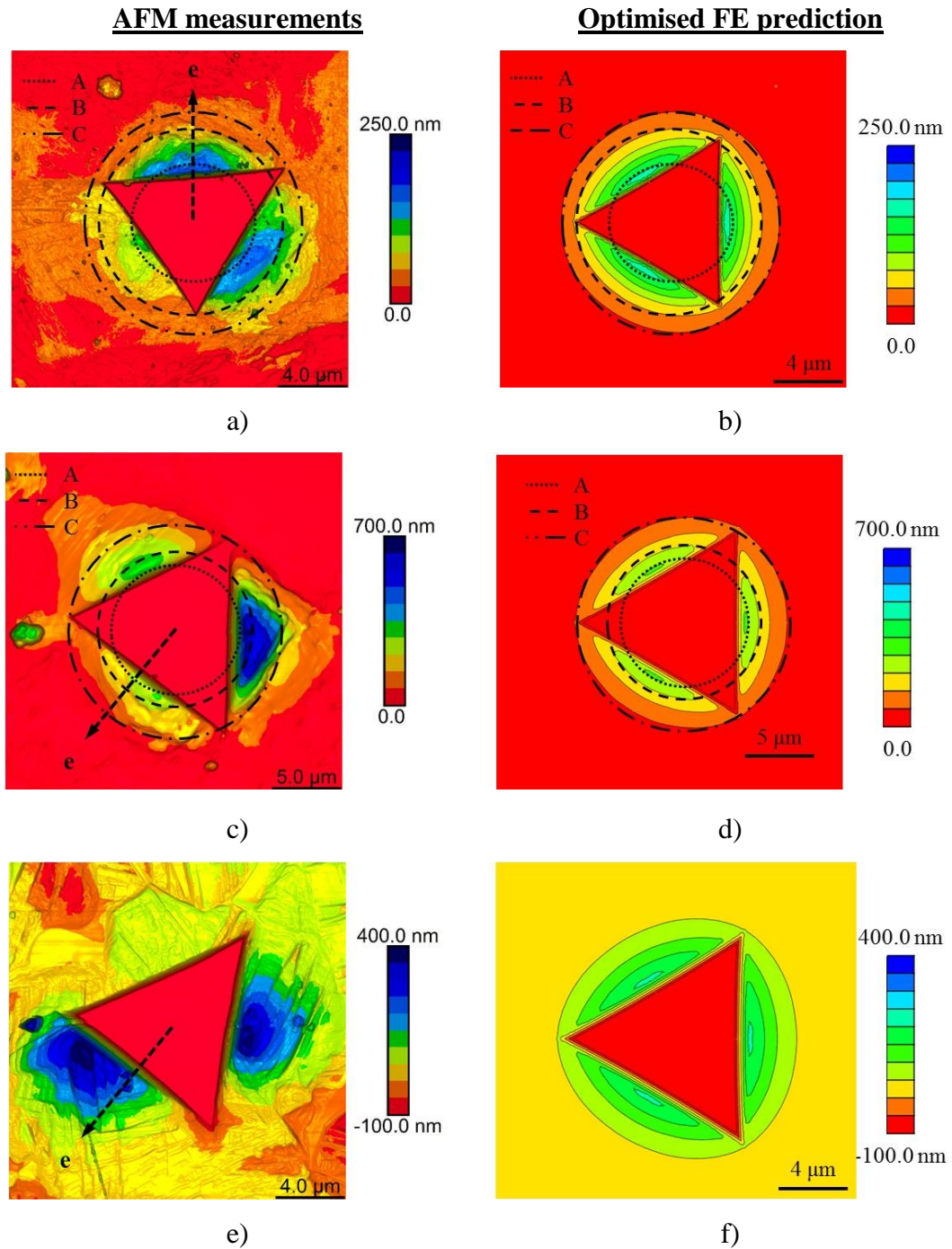


Figure 7.6. Top views of the residual imprints on specimens of a) CrMoV steel, b) C110 copper and c) Ti-6Al-4V. The left column presents the height measurements provided by the AFM and the right column the FE predictions using the optimised properties.

A more detailed assessment was conducted by studying the pile-up profiles extracted from the height measurements provided by the AFM as presented in Figure 7.7. To facilitate interpretation, Table 7.9 includes the quantitative information concerning the fitting of the SOF and MOF model to the experimental residual profile. Figure 7.7a, c

and e shows that despite the very consistent P - h curves, which are governed mostly by the E and σ_y parameters, the SOF model lacks the capability to recognise the significantly different behaviour of the plasticised material beneath the indenter, which is strongly linked to the parameter n . As a matter of fact, the material properties determined by the SOF model as presented in Table 7.5 to Table 7.7 are, correspondingly, ‘siblings’ to one another, i.e. their indentation response is nearly identical regardless of the dissimilar material properties that define their constitutive behaviour. For instance, the coefficient of variation between the P - h curves R2 and R3 shown in Figure 7.7c, which represent the indentation response of the material properties identified in Table 7.6, was less than 1% regardless of the significant deviation between the constitutive parameters of R2 in relation to R3, i.e. -23.7% in E , -22.2% in σ_y and 136% for n . Notwithstanding, the maximum pile-up height differed by greater than 30%. Therefore, the risk of the non-uniqueness issue of the inverse analysis of indentation poses a threat to the reliability of the inverse analysis purely based on P - h curves. Conversely, Figure 7.7b, d and f shows the consistency achieved in the prediction of the plastic response of the indented material with the MOF model. These figures also reveal important factors affecting the fitting of the pile-up profile due to the mechanism of plastic deformation of different microstructures such as a fine- and coarse-grained microstructure, e.g. tempered martensite in CrMoV steel and C110 copper, respectively, and a two-phase microstructure, e.g. Ti-6Al-4V. Tempered martensite grains are relatively fine (2-3 μm) compared to the area of indentation reached at $P_{max} = 0.24$ N, $A = 39$ μm^2 as reported in Table 5.3, and hence the plastic deformation approximates to some extent that of a continuum homogeneous material; the result was a pile-up profile considerably well predicted with a mean error for the value of the peak pile-up height (h_{peak}) of less than 11% as included in Table 7.9. In contrast, the mean h_{peak} predicted by the SOF deviated by up to 20% as illustrated in Figure 7.7a. The significantly coarser grains of C110 copper, which reach sizes of up to 100 μm , mean that indentations were likely to fall within a single grain as $A = 79.9$ μm^2 at $P_{max} = 0.12$ N. Therefore, the largest error for the case of C110 copper reported in Table 7.9 and shown in Figure 7.7d was not surprising as the continuum mechanics approach was unsuitable to represent the anisotropic behaviour of single crystals of copper, as detailed in a previous chapter. Lastly, grains of Ti-6Al-4V were not only of

an equivalent size to the indented area, i.e. an α -grain size of 20-30 μm and $A \sim 46.1 \mu\text{m}^2$ at $P_{max} = 0.24 \text{ N}$ (Table 5.3), but the changing material properties from grain to grain resulted in a highly distorted pile-up profile as observed in Figure 7.6e, which is understood by the optimisation algorithm as error in the form of noise and outliers. Notwithstanding, comparing Figure 7.7e and f, the MOF model attempted to provide a best fit between experimental and predicted data and hence the recovered material properties yielded to a mean error in $h_{peak} = 3.9\%$, which was lower than the error of 7.6% incurred by the SOF model. Furthermore, the residual depth, h_0 , after indentation in CrMoV steel was better predicted by the MOF as detailed in Table 7.9. Surprisingly, although the information beneath the free surface was not included in the optimisation of Ti-6Al-4V, the predicted h_0 by the SOF and MOF model closely approached the residual depth measured by the indentation instrument (h_r) to a relative deviation of less than 7.9% and 6.8% respectively. Therefore, the variation in the optimised n for Ti-6Al-4V and the discrepancy between the experimental and predicted pile-up profile after indentation in C110 copper was not a failure of the optimisation model, but rather a result of to the incompatibility between the macroscale approximation included in the FE model and the microscale plasticity behaviour of polycrystalline materials.

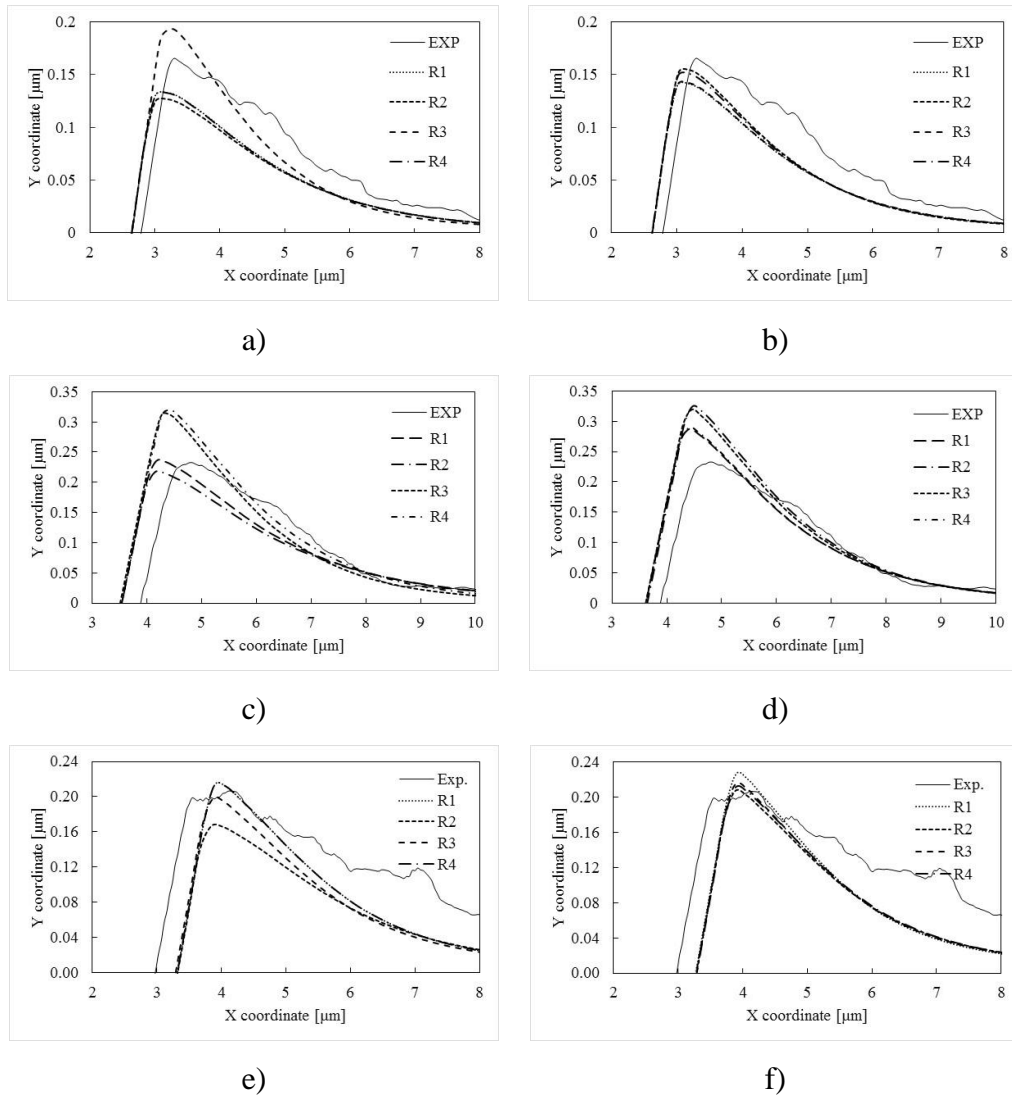


Figure 7.7. Experimental pile-up profile in indentations of a), b) CrMoV steel, c), d), C110 copper and e), f) Ti-6Al-4V fitted by the single- (left) and multiple- (right) objective function optimisation model

Table 7.9. Mean values of the peak pile-up height (h_{peak}) and residual depth (h_0) as predicted by the SOF and MOF.

Material	Single-objective function		Multi-objective function	
	$\Delta h_{peak}/h_{peak_Exp}$	$\Delta h_0/h_{0_Exp}$	$\Delta h_{peak}/h_{peak_Exp}$	$\Delta h_0/h_{0_Exp}$
CrMoV	19.9	8.7	11.0	8.1
Ti-6Al-4V	7.6	7.9 ⁽¹⁾	3.9	6.8 ⁽¹⁾
C110	19.7	0.7	31.3	3.6

(1) $\Delta h_0/h_{r_Exp}$

7.4.3 Comparison of small volume properties and bulk properties

Figure 7.8 presents a comparison of the constitutive relationship of the material at different scales. As expected, the stress-strain relationships of the material at micro- and macro-scale diverge as: On the one hand, the macroscale properties measured by the uniaxial tensile test describe the average of the mechanical response of the microstructure to external stimuli, i.e. the bulk properties. Furthermore, a uniaxial stress-strain curve represents an incomplete description of plastic deformation as it reduces a six-dimensional yield surface and its change upon loading to a one-dimensional (scalar) yield curve [147]. On the other hand, the optimised properties were recovered from the indentation response of the microstructure, which includes multiple phenomena neglected at macroscale, e.g. the heterogeneity of crystalline matter, the orientation dependence of the activation of the crystallographic deformation mechanisms, the extent of the mis-orientation between grains, the anisotropy of crystals and the strain gradient plasticity at low loads. Therefore, the significant difference in the predicted n by the MOF for the case of C110 copper can be attributed in part to the lack of a length parameter (required to account for ISE) in the continuum mechanics approach used in FE modelling. As the grain size in relation to indentation size is smaller in CrMoV steel and Ti-6Al-4V, microstructural effects are diminished and consequently a better prediction of the plastic-hardening (n) behaviour was achieved. Furthermore, a very good agreement between the predicted and measured elastic behaviour (E) can be noted in Table 7.10

Nonetheless, the stress-strain relationship during the plastic regime as generated by evaluating the optimised properties using Swift's material model, appear to be an offset of the uniaxial stress-strain curve, to an extent reasonably in agreement with the degree of the indentation size effect for the corresponding indentation. As previously presented in Table 7.1, due to ISE, the hardness at low load computed from the results of the depth-sensing indentation test (HM) is approximately 68, 16 and 2% higher in relation to the HV value measured by the conventional microhardness test in C110 copper, CrMoV steel and Ti-6Al-4V respectively. Correspondingly, the mean yield stress value optimised by the MOF model (σ_{y_opt}), as reported in Table 7.5 to Table 7.7, was 55-60, 13-17 and 32-41% higher compared to the yield stress extracted from

the uniaxial tensile test (σ_{y_uni}). In order to investigate the sensitivity of the constitutive parameters (E , σ_y and n) to ISE, an additional optimisation run was set up with the data of an indentation performed at a lower load, i.e. 0.12 mN. The model was initialised to $\mathbf{x}_0 = [200000, 1500, 0.05]$, with the intention of starting from slightly below the values reported in Table 7.5, and the solution converged at $\mathbf{x}_i = [214004, 1553, 0.0835]$. The magnitude of HM computed from the loading curves of the indentations performed at 0.24 and 0.12 N were 5000 and 5200 MPa, respectively, and thus similar properties were expected. In addition, as observed in Figure 7.9, the similarity in the shape of the pile-up profiles measured from the corresponding residual imprints is indicative of some, small, sensitivity of n to ISE. Comparing the results of this optimisation with the mean value reported for each parameter in Table 7.5, the Young's modulus and strain-hardening exponent appear to be slightly lower and the yield stress slightly higher. However, unlike E , the magnitude of σ_y appears to follow a trend of variation with the scale at which the measurements were taken, that is σ_y increased from 1325 MPa at macroscale (tensile test) to 1534 and 1553 MPa at microscale as optimised from the $P-h$ curves loaded to 0.24 and 0.12 N, respectively. A further assessment is required to confirm if the variation of n is in fact due to ISE or due to the error induced to the model by a pile-up profile more affected by the microstructural behaviour.

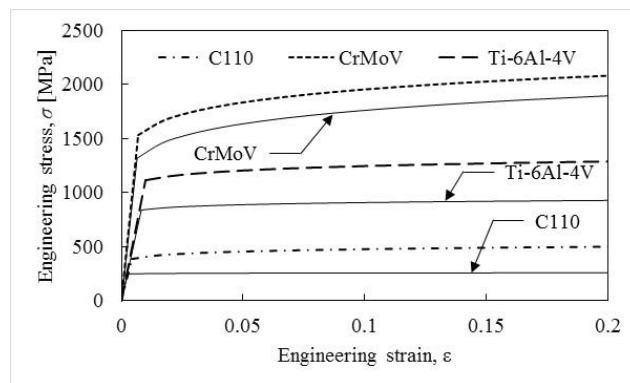


Figure 7.8. Constitutive relationship as determined by the multiple-objective function optimisation model (dashed lines). The engineering stress-engineering strain extracted from the tensile test has been superimposed (solid lines).

Table 7.10. Constitutive parameters as determined by the uniaxial tensile test and inverse analysis of depth-sensing indentation data via the MOF model.

Param.	CrMoV		C110		Ti-6Al-4V	
	Uniaxial	MOF ^{a)}	Uniaxial	MOF ^{b)}	Uniaxial	MOF ^{c)}
E [MPa]	204233	224218	99543	94420	103116	109669
σ_y [MPa]	1325	1534	249	392	839	1138
n	0.1055	0.0907	0.0090	0.0616	0.0315	0.0419

a) See Table 7.5

b) See Table 7.6

c) See Table 7.7

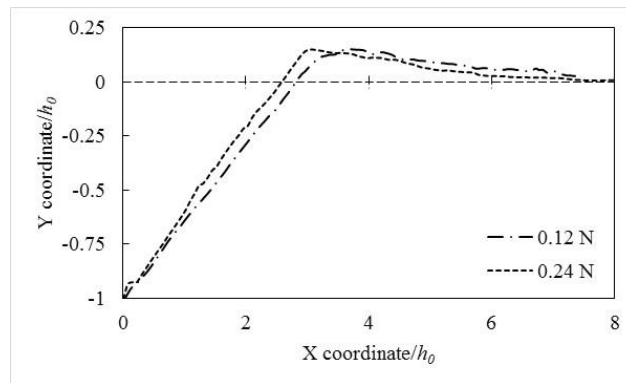


Figure 7.9. Pile-up profile extracted from the residual imprint left by the Berkovich indenter in CrMoV steel loaded to 0.24 and 0.12 N. Data have been normalised with h_0 for comparison.

7.5. Concluding remarks

The weak sensitivity of the $P-h$ curve to the plastic properties of power-law materials, i.e. the strain-hardening exponent (n), compared to the significant effects induced by the elastic properties such as Young's modulus (E) and yield stress (σ_y), make the interpretation of similar $P-h$ curves extracted from different materials a challenging problem. The second objective introduced in the multi-objective function optimisation model proposed in this study, provided valuable information concerning the plastic behaviour of the indented material and thus the robustness of the optimisation model was seen to be enhanced. The model provided very consistent results and proved to be capable of recovering from an apparent local solution. Furthermore, the complementary constraint added by the second objective was directly reflected in the

capability of the model to distinguish between ‘sibling’ materials and thus the MOF model effectively addressed the non-uniqueness issue of the inverse analysis of indentation. Overall, the MOF model resulted in a faster convergence and in a reduced variability in the solution. A great fitting power provided by the trust-region algorithm resulted in experimental $P-h$ curves extracted from all three materials fitted by the set of material properties to within an error of less than 2.4% and 8.4% the maximum (h_{max}) and residual (h_r) depth, respectively.

Of great interest was the remarkably well predicted topography of indentation by the MOF model provided that grain sizes are small enough in relation with the area covered by the indenter at full load. Both the shape of the edges and the area of the triangular residual imprint were in very good agreement with experimental data. The predicted indentation area deviated 5.1, 10.8 and 12.4% from the area measurements taken in indentations of CrMoV steel, C110 copper and Ti-6Al-4V, respectively. The validity of the predictions of the plastic flow of material beneath the indenter was supported by the strong consistency achieved by the MOF model with the AFM measurements. The error between the experimental and predicted maximum pile-up height (h_{peak}) was an average of 11% for indentations in CrMoV steel and 6.8% for Ti-6Al-4V. The variation in the pile-up profile predicted for C110 was attributed to the crystalline anisotropy of copper. Therefore, further developments are encouraged to include a more sophisticated crystal plasticity FE model in order provide a better approximation to the crystallographic deformation beneath the indenter.

A major contribution of this study concerns the still little known indentation size effects. The outcomes suggest that stress-strain curves exhibit similar behaviour during the elastic regime and plastic strain-hardening behaviour, with only the magnitude of the stress increasing as the load used to test the mechanical response of the material decreases. In other words, the stress-strain curve offsets to higher stresses at the corresponding plastic strain value.

Further conclusions can be drawn from the outcomes of the study presented in this chapter concerning the inverse analysis of experimental data by means of an optimisation procedure coupled with a conventional continuum mechanics FE model:

- A single loading and unloading sequence is preferred for the optimisation procedure, i.e. without load-holding periods, so as to allow the comparison with the time-independent solution provided by the FE model. The shortcoming is the risk of capturing significant displacements due to plastic recovery in the experimental P - h curves and consequently the optimisation model finding difficulties with fitting the experimental data. Furthermore, the dwell period at P_{max} results in an intrinsic error in the model due to the mismatch with the load-independent FE solution. Furthermore, it is recommended to leave the system over night to thermally stabilise to reduce thermal drift effects during measurements as typical FE models assume isothermal conditions.
- It is recommended to consider the possible challenges a significant time-dependent deformation may pose to the inverse analysis coupled with an FE model not provided with a time-dependent material model. Therefore, it is ideal to conduct a reference indentation experiment with a load-time sequence, i.e. dwell period and thermal drift, in order to establish the degree of error it may introduce to the optimisation model.
- Attempting to recover the mechanical properties of a material using a significantly deviated residual depth h_0 in relation with h_r may result in convergence issues. However, it was observed that satisfactory results can be obtained by including only the above surface topography of the residual imprint.

Chapter 8 - Characterisation of the across-weld properties in an inertia friction weld of SCMV steel

8.1. Introduction

The investigation discussed in this chapter builds upon the proven capabilities of the Multi-Objective Function (MOF) model to recover elastic-plastic properties of small volumes of material from data extracted via the depth-sensing indentation test. Therefore, the MOF model has been employed to generate the material property database of the as-welded condition of an inertia friction welded component of SCMV steel, namely the parent phase of tempered martensite (TM) and two child phases formed as an effect of the welding process, over-tempered martensite (OTM) and quenched martensite (QM). This was intended to create a material property database for use in FE models to improve the prediction of the residual stress distribution after welding. The input to the optimisation procedure and set up were defined in accordance with Chapter 7.

8.2. Conventional and depth-sensing indentations across the HAZ

As can be inferred from Figure 8.1, the thermo-mechanical history induced during the IFW process of SCMV steel results in a distribution in the material properties across the joint leading to an ~1.5:1 harder region and an ~0.76:1 softer region in relation to the base metal of tempered martensite, identified as TM (500HV0.5 ~ 4904 MPa). Note the Vickers hardness values extracted from the microhardness test have been converted to units of MPa, as reported in Figure 8.1, in order to provide a reasonable comparison with HM. The hard (750HV0.5 ~ 7355 MPa) and soft (380HV0.5 ~ 3748 MPa) zones are attributed to the formation of quenched martensite (QM) and over-tempered martensite (OTM) [85, 86] and situated within the HAZ between 0 - 3.25 and 3.25 - 6 mm, respectively, from the weld line. The hardness trough, hereafter taken as the position where martensite is considered fully over-tempered, was located at a distance of 4.7 mm. The Martens hardness (HM) was calculated from each experimental *P-h* curve and the mean value representing a set of indentations has been

superimposed on Figure 8.1. This comparison allows a rough estimate of ISE on the indentation response to be made. A similar trend of hardness variation across the joint can be seen, with the HM values slightly higher than HV due to Indentation Size Effects (ISE). Overall, HM is up to 10% stiffer relative HV in all but two characteristic regions, at 0 and 4.75 mm away from the weld line where QM and OTM, respectively, are known to exist. This could be explained by the microstructural evolution during IFW of the SCMV steel: The highest degree of ISE, measured as the relative difference between HM and HV ($\Delta H/HV$), in excess of 30%, was observed around the hardness trough ($\sim 4.75\text{mm}$), where the largest grain sizes [86] are formed due to the over-tempering of martensite and consequently the indentation covered a reduced number of grains. The highest dependency on the number of grains measured by the indenter could also explain, in part, the larger variation in the HM values in this region as the coefficient of variation lies between 7 and 13%. All other reported values of HM scatter within a coefficient of variation of 1.5 to 5.5%. On the contrary, ISE was observed to a lesser extent ($\Delta H/HV = 5.8\%$) at exactly the weld line as a result of the grain size reduction caused by dynamic recrystallization occurring in this region [86].

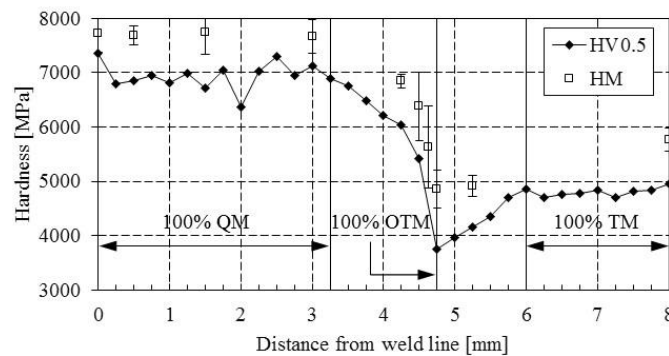


Figure 8.1. Microhardness profile across the HAZ of an SCMV steel weld trial. Error bars in the mean HM measurements represent 1 standard deviation.

Figure 8.2 shows the $P-h$ curves extracted from the indentation tests across the weld (see Figure 3.4). The curve with the minimum relative difference between HM and HV has been selected as representative of the indentation set. Furthermore, the indentations at 0, 4.75 and 8 mm away from the weld line represent, respectively, the QM, OTM and TM phases. Of relevant importance was the rapid change in the slope

observed at the bottom 2-4% unloading which suggests a significant displacement recovery during the unloading of the indenter. A closer inspection of the residual imprints left at the three characteristic regions, presented in Figure 8.3, provides evidence of this assertion as the material appears to have recovered plastically from an area close to the projected area, A_p , (dashed lines) reached at full loading, to an area, A , of the residual imprint formed after the completion of the unloading stage, as measured by the AFM. Therefore, material originally in contact with the edges of the indenter during loading appear to have bowed in the direction of the applied load during unloading due to the shrinkage of material, which consequently caused the convex shape of the sides of the triangle. This could be due to material recovering plastically as a result of avoiding, intentionally, dwell periods at maximum loading, multiple unloading cycles and thermal drift periods with the aim of obtaining a continuous $P-h$ curve suitable to compare with the time-independent FE simulated curve throughout the optimisation procedure. Table 8.1 summarises the values of hardness and area measured from the indentations used in the optimisation procedure.

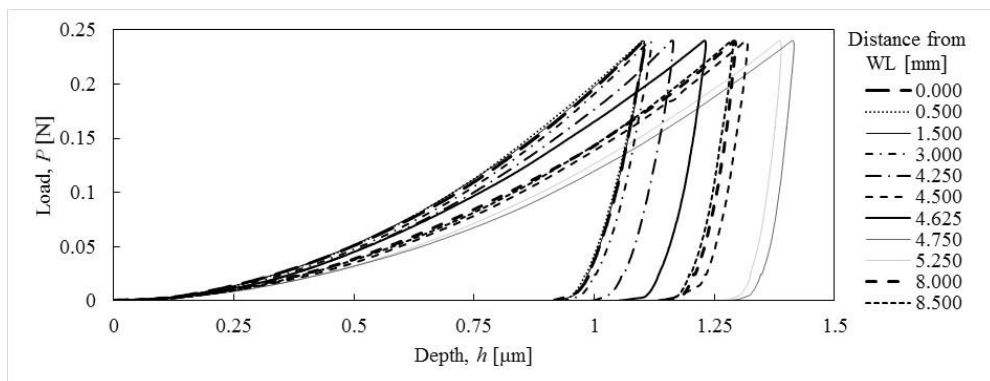


Figure 8.2. Experimental $P-h$ curves corresponding to tempered martensite (TM), quenched martensite (QM) and over-tempered martensite (OTM) phase.

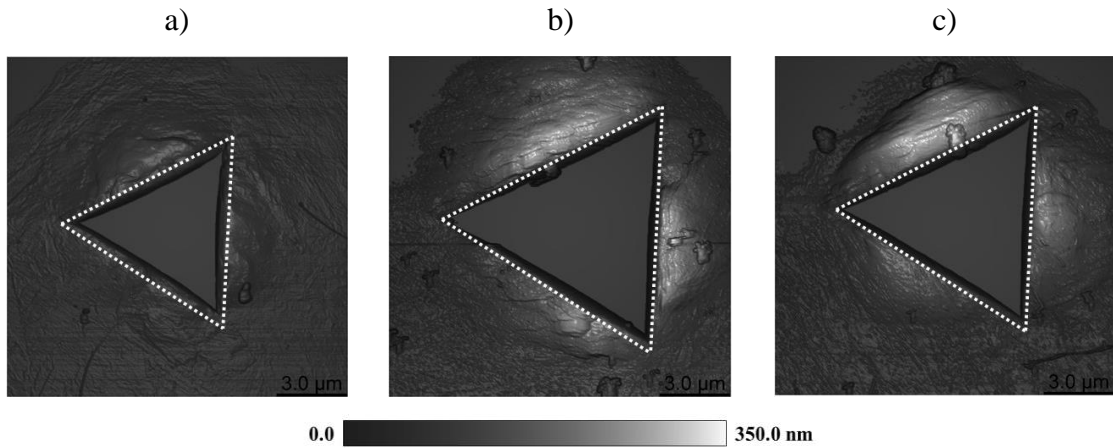


Figure 8.3. Height measurements in the characteristic regions a) QM, b) OTM and c) TM. Measurements below the reference (0 nm) have been suppressed to show the topography around the indentation in more detail. In addition, the projected area of the indenter (A_p) has been superimposed (dashed line) to illustrate the apparent extent of plastic recovery.

Table 8.1. Values of hardness and area of the residual imprints measured in indentations used in the optimisation procedures.

Region	HV0.5	HV0.5 [MPa]	HM [MPa]	A_p [μm^2]	A [μm^2]
QM	750	7355	7240	29.9	20.6
OTM	382	3748	4568	49.2	39.4
TM	500	4904	5419	41.1	32.9

8.3. Determination of elastic-plastic properties across the weld via the multi-objective function optimisation technique

8.3.1 Robustness in predictions of the mechanical response to indentation

In order to prove the robustness of the proposed multi-objective function optimisation model, no upper limits were imposed on the possible solutions to Young's modulus and yield stress. Bound constraints for the strain-hardening exponent were set between 0 and 1 so as to account for the plastic hardening behaviour of the majority of metallic materials [144]. Recalling from Chapter 3, the Poisson's ratio was kept constant to 0.3. Therefore the combinations of possible solutions to the inverse analysis of depth-sensing indentation in the present study lie within a space defined by:

$$\left\{ \begin{array}{l} E \geq 0 \\ \sigma_y \geq 0 \\ 0 \leq n \leq 1 \\ v = 0.3 \end{array} \right\} \quad 8.1$$

The initialisation of the optimisation procedure, as presented in Table 8.2, was set up as follows: For most steels, Young's modulus measured at macro-scale has a value of about 180-250 GPa [143] and therefore, 250 GPa is considered a suitable choice of initial guess for E . Following Tabor's relationship [134] of Vickers hardness (reported in Figure 8.1), the yield stress at 8% plastic strain ($\varepsilon_p = 0.08$) of martensite in the tempered, quenched and over-aged condition, formed from the IFW of SCMV steel is approximately 1600, 2500 and 1200 MPa, respectively. However, due to ISE, the yield stress at microscale is likely to be approximately 10% higher for TM and QM and 30% for OTM, based on the apparent ISE reported in Figure 8.1. Correspondingly, the initial parameters for σ_y ($\varepsilon_p=0$) were set to 1800, 2800 and 1500 MPa. Since steels generally exhibit low to moderate strain-hardening [144], the n value was initialised as 0.15. These sets of properties are hereafter referred to as the upper guess (UG) vector. Moreover, in order to prove the consistency of the model to converge to an optimum solution, the effects of the initial guess parameters on the optimised parameters have been evaluated by defining a lower guess (LG) vector as follows: E was set as the known lower value for steel as previously mentioned, i.e. 180 GPa, σ_y was reduced more than 40% the corresponding UG value and a low value of strain-hardening, i.e. 0.05, was selected for n . Therefore, E , σ_y and n were changed to start at values of at least 28, 40 and 67% of the corresponding UG parameters in the inverse analysis procedure of all three phases TM, QM and OTM.

Table 8.2 presents the quantitative information regarding the outcomes of the MOF model starting at both the LG and UG vectors. As a benchmark, additional simulations were performed using the SOF model starting at the corresponding LG and UG vector for each phase. Table 8.2 is used throughout this chapter to assess the applicability of the proposed method for characterising the properties formed across the joint of IFWed cylinders of SCMV steel.

Table 8.2. Set up and results for the optimisation of the across-weld properties in an inertia friction weld of SCMV steel.

Phase	Parameter	Initial guess		Optimised parameters			
		LG	UG	MOF		SOF	
				LG	UG	LG	UG
TM	E [MPa]	180000	250000	243579	253737	288496	288050
	σ_y [MPa]	1000	1800	1463	1427	1586	1439
	n	0.05	0.15	0.1153	0.1201	0.0499	0.0923
QM	E [MPa]	180000	250000	197173	199672	261409	262901
	σ_y [MPa]	1000	2800	2697	2632	2495	2281
	n	0.05	0.15	0.1183	0.1284	0.0664	0.1115
OTM	E [MPa]	180000	250000	237203	243594	259311	314534
	σ_y [MPa]	800	1500	1213	1198	1328	1159
	n	0.05	0.15	0.0917	0.0932	0.0323	0.0683

Figure 8.4 presents the iteration history throughout each optimisation. Convergence of all optimised parameters has been achieved rapidly in 5 to 10 iterations for the three phases. Furthermore, despite the value of the initial guess, the optimisation model converged to a solution to within a difference of less than 4, 2.6 and 7.9% in the optimised values of E , σ_y and n , respectively, relative to the values approximated by the original model for the three phases TM, QM and OTM, as plotted in Figure 8.5. The white and black bars represent, in respective order, the relative difference between the pair of parameters at the initial iteration, i.e. between the corresponding LG and UG parameters, and the final iteration, i.e., between the corresponding optimised parameters. The strong consistency in the optimised parameters was a remarkable achievement considering that arbitrary values of E , σ_y and n were chosen as initial guess and the fact that no upper limits were imposed on the model to constraint the solution.

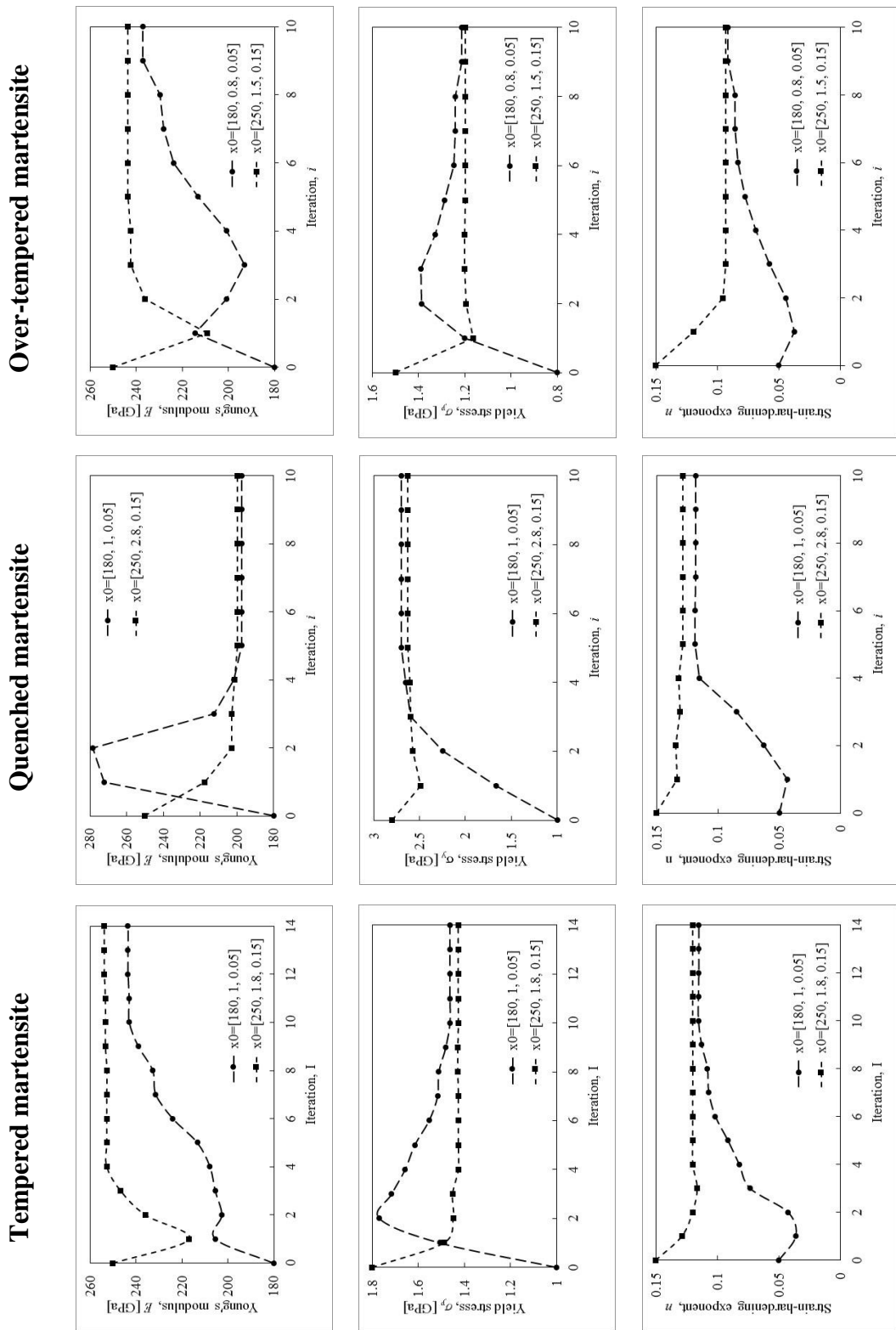


Figure 8.4. Evolution of the optimisation parameters from the initial guess values starting at LG and UG.

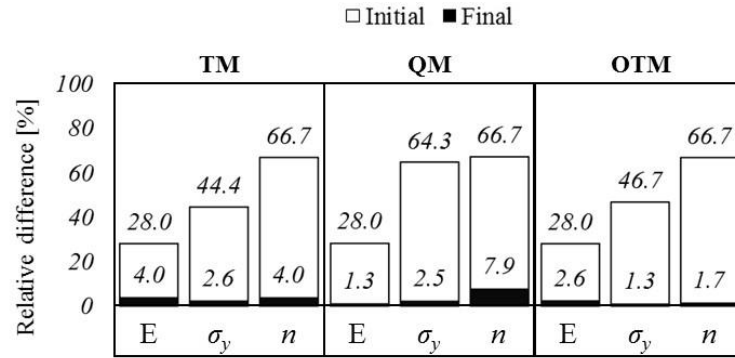


Figure 8.5. Relative difference [%] between each pair of optimisations at the initial (guess) and final (converged) iteration.

As observed in Figure 8.6, the MOF model was capable of fitting the three different experimental indentation $P-h$ curves to within a relative error in the predicted maximum indentation depth (h_{max}) of less than 0.18, 0.77 and 0.27% for the martensite in the tempered, quenched and over-tempered condition, respectively. The indentation response of the pair of materials for which the constitutive behaviour is represented by the properties determined by the MOF model starting from both the LG and UG vectors are virtually identical and thus, for clarity, only a single set of results is presented in Figure 8.6. Comparing the corresponding $P-h$ curves, the results show that the loading curvature C and maximum depth h_{max} of both the SOF and MOF optimisation are consistent with the experimental data yet the unloading curves deviate slightly. The SOF curve appears to more closely match the upper region of the experimental unloading curve, but in contrast, the MOF prediction was in better agreement with the bottom data points as is clearly visible in the detailed views provided in Figure 8.6. This is attributable to the constraints added to the MOF model by the second objective, which includes the information of the residual imprint left in the surface after the recovery of elastic and plastic displacements.

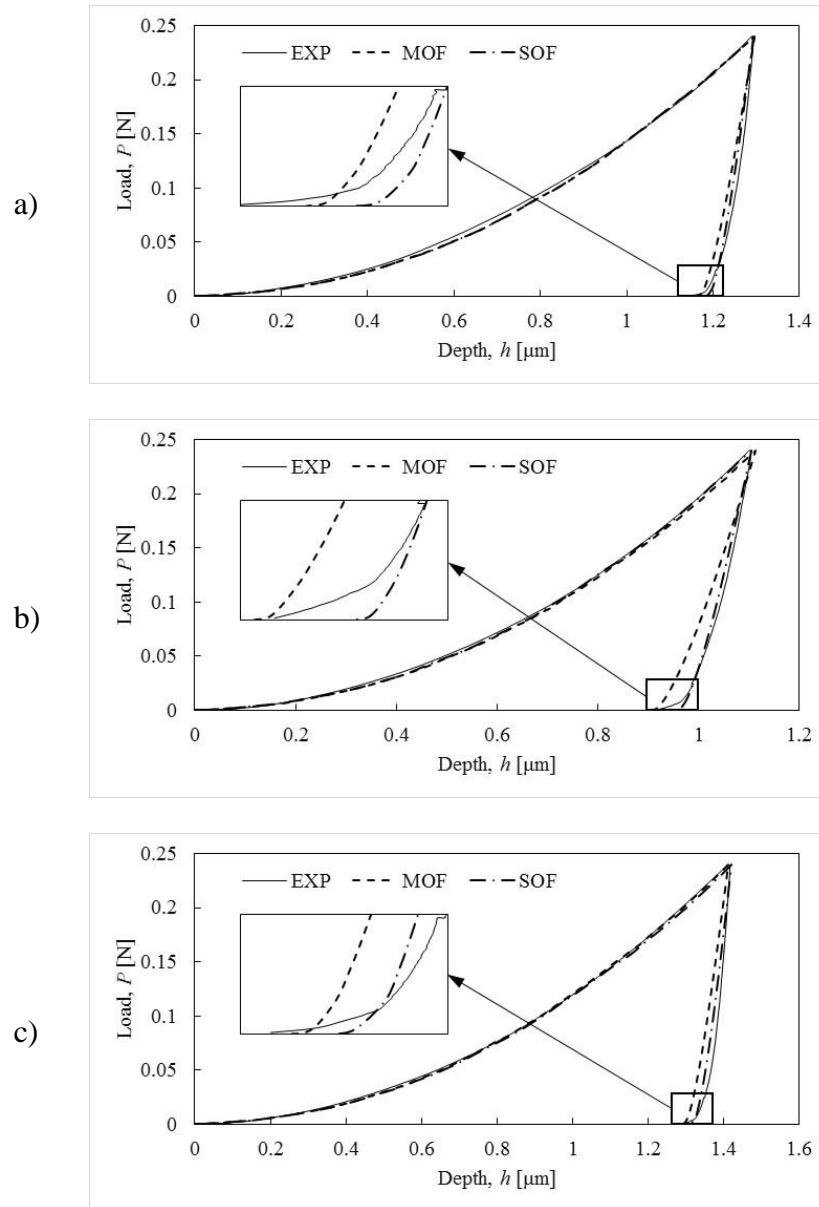


Figure 8.6. Comparison of P - h curves obtained from experimental data and FE model using the optimised parameters for martensite in the a) tempered, b) quenched and c) over-tempered condition.

However, although to some degree the FE model accounts for the recovery of plastic strains (PEEQ) upon the completion of unloading, as illustrated in Figure 8.7, the significant recovery of displacements at a microscopic scale, in particular the microstructural recovery of SCMV in the quenched condition (Figure 8.6b), was beyond its capabilities. Consequently, due to the inability of the FE model to account for the greater degree of plastic recovery, it appears the MOF model attempted to mutually fit the low bottom unloading curve and to conform to the residual imprint left

after elastic and plastic recoveries by changing the elastic contact stiffness, through the value of the Young's modulus, so that the slope of the FE predicted unloading curve provided a good fit between h_{max} and h_r provided evidence that when plasticity contributes to the recovery of displacements, the slope of the unloading curve is not only governed by the Young's modulus of the material.

Furthermore, the volume of material plastically displaced after the removal of the indenter was remarkably well predicted by the MOF model; the deviation between the predicted and experimental value of the maximum pile-up height lay between 0.3 and 9.6% as seen in Figure 8.8. In contrast, the solution provided by the SOF model, which is superimposed in Figure 8.8 for comparison, significantly overestimated by 79% the maximum pile-up height given the limited information available in the $P-h$ curve regarding the strain hardening behaviour of the indented material.

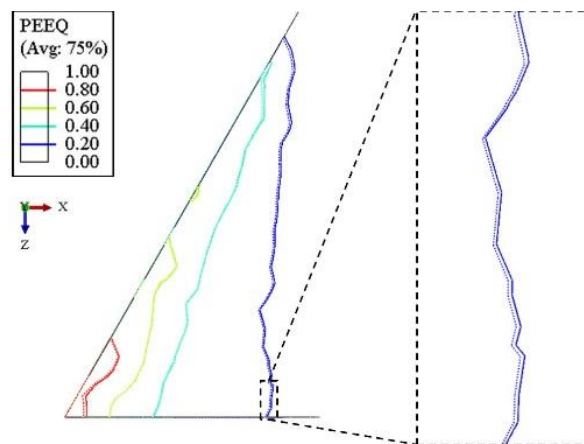


Figure 8.7. Contour plot (one-sixth of the domain) showing the plastic strains on the indented surface as predicted by the FE model at P_{max} (dotted) and P_0 (solid). The constitutive behaviour corresponds to optimised properties for QM as reported in Table 8.2.

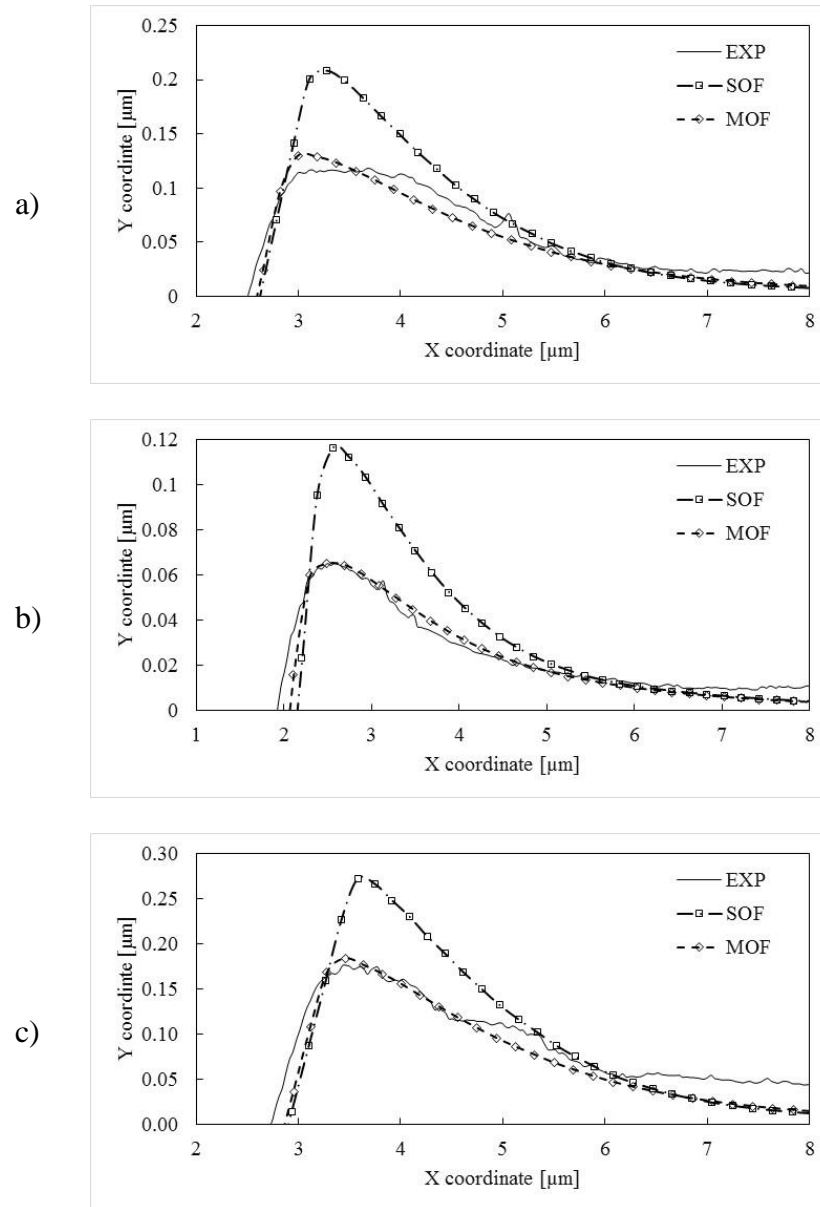


Figure 8.8. Comparison of pile-up profiles obtained from experimental data and FE model using the optimised parameters for martensite in the a) tempered, b) quenched and c) over-tempered condition.

8.3.2 Constitutive relationships as determined by the MOF model

Figure 8.9 presents a comparison of two stress-strain curves, a curve obtained experimentally from an axisymmetric compression test of SCMV steel in the tempered condition at room temperature [1] and a curve using Swift's relationship (Equation 3.6) with the average of the optimised material properties predicted for the tempered martensite, as reported in Table 8.2. The corresponding curves of martensite in the

quenched and over-tempered conditions were also included in Figure 8.9 to show the variation in mechanical properties across the joint as a result of the IFW process. However, it is to be recognised that Swift's law is an idealisation that usually does not represent the stress-strain relationship of a real engineering material. A difference of 19.2 and 3% in the optimised value of Young's modulus and yield stress respectively was found in relation to the macro-scale properties reported by Bennett [1], regardless of the initial guess value. After 8% of plastic strain ($\epsilon_p = 0.08$) the stress reached a relative difference of approximately 17%. As discussed in Chapter 7, these deviations are attributable to the dissimilar volume of material tested by each of the mechanical testing techniques, namely the microscopic (local) properties measured via indentation with a Berkovich and the macroscopic (bulk) properties extracted via compression testing [1]. Furthermore, the microstructure of the tempered martensite material consisted of equiaxed grains of α -ferrite (bcc) of about 2-3 μm plus spheroidised precipitates of Fe_3C (cementite) [148] and therefore different material properties were expected from grain to grain. The area left by the Berkovich indenter penetrating the tempered martensite at full load (0.24N) was calculated via AFM as that of an equilateral triangle of $A = 32.9 \mu\text{m}^2$ as shown in Figure 8.3c and schematically illustrated in Figure 8.10. Consequently, during the depth-sensing indentation test, the indenter was in contact with a region including only a small number of grains and therefore measured the average properties of a limited number. On the other hand, the compression test extracted the bulk stress-strain relationship of the tempered martensite in a sample comprised of several millions of grains. Furthermore, a depth dependency mechanism, e.g. indentation size effect (ISE), may be attributable for the difference of up to 10.5% between the hardness measurements provided by the Berkovich (HM) and Vickers (HV0.5) indenters as included in Table 8.1. The volume of material measured by the Vickers indenter loaded to 0.5 kg in the tempered martensite, as schematically illustrated in Figure 8.10, can be regarded as representative of the macroscopic properties, or size-independent, although both indentation procedures fall in the micro-scale category [13]. This claim was confirmed by the close agreement between to the stress level at 8% plastic strain provided by the compression test, $\sigma_{0.08} = 1694 \text{ MPa}$, and that from Tabor's relationship [134], i.e. $\sigma_{0.08} = \text{HV}/3 = 1635 \text{ MPa}$. Therefore, in accordance with the results of Chapter 7, the

predicted stress-strain curve from the mechanical response to indentation of the material at micro-scale were offset to higher levels of stress to an extent comparable with the degree of ISE.

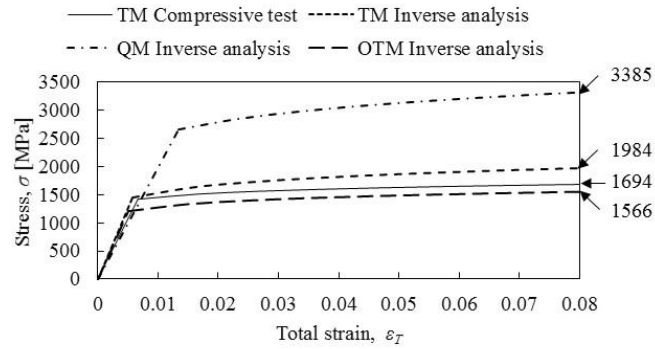


Figure 8.9. Comparison of the stress-strain curve generated experimentally from a compression test on a SCMV steel sample [1] and the curve built using the optimised material properties predicted by the inverse analysis.

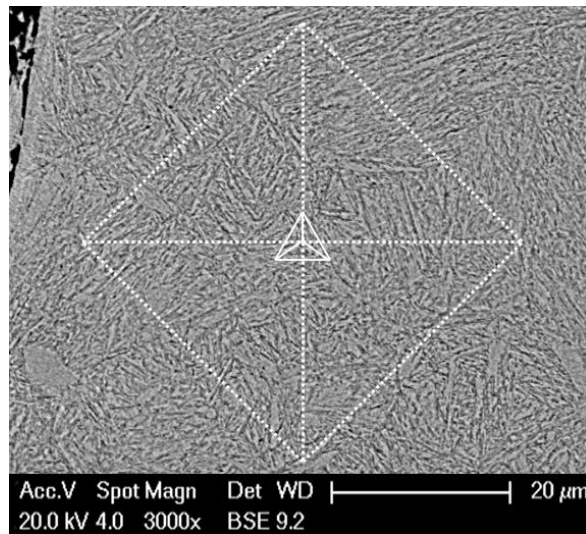


Figure 8.10. Schematic illustration of the impression left by a Vickers indenter loaded at 0.5 kg and the projected area of the Berkovich indenter penetrating the tempered martensite lattice.

Having validated the results of the inverse analysis with experimental data extracted from a SCMV steel in the tempered condition, TM can be used as a reference to test the results obtained for the QM and OTM as follows. As presented previously in Table 8.1, martensite in the quenched and over-tempered condition exhibited a Vickers

hardness of approximately 7355 MPa (750HV0.5), and 3748 MPa (382HV0.5) respectively, or 1.5 and 0.76 respectively the value of the tempered martensite located outside the HAZ (500HV0.5 ~ 4904 MPa). These ratios are consistent with the average of the optimised values of stress at 8% plastic strain obtained by the proposed inverse analysis technique as indicated in Figure 8.9: 3385 MPa for quenched martensite and 1566 MPa for over-tempered martensite, or 1.71 and 0.79 times the corresponding value of the tempered martensite (1984 MPa) respectively. The comparison was valid given the relationship between Vickers hardness and stress at 8% plastic strain as derived by Tabor [134].

Furthermore, an encouraging achievement was the apparent potential of the MOF model to sense the dependency of the Young's modulus on the microstructural evolution occurring during quenching. In quenching of carbon steels there is a decrease in the value of the Young's modulus [149] due to the mutual changes from both the decrease of the volume fraction of cementite and the supersaturation of the dislocation density resulting from the martensitic transformation. The extent of variation ($\Delta E/E$) is dependent upon the carbon content [149] and it has been reported in the literature that the change can be up to 4% in 42CrMo4 steel [150] and 13% in the chromium steel 9Kh18 [151]; the latter pair of studies employed a dynamic mechanical analysis to calculate E . In good accord, as reported in Table 8.2, the magnitude of E of martensite in the quenched condition (martensitic phase) reduced by 18-22% in relation to the tempered martensite condition (ferritic phase). Of course, a proportion of this difference can be attributed to uncertainty and to the fact that an extent of the plastic recovery recorded by the experimental data was interpreted as mostly elastic by the FE model, as previously detailed.

These results justify the applicability of the proposed inverse analysis in the characterisation of material property variation across an IFW of SCMV steel. The optimised parameters can be used therefore to generate the constitutive relationship of each of the material phases present during the process in order to improve the FE prediction of the residual stress field in the as-welded condition.

8.4. Residual stress field within the HAZ

8.4.1 Processing of the optimised constitutive relationships

It is generally agreed that under isothermal conditions, the tempering process involves three overlapped stages [139]: in a first stage, a proportion of the retained carbon in the bct (quenched) martensite precipitates out of solution as ϵ -carbides of type M_2C , also referred to as the transition carbides. During the second stage, retained austenite completely decomposes and subsequently ϵ -carbides are replaced by cementite such that the martensitic matrix completely loses its tetragonality and becomes α -ferrite (bcc) + Fe_3C (cementite). Lastly, in a third stage, cementite gradually coarsens and forms spheroids. During IFW, tempered martensite is thermally activated and hence the precipitated carbides continued to grow, as observed by Moat et al. [86]. In the absence of information concerning the continuing tempering process effected during the (non-isothermal) IFW process, it was assumed that martensite starts to over temper at the end of the precipitation of cementite. According to Bala et al. [152], this occurs at temperatures beyond 420 °C during tempering of a CrMoV steel at a heating rate 0.05 °C/s, however, accounting for the fact that the temperature at which the austenitisation begins increases with faster heating rates [1], it was reasonable to assume that the tempering process began at a higher temperature due to the heating rates experienced during IFW. This assumption along with the significant drop in the value of yield stress in SCMV observed at approximately 600°C [1], which possibly indicates the activity of carbon precipitates, justify setting up this temperature (600°C) as the start of the tempering process in the FE model. However, the kinetics of transformation during over-tempering of martensite and the lattice strains arising due to volumetric changes were out of the scope of this work, which was intended to investigate only the effects of the material property variations across the joint. Therefore, the tempering process was assumed as an athermal transformation with a sigmoidal type of curve where the fraction of the martensite being over-tempered was a function solely of the temperature. Moreover, in order to avoid inconsistencies in the flow stress at the transformation temperatures, the high temperature ($> 600^\circ C$) properties of the quenched and over-tempered martensite were set in compliance with the values determined experimentally for tempered martensite [1] as illustrated in

Figure 8.11. As in Chapter 4, the yield stress of austenite at low temperature ($T = 600, 400, 200, 20^\circ\text{C}$) was linearly extrapolated from the high temperature data in order to account for the stability of austenite at lower temperatures on cooling. However, as can be seen in Figure 8.11a, the transition from low to high yield stress values due the transformation of austenite to quenched martensite at A_{r3} was not set in the material database as this may induce a numerical singularity if the change is instantaneous or promote a condition in which the low yield stress of austenite changes rapidly to considerably high levels before the transformation to quenched martensite occurs. Notwithstanding, DEFORM uses the volume fraction within an element as a weight factor to define the level of stress between a pair of dissimilar stress-strain curves, in this case AUST and QM, which allowed transitioning continuously from low to high stresses as the volume fraction of austenite was decreased by the increasing volume fraction of quenched martensite. Lastly, the plastic behaviour of each phase at the corresponding temperature was represented by evaluating the optimised properties into Swift's material model (Equation 3.6). The strain-hardening coefficient was assumed temperature-independent and therefore it is not shown in Figure 8.11.

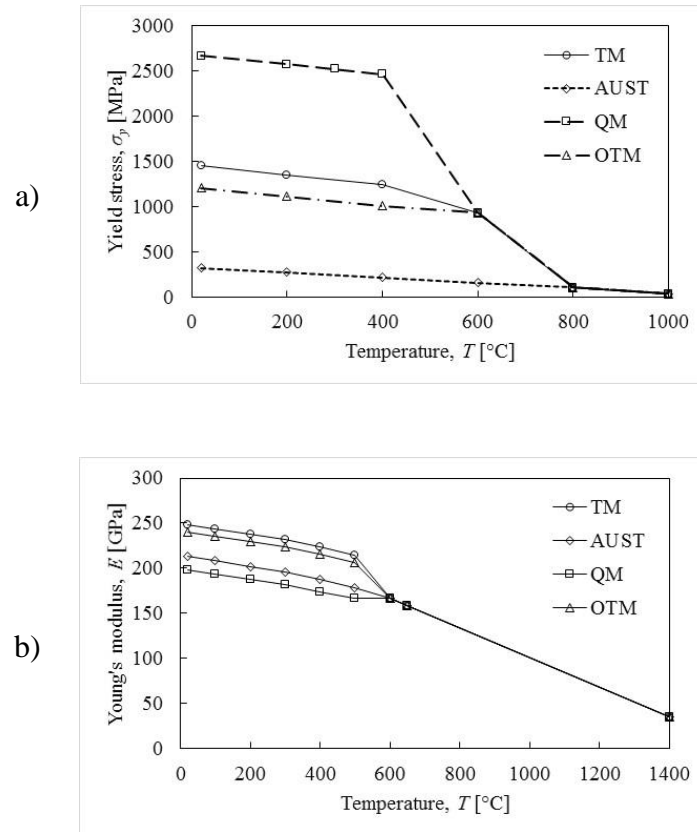


Figure 8.11. Processing of material properties to account for the temperature-dependency of the a) yield stress and b) Young's modulus and the continuity between phases at the transformation temperatures.

8.4.2 Inclusion of the softer over-tempered martensite phase

The improved material database previously detailed was implemented in FE modelling of IFW in order to account for the interaction of the austenite and the three martensitic phases (QM, TM and OTM). Consequently, the FE model discussed in Chapter 4 has been extended into a four-phase model. Figure 8.12a provides an overview of the volume fractions corresponding to each of the three solid phases as predicted by the four-phase FE model. A region composed of up to 97.2% QM was predicted within a distance of ~ 0 to 5.9 mm from the weld line. The remaining 2.8% is retained austenite but it has been omitted for clarity. Between ~ 5.9 to 10.3 mm, martensite over-tempered until 100% OTM was reached at a distance of 7.3 mm measured from the weld line. At regions located beyond 10.3 mm, outside the HAZ, tempered martensite remained unaffected such that this phase constitutes 100% of the material. Hence, as indicated in Figure 8.12, the regions of material composed of 97.2% QM and between

0 to 100% OTM extended to a proportion, respectively, of 0.57 and 0.43 the length of the HAZ (L_{HAZ}). In addition, the distance from the weld line to the region where martensite fully over-tempered (100% OTM) extended, proportionally, $0.71L_{HAZ}$. Therefore, as compared in Table 8.3, the FE prediction closely matched the proportion of the HAZ covered by each phase as inferred from the characteristic regions observed Figure 8.1, that is, 0.54 for QM and 0.46 for OTM.

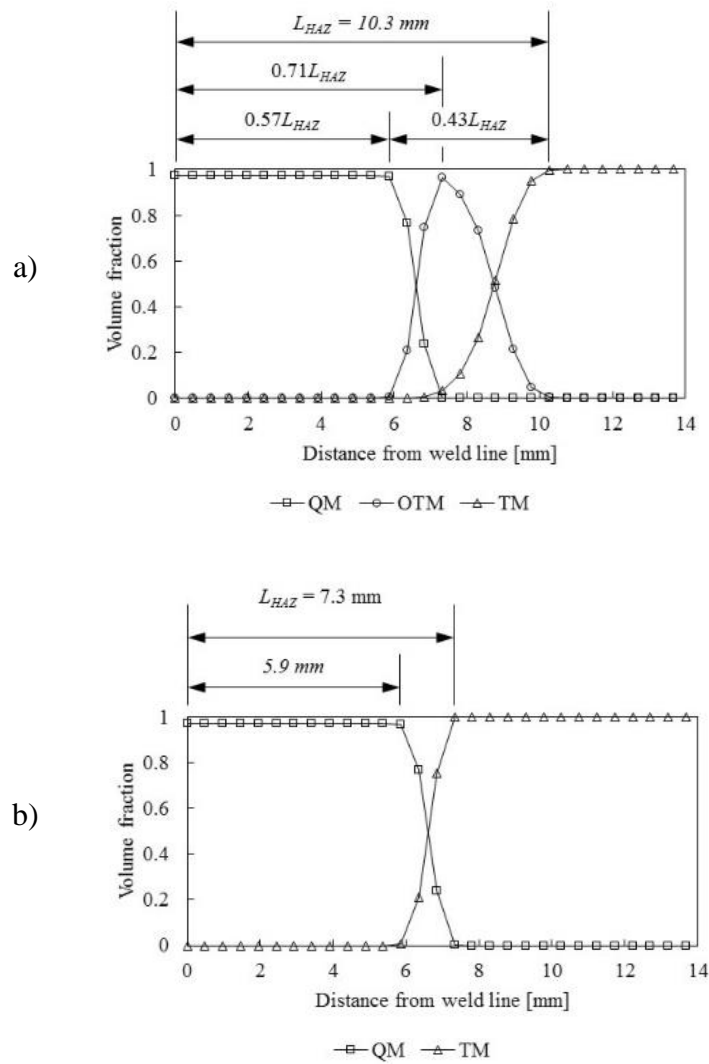


Figure 8.12. Volume fractions across the joint as predicted by the a) four-phase and b) three-phase FE model.

Table 8.3. Lengths covered by the martensite in the quenched and over tempered condition, in proportion to the length of the HAZ, as predicted by the FE model and those inferred from the microhardness test (Figure 8.1).

	100 % QM*	0-100 % OTM	100% OTM
Microhardness	0.54	0.46	0.79
FE prediction	0.57	0.43	0.71

* This region is comprised by QM, majorly, and very small amounts of retained austenite.

The gradual hardness drop recorded by the microhardness scan (Figure 8.1) approached a hardness through from both the QM and TM sides that can be related to the peak volume fraction of OTM observed in Figure 8.12a. Therefore, as shown in Figure 8.13a, strains were accommodated by the softer OTM phase at lower levels of stress compared with the stresses resulting from the interaction of two relatively hard phases, i.e. QM and TM as seen in Figure 8.13b. In order to de-convolute the very complex stress state in the as-welded condition, so as to provide a better understanding, plots of the magnitude of stress in the three cylindrical directions, axial (z), radial (r) and hoop (θ), are presented in Figure 8.14. As can be seen, the axial location of stresses appears unaffected by the presence of the softer phase (OTM). For instance, peak stresses in the hoop direction were generated at the same location of 7.3 mm away from the weld line, as shown in Figure 8.14, despite the fact that the HAZ was predicted to extend to 10.3 (Figure 8.12a) and 7.3 mm (Figure 8.12b) from the weld line by the four- and three-phase simulation, respectively. The trend observed in the prediction provided by the four-phase simulation appears to be supported by an experimental study conducted by Moat et al. [106] on IFW of SCM V to Aermet100 steels. As shown in Figure 8.15, peak stresses in the hoop direction are revealed at a distance corresponding to the extension of the QM region (inferred from the presence of retained austenite) and not with the region including both the QM and OTM, i.e. the boundary of the HAZ zone.

On the other hand, stress levels as predicted by the four-phase simulation were reduced in magnitude compared with those provided by the three-phase model; in other words, positive and negative stresses shifted to a less positive and less negative state, respectively. The accommodation of strains by the OTM phase therefore, relaxed

between 7 to 11%, 1 to 6% and 12.8 to 15.3% the peak values of stress in the radial, axial and hoop directions, respectively. The stress reduction however, was in regard to only the mismatch between the levels of flow stress of the phases included in the domain and thus, considering lattice strain due to the over tempering of martensite has been neglected, the result was that the residual stress field was significantly affected by the inclusion of the softer OTM phase.

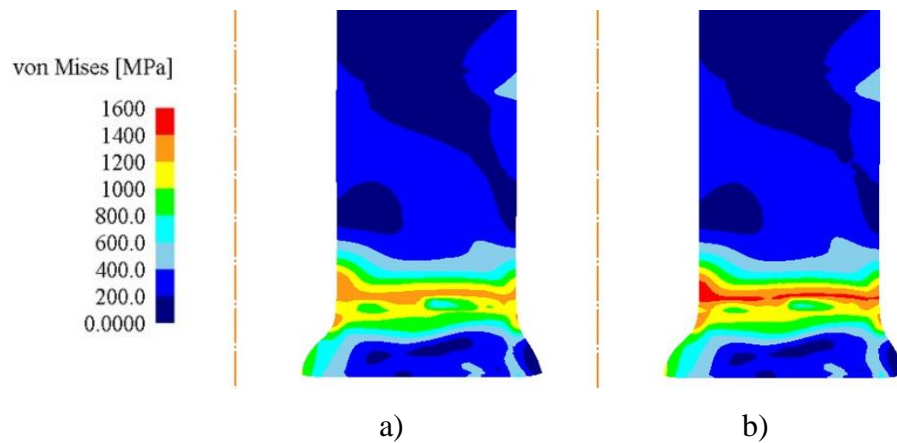


Figure 8.13. Contour plots showing the von Mises stress generated in the as-welded condition as predicted by the a) three-phase (TM, AUST, QM) and b) four-phase (TM, AUST, OTM, QM) FE model. The material database includes the constitutive behaviour of the corresponding phases as characterised by the MOF model.

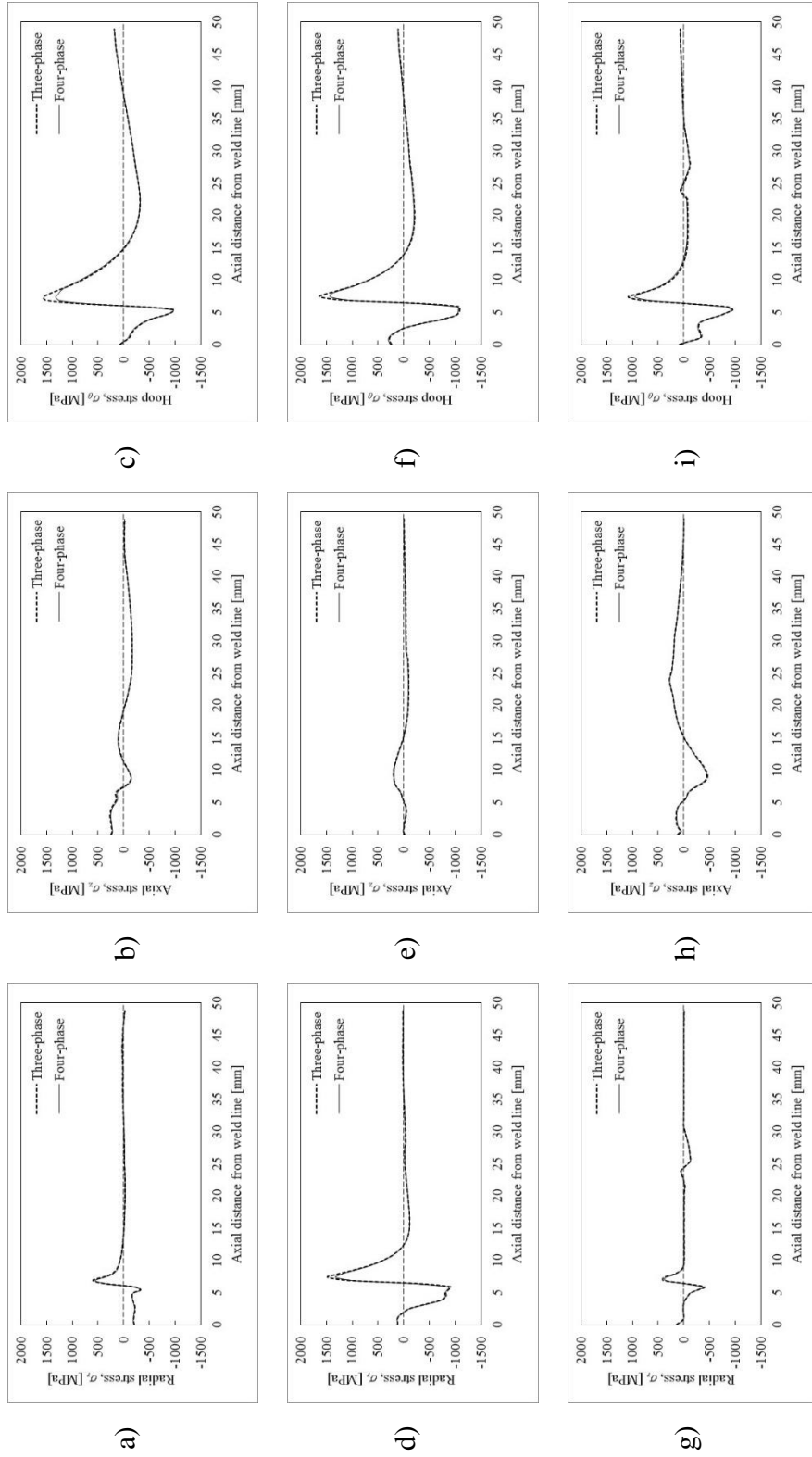


Figure 8.14. Residual stress profiles predicted in the as-welded component at a, b, c) 1 mm from the OD, d, e, f) MD and g, h, i) 1 mm from the OD by the three-phases (TM, AUST, QM) and four-phases (TM, AUST, QM) FE model. The stress direction is indicated by the title of the ordinate.

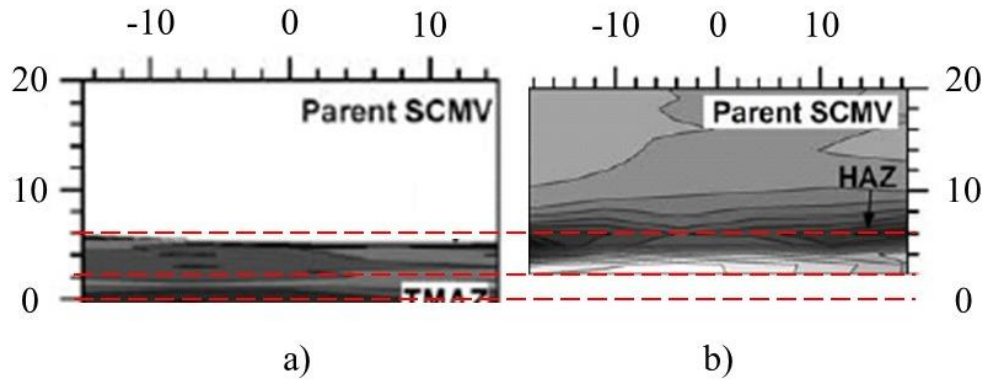


Figure 8.15. a) Retained austenite volume fraction as an indicative of martensitic transformation and b) hoop residual stress map [106]. Colour map from white to black represents a higher volume fraction and more positive stress in a) and b) respectively.

8.5. Concluding remarks

The robustness of the proposed inverse analysis to characterise three phases concerned with the IFW of an SCMV steel, namely the parent phase, tempered martensite, and two child phases, quenched martensite and over-tempered martensite, has been satisfactorily demonstrated. The reliability and repeatability of the inverse analysis was supported and validated by its capability to fit the mechanical response to indentation at different locations across the joint, where these phases are known to exist. The experimental $P-h$ curves were fitted with a maximum relative difference of 0.77% in the values of maximum indentation depth and the difference between the predicted and experimental value of the maximum pile-up height lay between 0.3 and 9.6%. Furthermore, the model converged to an optimum solution of E , σ_y and n with a variation of less than 4 and 2.6 and 7.9% respectively, regardless of the position of the initial guess parameters.

Based on the accepted relationship described by Tabor [134] between Vickers hardness (HV) and stress it was possible to associate the offset of 17% between the predicted and experimental level of stress at 8% plastic strain, with a difference of 10.5% between the corresponding values of hardness attributed to indentation size effects. Moreover, the ratio of $\sigma_{0.008}$ between the tempered martensite (TM) and each child phase, quenched martensite (QM) and over-tempered martensite (OTM), of 1.71:1 and 0.79:1 respectively, was consistent with the ratio of HV between each of

these pairs, i.e. 1.5:1 and 0.76:1, as shown in the microhardness test conducted across the joint of an inertia friction weld (IFW) of two cylindrical sections of SCM V steel.

The improved material database allowed the FE model to determine that 57% of the HAZ experienced a quenching process to form QM upon cooling and 43% experienced an over-tempering throughout the process. This was notably in good agreement with the characteristic regions observed in the microhardness test performed across the joint, in which QM and OTM occupied 54 and 46% the length of the HAZ. The parametric study carried out using a three- and four-phase FE model, concluded that the soft OTM phase relaxed between 7 to 11%, 1 to 6% and 12.8 to 15.3% the peak values of stress in the radial, axial and hoop directions respectively. Furthermore, in agreement with experimental measurements [106], it was observed that peak stresses in the hoop direction were formed at a distance corresponding with the extent of the QM region instead of with the boundary of the HAZ.

Chapter 9 - Conclusions and suggestions for future work

9.1. Inverse analysis of the depth-sensing indentation test

9.1.1 Conclusions

The multi-objective function (MOF) optimisation model described in this work has successfully addressed the non-uniqueness issue of the inverse analysis of indentation by complementing the information provided by the indentation instrument, i.e. the recorded $P-h$ curve, with AFM measurements, i.e. the geometry of the residual imprint. A thorough assessment of the iterative procedure delivered by the MATLAB *lsqnonlin* function, which has been used to solve the optimisation problem, was carried out to systematically define a pair of scaling coefficients in order to equilibrate the contribution of each objective function to the total error. Consequently, the information provided by the AFM measurement was introduced in the model in a way that enriches the lack of sensitivity of the $P-h$ curve to the strain-hardening exponent but without misleading the optimisation of the Young's modulus and yield stress. The result was a very robust model capable of converging with a variability of less than 0.5% regardless of the specification of the model parameters, such as the values of the initial guess vector and the size of the space delimited by the bound constraints. The model was also proved to be capable of distinguishing between mystical materials and therefore avoiding convergence on a solution which is a local minimum.

Three materials with different elastic-plastic behaviour, including moderate strain-hardening (CrMoV steel), a low strain-hardening (Ti-6Al-4V) and an elastic-perfectly plastic (C110 copper) material, have been selected to represent a wide range of ductile metallic materials so as to assess the generality of the MOF model. In general, the model converged faster than a single objective function (SOF) model and with a reduced variability in the solution. In addition, the MOF model was capable of recovering from an apparent local solution where the SOF model, in contrast, remained trapped. The superior fitting capabilities of the MOF model resulted in predictions of the maximum indentation depth (h_{max}) with a deviation of up to 2.4% from the value

recorded by the indentation instrument and the area of indentation with an error of less than 12.4% in relation to the measurements provided by the AFM instrument. Regardless of the very wide range of possible solutions allowed within the bound constraints, the MOF model was capable of reaching solutions to the Young's modulus, E , and yield stress, σ_y , with a variability (as characterised by one standard deviation) of less than 2.5% for all three materials. The variability of the solutions to the strain-hardening exponent, n , obtained from the indentation data of CrMoV steel was 7.2%; the larger variability of 12.5 and 21.7% in the optimised value of n that defines the strain-hardening behaviour C110 copper and Ti-6Al-4V, respectively, was attributed to the inability of the continuum mechanics approach to represent the individual crystal behaviour of the indented grains. The accurate representation of the mechanical response to indentation provided by the optimised FE models was supported by the close match with the characteristic trends observed from the AFM measurements.

This work provided a better understanding into the mechanics of indentation of crystalline materials of different microstructures, such as a fine- and coarse-grained microstructure, e.g. tempered martensite in CrMoV steel and C110 copper, respectively. In general:

- The flow of plastically deformed material is localised in a region adjacent to the indenter-material interface.
- The pile-up height decreases away from the centreline of the indenter and towards the corners of the triangular impression. Therefore, the plastically displaced material piles-up to form a dome shape with a base extending along the edge of the triangular impression; the extension of the base being dependent on the crystal behaviour of the indented grains and the size of the grains in relation to the indentation area. For instance, the base of the dome formed by the deformation of the fine grains of tempered martensite extended from corner to corner whereas the pile-up height on the very large grains of C110 copper

reduced steeply so that the end points of the base of the dome were not coincident with the corners of the triangular impression.

- In the neighbourhood of the corners of the triangle the material does not show a dominant plastic flow behaviour, i.e. piling-up or sinking-in.

However, the two-phase microstructure of Ti-6Al-4V exhibited a complex plastic deformation behaviour due to the changing material properties within individual grains of the α and β phases. Therefore, the residual imprint did not conform to any of the trends mentioned above.

The present work has shed light on some of the effects of the load scale on the mechanical response to indentation of different materials, i.e. indentation size effects (ISE). The outcomes suggest that stress-strain relationships describing the mechanical response at different scales show a similar elastic regime and plastic strain-hardening behaviour, with only the magnitude of the stress increasing as the testing load decreases. In other words, at lower scales the stress-strain curve offsets to higher stresses at the corresponding plastic strain value. In addition, experimental studies concluded that both the recovery of displacements during unloading and the degree of piling-up are relatively insensitive to ISE.

9.1.2 Suggestions for future work

For over two decades, a variety of methodologies concerned with the inverse solution to the indentation problem have been published in the literature, yet very little effort has been made to understand the mechanics of contact and plastic deformation beneath the indenter. Further studies however, should take into account the scale of the indentation in relation to the microstructural size and not only rely on the current indentation categories established by ISO 14577 [13], i.e. macro-, micro- and nano-indentation, which are based only on the maximum load and displacement of the indenter. This could add to the knowledge of the sensitivity of the plastic flow of material beneath the indenter to anisotropy and the interaction of the indenter with a number of grains and grain boundaries. Another important area for research in depth-

sensing indentation is the understanding of the effects of time-dependent displacements during loading and unloading, e.g. creep and plastic recovery, on the geometry of the residual imprint of indentation. This could provide additional information regarding the sensitivity of the mechanical response of the material to the scale of the indentation load. A plausible method to investigate the plastic history of the material during indentation is through the interpretation of the topographic measurements of the residual imprint of indentation extracted via atomic force microscopy. Nevertheless, an experimental framework concerned with the optimum operation of AFM instruments to extract useful information from the indentation surface is still absent.

The solution to the sub-micron indentation problem based on FE modelling still remains little explored due to the complexity of the formulation of the constitutive model and implementation as user-defined routines into commercial FE solvers. In addition, this requires further characterisation of the material to formulate the crystal plasticity constitutive model in order to account for the slip system subject to stress, e.g. the model introduced by Kalidindi et al. [153, 154], or the scale parameters in order to account for ISE, e.g. the mechanism-based strain gradient (MSG) [29, 30], or the conventional mechanism-based strain gradient (CMSG) plasticity theories [31]. To date, neither the crystal plasticity theory nor the mechanism-based strain gradient plasticity theory have been implemented in the inverse analysis of indentation and therefore this is logically a particular area of interest.

Furthermore, the following suggestions arise from the scrutiny of the variety of methodologies developed to recover the mechanical properties of an indented material:

- Although different mechanisms that produce a sensitivity of microhardness to indentation size effects have been reported in the literature for at least thirty years [37], it appears that there is little awareness in most of the investigations published concerned with the recovery of mechanical properties from depth-sensing indentation data regarding the gap between the mechanical response to indentation at different scales. In addition to ISE, it has been suggested that the

plastic flow of material beneath the indenter is strictly crystallographic and orientation dependent [140], instead of only being due to the ratio E/σ_y and hardening behaviour. Therefore, before moving onto the characterisation of the material, further developments should provide details of the area of indentation in relation to the size of the microstructure. Moreover, if indentations are constrained within single grains, an assessment of the sensitivity of the flow of material to the crystallographic orientation of the indented grain in relation to the edges of the indenter must be carried out.

- The three-dimensional problem of indentation using pyramidal indenters is typically approximated with a two-dimensional axisymmetric solution provided that the depth-to-projected area ratio is equivalent for a given pyramidal indenter. This approximation emerged during the early 1980s due to the limited computation resources. However, it is suggested to abandon this practice on the premise that the 2D approximation has been shown to be material dependent [155]. Furthermore, modern conventional PCs have enough computational power to solve a 3D continuum based FE model (quasi-static and isothermal) within minutes.

9.2. FE prediction of the residual stress field in inertia friction welded components

9.2.1 Conclusions

Up to three phases formed during the inertia friction welding process of a like-to-like SCM steel were characterised using the proposed inverse analysis technique. The improved material database was used to provide an insight into the residual stress formed during the inertia friction welding of the material through predictions using finite element modelling. The build-up of residual stresses was characterised in three stages: the welding stage and the initial and final cooling periods. It was concluded that the contribution of the welding stage to the residual stress field is negligible as the high temperatures present in this stage significantly reduce the yield stress of the material. In contrast, large temperature differentials are developed during the initial

cooling period yet the resulting thermal strains are accumulated as residual strains due to the difference in the magnitude and direction of strains in adjoining regions, and the constraint imposed by rigid or nearly rigid regions of material. Therefore, the initial cooling period contributes to the majority of the residual stresses developed during IFW. Phase transformations occurred only at the last cooling period, in accord with the temperatures of transformation observed in the dilatometry tests, and therefore the associated volumetric strains become dominant in the build-up of residual stresses during this period. The inclusion of the softer over-tempered martensite phase allowed the FE prediction to determine the proportion of the heat affected zone comprised by each phase in better agreement with the experimental weld-trial. Based on the interpretation of the microhardness test performed across the weld, the harder region formed due to the quenching process extends approximately 54% the length of the HAZ, whereas the rest 46% is comprised by the softer over-tempered martensitic phase. According to the FE prediction, the heat affected zone was composed by a proportion of 57% quenched martensite and 43% over-tempered martensite. A key observation from the results of the FE prediction was that the peak hoop residual stress is located at the boundary of the quenched and over-tempered martensite, and not at the edge of the heat affected zone. This observation was in agreement with the residual stress measurements published by Moat et al. [2].

9.2.2 Suggestions for future work

FE modelling of inertia friction welding involves a complex representation of multiple phenomena and thus, it is encouraging to ascertain the improvements achieved as a better representation of the material behaviour is implemented. Therefore, the inverse analysis of high temperature depth-sensing indentation is suggested as the next step towards the improvement of the material property database; the range of temperatures being limited by the capabilities of the depth-sensing indentation instrument, e.g. up to 750 °C with a NanoTest NTX instrument. This is feasible to characterise the mechanical properties that define the high temperature behaviour of the material during the cooling periods, when strain rates are low. Notwithstanding, other physical properties remain to be improved such as the thermal response with the aim of providing a better prediction of the volumetric strains resulting from thermal

expansion/contraction and phase transformation. The kinetics of precipitation of ϵ carbides and cementite during the tempering of martensitic steels has been investigated in both experimental [152], and numerical, [156] studies. However, these investigations were focused on the tempering process under a controlled temperature field and thus, there is a need to improve the understanding of the effects of the IFW process parameters on the behaviour of carbides during rapid heating cycles. This with the intention of measuring the corresponding material parameters that are required by the FE model to account for the volumetric changes experienced by the lattice throughout the tempering process.

References

1. Bennett, C.J., *Inertia Friction Welding of High Strength Aerospace Alloys*. 2007, The University of Nottingham: Nottingham.
2. Moat, R.J., Hughes, D.J., Steuwer, A., Iqbal, N., Preuss, M., Bray, S.E., Rawson, M., *Residual Stresses in Inertia-Friction-Welded Dissimilar High-Strength Steels*. Metallurgical and Materials Transactions A, 2009. **40A**: p. 2098-2108.
3. Messler, R.W., *Joining of materials and structures : from pragmatic process to enabling technology*. 1942, Boston ; Oxford Butterworth-Heinemann.
4. Oliver, W.C., McHargue, C.J., Zinkle, S.J. , *Thin film characterization using a mechanical properties microprobe*. Thin Solid Films, 1987. **153**(1-3): p. 185-196.
5. Myers, S.M., Knapp, J. A., Follstaedt, D. M., Dugger, M. T., *Mechanical properties of nickel ion-implanted with titanium and carbon and their relation to microstructure*. Journal of Applied Physics, 1998. **83**(3): p. 1256-1264.
6. Lim, Y.Y., Chaudhri, M.M., *Accurate determination of the mechanical properties of thin aluminum films deposited on sapphire flats using nanoindentations*. Journal of Materials Research, 1999. **14**(6): p. 2314-2327.
7. Dong, J., Lu, F., Wang, C., *Micromechanical behavior study of α phase with different morphologies of Ti-6Al-4V alloy by microindentation*. Materials Science and Engineering A, 2013. **580**: p. 105-113.
8. Ma, Q., Clarke, D.R., *Size dependent hardness of silver single crystals*. Journal of Materials Research, 1995. **10**(04): p. 853-863.
9. Suresh, S., Giannakopoulos, A. E., *A new method for estimating residual stresses by instrumented sharp indentation*. Acta Materialia, 1998. **46**(16): p. 5755-5767.
10. Pethica, J.B., Hutchings, R., Oliver, W.C., *Hardness measurement at penetration depths as small as 20 nm*. Philosophical Magazine A, 1983. **48**(4): p. 593-606.

11. Loubet, J.L., Georges, J. M., Marchesini, O., Meille, G., *Vickers Indentation Curves of Magnesium Oxide (MgO)*. Journal of Tribology, 1984. **106**(1): p. 43-48.
12. Doerner, M.F., Nix, W. D., *A method for interpreting the data from depth-sensing indentation instruments*. Journal of Materials Research, 1986. **1**: p. 601 - 609.
13. *ISO-14577-1:2015 Metallic materials - Instrumented indentation test for hardness and materials parameters - Part 1: Test method*. 2015: 1 rue de Varembé, 1211 Geneva 20 Switzerland.
14. Fischer-Cripps, A.C., *Nanoindentation*. Mechanical Engineering Series. 2004, New York: Springer
15. Cheng, Y., Cheng, C., *Scaling approach to conical indentation in elastic-plastic solids with work hardening*. Journal of Applied Physics, 1998. **84**: p. 1284-1291.
16. Cheng, Y., Cheng, C., *Scaling relationships in conical indentation of elastic-perfectly plastic solids*. International Journal of Solids and Structures, 1999. **36**(8): p. 1231-1243.
17. Giannakopoulos, A.E., Larsson, P.-L., Vestergaard, R. , *Analysis of Vickers indentation*. International Journal of Solids and Structures, 1994. **31**: p. 2679-2708.
18. Venkatesh, T.A., Van Vliet, K. J., Giannakopoulos, A. E., Suresh, S., *Determination of elasto-plastic properties by instrumented sharp indentation: guidelines for property extraction*. Scripta Materialia, 2000. **42**: p. 833-839.
19. Larsson, P.-L., Giannakopoulos, A. E., Söderlund E., Rowcliffe, D. J., Vestergaard, R., *Analysis of berkovich indentation*. International Journal of Solids and Structures, 1996. **33**(2): p. 221-248.
20. Oliver, W.C., Pharr, G.M., *An improved technique for determining hardness and elastic modulus using load and displacement sensing indentation experiments*. Journal of Materials Research, 1992. **7**(6): p. 1564-1583.
21. McElhaney, K.W., Vlassak, J.J., Nix, W.D., *Determination of indenter tip geometry and indentation contact area for depth-sensing indentation experiments*. Journal of Materials Research, 1998. **13**(5): p. 1300-1306.

-
22. Gao, H., Huang, Y., *Geometrically necessary dislocation and size-dependent plasticity*. Scripta Materialia, 2003. **48**: p. 113-118.
 23. Fleck, N.A., Muller, G.M., Ashby, M.F., Hutchinson, J.W., *Strain gradient plasticity: theory and experiment*. Acta Metallurgica et Materialia, 1994. **42**(2): p. 475-487.
 24. Nix, W.D., Gao, H., *Indentation size effects in crystalline materials: a law for strain gradient plasticity*. Journal of the Mechanics and Physics of Solids, 1998. **46**(3): p. 411-425.
 25. González, D., Alkorta, J., Martínez-Esnaola, J.M., Gil Sevillano, J., *Numerical analysis of the indentation size effect using a strain gradient crystal plasticity model*. Computational Materials Science, 2014. **82**(314–319).
 26. Begley, M.R., Hutchinson, J. W., *The mechanics of size-dependant indentation*. Journal of the Mechanics and Physics of Solids, 1998. **46**(10): p. 1938-1957.
 27. Alkorta, J., Martínez-Esnaola, J.M., Gil Sevillano, J., *Detailed assessment of indentation size-effect in recrystallized and highly deformed niobium*. Acta Materialia, 2006. **54**(13): p. 3445–3452.
 28. Huang, Y., Zhang, F., Hwang, K.C., Nix, W.D., Pharr, G.M., Feng, G., *A model of size effects in nano-indentation*. Journal of the Mechanics and Physics of Solids, 2006. **54**: p. 1668-1686.
 29. Gao, H., Huang, Y., Nix, W.D., Hutchinson, J.W., *Mechanism-based strain gradient plasticity - I. Theory*. Journal of the Mechanics and Physics of Solids, 1999. **47**(6): p. 1239–1263.
 30. Huang, Y., Gao, H., Nix, W.D., Hutchinson, J.W., *Mechanism-based strain gradient plasticity - II. Analysis*. Journal of the Mechanics and Physics of Solids, 2000. **48**(1): p. 99–128.
 31. Huang, Y., Qu, S., Hwang, K.C., Li, M., Gao, H., *A conventional theory of mechanism-based strain gradient plasticity* International Journal of Plasticity, 2004. **20**: p. 753–782.
 32. Swaddiwudhipong, S., Hua, J., Tho, K.K., Liu, Z.S., *C⁰ solid elements for materials with strain gradient effects*. International Journal for Numerical Methods in Engineering, 2005. **64**: p. 1400–1414.
-

-
33. Taylor, G.I., *Plastic strain in metals*. Journal of the Institute of Metals, 1983. **62**: p. 307-324.
 34. Liu, M., Tieu, A.K., Lu, C., Zhu, H., Deng, G., *A crystal plasticity study of the effect of friction on the evolution of texture and mechanical behaviour in the nano-indentation of an aluminium single crystal*. Computational Materials Science, 2014. **81**: p. 30–38.
 35. Liu, M., Lu, C., Tieu, A.K., *Crystal plasticity finite element method modelling of indentation size effect*. International Journal of Solids and Structures, 2015. **54**: p. 42–49.
 36. Liu, Y., Ngan, A.H.W., *Depth dependence of hardness in copper single crystals measured by nanoindentation*. Scripta Materialia, 2001. **44**(2): p. 237–241.
 37. Sargent, P.M., *Use of the Indentation Size Effect on Microhardness for Materials Characterization*, in *Microindentation Techniques in Materials Science and Engineering*, P.J. Blau, Lawn, B.R., Editor. 1986, ASTM International: Philadelphia. p. 160-174.
 38. Sneddon, I.N., *The relation between load and penetration in the axisymmetric Boussinesq problem for a punch of arbitrary profile*. International Journal of Engineering Science, 1965. **3**(1): p. 47-57.
 39. Ternovskii, A.P., Alekhin, V.P., Shorshorov, M.K., Khrushchov, M.M., Skvortsov, V.N., *Micromechanical testing of materials by depression*. Zavodskaya Laboratoriya, 1974. **39**(10): p. 1242–1247.
 40. Stillwell, N.A., Tabor, D., *Elastic Recovery of Conical Indentations*. Proceedings of the Physical Society, 1961. **78**(2): p. 169-179.
 41. King, R.B., *Elastic analysis of some punch problems for a layered medium*. International Journal of Solids and Structures, 1987. **23**(12): p. 1657-1664.
 42. Hay, J.C., Bolshakov, A., Pharr, G.M., *A critical examination of the fundamental relations used in the analysis of nanoindentation data*. Journal of Materials Research, 1999. **14**(06): p. 2296-2305.
 43. Tabor, D., *A Simple Theory of Static and Dynamic Hardness*. Proceedings of the Royal Society of London A, 1948. **192**: p. 247-274.

-
44. Oliver, W.C., Pharr, G.M., *Measurement of hardness and elastic modulus by instrumented indentation: Advances in understanding and refinements to methodology*. Journal of Materials Research, 2004. **19**(1): p. 3-20.
 45. Sneddon, I.N., *Boussinesq's problem for a rigid cone*. Mathematical Proceedings of the Cambridge Philosophical Society, 1948. **44**(4): p. 492 - 507.
 46. Alkorta, J., Martínez-Esnaola, J.M., Sevillano, J.G., *Absence of one-to-one correspondence between elastoplastic properties and sharp-indentation load–penetration data*. Journal of Materials Research, 2005. **20**(02): p. 432-437.
 47. Dao, M., Chollacoop, N., Van Vliet, K. J., Venkatesh, T. A., Suresh, S., *Computational modeling of the forward and reverse problems in instrumented sharp indentation*. Acta Materialia, 2001. **49**: p. 3899–3918.
 48. N'jock, M.Y., Chicot, D., Ndjaka, J.M., Lesage, J., Decoopman, X., Roudet, F., Mejias, A., *A criterion to identify sinking-in and piling-up in indentation materials*. International Journal of Mechanical Sciences, 2015. **90**: p. 145-150.
 49. Loubet, J.L., Bauer, M., Tonck, A., Bec, S., Gauthier, B. Manuel, *Mechanical properties and deformation behaviour of materials having ultra-fine microstructures*. NATO ASI Series. 1993.
 50. Bhattacharya, A.K., Nix, W.D., *Finite element simulation of indentation experiments*. International Journal of Solids and Structures, 1988. **24**(9): p. 881–891.
 51. Laursen, T.A., Simo, J.C., *A study of the mechanics of microindentation using finite elements*. Journal of Materials Research, 1992. **7**(3): p. 618-626.
 52. Johnson, K.L., *The correlation of indentation experiments*. Journal of the Mechanics and Physics of Solids, 1970. **18**(2): p. 115-126.
 53. Giannakopoulos, A.E., Suresh, S., *Determination of elastoplastic properties by instrumented sharp indentation*. Scripta Materialia, 1999. **40**(10): p. 1191–1198.
 54. Cheng, Y., Cheng, C., *Further analysis of indentation loading curves: Effects of tip rounding on mechanical property measurements*. Journal of Materials Research, 1998. **13**(4): p. 1059-1064.
 55. Cheng, Y., Cheng, C., *Relationships between hardness, elastic modulus, and the work of indentation*. Applied Physics Letters, 1998. **73**(5): p. 614-616.
-

-
56. Barenblatt, G.I., *Scaling, Self-similarity, and Intermediate Asymptotics*. 1996, Cambridge: Cambridge University Press.
 57. Ma, Z.S., Zhou, Y.C., Long, S.G., Zhong, X.L., Lu, C., *Characterization of stress-strain relationships of elastoplastic materials: An improved method with conical and pyramidal indenters*. *Mechanics of Materials*, 2012. **54**: p. 113-123.
 58. Tho, K.K., Swaddiwudhipong, S., Liu, Z.S, Zeng, K., *Simulation of instrumented indentation and material characterization*. *Materials Science and Engineering: A*, 2005. **390**(1-2): p. 202-209.
 59. Swaddiwudhipong, S., Tho, K.K., Liu, Z.S, Zeng, K., *Material characterization based on dual indenters*. *International Journal of Solids and Structures*, 2005. **42**: p. 69-83.
 60. Ogasawara, N., Chiba, N., Chen, X., *Representative Strain of Indentation Analysis*. *Journal of Materials Research*, 2005. **20**(08): p. 2225-2234.
 61. Bucaille, J.L., Stauss, S., Felder, E., Michler, J., *Determination of plastic properties of metals by instrumented indentation using different sharp indenters*. *Acta Materialia*, 2003. **51**: p. 1663–1678.
 62. Chollacoop, N., Dao, M., Suresh, S., *Depth-sensing instrumented indentation with dual sharp indenters*. *Acta Materialia*, 2003. **51**(13): p. 3713–3729.
 63. Ogasawara, N., Chiba, N., Chen, X., *Measuring the plastic properties of bulk materials by single indentation test*. *Scripta Materialia*, 2006. **54**: p. 65-70.
 64. Quian, X., Cao, Y., Lu, J., *Dependence of the representative strain on the hardening functions of metallic materials in indentation*. *Scripta Materialia*, 2007. **57**: p. 57-60.
 65. Zeng, K., Chiu, C.-h, *An analysis of load–penetration curves from instrumented indentation*. *Acta Materialia*, 2001. **49**(17): p. 3539–3551.
 66. Luo, J., Lin, J., Dean, T. A., *A study on the determination of mechanical properties of a power law material by its indentation force-depth curve*. *Philosophical Magazine*, 2006. **86**(19): p. 2881-2905.
 67. Luo, J., Lin, J., *A study on the determination of plastic properties of metals by instrumented indentation using two sharp indenters*. *International Journal of Solids and Structures*, 2007. **44**: p. 5803-5817.

-
68. Constantinescu, A., Tardieu, N., *On the identification of elastoviscoplastic constitutive laws from indentation tests*. Inverse Problems in Engineering, 2001. **9**: p. 19-44.
 69. Kang, J.J., Becker, A. A., Sun W., *Determining elastic–plastic properties from indentation data obtained from finite element simulations and experimental results*. International Journal of Mechanical Sciences, 2012. **62**(1): p. 34–46.
 70. Kang, J.J., Becker, A. A., Sun W., *A combined dimensional analysis and optimization approach for determining elastic-plastic properties from indentation test*. Journal of Strain Analysis for Engineering Design, 2011. **46**: p. 749-759.
 71. Chen, X., Ogasawara, N., Zhao, M., Chiba, N., *On the uniqueness of measuring elastoplastic properties from indentation: The indistinguishable mystical materials*. Journal of the Mechanics and Physics of Solids, 2007. **55**(8): p. 1618-1660.
 72. Cheng, Y., Cheng, C., *Can stress-strain relationships be obtained from indentation curves using conical and pyramidal indenters?* Journal of Materials Research, 1999. **14**(09): p. 3493-3496.
 73. Capehart, T.W., Cheng, Y., *Determining constitutive models from conical indentation: Sensitivity analysis*. Journal of Materials Research, 2003. **18**(04): p. 827-832.
 74. Tho, K.K., Swaddiwudhipong, S., Liu, Z.S, Zeng, K., Hua, J., *Uniqueness of reverse analysis from conical indentation tests*. Journal of Materials Research, 2004. **19**(08): p. 2498-2502.
 75. Liu, L., Ogasawara, N., Chiba, N., Chen, X., *Can indentation technique measure unique elastoplastic properties?* Journal of Materials Research, 2009. **24**(03): p. 784-800.
 76. Le, M.-Q., *A computational study on the instrumented sharp indentations with dual indenters*. International Journal of Solids and Structures, 2008. **45**(10): p. 2818-2835.
 77. Bolzon, G., Maier, G., Panico, M., *Material model calibration by indentation, imprint mapping and inverse analysis*. International Journal of Solids and Structures, 2004. **41**: p. 2957-2975.

-
78. Bolzon, G., Molinas, B., Talassi, M., *Mechanical characterisation of metals by indentation test: an experimental verification study for on-site applications*. Strain, 2012. **48**: p. 517-527.
 79. Moy, C.K.S., Bocciarelli, M., Ringer, S.P., Ranzi, G., *Identification of the material properties of Al 2024 alloy by means of inverse analysis and indentation tests*. Materials Science and Engineering A, 2011. **529**: p. 119-130.
 80. Kearns, W.H., *Welding Handbook: Resistance and solid state welding and other joining processes*. Vol. 3. 1980, Miami: American Welding Society.
 81. Bennett, C.J., Hyde, T. H., Williams, E. J., *Modelling and simulation of the inertia friction welding of shafts*. Journal of Materials Design and Applications, 2007. **221**(4): p. 275-284.
 82. Maalekian, M., *Friction welding - critical assesment of literature*. Science and technology of welding and joining, 2007. **12**: p. 738-759.
 83. Grant, B., Preuss, M., Withers, P.J., Baxter, G., and Rowlson, M. , *Finite element process modelling of inertia friction welding advanced nickel-based superalloy*. Materials Science and Engineering A, 2009. **513-514**: p. 366-375.
 84. Tumuluru, M.D., *A parametric study of inertia friction welding for low alloy steel pipes*. Welding Journal Supplement, 1984: p. 289s-294s.
 85. Moat, R., Karadge, M., Preuss, M., Bray, S., Rawson, M., *Phase transformations across high strength dissimilar steel inertia friction weld*. Journal of Materials Processing Technology, 2008. **204**(1-3): p. 48–58.
 86. Moat, R., Karadge, M., Preuss, M., Bray, S., Rawson, M., *Detailed Diffraction and Electron Microscopy Study of Inertia-Friction-Welded Dissimilar High-Strength Steels*. Metallurgical and Materials Transactions A, 2011. **42**(10): p. 3130-3140.
 87. Preuss, M., Pang, J.W.L, Withers, P.J., Baxter, G.J., *Inertia welding nickel-based superalloy: Part I. Metallurgical characterization*. Metallurgical and Materials Transactions A, 2002. **33**: p. 3215-3225.
 88. Huang, Z.W., Li, H.Y., Baxter, G., Bray, S., Bowen, P., *Electron microscopy characterization of the weld line zones of a inertia friction welded superalloy*. Journal of Materials Processing Technology, 2011. **211**: p. 1927-1936.
-

-
89. Daus, F., Li, H. Y., Baxter, G., Bray, S., Bowen, P., *Mechanical and microstructural assessments of RR1000 to IN718 inertia welds - effects of welding parameters*. Materials Science and Technology, 2007. **23**(12): p. 1424-1432.
 90. Senkov, O.N., Mahaffey, D.W., Semiatin, S.L., Woodward, C., *Inertia Friction Welding of Dissimilar Superalloys Mar-M247 and LSHR*. Metallurgical and Materials Transactions A, 2014. **45**: p. 5545-5561.
 91. Zhu, Y., Yin, Z., Liang, D., Li, J., Zhidong, X., *Microstructure and property of Ni76Cr19AlTi side in inertia friction weld joint of the superalloy Ni76Cr19AlTi and the martensite stainless steel 4Cr10Si2Mo*. ISIJ International, 2010. **50**(11): p. 1666-1670.
 92. Mortensen, K.S., Jensen, C.G., Conrad, L.C., Losee, F., *Mechanical properties and microstructures of inertia-friction-welded 416 stainless steel*. Welding Research Supplement, 2001: p. 268s-273s.
 93. Taban, E., Gould, J.E., Lippold, J.C., *Dissimilar friction welding of 6061-T6 aluminum and AISI 1018 steel: Properties and microstructural characterization*. Materials and Design, 2010. **31**: p. 2305–2311.
 94. Committee, A.S.M.I.H., *ASM Handbook, Volume 02 - Properties and Selection: Nonferrous Alloys and Special-Purpose Materials*. ASM International.
 95. Zhu, Y., Zhu, Z., Xiang, Z., Yin, Z., Wu, Z., Yan, W., *Microstructural evolution in 4Cr₁₀Si₂Mo at the 4Cr₁₀Si₂Mo/Nimonic 80A weld joint by inertia friction welding*. Journal of Alloys and Compounds, 2009. **476**: p. 341-347.
 96. Zhu, Y., Guo, Y., Yang, L., *Microstructure-Based Strength Distribution Across the Welds of Nickel-Based Superalloy Inconel 751 and Austenite Steel 21-4N Joined by Inertia Friction Welding*. Metallurgical and Materials Transactions B, 2013. **44**(2): p. 396–405.
 97. Cullity, B.D., *Elements of X-ray diffraction*. 1956: Addison-Wesley.
 98. Tiley, J.S., Mahaffey, D.W., Alam, T., Rojhirunsakool, T., Senkov, O., Parthasarthy, T., Banerjee, R., *Strengthening mechanisms in an inertia friction welded nickel-base superalloy*. Materials Science and Engineering: A, 2016. **662**: p. 26-35.

-
99. Parthasarathy, T.A., Rao, S.I., Dimiduk, D.M., *A fast spreadsheet model for the yield strength of superalloys*, in *Superalloys*, K.A. Green, Pollock, T.M., Harada, H., Howson, T.E., Reed, R.C., Schirra, J.J., Walston, S., Editor. 2004, TMS (The Minerals, Metals & Materials Society). p. 887-896.
 100. Attallah, M.M., Preuss, M., Boonchareon, C., Steuwer, A., Daniels, J.E., Hughes, D.J., Dungey, C., Baxter, G., *Microstructural and residual stress development due to inertia friction felding in Ti-6246*. *Materials Science and Engineering: A*, 2012. **43**: p. 3149-3161.
 101. Attallah, M., Bray, S., Preuss, M., *Microstructural development during linear friction welding of titanium alloys*, in *The 8th Int. Conf. on Trends in Welding Research*. 2008, ASM International: Pine Mountain, GA.
 102. Attallah, M., Zabee, S., Cernik, R.J., Preuss, M., *Comparative determination of the α/β phase fraction in $\alpha+\beta$ -titanium alloys using X-ray diffraction and electron microscopy*. *Materials Characterization*, 2009. **60**(11): p. 1248–1256.
 103. Sen, I., Ramamurty, U., *Elastic modulus of Ti–6Al–4V–xB alloys with B up to 0.55 wt.%*. *Scripta Materialia*, 2010. **62**(1): p. 37–40.
 104. Quinta da Fonseca, J., Preuss, M., Ryan, P., Withers, P.J. *Mechanical property mapping using image correlation and electronic speckle interferometry in Applied Mechanics and Materials*. 2004.
 105. Preuss, M., Withers, P.J., Bakker, G.J., *A comparison of inertia friction welds in three nickel base superalloys*. *Materials Science and Engineering: A*, 2006. **437**: p. 38-45.
 106. Moat, R.J., Hughes, D.J., Steuwer, A., Iqbal, N., Preuss, M., Bray, S.E., Rawson, M., *Residual Stresses in Inertia-Friction-Welded Dissimilar High-Strength Steels*. *Metallurgical and Materials Transactions A*, 2009. **40**(9): p. 2098-2108.
 107. Iqbal, N., Rolph, J., Moat, R., Hughes, D., Hofmann, M., Kelleher, J., Baxter, G., Withers, P. J., Preuss, M., *A Comparison of Residual Stress Development in Inertia Friction Welded Fine Grain and Coarse Grain Nickel-Base Superalloy*. *Metallurgical and Materials Transactions A*, 2011. **42**(13): p. 4056–4063.

-
108. Moal, A., Massoni, E., *Finite element simulation of the inertia welding of two similar parts*. Engineering Computations 1995. **12**: p. 497-512.
 109. Lee, K., Samant, A., Wu, W.T., Srivatsa, S., in *NUMIFORM*. 2001.
 110. Fu, L., Duan, L.Y., Du, S.G., *Numerical Simulation of Inertia Friction Welding Process by Finite Element Method*. Welding Journal Supplement, 2003: p. 65s-70s.
 111. Liwen, Z., Chengdong, L., Shaoan, Q., Yongsi, Y., Wenhui, Z., Shen, Q., Jinghe, W. , *Numerical simulation of inertia friction welding process of GH4169 alloy*. Journal of Physics, 2004. **120**: p. 681 - 687.
 112. Bu, W.D., Liu, J.H., *The Coupled Thermal Mechanical Modeling of the Inertia Friction Welding Process for Inconel718*. Materials Science Forum, 2012. **704-705**: p. 710-716.
 113. D'Alvise, L., Massoni, E., Walløe, S.J., *Finite element modelling of the inertia friction welding process between dissimilar materials*. Journal of Materials Processing Technology, 2002. **125–126**: p. 387–391.
 114. Jeong, H.S., Cho, J.R., Park, H.C., *Development of dissimilar inertia welding process of large superalloy spindle* Key Engineering Materials, 2007. **345-346**: p. 1429-1432.
 115. Balasubramanian, V., Li, Y., Stotler, T., Crompton, J., Katsube, N., Soboyejo, W.O., *Numerical simulation of friction welding of inconel 718*. American Society of Mechanical Engineers, Pressure Vessels and Piping Division (Publication) PVP, 1997. **369**: p. 289-295.
 116. Wang, F.F., Li, W.Y., Li, J.L., Vairis, A., *Process parameter analysis of inertia friction welding nickel-based superalloy*. The International Journal of Advanced Manufacturing Technology, 2014. **71(9)**: p. 1909–1918.
 117. Wang, L., Preuss, M., Withers, P.J., Baxter, G. Wilson, P., *Energy-input-based finite-element process modeling of inertia welding*. Metallurgical and materials transactions B, 2005. **36B**: p. 513-523.
 118. Balasubramanian, V., Li, Y., Stotler, T., and Crompton, J., *An energy balance method for the numerical simulation of inertia welding*. Materials and Manufacturing Processes, 1999. **14**: p. 755-773.
-

-
119. Preuss, M., Pang, J.W.L, Withers, P.J., Baxter, G.J., *Inertia welding nickel-based superalloy: Part II. Residual stress characterization*. Metallurgical and Materials Transactions A, 2002. **33**: p. 3227-3234.
 120. Bennett, C.J., Attallah, M.M., Preuss, M., Shipway, P.H., Hyde, T.H., and Bray, S., *Finite Element Modeling of the Inertia Friction Welding of Dissimilar High-Strength Steels*. Metallurgical and Materials Transactions A, 2013. **44**(11): p. 5054-5064.
 121. Soh, H., *Fretting wear studies of aeroengine materials*. 2006, The University of Nottingham: Nottingham.
 122. *ASTM-E8/E8M-15a Standard Test Methods for Tension Testing of Metallic Materials*. 2015, ASTM International: West Conshohocken, PA.
 123. Kuhn, H., Dana, M., *ASM handbook. Volume 8, Mechanical testing and evaluation*. 2000, ASM International: Materials Park, OH.
 124. *ISO 4287:1997 Geometrical Product Specifications (GPS) -- Surface texture: Profile method -- Terms, definitions and surface texture parameters*. 1997: 1 rue de Varembé, 1211 Geneva 20 Switzerland.
 125. Bruker, *NanoScope Analysis1.50*.
 126. Lim, Y.Y., Chaudhri, M.M., *Do residual nano indentations in metals and ceramics relax with time?* Journal of Physics D: Applied Physics, 2001. **34**(13): p. L70–L78.
 127. Sakharova, N.A., Fernandes, J. V., Antunes, J. M., Oliveira, M. C., *Comparison between Berkovich, Vickers and conical indentation tests: A three-dimensional numerical simulation study*. International Journal of Solids and Structures, 2009. **46**: p. 1095-1104.
 128. Meyers, M.A., *Mechanical behavior of materials*. 2009, Cambridge: Cambridge University Press.
 129. Yuan, Y. *A review of trust region algorithms for optimization*. in *ICIAM 99*. 2000. Edinburgh: Oxford University Press.
 130. Coleman, T.F., Y. Li. , *An Interior, Trust Region Approach for Nonlinear Minimization Subject to Bounds*. SIAM Journal on Optimization, 1996. **6**: p. 418–445.

-
131. Matlab, *Optimization Toolbox User's Guide*. 2016, The Math Works Inc.: USA.
 132. Mohammed, M.B., Bennett, C.J., Shipway, P.H., and Hyde, T.H., *Optimization of Heat Transfer in the Finite Element Process*, in *Heat Transfer 2010*. 2010: Tallinn, Estonia.
 133. SFTC, *DEFORM v10.2 and DEFORM v11.0 (Beta) Integrated 2D3D system manual*, J. Fluhrer, Editor. 2011: Columbus, Ohio.
 134. Tabor, D., *The hardness of metals*. Oxford Classic Texts in the Physical Sciences. 1951, Oxford: Oxford University Press.
 135. Kobayashi, S., *Metal forming and the finite element method*. 1989, New York, Oxford: Oxford University Press.
 136. Lippold, J.C., Odegard, B.C., *Microstructural Evolution During Inertia Friction Welding of Austenitic Stainless Steels*. *Welding Journal*, 1984. **63**: p. 35s-38s.
 137. Moat, R., Karadge, M., Preuss, M., Bray, S., and Rawson, M., *Phase transformations across high strength dissimilar steel inertia friction weld*. *Journal of Materials Processing Technology*, 2008. **204**: p. 48-58.
 138. Wang, K.K., Nagappan, P., *Transient Temperature Distribution in Inertia Welding of Steels*. *Welding Journal*, 1970. **49**: p. 419 - 426.
 139. Bhadeshia, H., Honeycombe, R., *Steels: Microstructure and properties*. 2006, Oxford: Butterworth-Heinemann,.
 140. Wang, Y., Raabe, D., Klüber, C., Roters, F., *Orientation dependence of nanoindentation pile-up patterns and of nanoindentation microtextures in copper single crystals*. *Acta Materialia*, 2004. **52**: p. 2229-2238.
 141. Callister, W.D., *Materials science and engineering : an introduction*. 7th ed. 1990, Hoboken, N.J. :: John Wiley & Sons,.
 142. Han, F., Tang, B., Kou, H., Li, J., Feng, Y., *Experiments and crystal plasticity finite element simulations of nanoindentation on Ti-6Al-4V alloy*. *Materials Science and Engineering A*, 2015. **625**: p. 28-35.
 143. Waterman, N.A., Ashby, M.F., *The Materials Selector*. 2nd ed. 1997, London: Chapman & Hall.

-
144. Altan, T., Oh, S., Gegel, H.L., , *Metal Forming: Fundamentals and Applications*. 1983 Metals Park, OH: ASM International.
 145. Coleman, T.F., Y. Li., *A reflective Newton method for minimizing a quadratic function subject to bounds on some of the variables*. SIAM Journal on Optimization, 1996. **6**(4): p. 1040-1058.
 146. Griepentrog, M., Ullner, C., Dück, A. *Instrumented indentation test for hardness and materials parameter from millinewtons to kilonewtons*. in *International Conference on Force, Mass, Torque, Hardness and Civil Engineering Metrology in the Age Globalization*. 2002. Celle, Germany.
 147. Roters, F., Eisenlohr, P., Hantcherli, L., Tjahjanto, D.D., Bieler, T.R., Raabe, D., *Overview of constitutive laws, kinematics, homogenization and multiscale methods in crystal plasticity finite-element modeling: Theory, experiments, applications*. Acta materialia, 2010. **58**: p. 1152–1211.
 148. Bhadeshia, H.K.D.H., Honeycombe, R., *Steels: Microstructure and Properties*. 2006, Oxford: Butterworth-Heinemann.
 149. Puškár, A., *Internal Friction of Materials*. 2001, Cambridge, U.K.: Cambridge International Science Publishing.
 150. Reitinger, B., Berer, T., Helm, O., Burgholzer, P., *Alteration of The Elastic Properties of Steel And Cast Iron Caused by Hardening*, in *Conference: International Symposium on Laser Ultrasonics*. 2008: Montreal, Canada.
 151. Medved', A.I., Bryukhanov, A. E. , *The variation of Young's modulus and the hardness with tempering of some quenched chromium steels*. Metal Science and Heat Treatment, 1969. **11**(9): p. 706–708.
 152. Bala, P., Pacyna, J., Krawczyk, J., *The kinetics of phase transformations during tempering of CrMoV medium carbon steel*. Journal of Achievements in Materials and Manufacturing Engineering, 2007. **20**(1-2): p. 79-82.
 153. Kalidindi, S.R., Bronkhorst, C.A., Anand, L., *Crystallographic texture evolution in bulk deformation processing of FCC metals*. Journal of the Mechanics and Physics of Solids, 1992. **40**(3): p. 537–569.
 154. Kalidindi, S.R., Anand, L., *Large deformation simple compression of a copper single crystal*. Metallurgical Transactions A, 1993. **24**(4): p. 989–992.

155. Swaddiwudhipong, S., Hua, J., Tho, K.K., Liu, Z.S., *Equivalency of Berkovich and conical load-indentation curves*. Modelling and Simulation in Materials Science and Engineering, 2006. **14**(1): p. 71-82.
156. Wang, Y., Denis, S., Appolaire, B., Archambault, P., *Modelling of precipitation of carbides during tempering of martensite*. Journal de Physique IV, 2004. **120**: p. 103-110.

Appendix I - Multi-objective function optimisation model MATLAB code

Script below is the MATLAB code used to solve the optimisation problem via the trust-region algorithm.

- Code main.m

```
clear;close all;
! del iteration_history.txt

global ParamHistory c1 c2 c3
format long

%===== MATERIAL PROPERTIES =====%
% Set initial guess
Ei=250000; syi=1800; ni=0.15;
%===== %

%===== OPTIMISATION SET-UP =====%
% Lower (lb)and upper (ub) bound constraints
lb=[0 0 0];
ub=[inf inf 10e-5];

% Scale coefficients for corresponding parameters
c1=1.0e-10; c2=1.0e-10; c3=1.0e-4;

% Scale initial parameters
x0=[Ei*c1 syi*c2 ni*c3];

ParamHistory=[];
tolfun=1e-15;
tolcon=1e-15;
tolx=1e-15;
maxI=1000;
maxF=1000;
%===== %

%===== LSQNONLIN =====%
options=optimset('TolFun',tolfun,'TolCon',tolcon,'TolX',tolx,...
    'MaxIter',maxI,'MaxFunEvals',maxF,'OutputFcn',@outfun);
[x,resnorm,residual,exitflag,output,lambda,jacobian]=...
    lsqnonlin(@objfunction,x0,lb,ub,options)
%===== %
```

- Function outfun.m

```
function stop = outfun(x,optimValues,state)
global c1 c2 c3
    stop = false;
    fout = fopen('iteration_history.txt','at');
    coeffs_scale=[c1 c2 c3];
```

```

xscale=x./coeffs_scale;

switch state
case 'init'
case 'iter'
    it=optimValues.iteration;
    its=num2str(it);
    x1=num2str(xscale(1));
    x2=num2str(xscale(2));
    x3=num2str(xscale(3));
    s=[its ' ' x1 ' ' x2 ' ' x3]
    fprintf(fout, '%s\n',s);
    plothp()
case 'done'
    hold off
otherwise
end
end
fclose(fout);
end

```

- Function objfunction.m

```

function f=objfunction(x)
global ParamHistory c1 c2 c3
format long
w1=1;
% Scale parameters to normal values
x1=x(1)/c1;
x2=x(2)/c2;
x3=x(3)/c3;

%===== TARGET CURVES =====%
load targetc.txt
ForceExp=targetc(:,1);
DispExp=targetc(:,2);
[Pmax_Exp,I_Exp]=max(ForceExp);

load targetsurf.txt
XSurf_Exp=targetsurf(:,1);
YSurf_Exp=targetsurf(:,2);
%===== %

%===== PREDICTED CURVES =====%
% Create new ABAQUS input file using the optimised parameters
v=0.3;
newinp(x1,x2,v,x3);

% Get load-depth curve generated by FE model using the optimised
% parameters.
load LoadDisp.txt
ForcePre=6*LoadDisp(:,1); DispPre=LoadDisp(:,2);
[Pmax_Pre,I_Pre]=max(ForcePre);

load CNcoord.txt
XData=CNcoord(:,2);
XData(2)=0;
YData=CNcoord(:,3);

```

```

[sortedX IX]=sort(XData);
sortedY=YData(IX);
%=====

%===== INTERPOLATION =====
Y1=ForcePre(1:I_Pre);
X1=DispPre(1:I_Pre);
p1=csapi(Y1,X1,ForceExp(1:I_Exp));

Y2=ForcePre(I_Pre+1:end);
X2=DispPre(I_Pre+1:end);
p2=csapi(Y2,X2,ForceExp(I_Exp+1:end));
pt=[p1;p2];

YSurf_Pre=csapi(sortedX,sortedY,XSurf_Exp);
%=====

%===== ERROR =====
% Error matrix
f1=w1*(DispExp-pt);
f2=(1-w1)*(YSurf_Exp-YSurf_Pre);
f=[f1;f2];
ErrNorm=sum(f.^2);
%=====

% Save parameter evolution history in "history.txt".
ParamHistory=[ParamHistory;[x1 x2 x3 OF1 OF2 ErrNorm cont]];
save('funeval_history.txt','ParamHistory','-ascii')
end

```

- Function newinp.m

```

function newinp(E,sy,v,n)

% Swift's power law material model
pstrain=[0:0.01:2];
s=sy.*(1+(E/sy).*pstrain).^n;

fid = fopen('FEmodules_TriLin\MaterialsModule.txt','wt');
fprintf(fid,['** MATERIALS\n**\n*Material,
name="SCMV"\n','*Elastic\n',...
num2str(E),' ','',num2str(v),'\n','*Plastic\n',])
for i=1:length(s)
    fprintf(fid,[num2str(s(i)),' ','',num2str(pstrain(i)),'\n']);
end
fclose(fid);

% Execute ABAQUS pre-processor, processor and post-processor
! type FEmodules_TriLin\PartModule.txt
FEmodules_TriLin\AssemblyModule.txt
FEmodules_TriLin\MaterialsModule.txt
FEmodules_TriLin\Int_Step_BC_Modules.txt> NanoTest.inp
! del tempfile.*
! copy NanoTest.inp tempfile.inp
! abaqus job=tempfile interactive cpus=8
pause(2)

```

```
! abaqus cae noGUI=ReadODB.py
end
```

- The following is an example of a script used to generate input data, i.e. *P-h* curve and surface profile:

```
% Experimental curve from depth-sensing indentation instrument
load RD_CrMoV1mic_240_I2_NoDwell.txt
ExpCurve=RD_CrMoV1mic_240_I2_NoDwell;
TotLoad=ExpCurve(:,1); TotDisp=ExpCurve(:,2);

% Interpolate displacement at given displacement points
[Pmax,I]=max(TotLoad)
PLoading=TotLoad(1:I);
PUnloading=TotLoad(I+1:end);
hLoading=TotDisp(1:I);
hUnloading=TotDisp(I+1:end);

NL=50; % Number of query points along loading curve
IntLoading=[linspace(0,0.24,NL+1)]';

NU=50; % Number of query points along unloading curve
IntUnloading=[linspace(0.24,0,NU+1)]';

p1=interp1(PLoading,hLoading,IntLoading);

p2=interp1(PUnloading,hUnloading,IntUnloading);

IntLoad=[IntLoading;IntUnloading];
IntDisp=[p1;p2];

IntExpCurve=[IntLoad IntDisp];

save ('targetc.txt', 'IntExpCurve', '-ascii')

% Experimental pile-up profile extracted from AFM instrument
load SurfTi64_240_I2_BB.txt
ExpSurf=SurfTi64_240_I2_BB;
Xcoord=ExpSurf(:,1); Ycoord=ExpSurf(:,2);

N=20; % Number of query points along pile-up profile
X_Int=[linspace(0,0.01,N+1)]';
Y_Int=interp1(Xcoord,Ycoord,X_Int);

IntSurf=[X_Int Y_Int]
save ('targetsurf.txt', 'IntSurf', '-ascii')
```